Optical and Optoelectronic Characterization of Lead Halide Perovskites and Its Solar Cells

Enzo Luigi Spera Anzalone

Programa de Posgrado en Física
Facultad de Ciencias, Facultad de Ingeniería
Universidad de la República

Montevideo – Uruguay
Octubre de 2025

Optical and Optoelectronic Characterization of Lead Halide Perovskites and Its Solar Cells

Enzo Luigi Spera Anzalone

Tesis de Doctorado presentada al Programa de Posgrado en Física, Facultad de Ciencias de la Universidad de la República, como parte de los requisitos necesarios para la obtención del título de Doctor en Física.

Director:
D.Eng. Prof. Ricardo Enrique Marotti Priero

Codirector:
D.Sc. Prof. Carlos Javier Perayra Alpuin

Montevideo – Uruguay
Octubre de 2025

Spera Anzalone, Enzo Luigi

Optical and Optoelectronic Characterization of Lead Halide Perovskites and Its Solar Cells / Enzo Luigi Spera Anzalone. - Montevideo: Universidad de la República, Facultad de Ciencias, Facultad de Ingeniería, 2025.

XII, 211 p. 29, 7cm.

Director:

Ricardo Enrique Marotti Priero

Codirector:

Carlos Javier Perayra Alpuin

Tesis de Doctorado – Universidad de la República, Programa en Física, 2025.

Referencias bibliográficas: p. 168 – 185.

1. Absorción, 2. Fotoluminiscencia, 3. Espectroscopía Modulada, 4. Dinámica de Portadores. I. Marotti Priero, Ricardo Enrique, *et al.* II. Universidad de la República, Programa de Posgrado en Física. III. Título.

INTEGRANTES DEL TRIBUNAL DE DEFENSA DE TESIS

D.Sc. Prof. Ariel Fernández Casoratti

D.Sc. Prof. Cecilia Stari Romano

D.Sc. Prof. Sofía Favre Samarra

D.Sc. Prof. Roberto Carlos Barragán Campos

D.Sc. Prof. Daniel Ramírez Ruiz

Montevideo – Uruguay
Octubre de 2025

A mi hijo Luca

Agradecimientos

Quisiera agradecer a todos los que hicieron este trabajo posible. A mis tutores Ricardo y Javier por todo el tiempo brindado, la orientación en mi formación y la oportunidad de formar parte de este grupo. A los colaboradores y los colegas de varios rincones del continente sin los cuales eso no sería posible.

A mis amigos, los del jardín y aquellos con los que trabajo en la sala 20 compartiendo la mayor parte del día y las actividades más divertidas del trabajo.

Muy especialmente agradezco a mi familia con la que crecí estos años, por estar siempre para mí. Empezamos siendo dos y ya somos tres.

Finalmente a todos en el instituto de física con quienes se disfruta enseñar y almorzar, siempre con una discusión interesante e inesperada. Y a todos los que ahora me olvido de nombrar con mis disculpas, por hacer que esto fuera posible.

We are at a unique stage in our history. Never before have we had such an awareness of what we are doing to the planet, and never before have we had the power to do something about that.

David Attenborough

RESUMEN

En esta tesis las propiedades ópticas (absorbancia y fotoluminiscencia) de la perovskita de yoduro de metilamonio y plomo desde temperatura ambiente hasta 15 K y su evolución con la degradación fueron estudiadas.

La absorbancia presentó un fuerte comportamiento excitónico incluso a temperatura ambiente. La fotoluminiscencia presentó diferentes comportamientos con la temperatura al transicionar de fase cristalina. Se le atribuyó un origen de recombinación de excitón libre para la fase tetragonal de alta temperatura y un origen de recombinación de excitón localizado para la fase ortorrómbica de baja temperatura.

La degradación, atribuida principalmente a la descomposición del metilamonio por radiación azul en el vacío, afectó mucho más a la fotoluminiscencia que a la absorbancia del material. Esta provocó un corrimiento de la transición de fase a mayor temperatura y una activación de la fotoluminiscencia por recombinación de excitón localizado a mayor temperatura. Esto se atribuyó al aumento de la concentración de estados de defecto.

En la segunda parte se estudian celdas solares de la perovskita yoduro de metilamonio y plomo y de bromuro de cesio y plomo. En el primer caso se analiza su perdida de eficiencia con la degradación. Ambos tipos de celdas fueron estudiadas con espectroscopias de intensidad modulada en un amplio espectro de frecuencias. Se implementaron varios modelos para analizar estas medidas.

Las celdas de yoduro de metilamonio y plomo mostraron dos ciclos en las espectroscopias de intensidad modulada que fueron atribuidos a la dinámica de huecos y electrones. Por otro lado las celdas bromuro de cesio y plomo mostraron un ciclo no ideal que fue atribuido a una distribución de procesos de transporte y también presentó una dinámica asociada a las vacancias de iones bromuro en el límite de baja frecuencia.

Palabras claves:
Absorción, Fotoluminiscencia, Espectroscopía Modulada, Dinámica de Portadores.

ABSTRACT

In this thesis the optical properties (absorbance and photoluminescence) of methylammonium lead iodide perovskite from room temperature to 15 K and its evolution with degradation were studied.

The absorbance showed strong excitonic behaviour even at room temperature. Photoluminescence exhibited different behaviours with temperature associated to the crystalline phase transition. A free exciton recombination origin was attributed to the high-temperature tetragonal phase and a localized exciton recombination origin to the low-temperature orthorhombic phase.

The degradation, attributed mainly to the decomposition of methylammonium by blue radiation in vacuum, affected the photoluminescence much more than the absorbance of the material. This caused a shift in the phase transition to higher temperatures and an activation of photoluminescence by localized exciton recombination at higher temperatures. This was attributed to the increased concentration of defect states.

In the second part, methylammonium lead iodide and caesium lead bromide perovskite solar cells are studied. In the first case, their loss of efficiency due to degradation is analysed. Both types of cells were studied using intensity-modulated spectroscopy over a broad frequency spectrum. Several models were implemented to analyse these measures.

The methylammonium lead iodide cells showed two cycles in the intensity modulated spectroscopies that were attributed to electrons and holes dynamics. On the other hand, the caesium and lead bromide cells showed a non-ideal cycle that was attributed to a distribution of transport processes and also presented a dynamic associated to bromide ion vacancies in the low frequency limit.

Keywords:
Absorption, Photoluminescence, Modulated Spectroscopy, Carrier Dynamics.

Contents

Chapter 1

Introduction

1.1 Motivation

The objective of this thesis is the study of the optical properties of lead halide perovskites (LHPs) and the optoelectronic properties of LHPs photovoltaic devices. Perovskites have an ABX_3 structure, where A is formed by fragments such as organic Methylammonium (MA^+: $CH_3NH_3^+$) or Formamidinium (FA^+: $CH(NH_2)_2^+$), inorganic elements such as Caesium (Cs^+) or a mixture of them, B is a divalent metal cation such as Lead (Pb^{2+}) or Tin (Sn^{2+}) and X is a halide such as chloride (Cl^-), bromide (Br^-), iodide (I^-) or a combination of them [1, 2]. This thesis studies two Pb perovskites. One of then, is the Methylammonium Lead Iodine (MAPI) perovskite and its structure is presented in fig. 1.1 as an example of general perovskite structure.

The research into perovskites solar cells experienced a surprising increase starting in 2009, when the first perovskite solar cell (PSC) using a hybrid sensitizer with a perovskite structure and having an efficiency of 3.8% was reported [4]. This work originated in the search for alternative materials for dye-based solar cells (dye cells or Grätzel cells). The efforts made by the scientific community in the decade and a half following this work, exploring new architectures and new materials, have currently allowed the efficiency of this type of PSCs to reach a value of 26.1% in single-junction architectures equivalent to the commercial *Si* cells [5]. This is of great importance for the photovoltaic industry, since it has been shown that the most efficient way to reduce production costs of photovoltaic energy is through increased efficiency [6]. An increase of this nature in energy conversion efficiency for a material

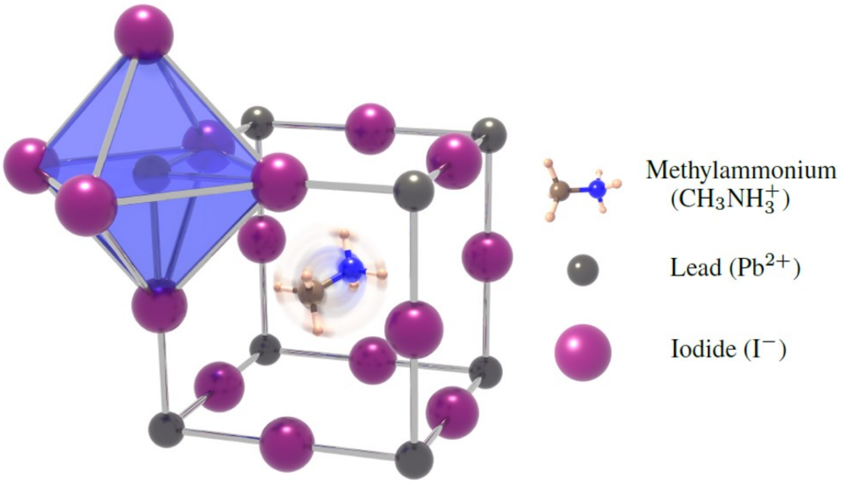

Figure 1.1: Methylammonium Lead Iodine perovskite crystal structure. Figure from [3].

(or family of materials) has never seen before in history. This led to PSCs using LHPs as absorbent materials currently being among the most efficient technologies [7, 8].

These studies have also provided deep insights into the optical and electronic properties of a wide variety of materials with the perovskite structure. These properties include: a direct bandgap, which can be tuned in the visible spectrum region using element substitution and quantum confinement effects [1], a high optical absorption coefficient [9], a diffusion length of the order of a micrometer for electrons and holes [10, 11], small values of the Urbach energy and high values of the photoluminescence efficiency with narrow emission spectra [12, 13]. Thanks to the discovery of these properties, LHPs have recently begun to be used for the manufacture of other optoelectronic devices such as lasers [14–17], light emission diodes (LEDs) [18–21], and radiation detectors [20–22] among others. On the other hand, their properties also make LHPs suitable for the manufacture of electrodes used to obtain Hydrogen from the oxidation of water molecules [23, 24] and organic compounds degradation [25].

While these devices have been highly successful in recent years and show very promising results that promise a future with perovskite-based devices on the market, they are still in the early stages of development. This is mainly because they still present stability problems that limit their duration [26, 27]. For example, PSCs show a rapid decline in their energy conversion efficiency, so their current use in commercial devices is limited. These problems are manifested in the PSCs of hybrid LHPs based on organic compounds. In principle, this problem could be overcome by using completely inorganic materials [20, 21, 26, 27]. One of the most studied inorganic LHPs has been $CsPbBr_3$. This is the other perovskite that was study in this thesis.

Another major challenge facing new perovskite-based technologies is their dependence on Pb to obtain devices with the desired properties. Pb is a highly polluting and toxic element for humans [28, 29]. Although the final step in the development of these technologies is a complete removal of Pb, this objective still seems far away, since devices that use another type of cation, for example Sn, have much lower efficiencies [30, 31]. With this in mind, this thesis also presents our collaboration for the development of a new Pb recycling technique for the manufacture of perovskites [32].

In this thesis, the degradation of MAPI perovskite samples will be studied in depth through their optical properties dependence with temperature from room temperature down to 15 K. In addition, full solar cells based on MAPI and $CsPbBr_3$ will be examined to analyse the impact of degradation on device performance. A concerted effort will be given to analyse and model their optoelectronic response across a wider frequency range than those previously reported.

By addressing these aspects, the thesis contributes to a opportune stage in perovskite research. A deeper understanding of degradation through optical and optoelectronic characterization provides essential insight into one of the main challenges limiting the long-term stability and technological deployment of perovskite solar cells

1.2 Thesis Structure

This thesis is structured in seven chapters including this introduction chapter.

The second one is the Theoretical Framework, which contains the detailed foundations of the knowledge necessary to understand all the subsequent results and conclusions of this thesis necessary for someone with a general knowledge of physics. Some of the sections of this chapter contain long and complex mathematical developments getting to the origin of the concepts. In this sense, some sections have an abstract to emphasize the main conclusions. Here the quantum mechanics and the Coulomb interactions that give origin to Wannier-Mott excitons is presented as well as their interaction with light and phonons.

The second half present the p-i-n perovskite solar cell structure and a detailed model for interpret intensity modulated photocurrent and photovoltage spectroscopy.

The chapter three is the experimental methodology chapter with implementation details. Here a brief description of the samples synthesis is included as well as the low temperature optical measurement experimental set up. Also, the description of current-voltage curves, external quantum efficiency and intensity modulated photocurrent and photovoltage spectroscopy measures is presented here.

The chapter number four present the results and conclusions about the dependence with temperature of the low temperature optical measurement on Methylammonium Lead Iodine perovskite and its changes due to the degradation process. This results lead to three peer reviewed publications, two as first author [32–34].

The chapter five presents the characterization of Methylammonium Lead Iodine perovskite solar cells. Here the current-voltage curves and its evolution under degradation are analysed. Its external quantum efficiency is presented and the intensity modulated spectroscopies are analysed and modelled. For this task, a new model is presented along with the one of chapter two. The main objective of this analysis is to model the response of the cell to a modulated illumination. This is something for which there are not much studies of this type of measures prior to 2017 in the analysed bibliography and in all cases, they are limited to analysing a portion of the frequency spectrum, either focusing on high-frequency electrons or low-frequency ions. This work attempted to study a wider frequency spectrum and for this purpose different models were implemented. Many attempts were made and not all were successful but are presented here to explain the development of the research.

The chapter six present the characterization of Caesium Lead Bromide perovskite solar cell. Here as in the previous chapter, along with current-voltage curves, the intensity modulated spectroscopies are analysed with different models, although not all were successful, they are also presented to explain the development of the research and how they lead to the final results and conclusions.

Finally, chapter seven have the general conclusions.

1.3 Publications

During this postgraduate studies the next peer reviewed papers were accepted:

- Enzo L Spera, Carlos J Pereyra, Yesica Di Iorio, Mariana Berruet, Marcela Vazquez, and Ricardo E Marotti. Charge dynamics in $CuInS_2$ photovoltaic devices with In_2S_3 as buffer layer. *Materials Chemistry and Physics*, 282:125871, apr 2022.
- Leunam Fernandez-Izquierdo, Enzo Luigi Spera, Boris Durán, Ricardo Enrique Marotti, Enrique Ariel Dalchiele, Rodrigo del Rio, and Samuel A. Hevia. CVD Growth of Hematite Thin Films for Photoelectrochemical Water Splitting: Effect of Precursor-Substrate Distance on Their Final Properties. *Molecules*, 28(4):1954, feb 2023.
- Enzo L. Spera, Carlos J. Pereyra, Daniel L. Gau, Mariana Berruet, and Ricardo E. Marotti. Excitonic optical properties of CH3NH3PbI3 perovskite and its dependence with temperature. *MRS Advances*, 9(2):39-44, jul 2023.
- Mariana Berruet, Matías A. Córdoba, Enzo L. Spera, Ricardo E. Marotti, Javier C. Pereyra, Analía V. Monti, and Kurt R. Taretto. Sustainable up-cycling of lead-acid battery waste for hybrid perovskite solar cells. *MRS Energy & Sustainability*, 11(2):606-615, 2024.
- Enzo L. Spera, Carlos J. Pereyra, Daniel L. Gau, Mariana Berruet, and Ricardo E. Marotti. Temperature dependent optical properties of methylammonium lead iodine perovskite: Influence of the initial degradation process. *Journal of Alloys and Compounds*, 1027:180553, 2025.

1.4 Other Works

During the development of this thesis several measurements were carried but they did not lead to promising results or were collaborations with other research groups. Here is presented a list of them:

- Transmittance, photo-response and intensity modulated photocurrent spectroscopy measurements of $TiO_2/Zn(O,S)/CuInS_2$ solar cells. These cells were synthesized by Ph.D. Yesica Di Iorio from the National University of Mar del Plata.

- Reflectance, transmittance and photo-resistance measurements of $BiSI$ and $Bi_{19}S_{27}I_3$. These films were synthesized by Ph.D. Maia Mombrú from the Chemistry Faculty of the University of the Republic.
- Current voltage curves and intensity modulated photocurrent spectroscopy measurements of dye-sensitized solar cells (DSSC) with anthocyanins as the absorber material. These cells were synthesized by Ph.D. Fernanda Cerdá from the Science Faculty of the University of the Republic.
- Reflectance characterization of FTO coated glasses with nanoparticles on Au. These films were synthesized D.Sc. Samuel Hevita from the Pontifical Catholic University of Santiago de Chile.
- Current voltage and intensity modulated photocurrent spectroscopy measurements of haematite electrodes for hydrogen synthesis. These films were synthesized Lic. Daniel Cerda from the Pontifical Catholic University of Santiago de Chile as part of his doctoral thesis work.

Chapter 2

Theoretical Framework

2.1 Excitons

2.1.1 The Concept

When a photon absorption take place, an electron from the valence band make a transition to the conduction band leaving a hole in the valence band. This electron and hole are created in the same spatial region and because of that, they can have a Coulomb like interaction. The negative electron feel an attractive force from the positive hole. This can create a bond between them which is an hydrogen like bond with the electron and the hole orbiting each other. This is known as a **Wannier-Mott exciton**. The Coulomb interaction link the carriers together making them move together like a quasi-particle.

But this hydrogen like system will not have the same energy levels that an hydrogen atom. To be able to apply the Bohr model, it must be considered that the electron and the hole moves inside a medium with a dielectric constant ϵ_{sc} [37]. But also must be considered the effective reduced mass μ of the system which is compose of the effective masses of the electron and the hole. This masses are different of the mass of a free electron (m_0) and depend of the concavity of the band in which the carrier moves. As a result, the energy levels as function of the quantum number (n) will be:

$$E(n) = -\left(\frac{\mu}{m_0}\right)\left(\frac{1}{\epsilon_{sc}^2}\right)\left(\frac{R_H}{n^2}\right) \tag{2.1}$$

being R_H the Rydberg constant (13.6 eV). Because of the multiplying factor, this energy levels are much smaller than those of an hydrogen atom, instead they are of the order of $10^{-3}eV$ (meV) just like shallow impurity states in semiconductors. Another effect besides the reduction of the binding energies is the increase in the Bohr radius because of the change in the effective masses and the dielectric constant. This change is given by:

$$a^* = \left(\frac{m_0}{\mu}\right) \epsilon_{sc}\, n^2 a_H \tag{2.2}$$

as a function of the Hydrogen Bohr radius a_H. This make the radius 100 times bigger than those of an hydrogen like atom and also bigger than the lattice constant.

All this makes the Wannier exciton a particle like system with an energy a few meV below the conduction band in most cases easily to break. In the solar cells case the excitons are separated by the electric field in the depletion region. This Wannier-Mott excitons can be formed in most of the inorganic semiconductors and can be dissociated by the thermal energy of the material if their binding energy is small enough.

There is another kind of exciton formed in strong ionic and organic materials in witch the electronic states do not form bands but instead have localized discrete estates on each atom position. In this materials the crystal can be seen as a set of individual atoms, each at a node of a periodic lattice. When the extension of the highest occupied atomic state and the lowest free atomic state are less than the lattice constant, an excitation of the crystal resemble an excitation of isolated atom. Then an excited atom can be seen as an electron-hole pair highly localized at one point in the lattice. In this case, because of the Coulomb interaction between the exited electron and a hole on the same crystal site a energetically favorable state is created. This is known as a **Frenkel exciton** and in this case, it has a stronger binding energy of the order of eV and its wave functions are shorter than the lattice constant [37]. Another Coulomb interaction with other energy levels in others crystal sites delocalize it allowing it to move trough the lattice [37].

2.1.2 Wannier Excitons Characteristics

The concept of Wannier excitons relies on a few accepted ideas [37]:

(i) The full valence band with an empty state can be replaced by a single quantum quasi-particle called hole, this particle have a positive charge

and a positive mass.

(ii) The valence hole and the conduction electron are taken with effective masses m_h and m_e respectively, both of which are different from the bare electron mass, this difference coming from their interactions with the periodic ion lattice. Appendix A can be consulted for more detail.

(iii) Electrons interactions in semiconductors, although affected by the periodic ion lattice witch means that their mass decreases by a factor of 10, still keep the Coulomb potential of free electrons, namely, $\frac{e^2}{\epsilon_{sc}\, r}$, this potential being simply reduced by the material dielectric constant ϵ_{sc} [37, 38].

(iv) Coulomb scatterings with zero-momentum transfer, $(\vec{q} = 0)$ are eliminated from the two particle interaction potential so it can indeed be taken equal to $\frac{4\pi e^2}{\epsilon_{sc} L^3 q^2}$ in 3D. It will be shown that the elimination of $\vec{q} = 0$ processes is achieved by properly choosing the average electron-electron potential in order to exactly compensate the long-range character of Coulomb forces.

(v) All valence-band electrons are in the description of Wannier excitons.

None of these points are obvious. They must be established on strong grounds. This is what will be done next following the developments of [37].

2.1.3 The Crystal Hamiltonian

Lets start with the Hamiltonian of N_s electrons in a periodic lattice of N_s fixed ions. In a globally neutral system, we consider that each ion has a $+|e|$ charge. The system Hamiltonian then reads in first quantization as

$$H = \sum_{j=1}^{N_s} \frac{P_j^2}{2m_0} + \sum_{j=1}^{N_s} \sum_{n=1}^{N_s} \frac{-e^2}{|\vec{r}_j - \vec{R}_n|} + \frac{1}{2} \sum_{j' \neq j}^{N_s} \frac{e^2}{|\vec{r}_j - \vec{r}_{j'}|} + \frac{1}{2} \sum_{n' \neq n}^{N_s} \frac{e^2}{|\vec{R}_n - \vec{R}_{n'}|} \quad (2.3)$$

where $\sum_{j' \neq j}$ denotes a double sum over (j', j), excluding $j' = j$ been j the index for the j-th electron. The first term is the kinetic energy of N_s free electrons, m_0 being the free electron mass in vacuum and P_j the j-th electron momentum. The three other terms are, in order, the electron-ion, electron-electron, and ion-ion potentials. Here n denotes the ion positions, $\vec{r}_j$ denotes the j-th electron position and $\vec{R}_n$ denotes the n-th ion position. The ion-ion potential does not act on electrons but ensures the neutrality of the overall system, as is necessary to cancel spurious singularities arising from the long-range character of Coulomb forces [37]. At this stage, there is no semiconductor dielectric constant in these potentials. It will appear later on when considering Coulomb excitations between valence and conduction states. Here the ions are consider as fixed, because there is no consideration about phonons here.

2.1.4 Splitting the Hamiltonian

First lets find an appropriate one-electron basis to describe semiconductors in which Wannier excitons exist. For this lets introduce an average electron-electron potential ($\overline{V}_{e-e}$)

$$\overline{V}_{e-e} = \sum_{j=1}^{N_s} \overline{v}_{e-e}(\vec{r}_j) \tag{2.4}$$

with $\overline{v}_{e-e}(\vec{r}_j)$ chosen at will for split the Hamiltonian in two parts

$$H = H_0 + V_{Coul} \tag{2.5}$$

been H_0 the one-body Hamiltonian

$$H_0 = \sum_{j=1}^{N_s} \frac{P_j^2}{2m_0} + \sum_{j=1}^{N_s} v(\vec{r}_j) = \sum_{j=1}^{N_s} h(\vec{r}_j) \tag{2.6}$$

$v(\vec{r}_j)$ is the average Coulomb potential felt by al electron in a neutral system.

$$v(\vec{r}_j) = \overline{v}_{e-e}(\vec{r}_j) + \sum_{n=1}^{N_s} \frac{-e^2}{|\vec{r}_j - \vec{R}_n|} + \frac{1}{2N_s} \sum_{n' \neq n}^{N_s} \frac{e^2}{|\vec{R}_n - \vec{R}_{n'}|} \tag{2.7}$$

the N_s in the third term cancels out when adding in j. What is called the "Coulomb potential" in eq. (2.5) is the two-body electron-electron potential but subtracting from it the average electron-electron potential introduced in H_0:

$$V_{Coul} = \frac{1}{2} \sum_{j' \neq j}^{N_s} \frac{e^2}{|\vec{r}_j - \vec{r}_{j'}|} - \overline{V}_{e-e} \tag{2.8}$$

Since we add and subtract $\overline{V}_{e-e}$ from the H Hamiltonian, this potential can be chosen at will. Yet, for $h(\vec{r})$ to have the lattice periodicity in order to possibly use the Bloch theorem to obtain its eigenstate characteristics, $\overline{V}_{e\text{–}e}$ must have this periodicity. In addition, its required that $\overline{V}_{e\text{–}e}$ to be such that V_{Coul} can be treated as a perturbation, that means, V_{Coul}, which governs the semiconductor many-body physics, must bring contributions that are small compared to the ones coming from H_0. So $\overline{V}_{e\text{–}e}$ must be choose such that it cancels the $\vec{q} = 0$ (zero momentum exchange case) term of the electron-electron interaction, which is singular due to the long-range character of Coulomb forces.

The simplest average electron-electron potential is a constant. This physically means to taking $\overline{V}_{e\text{–}e}$ as the Coulomb potential between one electron and a sea of electrons, that is, to all the $-N_s|e|$ electrons charge spread over the whole sample volume. More elaborate average potentials can be used to get better agreement with experiments, but this is enough for these calculations.

2.1.5 Bloch states

The Bloch states $\left|n, \vec{k}\right\rangle$ are eigenstates of the periodic Hamiltonian h

$$(h - \varepsilon_{n,\vec{k}}) \left|n, \vec{k}\right\rangle = 0 \tag{2.9}$$

The eigenstates are characterized by a momentum $\vec{k}$ quantized in $2\pi/L$ for a sample of size L, and a band index. The electron energies $\varepsilon_{n,\vec{k}}$ form bands which have a maximum and minimum. In samples with spherical symmetry (so that the electron effective mass does not depend on crystal orientation), $\varepsilon_{n,k}$ can be expanded close to its extrema as

$$\varepsilon_{n,\vec{k}} \simeq \varepsilon_{n,0} + \frac{\hbar^2 k^2}{2m_n} \tag{2.10}$$

m_n is the electron effective mass of the band n (See appendix A). This mass is negative for the valence band, $n = v$, which is the higher energy full band of the semiconductor, while m_n is positive for the conduction band, $n = c$, which is the lowest empty band. Usual effective masses in semiconductors are one order of magnitude smaller than the free electron mass in vacuum. This physically means that the lattice periodicity tends to lighten the electron, making it move more easily in a semiconductor crystal than in vacuum.

Notice that since $\left|n,\vec{k}\right\rangle$ are eigenstates of h, they are orthonormal.

$$\left\langle n',\vec{k}'\middle|n,\vec{k}\right\rangle = \delta_{n',n}\delta_{\vec{k}',\vec{k}} \tag{2.11}$$

2.1.6 The Hamiltonian with Bloch states Operators

For problems in which more than one electron are involved, it is convenient to use the second quantization formalism. Lets write the corresponding creation operator for the Bloch states as

$$\left|n,\vec{k}\right\rangle = a^{\dagger}_{n,k}\left|\emptyset\right\rangle \tag{2.12}$$

been $\left|\emptyset\right\rangle$ the vacuum state. From here on the arrow indicating the vector nature of $\vec{k}$ will be omitted in operators for clarity. So, the one-body part of the H Hamiltonian will be

$$H_0 = \sum_{n,k}\varepsilon_{n,k}a^{\dagger}_{n,k}a_{n,k} \tag{2.13}$$

Meanwhile, the two-body part of H in second quantization appears as

$$V_{Coul} = \frac{1}{2}\sum_{n'_1,n_1}\sum_{n'_2,n_2}\sum_{q',q}\sum_{k_1,k_2} V\begin{pmatrix} n'_2\vec{k}_2-\vec{q}' & n_2\vec{k}_2 \\ n'_1\vec{k}_1+\vec{q} & n_1\vec{k}_1 \end{pmatrix} a^{\dagger}_{n'_1k_1+q}a^{\dagger}_{n'_2k_2-q'}a_{n_2k_2}a_{n_1k_1} \tag{2.14}$$

where V is the scattering potential matrix. Since Coulomb interaction conserves momentum, the scatterings differ from zero for $\vec{q}=\vec{q}\,'$ only. As $\vec{q}\simeq 0$ processes come from large $\vec{r}$ Coulomb processes, the long-range character of $V_{e\text{–}e}$ would make the $\vec{q}=0$ scattering diverge in the large sample limit. However, it is possible to eliminate this singular $\vec{q}=0$ scattering, by choosing an appropriate average Coulomb potential $\overline{V}_{e\text{–}e}$ like the one resulting from N_s electrons delocalized into a negative sea, as described above.

The scattering in the small momentum transfer limit can be approximated as [37]

$$\lim_{(q',q\to 0)} V\begin{pmatrix} n'_2k_2-q' & n_2k_2 \\ n'_1k_1+q & n_1k_1 \end{pmatrix} \simeq \delta_{q,q'}\frac{4\pi e^2}{\epsilon_{sc}L^3q^2}\left\langle n'_1,k_1+q|n_1,k_1\right\rangle\left\langle n'_2,k_2-q'|n_2,k_2\right\rangle \tag{2.15}$$

Here $\langle n_1', k_1 + q | n_1, k_1 \rangle \simeq 1$ in this limit ($q \to 0$) and for intraband process ($n_1' = n_1$). While this scalar product cancels as $q \to 0$ for interband processes, $n_1' \neq n_1$.

The intraband process are those in witch the interacting electrons stays in their respective band. While interband process are those with one or more electrons changing its band. As a result dominant processes are going to be those in which the number of electrons in each band stays constant. Indeed, Coulomb scatterings appear with an energy denominator which is equal to the energy difference between the initial and final states of the considered Coulomb process. The processes in which one electron changes band, bring an energy change of the order of one band gap, while a processes bring an energy change of the order of two band gaps if two electrons change its bands. Due to these large energy changes, these processes can be safely dropped in many cases.

With only intraband processes the resulting effective Coulomb potential is, in terms of valence and conduction Bloch states

$$V_{Coul} \simeq \frac{1}{2} \sum_{q \neq 0} \frac{4\pi e^2}{\epsilon_{sc} L^3 q^2} \sum_{k_1, k_2} \sum_{n_1, n_2} a^\dagger_{n_1, k_1+q} a^\dagger_{n_2, k_2-q} a_{n_2, k_2} a_{n_1, k_1} \tag{2.16}$$

with n equal to c or v. Note that this potential keeps the number of electrons in each band constant.

2.1.7 Electron and Hole Operators

The next step to describe the Wannier excitons is to rewrite the Hamiltonian from conduction and valence electrons to electrons and holes. This is achieved by transforming conduction and valence electron creation operators into electron ($a^\dagger_k$) and hole ($b^\dagger_k$) creation operators along

$$a^\dagger_{c,k} = a^\dagger_k \tag{2.17a}$$

$$a_{v,k} = b^\dagger_{-k} \tag{2.17b}$$

Here the phase factors induced by the spin and orbital degrees of freedom of valence electrons are being neglected. These phase factors are crucial to properly account for polarization effects such as a photon with $\sigma+$ polarization creating an exciton with the same polarization, that is, with total spin $S = 1$. For completeness, lets mention the proper transformation of an electron with momentum $\vec{k}$ and angular momentum (j,m) into a hole

$$a_{k,j,m} = (-1)^{j-m} b^{\dagger}_{-k,j,-m} \tag{2.18}$$

This phase factor is unimportant in processes in which the number of valence electrons stays constant, as in the effective Coulomb potential of eq. (2.16). However, when this number changes, as for photon absorption or emission, having the correct phase factor is mandatory to ensure polarization conservation.

The one-body part H_0

This Hamiltonian from eq. (2.13) can be divided in conduction and valence electrons

$$H_0 = \sum_k \varepsilon_{c,k} a^{\dagger}_{c,k} a_{c,k} + \sum_k \varepsilon_{v,k} a^{\dagger}_{v,k} a_{v,k} \tag{2.19}$$

with the hole operator from (2.17) and with the relation $a^{\dagger}_{v,k} a_{v,k} = 1 - a_{v,k} a^{\dagger}_{v,k}$ for fermion operators leads to

$$H_0 = \sum_k \varepsilon_{v,k} + \sum_k \varepsilon_{c,k} a^{\dagger}_k a_k + \sum_k (-\varepsilon_{v,k}) b^{\dagger}_k b_k \tag{2.20}$$

where $\varepsilon_{c,k} \simeq \varepsilon_{c,0} + \frac{\hbar^2 k^2}{2m_c}$ with $m_c > 0$ close to the conduction band minimum and $-\varepsilon_{v,k} \simeq \varepsilon_{v,0} - \frac{\hbar^2 k^2}{2m_v}$ with $-m_v > 0$ close to the valence band maximum.

The Coulomb potential V_{Coul}

Working with eq. (2.16) which is restricted to intraband processes between conduction and valence electrons, with all scatterings identical and repulsive. Some of these scatterings becomes attractive when turning to work with holes. Lets divide it in three parts

(i) The Coulomb potential between two conduction electrons

$$V_{cc} = \frac{1}{2} \sum_{q \neq 0} V_q \sum_{k_1,k_2} a^{\dagger}_{c,k_1+q} a^{\dagger}_{c,k_2-q} a_{c,k_2} a_{c,k_1} \tag{2.21}$$

this simply become

$$V_{cc} = \frac{1}{2} \sum_{q \neq 0} V_q \sum_{k_1,k_2} a^{\dagger}_{k_1+q} a^{\dagger}_{k_2-q} a_{k_2} a_{k_1} \equiv V_{ee} \tag{2.22}$$

(ii) The Coulomb potential between a conduction electron and a valence

electron is given by

$$V_{cv} = \sum_{q\neq 0} V_q \sum_{k_1,k_2} a^\dagger_{c,k_1+q} a^\dagger_{v,k_2-q} a_{v,k_2} a_{c,k_1} \tag{2.23}$$

without the 1/2 prefactor because we can have $(n_1 = c, n_2 = v)$ or $(n_1 = v, n_2 = c)$. Since for non zero momentum transfer $a^\dagger_{v,k_2-q} a_{v,k_2}$ is equal to $-a_{v,k_2} a^\dagger_{v,k_2-q}$ and by renaming $\vec{k}'_2 = -(\vec{k}_2 - \vec{q})$,

$$V_{cv} = -\sum_{q\neq 0} V_q \sum_{k_1,k'_2} a^\dagger_{k_1+q} b^\dagger_{k'_2-q} b_{k'_2} a_{k_1} \equiv V_{eh} \tag{2.24}$$

It can be seen that the repulsive interaction between conduction and valence electrons turns into an attraction between electrons and holes, as expected for holes seen as positively charged particles. This is the potential responsible of the exciton formation.

(iii) The transformation of the Coulomb potential between two valence electrons,

$$V_{vv} = \frac{1}{2} \sum_{q\neq 0} V_q \sum_{k_1,k_2} a^\dagger_{v,k_1+q} a^\dagger_{v,k_2-q} a_{v,k_2} a_{v,k_1} \tag{2.25}$$

into the Coulomb potential between two holes is more complex. Indeed, for $\vec{q} \neq 0$, the relation $a^\dagger_{v,k_2-q} a_{v,k_2} = -a_{v,k_2} a^\dagger_{v,k_2-q}$ its still valid but $\vec{k}_2$ can be equal to $\vec{k}_1 + \vec{q}$

$$\begin{aligned} -a^\dagger_{v,k_1+q} a_{v,k_2} a^\dagger_{v,k_2-q} a_{v,k_1} &= -\left(\delta_{k_1+q,k_2} - a_{v,k_2} a^\dagger_{v,k_1+q}\right)\left(\delta_{k_2-q,k_1} - a_{v,k_1} a^\dagger_{v,k_2-q}\right) \\ = -\delta_{k_1+q,k_2} &\left(1 - a_{v,k_2} a^\dagger_{v,k_1+q} - a_{v,k_1} a^\dagger_{v,k_2-q}\right) - a_{v,k_2} a^\dagger_{v,k_1+q} a_{v,k_1} a^\dagger_{v,k_2-q} \end{aligned} \tag{2.26}$$

Using that $\delta_{k_1+q,k_2} = \delta_{k_2-q,k_1}$. As a result, the Coulomb potential between two valence electrons splits into three terms:

$$V_{vv} = -\frac{1}{2} \sum_{k_1} \sum_{k_2 \neq k_1} V_{k_2-k_1} + \frac{1}{2} 2 \sum_{k_1} a_{v,k_1} a^\dagger_{v,k_1} \sum_{k_2 \neq k_1} V_{k_2-k_1} + V_{hh} \tag{2.27}$$

The V_{hh} potential comes from the last term in eq. (2.26). Now using $a^\dagger_{v,k_1+q} a_{v,k_1} = -a_{v,k_1} a^\dagger_{v,k_1+q}$ for $\vec{q} \neq 0$ and the hole operators, this last term can become

$$V_{hh} = \frac{1}{2} \sum_{q \neq 0} V_q \sum_{k'_1, k'_2} b^{\dagger}_{k'_2 - q} b^{\dagger}_{k'_1 + q} b_{k'_1} b_{k'_2} \tag{2.28}$$

where we have set $\vec{k}'_2 = -(\vec{k}_2 - \vec{q})$, and $\vec{k}'_1 = -(\vec{k}_1 + \vec{q})$. This Coulomb potential between two positively charged holes is repulsive, just like the Coulomb potential between two valence electrons.

The first term of the valence-valence potential is a constant. It comes from the Coulomb interaction between all the valence electrons, which is forgotten when valence electrons vacancies turn into holes.

The second term in terms of hole operators is

$$\sum_k b^{\dagger}_k b_k \sum_{k' \neq k} V_{k'-k} \tag{2.29}$$

It brings an additional contribution $\sum_{k' \neq k} V_{k'-k}$ to the hole kinetic energy $(-\varepsilon_{v,k})$ in eq. (2.20). This energy shift comes from the Coulomb interaction of the valence electron $\vec{k}$ with all the other valence electrons, which is forgotten in the electron-hole description of the problem. This term appears when the $\vec{k}$ valence state is empty, that is, occupied by a hole, in order to compensate for the Coulomb interaction between all valence electrons, as given by the first term of eq. (2.27).

2.1.8 The electron-hole Hamiltonian

Leaving aside the constants in eq. (2.20) and (2.27) the Hamiltonian is rewritten as

$$H = H_e + H_h + V_{eh} + V_{ee} + V_{hh} \tag{2.30}$$

which is call the electron-hole Hamiltonian. Here are present in order the term corresponding to the free electron energy, the free hole energy, the interaction between them that give place to the exciton formation and two terms corresponding to the many-body physics interaction. The electron kinetic Hamiltonian and the hole kinetic Hamiltonian are re arranged as

$$H_e = \sum_k \varepsilon^{(e)}_k a^{\dagger}_k a_k \tag{2.31a}$$

$$H_h = \sum_k \varepsilon^{(h)}_k b^{\dagger}_k b_k \tag{2.31b}$$

with a redefinition of the hole energy to take in to account the contributions from eq. (2.27)

2.1.9 One-pair eigenstates

The correlated one-pair eigenstates of $H_{eh} = H_e + H_h + V_{eh}$ are the Wannier excitons. Their spectrum consists of bound and extended states for the electron-hole pair relative motion, the pair center of mass being delocalized as a plane wave with momentum $\vec{Q}$ over the sample volume L^3.

The formal basis

In the absence of the electron-hole potential V_{eh}, the one-pair eigenstates of $H_e + H_h$ are the free electron-hole states.

$$\left|\vec{k}_e, \vec{k}_k\right\rangle = a^\dagger_{\vec{k}_e} b^\dagger_{\vec{k}_h} \left|\emptyset\right\rangle \tag{2.32}$$

these states form a complete basis in the single-pair subspace, with a closure relation as

$$\overset{\leftrightarrow}{\mathbb{I}}_1 = \sum_{\vec{k}_e, \vec{k}_k} \left|\vec{k}_e, \vec{k}_k\right\rangle \left\langle \vec{k}_e, \vec{k}_k\right| \tag{2.33}$$

This basis can be used as a one-pair basis for the correlated pair state $|i\rangle$, eigenstate of the Hamiltonian in the presence of Coulomb attraction:

$$\left(H_e + H_h + V_{eh} - E_i\right)|i\rangle = 0 \tag{2.34}$$

$|i\rangle$ can be expanded in the one-pair basis

$$|i\rangle = \sum_{\vec{k}_e, \vec{k}_k} \left|\vec{k}_e, \vec{k}_k\right\rangle \left\langle \vec{k}_e, \vec{k}_k \middle| i\right\rangle \tag{2.35}$$

Now it is possible to define a creator operator for the correlated pair

$$|i\rangle = B^\dagger_i \left|\emptyset\right\rangle \tag{2.36}$$

This creation operator for excitons can be related to the free electron and free hole creation operators as

$$B^\dagger_i = \sum_{\vec{k}_e, \vec{k}_k} a^\dagger_{\vec{k}_e} b^\dagger_{\vec{k}_h} \left\langle \vec{k}_e, \vec{k}_k \middle| i\right\rangle \tag{2.37}$$

Since Coulomb interaction conserves momentum, the free pair states $\left|\vec{k}_e, \vec{k}_k\right\rangle$, which are scattered by Coulomb processes and become the correlated pair state $|i\rangle$, their total momentum $\vec{k}_e + \vec{k}_h$ is conserved, this momentum being the center-of-mass momentum $\vec{Q}_i$ of the correlated pair $|i\rangle$; so, the double sum can be reduced to one sum.

Because of this, it is possible to re write the momentum of the free electron and the free hole as

$$\hbar\vec{k}_e = \vec{p} + \beta_e \hbar\vec{Q}_i \tag{2.38a}$$

$$\hbar\vec{k}_h = -\vec{p} + \beta_h \hbar\vec{Q}_i \tag{2.38b}$$

with $\beta_e = 1 - \beta_h = \frac{m_e}{m_e+m_h}$. Then the free pair kinetic energy will be

$$\varepsilon^{(e)}_{p+\beta_e Q_i} + \varepsilon^{(h)}_{-p+\beta_h Q_i} = \frac{\hbar^2 Q^2}{2M_x} + \frac{p^2}{2\mu_x} + E_{gap} \tag{2.39}$$

with $M_x = m_e + m_h$ the total mass, $\mu_x^{-1} = m_e^{-1} + m_h^{-1}$ and E_{gap} the semiconductors bandgap.

With this changes for the momentum, the exciton creation operator can be written as

$$B^\dagger_{Q_i,\nu_i} = \sum_p \xi^{(\nu_i)}_p a^\dagger_{p+\beta_e Q_i} b^\dagger_{-p+\beta_h Q_i} \tag{2.40}$$

where the prefactor $\xi^{(\nu_i)}_p$ is the relative motion wave function of the electron-hole pair forming the $i = (Q_i, \nu_i)$ Wannier exciton state with ν_i being the relative motion state (solidary to the center of mass) taken so:

$$\xi^{(\nu_i)}_p = \langle \vec{p}\,|\nu_i\rangle \tag{2.41}$$

The relative motion wave function of a Wannier exciton

If the interaction term between the electron and the hole that create the exciton is considered:

$$\begin{aligned} &(H_e + H_h + V_{eh})\, B^\dagger_{Q_i,\nu_i} |\emptyset\rangle \\ &= \sum_p \left\{ \left(E_{gap} + \frac{\hbar^2 Q^2}{2M_x} + \frac{p^2}{2\mu_x} \right) \xi^{(\nu_i)}_p - \sum_{q\neq 0} V_q \xi^{(\nu_i)}_{p-q} \right\} a^\dagger_{p+\beta_e Q_i} b^\dagger_{-p+\beta_h Q_i} |\emptyset\rangle \end{aligned} \tag{2.42}$$

This shows that $B^\dagger_{Q_i,\nu_i}|\emptyset\rangle$ is an eigenstate of the one-pair correlated Hamiltonian H_{eh} with an energy $E_{gap} + \frac{\hbar^2 Q^2}{2M_x} + \varepsilon_{\nu_i}$ and that the wave function $\xi_p^{(\nu_i)}$ fulfills

$$\frac{p^2}{2\mu_x}\xi_p^{(\nu_i)} - \sum_{q\neq 0} V_q \xi_{p-q}^{(\nu_i)} = \varepsilon_{\nu_i}\xi_p^{(\nu_i)} \tag{2.43}$$

The above equation is nothing but the Schrödinger equation for the relative motion of a hydrogen-like atom with effective mass μ_x in a medium having a dielectric constant ϵ_{sc}. This result confirm the initial description of a wannier exciton as an hydrogen like system with a much smaller binding energy.

The total energy of a Wannier exciton then has a contribution from the hydrogen like system, the bandgap energy and the kinetic energy of the center of mass of the exciton

$$E_{\nu_i}(\vec{Q}, n) = E_{gap} + \frac{\hbar^2 Q^2}{2M_x} - \frac{R_H^*}{n^2} \tag{2.44}$$

The energy spectrum of a Wannier exciton is shown schematically in fig. 2.1. This is a diagram of the energy of an exciton as a function of its center of mass wavevector (K in the figure) for different values of its quantum number n. Since the exciton is a two-particle state, its energy levels cannot be represented by one electron energy levels. In the one-electron picture the ground state of the semiconductor is represented by a filled valence band and an empty conduction band. Since there are no electron–hole pairs in the ground state, this state is represented by the origin in the two-particle picture. Because of this it is not strictly correct to compare this with a band diagram. When the exciton energy is above the free pair energy the exciton is ionized and we recover the free conduction electron and the the free hole.

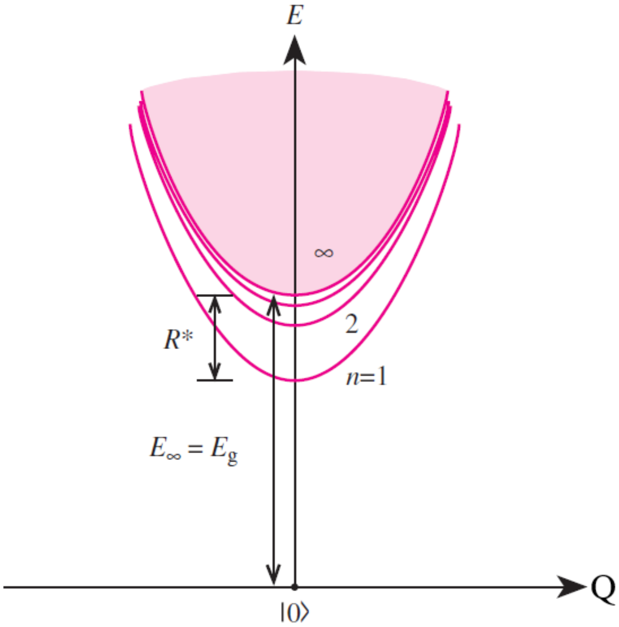

Figure 2.1: The energy states of a Wannier exciton showing both its bound states $n = 1$ to *3* and the continuum states. E_g is the bandgap and R_H^* the exciton binding energy. Figure from [39]

2.2 Photocreation of a Wannier exciton

The exciton creation through the absorption of a photon is a complex process that also involves a phonon as a mediator. The calculation of the excitonic absorption spectra was first done by Elliott in 1957 [40]. The main results are that as the exciton is an hydrogen like energy system, the absorption spectra have a set of discrete energy levels with decreasing amplitude with the quantum number and above them, a continuum energy set of states. This is because for energies higher than the binding energy, the exciton is ionized and leads to a transition to an electron in the conduction band and a hole in the valence band. But even this interband absorption behaves differently from a direct band absorption because this process involve the creation of a high energy exciton that then dissociates leaving a free electron in the conduction band and a free hole in the valence band. This absorption process is much stronger than the direct band to band absorption which make the materials with this kind of absorption much better absorbers than other materials. A comparison of the excitonic absorption and the direct band to band absorption can be seen in fig. 2.2

In principle, the absorption spectra of excitons can be calculated by introducing an interaction Hamiltonian between excitons and photons. Conceptually, however, the optical absorption by excitons is different from optical absorption in the one-electron picture. When an exciton-photon interaction (even a weak one) is introduced, the resultant eigenstates are linear combinations of the photon and exciton eigenstates. Such a “coupled state” of an exciton with a photon is known as an exciton-polariton.

In general, “polariton” is the name given to any coupled electromagnetic and polarization wave travelling inside a medium. The polarization wave in the present case is associated with the electric dipole moments of the excitons (assumed to be non-zero). As excitons travel in the medium they radiate electromagnetic waves. In turn, the electromagnetic waves can excite excitons. In principle, there is no way to separate the exciton wave from the electromagnetic wave. Thus introducing an exciton–photon interaction does not necessarily mean that energy will be lost by photons inside the medium. In this polariton picture energy is converted from photons to excitons and vice versa. Suppose the sample is a thin plate and light is incident on the sample from the left. Outside the sample there is only an electromagnetic field associated with the photons. As it enters the sample the electromagnetic wave is converted into a polariton wave. Unless there are other interactions that can scatter the polaritons inside the sample, they will travel unattenuated to the sample surface on the right. On exiting the plate from the right surface, the polaritons are reconverted into photons with no loss except for those polaritons reflected back at the surface. Thus no optical absorption has occurred inside the medium. In order for absorption to occur (that is, for energy to be dissipated from the photon field that enters the sample) polaritons have to be scattered inelastically, e. g., by phonons. After inelastic scattering some polaritons will be absorbed and others eventually exit the sample and appear in the form of emission (photoluminescence) at a different photon energy.

It is rather complicated to calculate the optical absorption using the exciton-polariton picture since it is necessary to introduce energy dissipation processes for polaritons via phonon scattering. One way to avoid this difficulty is to assume that, as a result of scattering between excitons and phonons, the exciton damping constant is larger than the exciton–photon interaction. In this approximation one can replace polaritons by the photons and excitons just interacting. Whenever a photon is converted into an exciton it will lose its energy completely inside the medium via exciton damping processes. As a result, the rate of dissipation of energy from the photon field is completely determined by the rate of conversion of photons into excitons [39].

This interaction between excitons and photons can be write using the linear term of the field potential of the photons-electron interaction.

$$W = \frac{e}{mc}\vec{A}\cdot\vec{p} \tag{2.45}$$

with

$$A = -\frac{E_0}{2Q_\gamma}\left[e^{i\left(\vec{Q}_\gamma\cdot\vec{r}-\omega t\right)} + c.c.\right] \tag{2.46}$$

Where $\vec{Q}_\gamma$ is the photon momentum, E_0 the electric field and c.c. stands for complex conjugate. This interaction includes the annihilation of a valence electron, the creation of a conduction electron and the annihilation of a photon. But this also can be written as the creation of a hole and an electron with the operators defined in eq. (2.17) forgetting phase factors linked to spin and orbital degrees of freedom and restricting ourselves to the electric dipole transitions.

$$W = \sum_{Q_\gamma}\Omega_{Q_\gamma}\alpha_{Q_\gamma}\sum_{p}a^\dagger_{p+\beta_e Q_\gamma}b^\dagger_{-p+\beta_h Q_\gamma} \tag{2.47}$$

Where α_{Q_γ} is the photon annihilation operator and $\Omega_{Q_\gamma} = A(Q_\gamma)|P_{cv}|$ the field potential amplitude times the transition matrix element which can be approximated as a constant in the $\vec{k}\to 0$ limit. This means that this also can be rewrite in terms of the exciton creation operator (2.40)

$$W = \sum_{Q_\gamma}\Omega_{Q_\gamma}\alpha_{Q_\gamma}\sum_{\nu_i}B^\dagger_{Q_i,\nu_i}\sum_{p}\langle\nu_i|p\rangle \tag{2.48}$$

The sum over $\vec{p}$ is calculated through a trick. Since the free electron wave function in a size L sample is given by $\langle r|k\rangle = e^{i\vec{k}\cdot\vec{r}}/L^{D/2}$, where D is the space dimension, we can replace 1 with $L^{D/2}\langle p|r=0\rangle$. So,

$$\sum_{p}\langle\nu_i|p\rangle = L^{D/2}\sum_{p}\langle\nu_i|p\rangle\langle p|r=0\rangle = L^{D/2}\langle\nu_i|r=0\rangle \tag{2.49}$$

Using this result its possible to write the potential as

$$W = \sum_{i}\sum_{Q_\gamma}\Omega_{Q_\gamma,i}B^\dagger_i\alpha_{Q_\gamma} \tag{2.50}$$

where the coupling between an $i = (Q_i, \nu_i)$ exciton and a Q_γ photon is given by

$$\Omega_{Q_\gamma,i} = \Omega_{Q_\gamma} L^{D/2} \langle \nu_i | r = 0 \rangle \, \delta_{Q_\gamma,Q_i} \tag{2.51}$$

The standard way to calculate photon absorption is through the Fermi golden rule. Using it to calculate the optical transition probability per unit volume from a state without excitons $|I\rangle$ to a final state $|F\rangle$ we get

$$R = \frac{2\pi}{\hbar} \sum_F | \langle F | W | I \rangle |^2 \delta(E_F - E_i) \tag{2.52}$$

being E_F the final state energy and E_i is the initial state energy.

The contributions to the imaginary part of the dielectric function (ϵ_i) due to exciton absorption consists of two parts: one arising from the bound states and the other from the continuum. For the discrete bound states, we have a initial state $|I\rangle$ made of N_γ photons and no excitons so,

$$|I\rangle = |N_\gamma\rangle \otimes |\emptyset\rangle \tag{2.53}$$

thus

$$W |I\rangle = \sum_i \Omega_{Q_\gamma} \alpha_{Q_\gamma} |N_\gamma\rangle \otimes B_i^\dagger |\emptyset\rangle \tag{2.54}$$

Since $\alpha_\gamma |N_\gamma\rangle = \sqrt{N_\gamma - 1}\, |N_{\gamma-1}\rangle$, while $|N_{\gamma-1}\rangle \otimes B_i^\dagger |\emptyset\rangle$ is an eigenstate of the exciton-photon interaction Hamiltonian with an energy $(N_\gamma - 1)\hbar\omega + E_i$ (defined in eq. (2.44)) we get, including the photon-exciton coupling (2.51) an absorption coefficient

$$A = 2N_\gamma \frac{|P_{cv}|^2}{\hbar\omega} L^D \sum_{\nu_i} | \langle \nu_i | r = 0 \rangle |^2 \delta \left(E_{gap} + \frac{\hbar^2 Q^2}{2M_x} - \frac{R_H^*}{n^2} - \hbar\omega \right) \tag{2.55}$$

As is physically reasonable, the absorption rate is proportional to the light intensity through the photon number N_γ. The absorption spectrum appears as a set of delta peaks for photon energies $\hbar\omega_\gamma$ equal to all possible bound exciton energies. The amplitude of these peaks scales as $| \langle \nu_i | r = 0 \rangle |^2$. Since the square of the $r = 0$ wave functions for 3D bound states is nonzero only for $l = 0$, **only excitons with s symmetry can be optically excited**. Using the hydrogen atom wavefunctions with energy $\varepsilon_n = -\frac{R_H^*}{n^2}$, one can show that the oscillator strength of the bound states with quantum number n decreases as n^{-3} so the absorption spectrum is dominated by the ground-state peak.

Then its possible to prove [38, 39] that the imaginary part of the dielectric function is proportional to

$$\epsilon_i \propto \frac{|P_{cv}|^2}{\hbar\omega^2} \sum_{n=1} \frac{2\pi R_H^*}{n^3} \delta\left(\hbar\omega - \frac{R_H^*}{n^2}\right) \tag{2.56}$$

For the continuum states the exciton wavefunctions can be expressed in terms of confluent hypergeometric functions. In this case its necessary to recalculate the probability per unit of time for the exciton direct transition for an incident radiation of density $\rho(\omega)$ given by [39]:

$$R = |\langle F|W|I\rangle|^2 \delta(E_i - E_f - \hbar\omega)\rho(\omega) \tag{2.57}$$

here the initial state is the vacuum state as previously discussed but in this case the final state is in the continuum states of excitons. This exciton wave functions $|F\rangle$ are expressed in terms of the hypergeometric functions within the hydrogenic approximation. These continuum wave functions can be decomposed into the product of a radial wave function $R(r)$ and the spherical harmonic. $R(r)$ have a dependency with the exciton kinetic energy E and wave vector $\vec{K}$ and has the form:

$$R(r) = \left[\frac{e^{\pi x}}{V^{1/2}(l-1)!}\right] |\Gamma(l+1-ix)|(2Kr)^l e^{i\vec{K}\cdot\vec{r}} F(l+1-ix, 2l+2, -2iKr) \tag{2.58}$$

In this expression l is the usual angular momentum quantum number of the exciton and V is the unit cell volume, x is a dimensionless quantity related to the exciton kinetic energy $E(K) = \frac{\hbar^2 K^2}{2M_x}$ (M_x is the exciton mass) and the R^* exciton Rydberg constant

$$x = \left(\frac{R^*}{E}\right)^{1/2} \tag{2.59}$$

Γ is the Gamma function and F is the confluent hypergeometric function [41]. They are defined by an infinite series of the form:

$$F(a, b, z) = 1 + \frac{a}{b}\frac{z}{1!} + \frac{a(a+1)}{b(b+1)}\frac{z^2}{2!} + ... \tag{2.60}$$

From this definition it is clear that b cannot be 0 or a negative integer. For $b > 0$ the series will converge for all finite z provided both a and b are real. We are, however, only interested in direct and allowed excitonic optical transitions. As shown in (2.51) the transition matrix element depends on the magnitude of the final exciton wave function $|F\rangle$ at $r = 0$. For direct and allowed transitions $l = 0$. The radial wave function its simplified to:

$$\begin{aligned} R(0) &= \left[\frac{e^{\pi x}}{V^{1/2}(l-1)!}\right] |\Gamma(1-ix)| F(1-ix, 2, 0) \\ &= \left[\frac{e^{\pi x}}{V^{1/2}(l-1)!}\right] |\Gamma(1-ix)| \end{aligned} \tag{2.61}$$

Now its necessary to calculate the magnitude of the Gamma function with a complex argument. We will use the Gamma function properties:

$$\Gamma(1+n) = n\Gamma(n) \tag{2.62a}$$

$$\Gamma(n)\Gamma(1-n) = \frac{\pi}{sen(\pi n)} \; for \; 0 < n < 1 \tag{2.62b}$$

From the above results one can show that:

$$\Gamma(1-ix) = (-ix)\Gamma(-ix) \tag{2.63}$$

and hence

$$\Gamma(ix)\Gamma(-ix) = \frac{-\pi}{(ix)sen(ix\pi)} \tag{2.64}$$

From the Weierstrass definition of the Gamma function we can show that the complex conjugate of $1/\Gamma(ix)$ is $1/\Gamma(-ix)$. Combining these results together we find the magnitude of the Gamma function with an imaginary argument:

$$|\Gamma(1-ix)|^2 = |x|^2|\Gamma(-ix)|^2 = \frac{\pi x}{senh(\pi x)} \tag{2.65}$$

Finally, when we substitute this expression for $|\Gamma(1-ix)|^2$ into $|R(0)|^2$ we obtain:

$$|R(0)|^2 = \frac{\pi x e^{\pi x}}{senh(\pi x)} \tag{2.66}$$

For a given photon energy $\hbar\omega$ bigger than the energy gap E_g, the kinetic energy is $E = \hbar\omega - E_g$ and $x = [R^*/(\hbar\omega - E_g)]^{1/2}$.

The corresponding contribution of exciton absorption for a direct allowed transition to the imaginary part of the dielectric function is given by

$$\epsilon_i \propto \frac{|P_{cv}|^2(\hbar\omega - E_g)^{1/2}\pi x e^{\pi x}}{\hbar^2\omega^2 senh(\pi x)} \tag{2.67}$$

Fig. 2.2 shows schematically the exciton absorption coefficient, including contributions from both the bound and continuum states. The broken curve displays the corresponding absorption coefficient when the exciton effect is neglected. We note that the exciton effect enhances the absorption coefficient both above and below the bandgap. Instead of decreasing to zero at the bandgap, the absorption coefficient approaches a constant.

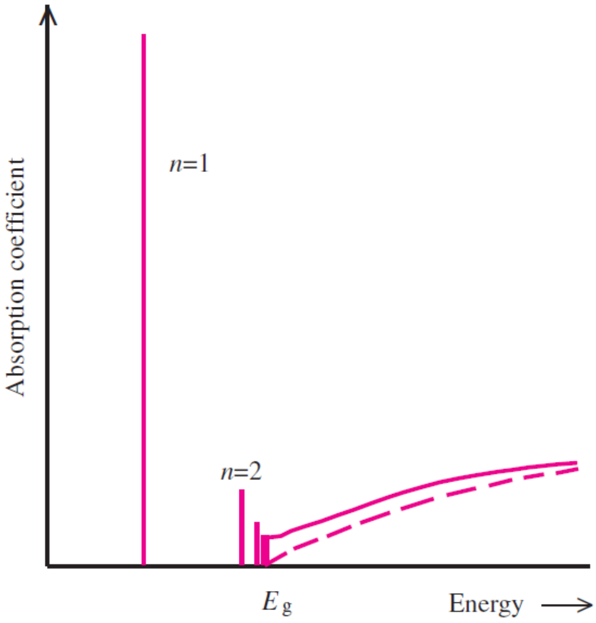

Figure 2.2: Comparison between the absorption spectra in the vicinity of the bandgap of a direct-gap semiconductor with (*solid lines*) and without (*broken curve*) exciton effects. Figure from [39].

This previous, perhaps somewhat tedious, development was first carried out by Elliott, which gave rise to Elliott's model [40] for excitonic absorbance in materials with permitted direct transitions, which will be used later:

$$\alpha(\hbar\omega) \propto \frac{P_{cv}^2}{\hbar\omega}\left[R_H^* \sum_{n=1}^{\infty} \frac{2\pi}{n^3}\delta\left(\hbar\omega - E_g + \frac{R_H^*}{n^2}\right) + \Theta(\hbar\omega - E_g)\frac{\pi e^{\pi x}}{sinh(\pi x)}\right] \tag{2.68}$$

In practice, for the Elliott model implementation to fit experimental measures, only the first peak will be considered ($n = 1$) and the Dirac delta δ distribution will be implemented as Lorentzian, Gaussian and Pseudo-Voigt functions, and Θ is a Heaviside step distribution implemented as a sigmoidal function.

2.3 Phonon Contribution to absorption

The absorption of a photon and the creation of an exciton is mediated by a phonon through an inelastic scattering. This scattering implies the absorption or emission of phonons associated to the photon absorption. This leads to a broadening of the absorption peaks which otherwise would be sharp delta peaks. This broadening process can be explained with a harmonic oscillator model with a damping constant that quantify the life time of the phonon interaction. Using the response function theory is possible to calculate the complex and frequency dependent dielectric function of the material. The dielectric function, as will be show next, have a Lorentzian shape for the imaginary part (associated to the absorption processes). This is the expected shape for an homogeneous absorption and allow to relate the width of the absorption peak with the aforementioned damping constant.

Previously it was discussed that the coupled state of polaritons made from photons and excitons does not losses energy and that inelastic scattering with phonons is necessary to explain the absorption process. We assume that whenever a photon is converted into an exciton it will lose its energy completely inside the medium via exciton damping processes and we have been able to calculate an absorption spectra leading to the Elliott model with delta functions. In practice, no delta function absorption is ever observed. A real measure have peaks with a width of tens of meV due to the inelastic scattering with phonons. This can be taken into account considering that the polaritons do not last forever but instead have a damping rate associated to a finite lifetime τ. This lead to the homogeneous widening of the absorption.

Its possible to explain with it a classical model where the absorption is considered like an harmonic oscillator with an eigenfrequency ω_0 associated to the energy of the transition with a damping rate $\Gamma = \frac{1}{\tau}$ that take in consideration the inelastic phonon dispersion. Indeed, let us assume that the oscillator has been excited in the past and is now performing damped oscillations. Clearly, the energy from the oscillator will dissipate with time. The equation of free motion of a damped oscillator is:

$$m\ddot{u} + 2\Gamma m\dot{u} + m\omega_0^2 u = 0 \tag{2.69}$$

Solving for u, we obtain an oscillation with an envelope decreasing exponential.

$$\vec{u} = \vec{u}_0 e^{-\Gamma t} e^{\pm i\tilde{\omega}_0 t} \tag{2.70}$$

defining $\tilde{\omega}_0 = \sqrt{\omega_0^2 - \Gamma^2} \simeq \omega_0$ for $\omega_0 >> \Gamma$.

Then for a single induced dipole moment $\vec{p} = -q\vec{u}$, the polarization of N dipoles turns out to be:

$$\vec{P} = -Nq\vec{u}_0 e^{-\Gamma t} e^{\pm i\tilde{\omega}_0 t} \tag{2.71}$$

This would be the transient polarization in a material after turning off the excitation. To show that this behaviour leads to the homogeneous widening of the absorption, we will use the response function theory [42]. So, lets dedicate a few paragraphs to explain it.

The polarization of the medium is caused by the external electric field (disregarding ferroelectric materials). Due to the causality principle, the polarization at a given time t depends on the field at the same moment as well as at previous moments t', but not on the field behaviour in the future. We therefore postulate the following general relationship for the polarization as a functional of the electric field [42]:

$$\vec{P}(t) = \varepsilon_0 \int_{-\infty}^{t} \kappa(t,t')\vec{E}(t')dt' \tag{2.72}$$

This postulates that the polarization at any time t may principally depend on the first power of the field at the current and all previous moments, as follows from the integration interval that is chosen in correspondence with the mentioned causality principle. The specific way, in which the system "remembers" the field strength at previous moments, is hidden in the response function $\kappa(t,t')$, which must be specific for any material. Eq. (2.72) is in fact the first (linear) term of an expansion into a Taylor power series of $\vec{E}$. As we hold only the linear term of the series, all optical effects that arise from (2.72) form the field of linear optics.

In general, when the materials are anisotropic, $\kappa(t,t')$ is a tensor. As we restrict our attention here to optically isotropic materials, $\vec{P}$ will always be parallel to $\vec{E}$, so that $\kappa(t,t')$ becomes a scalar function.

Its possible to do a further simplification due to the homogeneity of time, $\kappa(t,t')$ will in fact not depend on both times t and t' separately, but only on their difference $\zeta \equiv t - t'$.

$$\vec{P}(t) = \varepsilon_0 \int_0^{\infty} \kappa(\zeta)\vec{E}(t-\zeta)d\zeta \tag{2.73}$$

Now, if we assume that the electric field oscillate harmonically with a frequency ω like $\vec{E}(t) = \vec{E}_0 e^{-i\omega t}$, then

$$\vec{E}(t-\zeta) = \vec{E}_0 e^{-i\omega t} e^{i\omega\zeta} \tag{2.74}$$

With this monochromatic field, the polarization would be:

$$\vec{P}(t) = \vec{E}_0 e^{-i\omega t} \varepsilon_0 \int_0^{\infty} \kappa(\zeta) e^{i\omega\zeta} d\zeta \tag{2.75}$$

We define the linear dielectric susceptibility χ, complex and frequency-dependent as expected, according to:

$$\chi(\omega) = \varepsilon_0 \int_0^{\infty} \kappa(\zeta) e^{i\omega\zeta} d\zeta = \epsilon(\omega) - 1 \tag{2.76}$$

This theory allows us to calculate the susceptibility and consequently the dielectric function.

Let us return now to our transient polarization in eq. (2.72) and lets calculate the response function assuming that the polarization is the response to a delta peak of electric field. This would represent an incoming photon that is absorbed.

$$\vec{E}(t) = \vec{E}_0 \delta(t) \;\Rightarrow\; \vec{P}(t) = \varepsilon_0 \kappa(t) \vec{E}_0 \tag{2.77}$$

Using (2.71)

$$\Rightarrow\; \kappa(t) \propto e^{-\Gamma t} e^{\pm i\tilde{\omega}_0 t} \tag{2.78}$$

Now, the response function is real and the polarization must be continuous so κ have the form:

$$\kappa(t) \propto e^{-\Gamma t} sen(\tilde{\omega}_0 t) \tag{2.79}$$

The susceptibility associated to this response function is calculated as

$$\chi \propto \int_0^\infty e^{-\Gamma\zeta} sen(\tilde{\omega}_0\zeta) e^{i\omega\zeta} d\zeta = \int_0^\infty e^{-\Gamma\zeta} \left(\frac{e^{i\tilde{\omega}_0\zeta} - e^{-i\tilde{\omega}_0\zeta}}{2i} \right) e^{i\omega\zeta} d\zeta \tag{2.80}$$

This lead to two integrals

$$\begin{aligned} \chi(\omega) &= \frac{1}{2i} \left[\int_0^\infty e^{[-\Gamma\zeta + i(\omega+\tilde{\omega}_0)]\zeta} d\zeta - \int_0^\infty e^{[-\Gamma\zeta + i(\omega-\tilde{\omega}_0)]\zeta} d\zeta \right] \\ &= \frac{1}{2i} \left[-\frac{1}{-\Gamma + i(\omega+\tilde{\omega}_0)} + \frac{1}{-\Gamma + i(\omega-\tilde{\omega}_0)} \right] \end{aligned} \tag{2.81}$$

We multiply and divide by the conjugate to obtain the expressions we are loking for

$$\chi \propto \frac{1}{2} \left[\frac{(\omega+\tilde{\omega}_0) - i\Gamma}{\Gamma^2 + (\omega+\tilde{\omega}_0)^2} + \frac{i\Gamma - (\omega-\tilde{\omega}_0)}{\Gamma^2 + (\omega-\tilde{\omega}_0)^2} \right] \tag{2.82}$$

The first term of this expression for χ is clearly much smaller than the second and can be neglected, although it ensures the symmetry relationships of the real and complex parts of susceptibility derived from the Kramer-Kronig relations. The imaginary part of the susceptibility is equal to the imaginary part of the dielectric function and show the Lorentzian behaviour we were expecting to see for the homogeneous broadening of an absorption or emission process. This was accomplished by taken into consideration the life time of the polariton interacting with phonons.

This calculations were carried out considering the damping of the oscillation amplitude with a decay rate of Γ. As the energy is proportional to the square of the amplitude, it will dissipate with double the decay rate $\Gamma_E = 2\Gamma$.

Noticing that the imaginary part of the dielectric function is Lorentzian, is easy to see that the *Full Width at Half Maximum* (FWHM) is indeed 2Γ.

In the case we have presented, a weak coupling between excitons and phonons is assumed and then the line shape is Lorentzian, with half of the width given by the reciprocal of the life-time of the exciton due to phonon scattering. In the opposite limit of strong coupling, where the fluctuation of exciton energy due to lattice vibrations is larger than the width of the exciton energy band (that is, the transfer energy of an exciton between neighboring lattice sites), the line shape is Gaussian, being determined from the Franck-Condon principle applied to the adiabatic potential for the localized exciton [43]. This is because electronic transitions are relatively instantaneous compared with the time scale of nuclear motions, therefore if a molecule is to move to a new vibrational level during the electronic transition, this new vibrational level must be instantaneously compatible with the nuclear positions and momenta of the vibrational level of the molecule in the originating electronic state.

2.4 Temperature dependent exciton linewidth Model

As was presented before, the linewidth of absorption and emission of photons by excitons is determined by the scattering with phonons. But each type of phonon (i.e. optical or acoustic) interact different with excitons. In this section, the characteristics of this interactions are analyzed to separate the temperature dependency of the linewidth which are originated from the interaction with longitudinal optical and acoustic phonons. This lead to an Bose-Einstein like and a linear dependency respectively. A constant contribution to the linewidth its also added because of the scattering of excitons with impurities and imperfections in a crystal that as any other is not perfect.

The contributions to Γ arises from the various phonon scattering mechanisms which can be considered independent because we are considering contributions from different optical and acoustic phonon modes.

The interactions of excitons with Longitudinal Optical (LO) phonons are described by the Fröhlich interaction. In a polar or partly ionic crystal with two or more atoms per unit cell, the long wavelength LO phonon can induce an oscillating macroscopic polarization, the interaction between an electron and this macroscopic Coulomb potential is known as the Fröhlich interaction. Transverse Optical (TO) phonons can not induce a macroscopic polarization because they involve atomic displacements perpendicular to the wavevector of the phonon. This does not generate a macroscopic electric field because the polarization remains neutral in the longitudinal direction.

This can be understood by considering that the divergence of the electric displacement must be zero to ensure the charge neutrality $\nabla \cdot \vec{D} = 0$. For a harmonic field this means $\varepsilon(\vec{k} \cdot \vec{E}) = 0$. So, ether $\vec{k} \cdot \vec{E} = 0$ i.e. a Transversal wave or $\varepsilon = 0$ which doesn't mean that $\vec{E} = 0$ but instead $\vec{E} = -\vec{P}/\varepsilon_0$ meaning that this longitudinal field is macroscopic.

The processes involving the LO-phonon interaction are shown on the right-hand side of fig. 2.3, where it is seen that the phonon can scatter the exciton to the same bound state (intraband contribution), to higher-lying bound states, and to continuum states.

In calculating the contribution to the exciton linewidth from acoustic phonons, the deformation-potential is considered. The processes involving acoustic phonons are shown on the left-hand side of fig. 2.3, where it is seen that only intraband scattering contributes because of the small velocity of sound which means low photon energy.

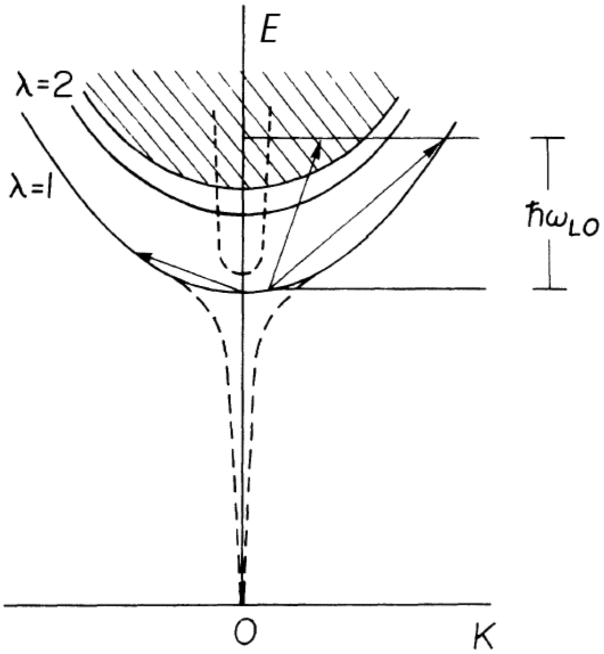

Figure 2.3: Illustration of the processes contributing to the phonon-induced lifetime of the lowest-lying exciton state. The solid lines indicate exciton-bound states, the hatched area indicates continuum states, and the dashed lines show the polaritons dispersion branches. Processes involving LO phonons are shown on the right hand side of the figure, and processes involving acoustic phonons are shown on the left. Figure from [44]

To explain the shape of each contribution to the exciton linewidth lets start by presenting an interaction Hamiltonian:

$$H_{ex-ph} = \sum_{i,i',k,q} V^{i,i'}(q) B^{\dagger}_{i,k+q} B_{i',k} (a^{\dagger}_{q} + a_{-q}) \tag{2.83}$$

This Hamiltonian takes into account the state change of an exciton from i' to i and its change in momentum k through the creation or annihilation of a phonon of momentum q represented by the creation an annihilation operators a_q. The interaction is mediated by the matrix element for exciton-phonon interactions that can be written as [44]:

$$V^{i,i'}(q) = \int d^3 r \phi_i^*(r)\phi_{i'}(r)\left[u_q^e e^{\left(-iq\cdot r\frac{m_e}{M}\right)} - u_q^h e^{\left(iq\cdot r\frac{m_h}{M}\right)}\right] \tag{2.84}$$

where $\phi(r)$ are the wave functions for the exciton, m_e and m_h are the effective masses of the electron and the hole that form the exciton and M is the total mass of the exciton.

For the case of the Fröhlich interaction [39, 44],

$$u_q^e = u_q^h = \left[\frac{2\pi e^2 \hbar\omega_{LO}}{V}\left(\frac{1}{\epsilon_\infty} - \frac{1}{\epsilon_0}\right)\right] q^{-1} \tag{2.85}$$

being V the cell volume, $\hbar\omega_{LO}$ the phonon energy, q its wave vector and ϵ_∞ and ϵ_0 the high frequency and low frequency limit of the dielectric function respectively. Meanwhile, for the deformation-potential interaction with acoustic phonons [39, 44],

$$u_q^{e,h} = q^{1/2}\left(\frac{\hbar}{2V\rho v}\right)^{1/2} D_{e,h} \tag{2.86}$$

where v is speed of sound, $D_{e,h}$ are the deformation constants, and the isotropy of the elastic properties of the system has been assumed.

We will be taking into consideration only the *1S* state for excitons with energy E_{1S}, witch makes sense because we have seen that the first exciton state have the biggest amplitude and that only excitons with S symmetry can be optically excited. So the contribution of each type of interaction to the exciton linewidth is Γ_{1s} [44],

$$\Gamma_{1s} = 2\pi V \sum_i \int \frac{d^3 q}{(2\pi)^3} N(q)|V^{i,1s}(q)|^2 \delta(E_{1S} - E_i(q) + \hbar\omega) \tag{2.87}$$

where $E_i(q)$ is the energy of any other state with wave vector q and $N(q)$ is the Bose Einstein distribution for phonons:

$$N(q) = \frac{1}{e^{\frac{\hbar\omega}{k_B T}} - 1} \tag{2.88}$$

For the case of the LO phonon interaction, using the energy dispersion of eq. (2.44) for excitons in the state *1S*, substituting (2.85) in (2.87) and integrating over q, the contribution to the exciton linewidth is,

$$\Gamma_{1S}^{LO}(E_{1S}) = \frac{CM}{\hbar^2} \sum_i q_{1,i}^{-1} |v_{1S,i}(q)|^2 \tag{2.89}$$

Here $q_{1,i}$ is given by

$$\frac{\hbar^2 q_{1,i}^2}{2M} = \hbar\omega_{LO} + E_{1S} - E_i \tag{2.90}$$

C is,

$$C = N_{LO}(T) e^2 \hbar\omega_{LO} \left(\frac{1}{\epsilon_\infty} - \frac{1}{\epsilon_0} \right) \tag{2.91}$$

and

$$v_{1S,i}(q) = \int d^3r \phi_i^*(r) \phi_{i'}(r) \left[e^{\left(iq\cdot r \frac{m_h}{M}\right)} - e^{\left(-iq\cdot r \frac{m_e}{M}\right)} \right] \tag{2.92}$$

From this result, it is possible to separate the temperature dependent part from the rest.

$$\Gamma_{1S}^{LO} = \gamma_{1S}^{LO} N_{LO}(T) \tag{2.93}$$

The γ parameter can be calculated to see its dependence with the phonon momentum and the contribution to it of excitons in the discrete and continuum states. This calculations are kind of tedious and the γ parameter can also be estimated experimentally so this calculation will not be included here.

For the case of the deformation potential of the acoustic phonons, let's start by pointing out that for the *1S* ground state of the exciton with momentum $k \approx 0$, energy conservation for one-phonon absorption gives

$$E_i + \frac{\hbar^2 q^2}{2M} - E_{1S} - \hbar v q = 0 \tag{2.94}$$

where v is the averaged sound velocity. Substituting this equation and eq. (2.86) in (2.87) and considering that for $T \geq 10K$ the Bose factor for the acoustic phonons can be expanded to give $N_q \approx \frac{k_B T}{\hbar v q}$ we can calculate [44]:

$$\frac{\Gamma^{def}}{k_B T} = \frac{M^2}{\pi v \hbar^3 \rho} \left[D_e (1 + a_B^{*2} P_e^2)^{-2} - D_h (1 + a_B^{*2} P_h^2)^{-2} \right]^2 \tag{2.95}$$

where $P_i = m_i v/\hbar$, ρ is the density, and a_B^* is the exciton Bohr radius.

Once again we reach an expression that gives the dependence with the temperature

$$\Gamma^{def} = \gamma_{def} T \tag{2.96}$$

Finally another constant term Γ_0 should be added to de linewidth because of scattering due to impurities and imperfections in a crystal that as any other is not perfect.

Summarizing we have a temperature dependent expression for the different contributions to the linewidth of the exciton absorption and emission peaks known as the Segull expression

$$\Gamma = \Gamma_0 + \gamma_{def} T + \gamma^{LO} N_{LO}(T) \tag{2.97}$$

This expression will allow us to analyze the changes in the linewidth of the absorption peaks when varying the temperature of the samples down to 10 K.

2.5 Gurioli Model for Free Exciton Thermalization

In this section a model for the photoluminescence originated in the recombination of free excitons (free to move through the crystal) is presented. This model, analyze the Stokes Shift defined as the difference between the excitonic absorption peak and the photoluminescence peak energy position as a function of the temperature. The model assumes that the Stokes Shift is due to a thermalization of the exciton gas in the lattice. Assuming the inverse generation mechanism for the recombination it is possible to linearly relate the square of the Full Width at Half Maximum of the absorption peak with the Stokes Shift times the temperature and the Boltzmann constant. When this behaviour is observed, it is reasonable to assume that the proposed recombination mechanism is then correct.

When the excitonic absorption and the photoluminescence (PL) spectra of different materials are compared, some PL peak show a red shift from the absorption peak and others do not. This difference is called Stokes Shift (SS). This is originated in the thermalization within the inhomogeneously broadened exciton band. This inhomogeneity can be understood considering that the exciton band is composed of sets of states due to the phonon contribution to the energy. The transitions between this states is not homogeneous but instead is ruled by the Franck–Condon principle which states that an electronic transition is most likely to occur without changes in the positions of the nuclei in the molecular entity and its environment. The resulting state is called a Franck–Condon state, and the transition involved, is a vertical transition (without momentum change). The quantum mechanical formulation of this principle is that the intensity of a vibronic transition is proportional to the square of the overlap integral between the vibrational wavefunctions of the two states that are involved in the transition. Fig. 2.4 illustrates the Franck–Condon principle for vibronic transitions in a molecule with Morse-like potential energy functions in both the ground and excited electronic states. In the low temperature approximation, the molecule starts out in the $\nu = 0$ vibrational level of the ground electronic state and upon absorbing a photon of the necessary energy, makes a transition to the excited electronic state. The electron configuration of the new final state may result in a shift of the equilibrium position of the nuclei constituting the molecule (dq). The transition is indicated by a vertical arrow due to the assumption of constant nuclear coordinates during the transition. The probability that the system can end up in any particular vibrational level is proportional to the square of the overlap of the vibrational wavefunctions of the original and final state. The electronic excited state quickly relax to the lowest vibrational level of the lowest electronic excitation state (Kasha's rule), and from there can decay to the electronic ground state via photon emission.

The free excitons created due to photon absorption, after momentum and energy relaxation, populate the exciton states with a quasi equilibrium distribution described by an effective temperature T_E. Then, if the inhomogeneous broadening is small compared to the thermal energy $k_B T_E$, each exciton state have essentially the same thermal population: the PL resemble the absorption and the SS is not observable. On the contrary, if the excitonic linewidth exceeds the thermal energy, the low energy side of the inhomogeneous exciton band is enhanced by the thermal population and a SS appears. Based on this simple model, it is possible to find a general relation between the SS, the photogenerated excitons temperature T_E and the absorption linewidth Δ.

The temperature T_E can be different from the lattice temperature T_L and in general, has been shown that is higher [45]. This is because T_E is the temperature of a quasiequilibrium state inducted by a continuous radiation

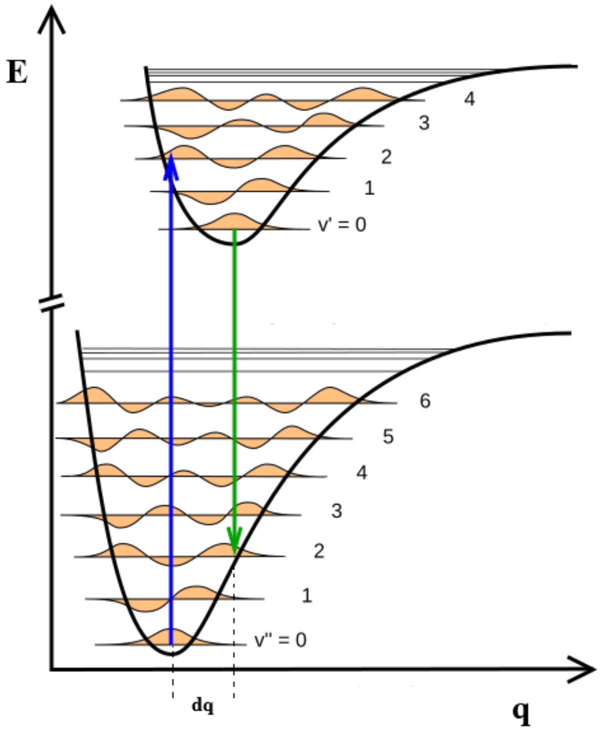

Figure 2.4: Franck–Condon principle energy diagram. Since electronic transitions are very fast compared with nuclear motions, the vibrational states to and from which absorption and emission occur are those that correspond to a minimal change in the nuclear coordinates. As a result, both absorption and emission produce molecules in vibrationally excited states. The potential wells are shown favoring transitions with changes in ν.

flux. If it is taken off, the excitons will recombine and this temperature will have no meaning.

Let discuss the effect of thermalization on the PL line shape. If the photogenerated excitons are in thermal equilibrium at temperature T_E, the PL spectrum will by given by [46]

$$I_{PL}(E) \approx \alpha(E)e^{\left(-\frac{E-E_0}{k_BT_E}\right)} \tag{2.98}$$

where the absorption spectrum $\alpha(E)$ is multiplied by the Boltzmann distribution with the exciton transition energy E_0 taken as the inflection point for the thermal distribution. Rewriting $\alpha(E) = \alpha_0(E)+\overline{\alpha}(E)$, where $\alpha_0(E)$ is the fundamental (first) excitonic transition and $\overline{\alpha}(E)$ represent the higher excitonic states including the continuum. Assuming also that $\alpha_0(E)$ has a Gaussian profile due to inhomogeneities in the material, 2.98 becomes

$$\begin{aligned} I_{PL}(E) &\approx \alpha_0(E_0) e^{\left(-\frac{(E-E_0)^2}{2\sigma^2}\right)} e^{\left(-\frac{E-E_0}{k_B T_E}\right)} + \overline{\alpha}(E) e^{\left(-\frac{E-E_0}{k_B T_E}\right)} \\ &= \alpha_0(E_0) e^{\left(-\frac{(E-E_0+\sigma^2/k_B T_E)^2}{2\sigma^2} + \frac{\sigma^2}{2(k_B T_E)^2}\right)} + \overline{\alpha}(E) e^{\left(-\frac{E-E_0}{k_B T_E}\right)} \end{aligned} \tag{2.99}$$

The dominant contribution to the PL is therefore a Gaussian band with the same linewidth as the absorption, but peaked at the energy $E_0' = E_0 - \sigma^2/k_B T_E$. From the hypothesis of thermal distribution and the assumption of a Gaussian excitonic band, the SS ($SS = E_0 - E_0'$) between the absorption and the PL lines is

$$SS = \frac{\sigma^2}{k_B T_E} \approx 0.18 \frac{\Delta^2}{k_B T_E} \tag{2.100}$$

where $\Delta = 2\sqrt{2ln2}\sigma$ is the full wight at half maximum (FWHM) of the Gaussian absorption line.

Note that, assuming a Gaussian line shape, the only effect of the thermalization in the inhomogeneous band is the SS, neither the validity of the thermal equilibrium hypothesis nor the value of the exciton temperature T_E can be determined by the PL line shape analysis. Then it could be questioned whether a Gaussian profile is a realistic assumption.

In any case, assuming an arbitrary line shape $\alpha_0\left((E - E_0)/\Delta\right)$ for the exciton band, the Stokes Shift will be determined by imposing $E_0' = E_0 - SS$, this equalizing to zero the first derivative of I_{PL} from (2.98)

$$\frac{1}{\Delta}\alpha_0'\left(-\frac{SS}{\Delta}\right) - \frac{1}{k_B T_E}\alpha_0\left(-\frac{SS}{\Delta}\right) = 0 \tag{2.101}$$

where $\alpha_0'(x)$ is the first derivative of $\alpha_0(x)$. Defining $G(x) = \alpha_0'/\alpha_0$, the Stokes Shift expression is

$$SS = -\Delta\, G^{-1}\left(\frac{\Delta}{k_B T_E}\right) \tag{2.102}$$

which, for $\Delta < k_B T_E$ becomes

$$SS \cong \frac{\Delta^2}{k_B T_E}\frac{\alpha_0(0)}{\alpha_0''(0)} \tag{2.103}$$

where $\alpha_0''(x)$ is the second derivative of $\alpha_0(x)$. Therefore even if (2.100) is only correct for a Gaussian line shape, it is found that, apart from the 0.18, the predicted dependence of SS with both temperature and lineweight are valid independently of the exact absorption line shape.

As an example, if $\alpha_0(x)$ were a hyperbolic secant, in the limit $\Delta \leq k_B T_C$, the Stokes Shift would be $SS \cong 0.14\Delta^2/k_B T_C$.

2.6 Steady-State Luminescence of a Localized-State Ensemble

Here a model for the photoluminescence originated in the recombination of carriers in localized states is presented. An equation for the population density balance of this states is used to analyze the carriers dynamic. It considerate a generation rate due to the pumping light, an escape mechanism, a recapture mechanism and an optically active recombination one. All this processes are considered to have a constant rate. The model is complementary to others empirical rules and tries to predict the behaviour of the peak position, the FWHM and the integrated PL with the temperature. This results are summarized in fig. 2.5b.

Carrier localization is a common phenomenon in many material systems such as semiconductor alloys, quantum wells (QWs), and self-assembled quantum dots (QDs). It has profound effects on electrical and optical properties of the materials. It has been known for long time that a number of anomalous temperature-dependent luminescence behaviours are related to carrier localization, including the “S-shaped” temperature dependence of the luminescence peak position [47] and a reduction of luminescence linewidth with increasing temperature [48]. In this section a distribution function for localized carriers will be derived and a model for the luminescence of localized-state ensemble (LSE) will be developed. The model suggests that thermal redistribution of localized carriers within the localized states is the cause of the anomalies in the temperature dependence of the luminescence peak. For a system with localized electronic states having the density of states (DOS) $\rho(E)$, the rate of change of carrier population density $N(E,T)$ in the state at energy E and temperature T is given by [49, 50]

$$\frac{dN(E,T)}{dt} = G(E) + \frac{\gamma_c N'}{\Lambda}\rho(E) - \frac{N(E,T)}{\tau_{tr}} e^{(E-E_a)/k_B T} - \frac{N(E,T)}{\tau_r} \tag{2.104}$$

where E_a is the energy position of a delocalized state to which the localized carriers thermally escape. The first term on the right, $G(E)$, represents the rate of carrier generation due to optical pumping or electrical injection, which is proportional to $\rho(E)$ according to $G(E) = \kappa\rho(E)$ [49, 50], where κ is a constant. The second term on the right represents the number of carriers re-captured by the localized states per unit time, in which γ_c is the recapture coefficient, N' is the total number of carriers that are thermally activated away from the localized states as given by

$$N' = \int_{-\infty}^{+\infty} \frac{N(E', T)}{\tau_{tr}} e^{(E'-E_a)/k_B T} dE' \tag{2.105}$$

in which $\frac{1}{\tau_{tr}}$ is the attempt-to-escape rate of the localized carriers. $\Lambda = \int_{-\infty}^{+\infty} \rho(E')dE'$ is the total number of localized states. The third term on the right-hand side of (2.104) gives the thermal escape rate of the localized carriers and the last term describes the de-population rate of the carriers due to radiative recombination. The term $\frac{1}{\tau_r}$ represents the rate of radiative recombination. For simplicity, τ_{tr} and τ_r are assumed to be constants.

The solution of (2.104) under steady-state condition ($\frac{dN}{dt} = 0$) is [50]

$$N(E, T) = A(T)n(E, T) \tag{2.106}$$

where

$$A(T) = \frac{\kappa\tau_{tr}}{(1-\gamma_c) + (\tau_{tr}/\tau_r\gamma_c)\xi_1(T)/\Lambda} \tag{2.107a}$$

$$n(E, T) = \frac{\rho(E)}{e^{(E-E_a)/k_B T} + \tau_{tr}/\tau_r} \tag{2.107b}$$

In (2.107b), $\xi_1(T) = \int_{-\infty}^{+\infty} n(E', T)dE'$. Expressing $n(E, T)$ as $n(E, T) = f(E, T)\rho(E)$ a distribution function can be obtained

$$f(E, T) = \frac{1}{e^{(E-E_a)/k_B T} + \tau_{tr}/\tau_r} \tag{2.108}$$

Note that $n(E, T)$ essentially describes the shape of the luminescence spectrum given by $N(E, T)/\tau_r$, because A is a function of T only.

Consider a general case, i.e., a localized-state ensemble system with a Gaussian-type DOS, which may result from defects or alloy composition small differences:

$$\rho(E) = \rho_0 e^{-\frac{(E-E_0)^2}{2\sigma^2}} \tag{2.109}$$

In the above, ρ_0 and E_0 are the amplitude and peak energy position, respectively, while σ is the standard deviation of the distribution.

As mentioned earlier, $n(E,T)$ represents the "shape" of the luminescence spectrum and the luminescence peak position can be found by setting $\frac{\partial n(E,T)}{\partial E} = 0$. It was found that [51] at

$$E = E_0 - x \cdot k_B T \tag{2.110}$$

$n(E,T)$ reaches a maximum. The temperature dependent coefficient $x(T)$ can be obtained by numerically solving the following equation [51]:

$$xe^x = \left[\left(\frac{\sigma}{k_B T}\right)^2 - x\right]\left(\frac{\tau_{tr}}{\tau_r}\right) e^{\frac{(E_0-E_a)}{k_B T}} \tag{2.111}$$

It should be noted that the temperature dependence described by (2.110) is only due to carriers thermal redistribution within the localized states. It is known that the band gap of an idealized semiconductor material without localized electronic states is itself temperature dependent, which is usually described by the Varshni empirical formula for conventional tetragonal semiconductors [52]. There is a remaining discussion if this empirical model is applicable for perovskites but after taking it into account this factor, the variation of the peak position of luminescence from LSE would be given by

$$E = E_0 + \frac{\alpha T^2}{\Theta + T} - x \cdot k_B T \tag{2.112}$$

where α is the Varshni parameter and Θ the Debye temperature of the material.

The Full width at half-maximum height (FWHM) is an important parameter for a luminescence spectrum, which is also embedded in $n(E,T)$. The FWHM $\Gamma(T)$ of $n(E,T)$ can be obtained by numerically solving $n(E,T) = n(E_{pk},T)/2$. As will be shown below, the variation of $\Gamma(T)$ with temperature exhibits a "valley", i.e., $\Gamma(T)$ decreases first and then increases with raising temperature. Besides the variation in linewidth due to the thermal redistribution of carriers within LSE, the broadening due to phonon and impurity/imperfection scattering should be taken into consideration. The effective FWHM of the luminescence peak is determined by making convolution of $n(E,T)$ and a Lorentzian function (or a Gaussian function). Using a Lorentzian function $[4E^2 + (\Gamma_0 + \Gamma_{ph})^2]^{-1}$ were Γ_0 is due to impurity/imperfection scattering and $\Gamma_{ph} = \gamma_{def}T + \gamma^{LO}N_{LO}(T)$ due to phonon scattering as presented in (2.97) [44].

The integrated intensity of the luminescence spectrum is proportional to the total number of localized carriers, i.e.,

$$I(T) \propto \int_{-\infty}^{+\infty} N(E',T)dE' = A\int_{-\infty}^{+\infty} n(E',T)dE' \tag{2.113}$$

Using an integral approximation [50]:

$$\int_{-\infty}^{+\infty} \frac{e^{-x^2}}{1+e^{a(x+b)}}dx \approx \frac{\sqrt{\pi}}{1+e^{2.41bsin\theta}} \tag{2.114}$$

where $\theta = arctan(a/2.41)$. The equation can be derived as

$$I(T) \propto \left\{ (1+\gamma_c)exp\left[\frac{(E_0 - E_a)k_BTLn(\tau_r/\tau_{tr})}{\sqrt{(k_BT)^2 + 2(\sigma/2.41)^2}}\right]\right\}^{-1} \tag{2.115}$$

For $\sigma = 0$ (i.e., δ-functional DOS), the above expression is reduced to the well known model describing thermal quenching of luminescence for a two-level system. Indeed, for the case of $\sigma = 0$, no thermal redistribution takes place and the system becomes essentially an equivalent two level system. This fact thus further validates the current model, which is more general. Note that for the two level system, $E_a - E_0$ is in effect the thermal activation energy of the carriers.

Figure 2.5a shows the calculated profile for $N(E,T)$ using $E_0 = 1.185\ eV$, $E_a = E_0 + 0.073\ eV$, $\sigma = 13\ meV$, $\tau_{tr}/\tau_r = 0.027/250$, $\gamma_c = 0.9$. From the figure, it is seen that the typical anomalies in the temperature dependent luminescence are reproduced. Figure 2.5b.i shows the peak positions of the spectra as a function of temperature together with that predicted by Varshni empirical formula using the Varshni parameter $\alpha = 0.48\ meV/K$ and the Debye temperature $\Theta = 270\ K$. The sum of the two contributions is given by the solid curve, which is seen to agree excellently with the experimental data for an $In_{0.35}Ga_{0.65}As$ QD sample.

Figure 2.5b.ii presents the dependence of the FWHM on temperature, from

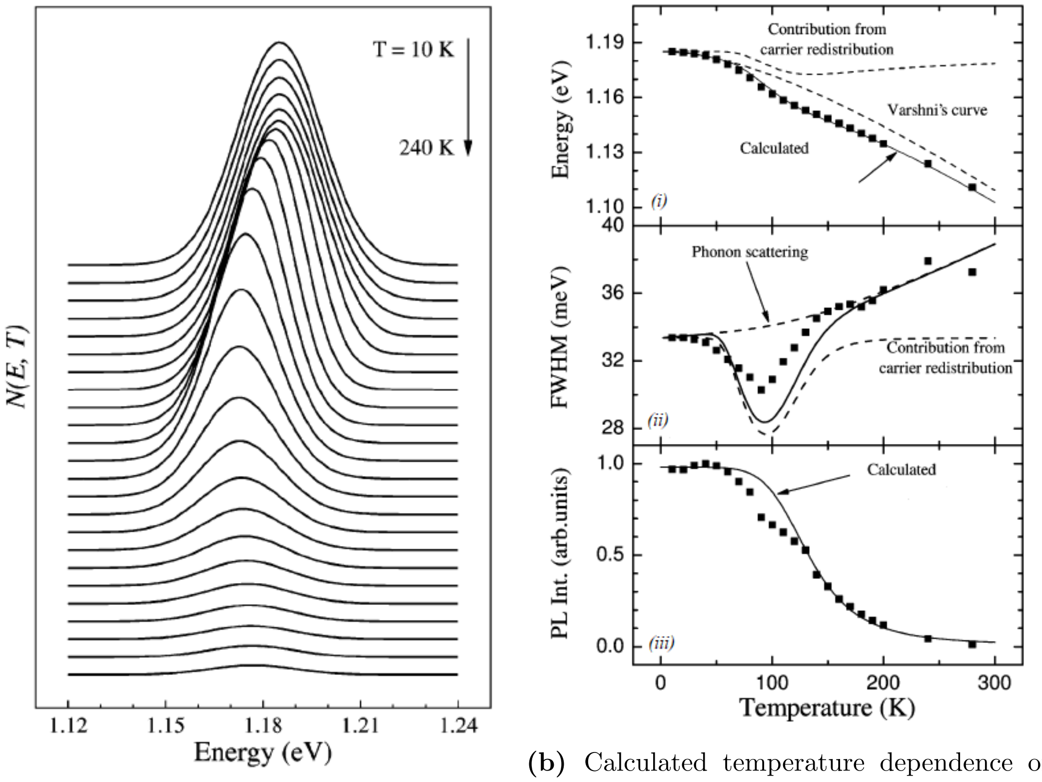

(a) Calculated population densities of localized carriers $N(E, T)$ for system which resemble luminescence spectra, as a function of energy and temperature for the case of $E_a - E_0 > 0$. The curves are shifted along vertical direction for clarity.

(b) Calculated temperature dependence of luminescence peak position *(i)*; FWHM *(ii)*; and integrated intensity *(iii)* for the case of $E_a - E_0 > 0$ using the parameters given for fig. 2.5a. The squares are experimental data and the solid lines are calculated using corresponding equations as denoted.

Figure 2.5: Calculated spectra for different temperatures and experimental data of an $In_{0.35}Ga_{0.65}As$ QD sample. Figure from [50].

which it is seen that the reduction of FWHM in the luminescence spectra is mainly due to the effect of redistribution of localized carriers. The effect of phonon scattering broadens the spectra monotonously as the temperature increases, whereas carrier thermal re-distribution results in a dependence showing a valley as already mentioned earlier. The combination of the two effects leads to the anomalous dependence of FWHM on temperature shown by the solid curve in fig. 2.5b.*ii*. In the calculations, the values of $\gamma_0 = 5.0\ meV$, $\gamma_{def} = 10\ \mu eV/K$, $\gamma^{LO} = 18.8\ meV$ and $\hbar\omega_{LO} = 36\ meV$ were used. Finally, fig. 2.5b.*iii* gives the integrated intensity of the luminescence. It can be found that the calculated intensity agrees well with the experimental data.

The results presented above are for $E_a - E_0 > 0$. The value of $E_a - E_0$ measures the mean thermal activation energy for the localized carriers. For the case of $E_a - E_0 < 0$, the calculated luminescence peak position as a function of temperature will show a "S-shaped" temperature dependence of luminescence peak [53]. In fact, there are experimental data for $InGaN/GaN$ QWs samples that exhibit this behaviour. Then the anomalous temperature dependence of the anti-Stokes photoluminescence peak can also be reproduced with the current model.

Finally, a briefly discussion on the physical meaning of E_a it is given. Like the Fermi level in the Fermi-Dirac distribution function, E_a in the distribution function derived above gives a energy level below which all the localized states are occupied by carriers. Its relative position to E_0 (the free states beginning energy) essentially determines anomalous temperature dependence of luminescent peak position. E_a may be the quasi-Fermi level of samples, which depends on concentration of carriers optically/electrically injected and magnitude of the built-in electric field within the samples.

This model quantitatively describes the temperature dependence of the luminescence spectra from localized carriers. It reproduces almost all the anomalies observed for the luminescence of LSE systems and shows that the luminescence quenching model of a two-level system is simply an approximation of the current model under certain limiting conditions [50].

2.7 Urbach-Martienssen Energy Tail

For a number of insulators including ionic crystals, semiconductors and organic crystals, it has been found that the low energy tail of the fundamental optical absorption follows the empirical rule expressed as [54–56]

$$\alpha(E) \propto \alpha_0 \, e^{-\frac{(E_0 - E)}{k_B T}} \tag{2.116}$$

at sufficiently high temperatures, where α_0 and E_0 are almost independent of the incident photon energy E and the temperature. This expression states that the logarithms of the absorption coefficient can be well approximated by a straight line with respect to energy E in the low energy tail, and that the straight lines for various temperatures cross each other almost at one point $E = E_0$ which is called the Urbach Focus.

In view of the temperature dependence, it is almost evident that this exponential tail originates in the exciton-phonon interaction. For a certain group of crystals such as alkali halides, the slope tends to a finite value as $T \to 0$, in which case $k_B T$ in (2.116) have to be replaced by the effective value defined by

$$k_B T' = U_0 \, coth \left(\frac{E_{ph}}{2k_B T} \right) \tag{2.117}$$

at low temperatures. Here U_0 can be understood as a temperature-independent contribution reflecting the level of static disorder [56] and the energy E_{ph} is on the order of phonon energy. This empirical rule was discovered by Urbach for silver halides (indirect edge) [57], and established by Martienssen for alkali halides (direct edge) [58]. Therefore its known by the Urbach-Martienssen rule (U-M rule or tail).

Authors ascribe the U-M tail to the exciton-phonon interaction with two approaches to the problem [54]. In the first one, higher-order perturbational expansions with respect to the exciton-phonon interaction are performed. In the second one, momentary trapping of an exciton by the local lattice deformation due to thermal lattice vibrations is considered. The former is the approach from the mobile nature of exciton in the lattice, whereas the latter is that from the localized nature of exciton.

As for the experiments, there are two types of crystals depending on the low temperature behaviours of the low energy tail of the exciton absorption peak. In CdTe which belongs to the first type, it has been observed the LO-phonon sidebands on the low energy side of the exciton peak at low temperatures, which grow up and are smoothed out, tending to the U-M tail as temperature rises [54]. This situation at low temperatures can be understood with the perturbation theory as was analyzed by Segall [59]. Therefore, one can take the U-M tail for CdTe as the many-phonon assisted optical creation of excitons which is blurred by the overlap between many phonon sidebands. In alkali halides which belong to the second type, the absorption spectrum of excitons has a low energy tail of exponential form without any phonon structure even at the lowest temperatures. One cannot understand this tail with the perturbation theory because at very low temperatures there are no phonons to be absorbed in creation of the exciton. It is known, however, the exciton in alkali halides has states lower than the free exciton states in the undeformed lattice, namely it becomes self-trapped by a local lattice deformation induced by itself [60]. It can then be supposed that the optical transitions to various vibrational states of the self-trapped exciton will give rise to the low energy tail of the, absorption peak of the free exciton even at 0 K [54].

It might be supposed that the first of the two approaches mentioned before can be applied to the case where the exciton-phonon interaction is comparatively weak (crystals of the first type), and that the second to the case where it is comparatively strong (crystals of the second type). However, in order to describe the U-M tails in the two different types of crystals from a unified viewpoint, it seems necessary to take appropriate account of the localized states of exciton in the phonon field. This is evident for the second type, no so much, for the first type where the low energy tail seems to be understood in terms of the many phonon processes of exciton absorption. It is more intelligible to describe this tail in terms of the exciton trapped momentarily by local lattice deformation since many phonons associated with an exciton can be interpreted by a local lattice deformation around it. Such trapped states appear from place to place and from time to time during thermal lattice vibrations, although they require finite lattice energy and are not stable relative to the free exciton states in crystals of the first type.

The calculation of the absorption lines for this model were made by Cho and Toyozawa. They took the states of the composite particle of Frenkel exciton plus phonons which are localized at the exciton site in order to take explicit account of their localized nature and obtained the exciton absorption spectrum at T= 0 K, which consists of a sharp peak due to the mobile exciton with or without the low energy tail (approximately exponential) according as the self-trapped state is stable (the second type) or not (the first type) [61]. Their treatment explains well the situation at 0 K on the low energy side of the exciton peak. Although, in this case they use the Frenkel exciton model to emulate the self-trapped exciton. Their treatment is not fully adequate since the exciton is confined to the same lattice site as the lattice deformation. This seems to result in drawbacks of the absorption spectrum obtained for energy close to or above the exciton peak, since the exciton in this energy region can be considered to move almost apart from the local lattice deformation. In fact, in the absorption spectrum obtained by their first approximation, there appears a broad Gaussian band, reminiscent of the bound exciton, on the high energy side of the sharp exciton peak valid for the second type but not the first one. The absorption spectrum of a self-trapped exciton has Gaussian shape, while that of a free exciton has Lorentzian shape.

2.8 Perovskite Cell Operation

The objective of this section is to explain the working principle of perovskites solar cells and in a broader sense all the p-i-n type of cells. The main characteristic of this devices is that the absorber material (in this case a perovskite) is an intrinsic semiconductor (or lightly doped). This absorber is placed in between two highly doped materials that act as selective contacts for each type of photogenerated charge carriers in the active material. These layers are commonly known as Hole Transport Layer (HTL) and Electron Transport Layer (ETL). At least one of this layers, the one on the light incident side, must be transparent so the light can reach the active layer.

However, the analysis of this technology's working principles can be blurred by substantial densities of mobile ions in these mixed ionic-electronic semiconductors. In fact, mobile ions modulate the electric field and charge carrier distribution within the perovskite absorber [62, 63]. Both quantities directly affect the solar device optoelectronic properties (bulk/interphase carrier recombination and transport), mechanical properties (compressive film strain), and photovoltaic behaviour (reverse bias breakdown, photo-induced halide segregation, hysteresis, degradation, etc.). Understanding this technology, therefore, requires an accurate band diagram that accounts for a distribution of electric field in perovskite solar cells that is consistent with experimental results.

Two main features of the electric field distribution have been experimentally unveiled in perovskite devices. The electric field is shielded in bulk and is distributed asymmetrically within the absorber. The first evidence of this is the observation of a negative photocurrent opposite to the photocurrent induced by carrier extraction right after applying a forward voltage (i.e., a negative field) to a device initially at equilibrium [64, 65]. To explain this observation, it has been proposed that the positive built-in voltage drops at the contacts and is zero in the bulk at equilibrium. Hence, the negative applied field creates a net negative field in the bulk that drives most photogenerated carriers away from their selective contacts and leads to a negative photocurrent. The second experimental evidence is the observation of reverse bias breakdown currents for relatively small reverse bias values (between -1 and -5 V) [66]. This behaviour has been ascribed to carrier tunneling from the perovskite into one of the transport layers. This only occurs when most of the voltage within the absorber drops close to one of the contacts, allowing for a thin tunneling barrier

[66]. Most of the potential dropping close to one contact implies that the field is distributed asymmetrically and suggests that the bulk is field-free at steady state. The last evidence is that provided by Weber et alii [67]. These authors revealed an asymmetric potential distribution within the perovskite absorber using Kelvin probe force microscopy after applying 0.5 V in the dark. They showed that after 700 ms, $\sim$ 80% of the applied voltage drops close to the ETL, and the remaining $\sim$ 20% drops close to the HTL, leaving no voltage drop within the bulk.

Let us start by establishing the general framework that will be used throughout this section. First, we consider an intrinsic perovskite semiconductor in the dark without any contact (Figure 2.6.A). All the ionic species are distributed homogeneously in the film with a concentration N_0 (in cm^{-3}). Then the film is contacted with an ETL on the left ($x = 0$) and an HTL on the right ($x = L$). Both transport layers are assumed to be heavily doped so that no voltage drops within the contacts. The built-in voltage resulting from the difference in contact work functions drops linearly between the HTL and ETL (Figure 2.6.B). The built-in field triggers the migration of positively charged halide vacancies toward the HTL. This is because to date, most studies suggest that ionic transport is mostly mediated through halide vacancies (V_X^+) [68, 69]. This process induces the formation of a halide-vacancy-depleted region close to the ETL containing an excess of anions (Figures 2.6.C and 2.6.D). Note that if negatively charged mobile halides migrated instead of positively charged halide vacancies, the halide-depleted region would be formed close to the HTL and the halide-accumulation region would be created close to the ETL.

The following model assume that the field is governed by mobile ions only given that N_0 exceeds the carrier density under operational conditions ($\sim 10^{16} cm^{-3}$). The volume effects are neglected due to large ion concentrations at the interface (this includes double layer effects). We define w_+, w_-, V_+, and V_- to be the width and voltage drops within the vacancy-accumulation (+) and vacancy-depleted (-) regions. We choose the convention: $V_+ > 0$ and $V_- < 0$. We define Q_{ion} to be the total ionic charge (in $C.cm^2$) in the vacancy-depleted and vacancy-accumulation regions.

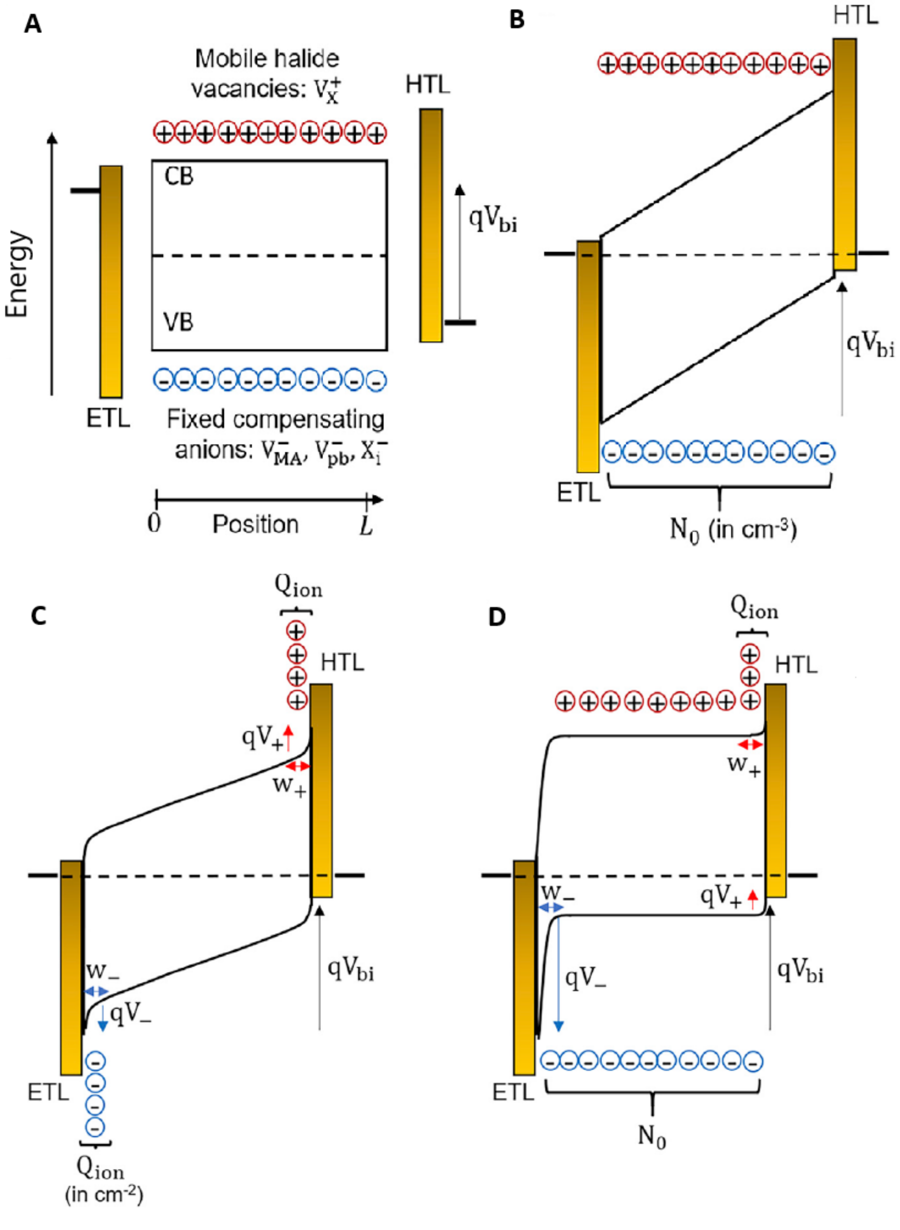

Figure 2.6: Schematic energy diagrams of an intrinsic perovskite film in dark equilibrium. (A)The film does not have contacts. (B) After the ETL and HTL have been deposited on either side of the film, a built-in potential (V_{bi}) is created that linearly drops within the film and triggers the drift of mobile ions toward the contacts. (C) Case where both cations and anions are mobile. Both ions are symmetrically distributed. (D) Case where halide vacancies are mobile and anions are immobile. This theory predicts an asymmetric ion distribution. Figure from [63].

2.8.1 Ions Charge Distribution

To calculate the ions charge we will present method called the "surface polarization" (SP) theory to semi-analytically solve the Poisson equation. In this approach proposed by Richardson et alii [70–73], the ionic charge at the contacts is obtained by analytically calculating the first integral of the Poisson equation, with the condition that anions are immobile. This model predicts that the ionic vacancy charge is distributed asymmetrically.

To do this first let's analyse the ions current density $\vec{j}_{V_X^+}$ inside the material:

$$\vec{j}_{V_X^+} = -qD_{ion}\nabla n_{vac} + q^2 n_{vac}\mu_{ion}\vec{E} \tag{2.118}$$

Here q is the ions charge D_{ion} is the ions diffusion coefficient, n_{vac} the ions concentration per volume, μ_{ion} the ions mobility and $\vec{E}$ the internal electric field. As the ions are contained in the material the condition $\vec{j}_{V_X^+} = 0$ must be imposed. And now assuming a concentration gradient only in the x direction and replacing the electric field with its dependency with the potential $E = -\frac{\partial\phi}{\partial x}$ we get:

$$D_{ion}\frac{\partial n_{vac}}{\partial x} = n_{vac}\mu_{ion} q\left(-\frac{\partial\phi}{\partial x}\right) \tag{2.119}$$

using the Einstein relation ($D_{ion} = \mu_{ion} k_B T$)

$$k_B T\frac{\partial n_{vac}}{\partial x} = -q n_{vac}\frac{\partial\phi}{\partial x} \tag{2.120}$$

and now defining $V_T = k_B T/q$

$$\frac{\partial n_{vac}}{\partial x} = -\frac{n_{vac}}{V_T}\frac{\partial\phi}{\partial x} \tag{2.121}$$

This differential equation can be solved with the condition $n_{vac}(\phi = 0) = N_0$

$$n_{vac}(x) = N_0 e^{\frac{-\phi}{V_T}} \tag{2.122}$$

Next, this cation concentration along with fixed N_0 anions concentration is substituted in the poison equation.

$$\frac{\partial^2\phi}{\partial x^2} = -\frac{\rho}{\epsilon\epsilon_0} = -\frac{qN_0}{\epsilon\epsilon_0}\left(e^{\frac{-\phi}{V_T}} - 1\right) \tag{2.123}$$

with ϵ_0 and ϵ are the dielectric constant of the vacuum and the material dielectric function respectively. Now, this expression is pre-integrated by multiplying by $\frac{\partial\phi}{\partial x}dx$ and integrating. On the left sine the change of variable $\frac{\partial\phi(x)}{\partial x} = u$ is used

$$\int_0^x \frac{\partial^2\phi}{\partial x^2}\frac{\partial\phi}{\partial x}dx = \int_0^{\frac{\partial\phi(x)}{\partial x}} udu = \frac{1}{2}\left(\frac{\partial\phi}{\partial x}\right)^2 \tag{2.124a}$$

$$\int_0^x \left(e^{\frac{-\phi}{V_T}} - 1\right)\frac{\partial\phi}{\partial x}dx = \int_0^{\phi}\left(e^{\frac{-\phi}{V_T}} - 1\right)d\phi = -V_T e^{\frac{-\phi}{V_T}} - \phi + V_T \tag{2.124b}$$

leading to

$$\frac{1}{2}\left(\frac{\partial\phi}{\partial x}\right)^2 = \frac{qN_0V_T}{\epsilon\epsilon_0}\left(e^{\frac{-\phi}{V_T}} + \frac{\phi}{V_T} - 1\right) \tag{2.125}$$

which leaves us to

$$\frac{\partial\phi}{\partial x} = \pm\sqrt{\frac{2qN_0V_T}{\epsilon\epsilon_0}}\left(e^{\frac{-\phi}{V_T}} + \frac{\phi}{V_T} - 1\right)^{1/2} \tag{2.126}$$

Finally, using the gauss law applied to the infinite plane result we get the charge per unit area related to the electric field

$$\sigma_{ion} = \epsilon\epsilon_0\left(-\frac{\partial\phi}{\partial x}\right) \tag{2.127}$$

which leads to charge distribution proposed by Richardson et alii [70–73]. Here we have change the sign of the potential to match the convention used by Richardson.

$$\sigma_{ion}^{SP} = \mp\sqrt{2q\epsilon\epsilon_0N_0V_T}\left(e^{\frac{-\phi}{V_T}} - \frac{\phi}{V_T} - 1\right)^{1/2} \tag{2.128}$$

2.8.2 Potential profile in the cell

In this section we will model the potential profile in the cells interfaces. The Poisson equation relates the electrostatic potential field, ϕ, to the distribution of charged species. As previously mentioned, the prevailing charged species in the perovskite absorber are mobile vacancies with density n_{vac} that are compensated by anions with density N_0. Hence, the general Poisson equation already used reads:

$$\frac{\partial^2\phi}{\partial x^2} = -\frac{q}{\epsilon_0\epsilon}\left(n_{vac} - N_0\right) \tag{2.129}$$

To find an analytical solution, in this case, it will be necessary to assume that changes in ion concentration take the form of step functions rather than continuous functions previously presented. For a given field, vacancies migrate toward the HTL to shield the applied field until a field-free region is created in the bulk of the absorber (when the drift-diffusion current of these mobile vacancies is zero). Simultaneously, the vacancy-depleted region grows wider as vacancies drift toward the HTL. This leads to the asymmetric distribution of figure 2.7.

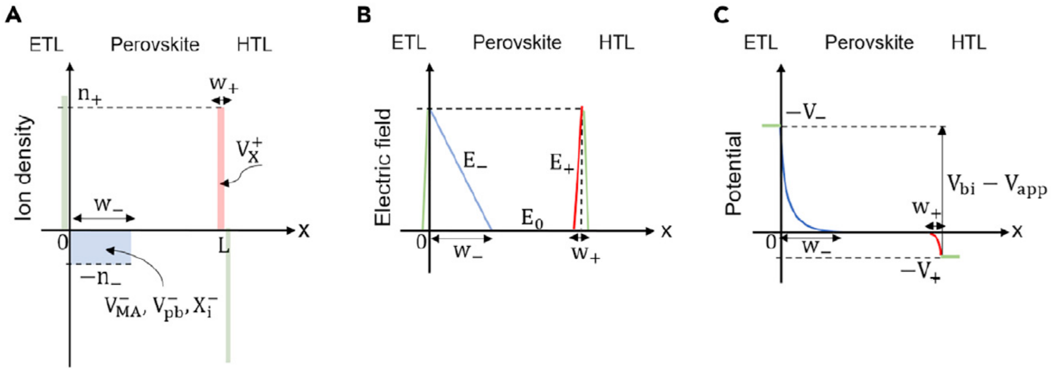

Figure 2.7: Schematic diagram of (a) the Ion Density, (b) Electric Field, and (c) Electrostatic Potential Profile. Figure from [63].

Case $w_- + w_+ < L$

Using these hypotheses, an analytical solution can be obtained in the vacancy depleted (-), neutral (0) and vacancy accumulation (+) regions.

$$\begin{cases} \frac{\partial E_-}{\partial x} = -\frac{q}{\epsilon_0 \epsilon} n_- \;\; V_+ \; depleted \; region \\ \frac{\partial E_0}{\partial x} = 0 \;\; Neutral \; region \\ \frac{\partial E_+}{\partial x} = \frac{q}{\epsilon_0 \epsilon} n_+ \;\; V_+ \; acumulation \; region \end{cases} \tag{2.130}$$

To obtain the electric field in each region, the equation (2.129) is integrated for each region using the continuity of the electric field and the fact that the field is zero in the neutral region:

$$\begin{cases} E_-(x) = -\frac{\partial \phi_-}{\partial x} = -\frac{q}{\epsilon_0 \epsilon} n_-(x - w_-) \;\; V_+ \; depleted \; region \\ E_0(x) = -\frac{\partial \phi_0}{\partial x} = 0 \;\; Neutral \; region \\ E_+(x) = -\frac{\partial \phi_+}{\partial x} = \frac{q}{\epsilon_0 \epsilon} n_+(x - L + w_+) \;\; V_+ \; acumulation \; region \end{cases} \tag{2.131}$$

The electric field profile is depicted in figure 2.7.B. The charge neutrality condition imposes that the total ionic charge in the vacancy-depleted region must be equal to that in the vacancy-accumulation region:

$$n_+ w_+ = n_- w_- \tag{2.132}$$

This implies that $E_-(0) = E_+(L)$. We obtain the electrostatic potential by integrating again, using the continuity of the potential and with the reference potential in the neutral region:

$$\begin{cases} \phi_-(x) = \frac{q}{2\epsilon_0\epsilon} n_-(x - w_-)^2 \ \ V_+ \ \textit{depleted region} \\ \phi_0(x) = 0 \ \ \textit{Neutral region} \\ \phi_+(x) = -\frac{q}{2\epsilon_0\epsilon} n_+(x - L + w_+)^2 \ \ V_+ \ \textit{acumulation region} \end{cases} \tag{2.133}$$

The electrostatic potential profile is depicted in figure 2.7.C.

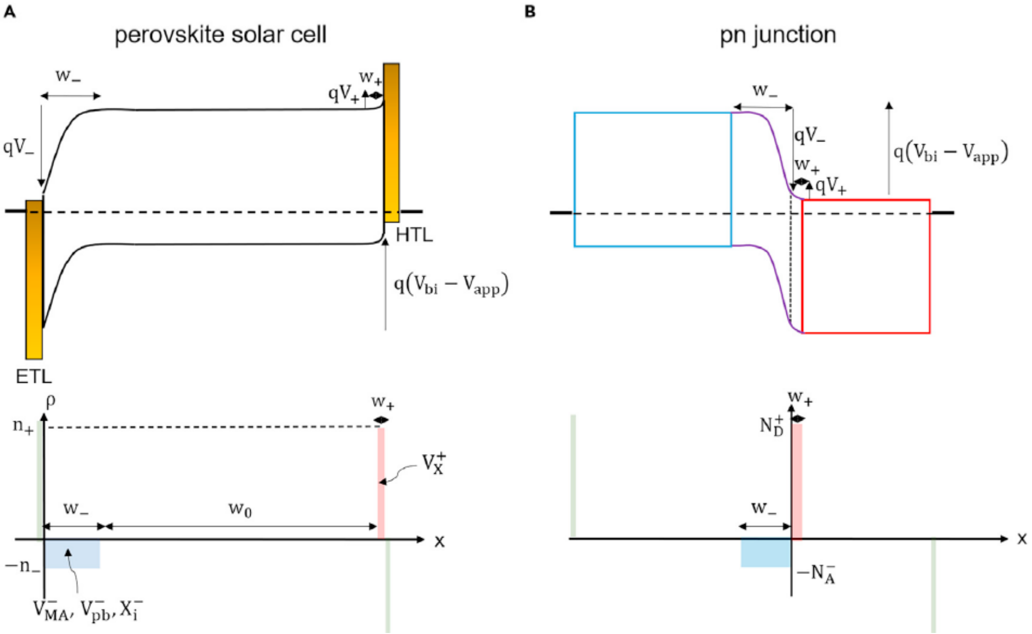

Figure 2.8: (A) perovskite solar cell, where the band profile is determined by the distribution of accumulating vacancies close to the HTL and the remaining immobile anions in the vacancy-depleted region close to the ETL. (B) A p-n junction, where the band profile is determined by the distribution of fixed ionized donors and acceptors in the n and p semiconductors respectively. Figure from [63].

We can now use the electrostatic potential distribution given by equation (2.129) and multiply it by the electron charge $(-q)$ to plot the energy diagram shown in figure 2.8.A. As expected, this energy diagram is highly asymmetric and is featured by a field-free region in the bulk of the absorber. A direct analogy can be established with a *p*-*n* junction, as shown in figure 2.8.B. In fact, the vacancy-depleted region in the perovskite solar cell would correspond to a weakly doped p-type semiconductor in a $p - njunction$, while the vacancy-accumulation region would correspond to a highly doped n-type semiconductor.

Case $w_- + w_+ = L$

This condition implies that the mobile vacancy concentration is too small to fully shield the potential difference between the ETL and HTL and the field-free region disappears. The critical vacancy concentration that determines when the electric field is no longer screened in the perovskite bulk is found by solving the equation $w_- + w_+ = L$. For a 400 nm thick perovskite device with a voltage drop of 1 V and dielectric constant of 24, this condition is satisfied when $N_0 = 5 \times 10^{15} cm^{-3}$ [63]. Under this conditions, the mobile vacancies will not fully screen the electric field in the bulk of the absorber. In this case, the potential distribution is the sum of the potential due to mobile ion shielding the potential, as defined by equation (2.133), and the part of the potential that is not shielded that drops linearly within the absorber.

This model assumes the migration of one type of mobile ion that accumulates at the HTL, in line with studies that show halide vacancies to be the dominant mobile ion in halide perovskites. Note, however, that this model does not consider the existence of other mobile ions with smaller concentrations since these ions would not affect the electric field distribution. The model predicts that if 1 V drops within a 400 nm thick perovskite absorber with a mobile vacancy concentration $> 5 \times 10^{15} cm^{-3}$, most of this voltage drops within the vacancy-depleted region close to the ETL. In the case where negatively charged ions would be mobile instead of positively charged vacancies, the vacancy-depleted region would be formed at the HTL and the accumulation region at the ETL. This simple model reproduces the field asymmetry and the field-free bulk features discussed previously and can easily be used to extract the mobile vacancy concentrations and the main band diagram features (N_0, w_+, w_-, V_+ and V_-) from charge measurements (Q_{ion}). It is worth mentioning that this approach is valid to reproduce the electric field even under illumination given that the concentration of free carriers for a working solar cell ($\leq 10^{16} cm^{-3}$) [74] is negligible with respect to the ion concentration.

2.9 IV curves

A photovoltaic cell works in the same way that a diode in dark conditions. But under illumination, due to the absorption process the carrier concentration changes. When light is absorbed a pair e^- - h^+ is created and separated in a depletion region in the same way that happen to the pair created due to thermal agitation which give place to the saturation current. As a result, a photo-current is generated in the same direction that the saturation current. This photo-current is due to the photo-generated carriers and because of that, it will only depend on the generation and recombination rates. Because of this, we can considerate photo-current as an additive term to the diode current on the Shockley diode equation.

$$I(V) = I_{sat}\left(e^{\frac{qV}{kT}} - 1\right) - I_{light} \tag{2.134}$$

The most common parameters reported for a photovoltaic cell can be seen in figure 2.9 and they are:

i) The short circuit current I_{sc}, defined as the current when the applied potential is zero.

ii) The open circuit voltage V_{oc}, defined as the voltage when the current is zero.

iii) The current I_{max} and the voltage V_{max} corresponding to the point of maximum power $(P = VI)$ of the current-voltage curve.

iv) The Fill Factor (FF) defined as

$$FF = \frac{I_{max}V_{max}}{I_{sc}V_{oc}} \tag{2.135}$$

it is the quotient between the maximum power of the cell and the maximum power of an ideal cell in which the IV curve is a rectangle. This parameter is normally between 0.7 ad 0.85 for a Si commercial solar cell.

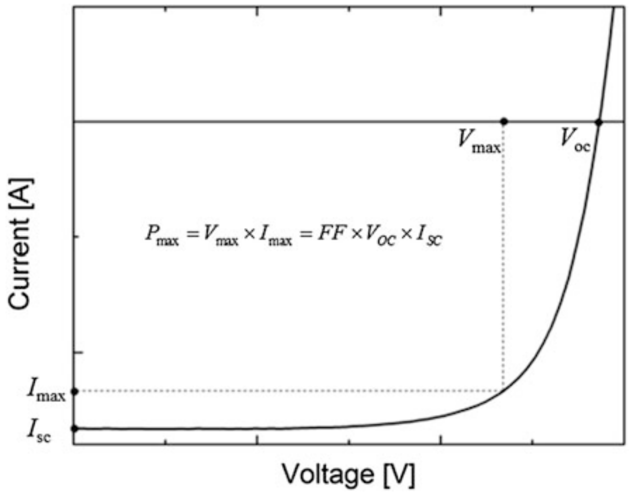

Figure 2.9: Typical curve of current vs voltage for a photovoltaic cell under illumination. Figure from [75]

Knowing this parameters is possible to calculate the efficiency dividing the max power by the incident power or:

$$\eta = \frac{I_{sc} V_{oc} FF}{A E_0} \tag{2.136}$$

Where A is the effective area of the cell and E_0 is the global incident standard spectrum irradiance on earth surface after crossing 1.5 times air masses ($E_0 \approx 1000 W/m^2$). This intensity is defined on a sunny day, with the sun at 48.19° degrees from the zenith and taking in consideration the dispersion and reflections. This is the standard intensity used to report solar cells.

In practice, when characterizing photovoltaic cells there are factors that are not taken into account by the model (2.134) like the internal resistance of the semiconductor or the contacts which can be modelled as a series resistance R_S [76, 77]. For voltages higher compared to V_{oc}, diodes and cells show an ohmic behaviour. The current leaks, the recombination outside the depletion region and the possible short circuits on specific points of the junction can be modelled as a parallel shunt resistance R_{sh} The recombination lost in the depletion region lead to changes in the behaviour observed in equation (2.134) can be modeled with an ideality factor. This factor m goes in the denominator of the exponential argument in accordance with Sah, Noyce and Shockley theory [78]. The ideality factor is going to be 1 in the ideal case, meanwhile if the recombination in the depletion region is mediated by the Shockley Read Hall recombination process, the factor is going to be 2. Different values between

1 and 2 are due to more complex process [79]. All this affects the Fill Factor and in consequence the efficiency η. Taking all this into consideration, a better model presented in figure 2.10 can be constructed.

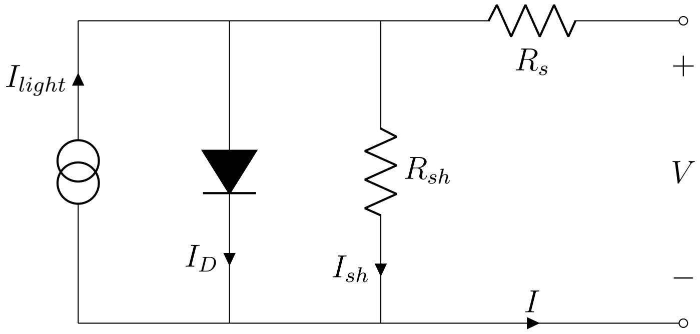

Figure 2.10: Equivalent circuit for a real photovoltaic cell.

The photo-generated current is represented by the current source. The Shockley model gives the I_D current through the diode taking in consideration the voltage drop in the series resistance R_s. The shunt current I_{sh} though the resistance R_{sh} represent the loses and finally the current through the R_s is the total current from the cell. The current voltage relation is given by the expression:

$$I = I_0 \left(e^{\frac{q(V-R_sI)}{mk_bT}} - 1 \right) + \frac{V - R_sI}{R_{sh}} - I_{light} \tag{2.137}$$

This expression can only be evaluated numerically, but using Lambert's W function, which is defined as the inverse function of $y = xe^x$(i.e. $lamW(y) = x$), an expression for the current is obtained [76]:

$$\begin{aligned} I = \frac{V}{R_s} - \frac{R_{sh}(R_sI_{light} + R_sI_0 + V)}{R_s(R_{sh} + R_s)} \\ + \frac{mk_bT}{qR_s} lamW \left[\frac{qR_sI_0R_{sh}}{(R_s + R_{sh})mk_BT} e^{\frac{R_{sh}q(R_sI_{light}+R_sI_0+V)}{mk_bT(R_s+R_{sh})}} \right] \end{aligned} \tag{2.138}$$

This expression depends on 5 parameters, I_0, I_{light}, m, R_s and R_{sh}. Besides that, its difficult to separate the currents I_0 e I_{light} which normally have orders of magnitude of difference. It will be convenient to simplify the expression (2.138) for the current. To do this, equation (2.137) is evaluated in short circuit and open circuit conditions ($I = 0$ y $V = V_{OC}$). This lead to expressions for

I_0 y I_{light} which help to eliminate variables in (2.138)

$$I_0 = \frac{\left(I_{SC} + \frac{R_s I_{SC} - V_{OC}}{R_{sh}}\right) e^{\frac{-qV_{OC}}{mk_bT}}}{1 - e^{\frac{q(R_s I_{SC} - V_{OC})}{mk_bT}}} \tag{2.139a}$$

$$I_{light} + I_0 = \frac{I_{SC} + \frac{R_s I_{SC} - V_{OC}}{R_{sh}}}{1 - e^{\frac{q(R_s I_{SC} - V_{OC})}{mk_bT}}} + \frac{V_{OC}}{R_{sh}} \tag{2.139b}$$

With this, substituting in (2.138) the dependence with I_0 e I_{light} can be eliminated reducing to 3 the parameters.

On the other hand, a way to estimate this parameters is with an expression for $\frac{dV}{dI}$ obtained from (2.137):

$$\frac{dV}{dI} = \frac{mk_bT/q}{I_{light} + I_0 + I - (V - R_s I - mk_bT/q)/R_{sh}} + R_s \tag{2.140}$$

From here it can be obserbed that for high voltages, the cell will have an ohmic behaviour and the series resistance R_s can be estimated as the slope of the plot of V vs I. meanwhile, in short circuit conditions, the approximation

$$\left.\frac{dV}{dI}\right|_{I=I_{SC}, V=0} \approx R_{sh} + R_s \tag{2.141}$$

can be made.

2.10 IMPS and IMVS Models

With every new solar cell technology great research efforts are made and perovskites solar cells are not the exception. Consequently, a priority of current research is the characterization of electronic parameters such as the electron diffusion coefficient, D_n, and the electron recombination lifetime, τ_n. The lifetime of photogenerated charge carriers is one of the most important parameters in solar cells, as it rules the recombination rate that defines the open circuit voltage and the required minimum extraction time. Lifetime evaluation of solar cells is frequently conducted via transient electrical methods like Open Circuit Voltage Decay (OCVD) and transient optical methods when its possible like Photoluminescence Decay (PLD). This methods often lead to large discrepancy between optically and electrically determined lifetimes. This is because the assigned lifetimes are being severely influenced by capacitive decay rates of spatially separated charge carriers. These "lifetimes" have thus very little in common with lifetimes relevant under steady state operational conditions of the solar cell. The problem of lifetime determination via electrical means arises from that the relaxation of such charges, being associated with quasi-static capacitances of geometric type or from space-charge regions in the device [80]. This is mayor issue in devices with a strong ionic behaviour like perovskites.

But, a way to face this issue is to use frequency domain techniques instead of time domain techniques. The frequency spectroscopic measurements show features that distinguish the different processes and regimes that are present in the devices according to their different characteristic frequencies. The Intensity Modulated Photocurrent Spectroscopy (IMPS) and Intensity Modulated Photovoltage Spectroscopy (IMVS) are two techniques for the study of carrier dynamics that were first developed to study electrolytic cells but are applicable to solid state cells [81].

The objective of these experiments is to measure the characteristic times associated to the processes that occur inside the cells. For this, their optoelectronic response to light whose intensity is modulated at variable frequencies is studied. This is done using a LED/laser with a fraction of its intensity modulated and the frequency response of the photocurrent is measured for the case of IMPS, and the photogenerated voltage for the case of IMVS. By doing this, currents or voltages are obtained and is useful to plot then on Nyquist diagrams (real or in phase versus imaginary part or in quadrature of the currents and voltages as the case) or Bode plots (Real, imaginary or module and phase against its frequency dependence). From these measurements the characteristic frequencies of the system can be obtained.

These measures were first developed with white light but an advantage of using lasers is that it is possible to see different features associated with the effects that each photon energy has on the device.

The result of this measures are similar to those of Impedance Spectroscopy (IS), they also present semicircles in the complex plane which goes to zero in the high frequency limit. The electronic diffusion effect is observed at high frequency, far from the low frequency ionic polarization allowing the separation of the effects. Therefore, it is important to find the spectral signatures of diffusion. The diffusion effect is usually manifested as a 45^o inclined line at high frequency in the complex plane representation of the spectra. This is the

Warburg impedance with the square root dependence on the angular frequency as $Z(\omega) \propto (i\omega)^{-1/2}$, clearly indicating the presence of a diffusion transport resistance [82].

But, an enormous number of papers have analyzed the IS response of Perovskites Solar Cells, and such a response has not been observed. The usual reason to explain the absence of such an observation is that the transport resistance it too small due to the large electron mobility/diffusion coefficient and becomes absorbed in the series resistance. There have been also a number of studies of Metal Halide Perovskites (MHP) using IMPS, but the spectral observation of Warburg features has not been achieved. Often, the IMPS transfer function in MHP shows the curious feature that the spectra turn to real negative values (Third quadrant) at high frequency. This high frequency feature has been often explained in the literature as the effect of RC attenuation [35, 83, 84], that is, the large frequency negative feature is associated with the impedance of series and parallel elements in addition to diffusion. This type of effect is obviously uninteresting for the observation of diffusion. In any case, it provides a correction of the spectra by the impedance elements that can be measured independently. However, another effect associates a negative spiraling IMPS feature with the photocurrent created by carriers generated far from the collecting contact. Interestingly, the excursion to the third quadrant, in which the real part of the IMPS transfer function becomes negative, is found in a configuration with a large perovskite layer that provokes a nonuniform generation profile. In this case, the generation profile is that represented in figure 2.11, where the generation of one kind of carrier is localized far away from their collecting contact.

To understand these effects, a model is necessary to explain the behaviour and the meaning of the measured characteristic frequencies. As can be seen in figure 2.11, assuming that electrons are the carriers that go through the material, we will consider their concentration balance in the absorber. In this model it is assumed that the loss of electrons due to recombination is proportional to the concentration of conduction electrons in the semiconductor and that the diffusion current is proportional to the gradient of the concentration. It is assumed that charge transport in the semiconductor is by diffusion, that is, transport by electric field is negligible, and that the free and trapped electrons are still in thermal equilibrium. This is reasonable considering to the

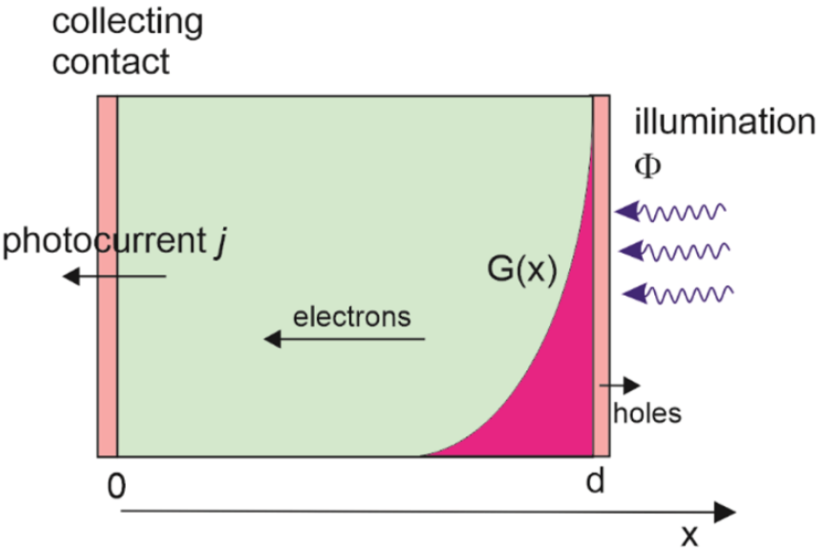

Figure 2.11: Scheme of a p-i-n cell under illumination generating electrons far from the collecting contact. $G(x)$ is the exponential profile of generation dependent on the absorption coefficient α. Figure from [85]

discussion of section 2.8. The transport equation is:

$$j(x) = qD_n \frac{\partial n}{\partial x} \tag{2.142}$$

Where n is the concentration of photogenerated electrons in the conduction band, q is the charge of the carriers and D_n is the diffusion coefficient of the electrons in the conduction band (CB).

Writing down a continuity equation with this current density: as in figure 2.11, considering an incident photon flux Φ that arrives at the solar cell at $x = d$. The equation for the excess electron density n is:

$$\frac{\partial n}{\partial t} = i\omega n = \frac{1}{q}\frac{\partial j}{\partial x} + G(x,t) - R(x,t) = D_n \frac{\partial^2 n}{\partial x^2} + G(x,t) - R(x,t) \tag{2.143}$$

Where $G(x,t) = \alpha\Phi exp(\alpha(x-d))$ is the injection rate of electrons from the excited states of the absorber and $R(x,t)$ the recombination term which is assumed proportional to n with a rate $1/\tau_n$. For a light intensity sinusoidally ($e^{i\omega t}$) modulated, we get:

$$\frac{\partial n}{\partial t} = D_n \frac{\partial^2 n}{\partial x^2} + \alpha\Phi e^{\alpha(x-d)} - \frac{n}{\tau_n} \tag{2.144}$$

The solutions to this differential equations are [83]:

$$n(x,t) = [Ae^{\alpha x} + Be^{-\frac{Z}{L_n}x} + Ce^{\frac{Z}{L_n}x}]e^{i\omega t} \tag{2.145}$$

With $L_n = (D_n \tau_n)^{1/2}$ the diffusion length, $Z = (1 + i\omega\tau_n)^{1/2}$ and $A = [\alpha L_n^2(\phi/D_n)/(Z^2 - \alpha^2 L_n^2)]\, e^{-\alpha d}$. The parameters B and C are defined by the boundaries conditions for short circuit and open circuit. These boundary conditions under short-circuit are $n(x=0) = 0$ and

$$\left.\frac{\partial n}{\partial x}\right|_{x=d} = 0 \tag{2.146}$$

The photocurrent density j at the collecting contact at $x = 0$ is

$$j = D_n \left.\frac{\partial n}{\partial x}\right|_{x=0} \tag{2.147}$$

The IMPS transfer function $\tilde{Q}(\omega) = Q'(\omega) + iQ''(\omega)$ is obtained by the quotient of the small modulated input/output

$$\tilde{Q}(\omega) = \frac{\tilde{j}}{q\phi e^{i\omega t}} \tag{2.148}$$

The result is:

$$\tilde{Q}(\omega) = \frac{1 - e^{-\alpha d}\left[e^{Zd/L_n} + \left(\frac{Z}{L_n\alpha} - 1\right)\sinh\left(\frac{Zd}{L_n}\right)\right]}{\left[1 - \left(\frac{Z}{L_n\alpha}\right)^2\right]\cosh\left(\frac{Zd}{L_n}\right)} \tag{2.149}$$

The shapes of the IMPS spectra generated by equation (2.149) depend on the light absorbance mode and the diffusion-recombination features of the material. The physical parameters for absorbance and extraction affecting the form of the spectra are the light absorption length, α^{-1}, and the diffusion length, L_n, respectively. These parameters transform the spectral shape depending on whether they are shorter or longer than the cell thickness d, and the different kind of spectra that are obtained are shown in figure 2.12 (please note that in these plots the sign of the imaginary part has been changed, this is something common in papers for no apparent reason). In the spectra, its included the characteristic time constants for diffusion across the layer thickness

$$\omega_d = 2\pi \frac{D_n}{d^2} \tag{2.150}$$

and for recombination

$$\omega_{rec} = \frac{2\pi}{\tau_n} \tag{2.151}$$

Note the proportions between characteristic distances and frequencies

$$\frac{\omega_d}{\omega_{rec}} = \left(\frac{L_n}{d}\right)^2 \tag{2.152}$$

A Warburg-like spectral feature at high frequencies $(i\omega)^{-1/2}$ is obtained when the light is generated across the full thickness ($\alpha^{-1} > d$), either for short or long L_n (top row of figure 2.12). In the bottom rows, it is noted that looping spectra producing a negative real component Q' at high frequency appear only when the absorption length is much shorter than the cell thickness. Another required condition for this feature is the diffusion length being longer than the absorption. These conditions are expressed respectively as $\alpha^{-1} << d$ and $\alpha^{-1} < L_n$. Then, loops appear in the $\alpha^{-1} < d < L_n$ case and also in the $\alpha^{-1} < L_n < d$ case. This analysis confirms that this loop is associated with a collection of charges generated only far from the collecting contact. When the light is absorbed in a distance comparable to that of the cell (second row), no negative values of Q' are obtained but the spectra turn from Warburg like into a semicircle as the L_n increases.

As was previously mentioned, it has been suggested in the literature that the additional impedances in the solar cell can produce a negative loop in the measured IMPS response, $\tilde{Q}_{exp}$. The previous transfer function due to diffusion only is modified as

$$\tilde{Q}_{exp}(\omega) = \tilde{Q}(\omega)A(\omega) \tag{2.153}$$

In the case of series resistance R_s and geometrical capacitance C_g, the attenuation factor $A(\omega)$ is

$$A(\omega) = \frac{1}{1 + i\omega R_s C_g} \tag{2.154}$$

The RC attenuation can produce a considerable effect in high frequencies, as can be seen in figure 2.13. The RC attenuation with high RC values turns positive theoretical IMPS responses into the Q' negative axis, as seen in figure

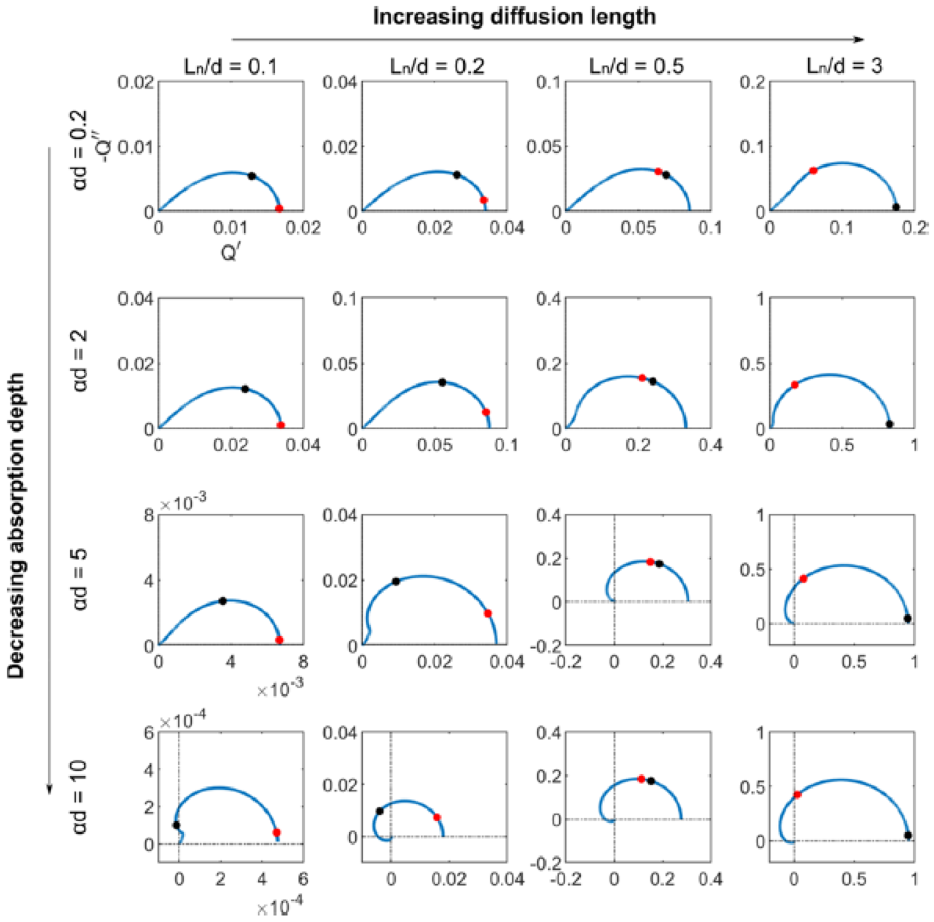

Figure 2.12: Complex plane plots of the IMPS transfer function for several relative values of light absorption distance and diffusion length. Rows are for equal absorption length and columns for equal diffusion length. Red points indicate the characteristic time constant for diffusion, $\omega_d = D_n/d^2$, and the black ones are the characteristic time for recombination, $\omega_{rec} = 2\pi/\tau_n$. No RC attenuation is considered. Figure from [85]

2.13. This effect makes the loop and Warburg IMPS responses undistinguished, whether light is completely absorbed or not. However, due to the fact that the RC values can be measured by the impedance spectroscopy technique, the RC attenuation can be controlled and removed to obtain the pure diffusion features.

For the IMVS case, the boundaries conditions are

$$\left.\frac{\partial n}{\partial x}\right|_{x=0} = 0 \tag{2.155a}$$

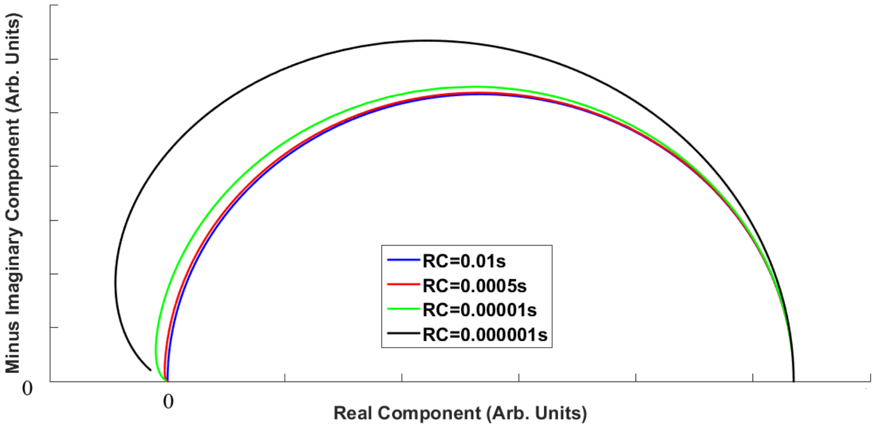

Figure 2.13: Numerical calculation of the response of a cell applying the afford mentioned model with the RC attenuation. The used parameters were $\alpha d = 4/3$, $\tau_n = 1\mu s$ and $L_n = 450\ nm$.

$$\left.\frac{\partial n}{\partial x}\right|_{x=d} = 0 \tag{2.155b}$$

Which means that there in no current coming out of either side of the absorber. Now we have to consider the relation of carrier density to the voltage at the selective contact. For the Boltzmann statistics, we have that

$$n(0,t) = n_0 e^{-\frac{qV}{k_B T}} \tag{2.156}$$

considering that the voltage due to increasing electron density is negative. For a small perturbation of the voltage, we have with a Taylor expansion

$$\tilde{W}(\omega) = -\left(\frac{dn}{dV}\right)^{-1} \tilde{n}(0,\omega) \tag{2.157}$$

assuming that the derivative is constant, it is possible to write

$$\tilde{W}(\omega) \propto \tilde{n}(0) \tag{2.158}$$

This lead to the transfer function for IMVS which has the form [86]

$$\tilde{W}(\omega) \propto \frac{1 - e^{-\alpha d}\left\{e^{\frac{Z}{L_n}d} + \left[\frac{Z}{\alpha L_n} - 1\right]\sinh\left(\frac{Z}{L_n}d\right)\right\}}{\left(\frac{Z}{L_n}d\right)\left[1 - \left(\frac{Z}{\alpha L_n}\right)^2\right]\sinh\left(\frac{Z}{L_n}d\right)} \tag{2.159}$$

Finally, a comprehensive classification of spectra by the sets of parameters indicated in table 2.1 is shown in figure 2.14. It include a third characteristic frequency $\omega_\alpha = D_n \alpha^2$ which is the diffusion over light absorption distance. The cases for a short penetration of the light are particularly interesting (high absorbance), as the spectra spiraling to the origin allow the determination of electron diffusion coefficient and lifetime as shown experimentally.

	fig.2.14.a	fig.2.14.b	fig.2.14.c	fig.2.14.d
D_n	10^7	10^5	10^7	10^5
α	10/d	10/d	0.1/d	0.1/d
ω_{rec}	9090	9090	9090	9090
ω_d	10^5	10^3	10^5	10^3
ω_α	10^7	10^5	10^3	10
L_n/d	3.31	0.331	3.31	0.331

Table 2.1: Values of Parameters Selected for figure 2.14. Distances in μm, frequency in $rads^{-1}$, D_n in $\mu m^2 s^{-1}$ and $d = 10\mu m$ for all cases.

As can be seen the cases with a low ω_α C and D show a single cycle for IMVS and a straight line at $\frac{\pi}{4}$ for high frequency limit For the IMPS case. This behaviour is known as as a diffusion limited case. This case can be represented with a Warburg element in a equivalent circuit and represent charge-transfer resistance and a double-layer capacitance. These cases also, are those with a long absorption length (10 times the material length). The absorption is taking place all over the material.

In the other two cases the absorption length is a tenth of the material length. Now the absorption only happen on the side of the material where the light goes in. Then the photogenerated charges have to travel through the material to reach the other selective contact. This transport generate a delay in the response which produce the capacitive effect observed in the plots A and B.

Finally, the main difference between a and b cases is that the first one have diffusion length longer than the material length and the other does not. The short diffusion length is detrimental for the efficiency because it means that recombination is taking place before the carriers can leave the device.

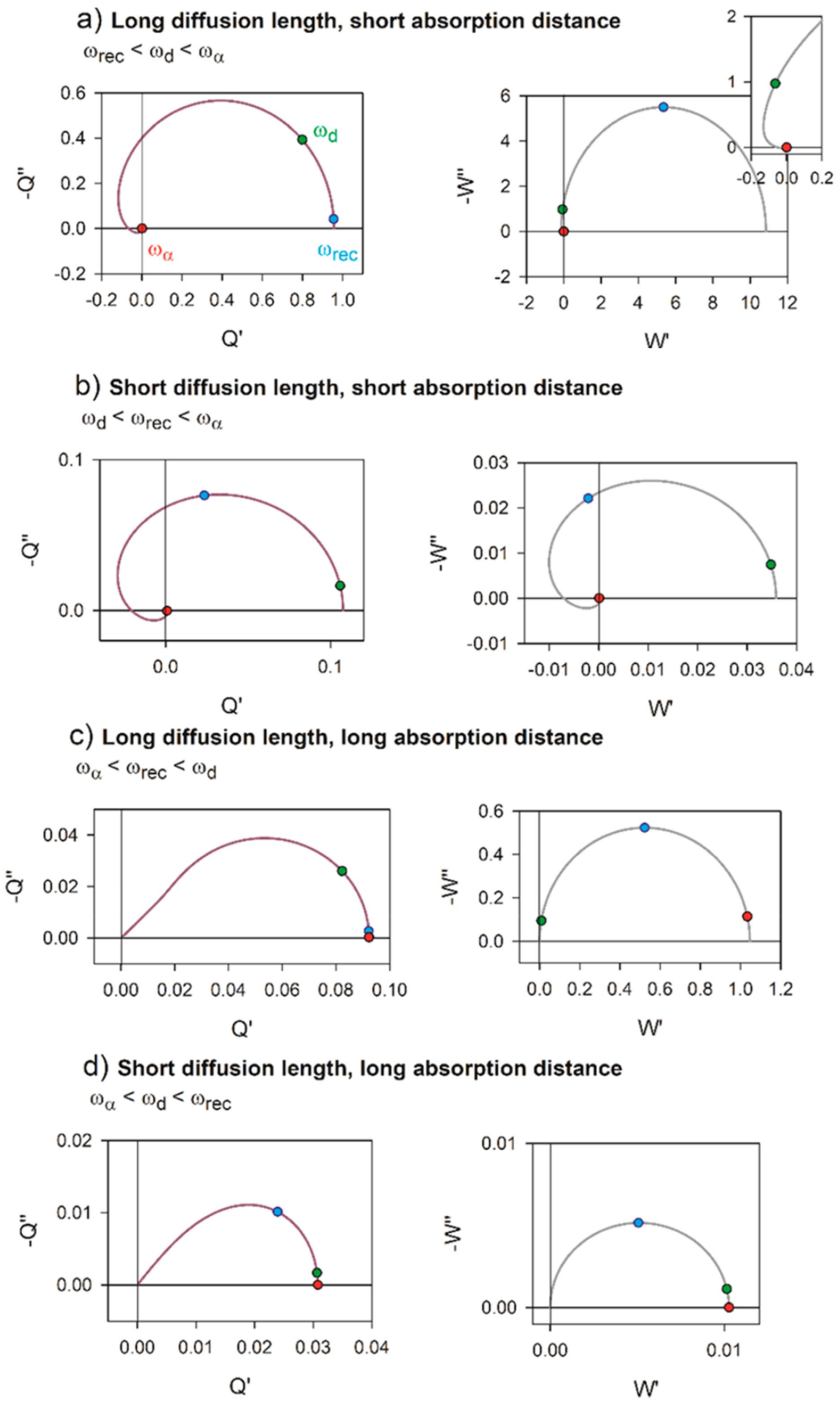

Figure 2.14: Representation of $\tilde{Q}$ and $\tilde{W}$ for the generation-diffusion-recombination model. For the used parameters, given in table 2.1, the three highlighted characteristic frequencies are: ω_{rec} (blue), ω_α (red) and ω_d (green). Figure from [86].

Chapter 3

Experimental Methodology

3.1 Sample Synthesis

The Methylammonium Lead Iodide (MAPI) perovskite synthesis begins with commercial glass substrates, CH_3NH_3I Methylammonium Iodide (MAI, Greatcell solar), PbI_2 (Sigma Aldrich, 99%), $HCON(CH_3)_2$ Dimethylformamide (DMF Sigma Aldrich, anhydrous 99.8%),$(CH_3)_2SO$ Dimethyl sulfoxide (DMSO Emsure ACS, 99.9%), C_6H_5Cl chlorobenzene (Merck, 99.5%).

The MAPI precursor solution was made with a preparation of DMF solutions (50 weight %) containing 1.35 $molL^{-1}$ of MAI, PbI_2, and DMSO (1:1:1 mol %), respectively.

Glass slide substrates were cut in pieces of 25 × 25 mm followed by cleaning with detergent solution and rinsed with distilled water. Afterward, the substrates were sonicated for 15 min in acetone and mixed with 50:50 ethanol–isopropanol and dried in air. Then, the substrates were treated in a UV–O_3 chamber for 15 min. Immediately, the substrates were transferred to a glovebox and heated at 100 $˚C$ for 5 min to evaporate residual humidity on the surface. The perovskite precursor solution was spin-coated at 4000 rpm for 50 s. During this step, DMF was selectively washed with chlorobenzene just before the white solid begins to crystallize in the substrate. Afterward the substrate was annealed at 100 $˚C$ for 10 min [33].

3.1.1 Preparation of Photovoltaic Devices

Photovoltaic solar cells were prepared following the layer stack $Glass/FTO/c–TiO_2/mp - TiO_2/MAPI/C$, where the c- and mp- prefixes indicate compact and meso-porous titanium dioxide, respectively. The FTO serves as the front contact, while a carbon electrode was chosen for the back contact. The TiO_2 serves as an electron transport layer (ETL) for photogenerated electrons, while the corresponding photogenerated holes are transmitted directly to the carbon back contact [32].

3.2 Low temperature Measurements

The evolution of the MAPI films optical properties (absorbance and Photoluminescence (PL)) with temperature were measured using the experimental setup presented in fig. 3.1. The films were grow on glass or FTO (Flour doped Tin Oxide) coated glass. As FTO is transparent in the visible region, the absorbance and the PL can be measured by light transmittance. The samples were placed inside the vacuum chamber of a closed cycle cryostat (CTI Cryogenics CRYODYNE) with quartz windows and the temperature was varied from room temperature to 12 K with a ramp set at 1 K/min using a LAKESHORE 321 temperature controller.

For the Absorbance measurements, an Ocean Optics HL2000 tungsten lamp was used as light source and an Ocean Optics S2000 spectrometer (OOS2000) was used to measure the transmitted light spectrum and the reference spectrum. The Elliott formula for absorption spectra of eq. (2.68) was used to fit the measurements. This was done implementing the (δ) Dirac delta distribution as a gaussian function, and the (Θ) Heaviside step distribution as a sigmoidal function. An example of this fitting can be seen in the fig. 3.2.

For the Photoluminescence measurements, a *455 nm* LED Thorlabs M455F1 was used to stimulate the PL and the spectrometer OOS2000 as before was used to measure the outcoming light. A Newport FSR-OG550 550 nm long pass filter was used to remove most of the LED light after the film and before coupling it to the spectrometer. To fully separate the remaining transmitted light of the LED from the PL emission, the LED spectrum after going through the *550 nm* filter was multiplied by the transmittance spectra of the film at each temperature and subtracted from the measurement. An example of this separation can be seen in fig. 3.3.

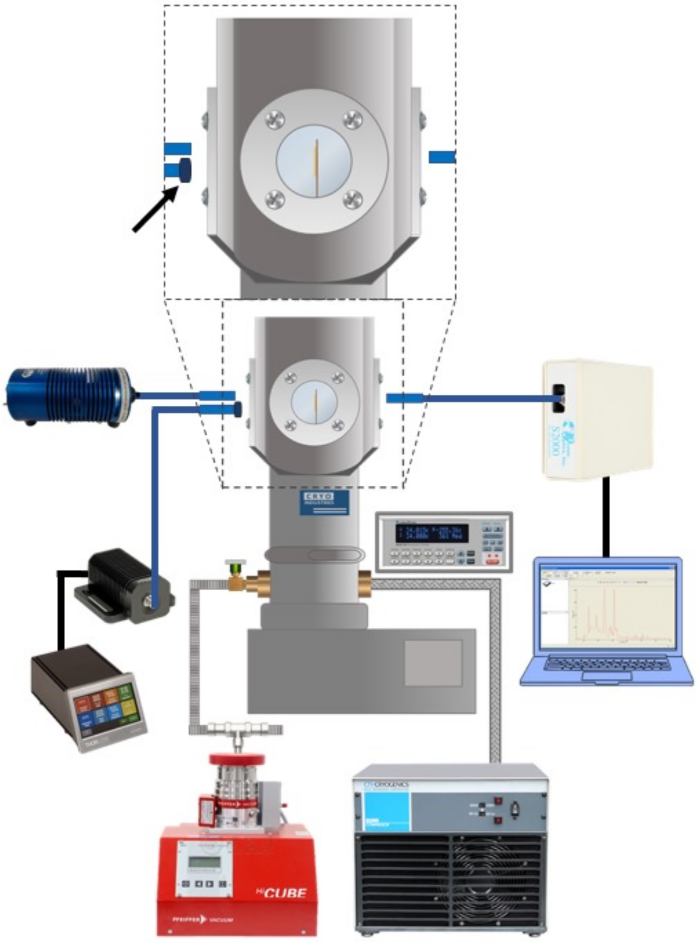

Figure 3.1: Experimental setup used for the low temperature optical measurements. It is showed the cryostat coupled to the HL2000 lamp, the LED and the OOS2000 spectrometer. Figure courtesy of B.Sc. Carina Cabrera.

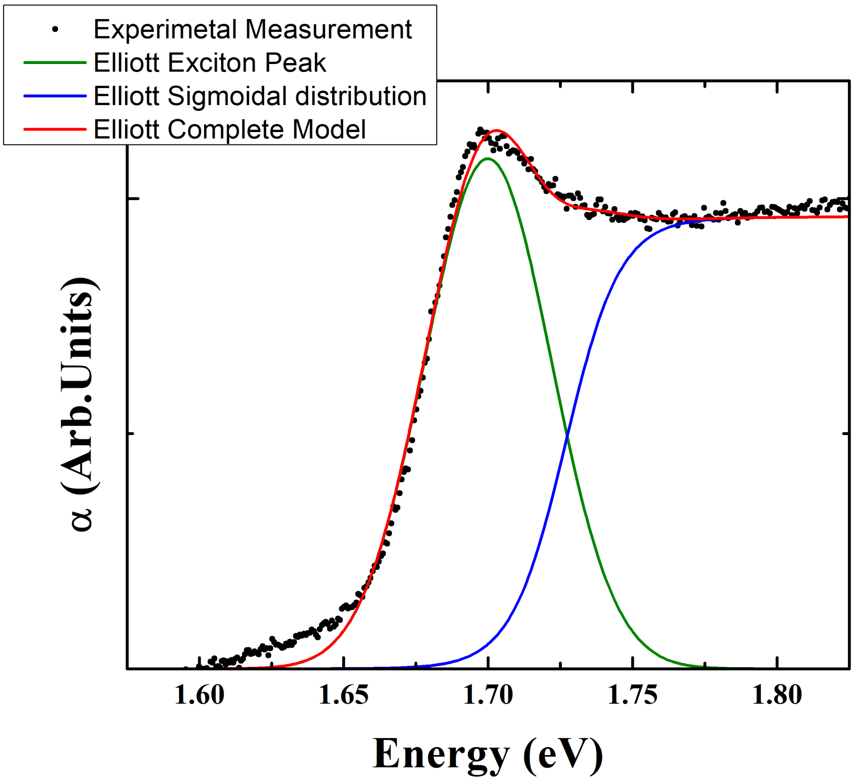

Figure 3.2: Example of a 20 K absorbance measurement (Black), Excitonic absorption peak (Green), Elliott sigmoidal model for interband absorption (Blue) and the whole Elliott model for the absorption (Red).

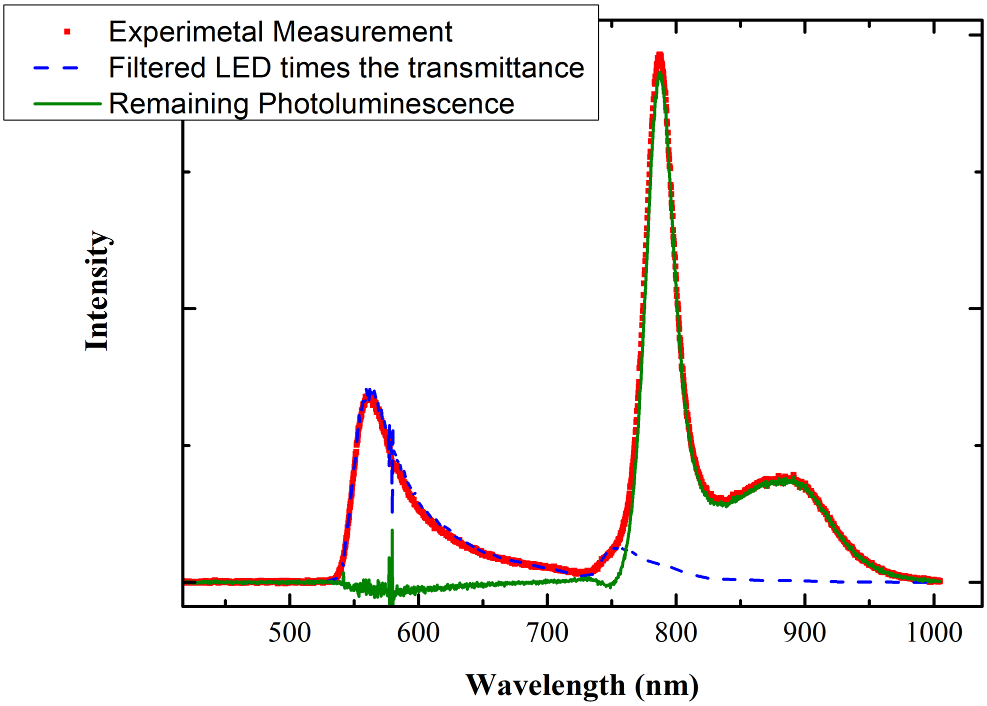

Figure 3.3: Example of a 50 K PL measurement with remaining LED light (Red), Filtered remaining LED spectrum times the transmittance (Blue), PL after subtracting the LED spectrum (Green).

3.3 IV Measurements

The characterization of the cells were made by measuring the voltage (V) vs current (I) curves in dark and under illumination. For this a solar simulator with a Xe lamp (Oriel-Newport 69907) with a NEWPORT 69907 energy source and a power controller NEWPORT 68945 was used. An air-mass filter 1.5G was used to make the spectrum more alike the solar irradiation on the earth surface with an 48.19 degree incidence from zenith, which is the standard laboratory procedure.

A solar simulator must emit the same fraction of intensity that the sun spectrum in six regions of 100 nm wide, ranging from 400 nm to 1000 nm. The intensity emitted in each of the six regions is divided by the total intensity. Then these fractions are compared with the fractions corresponding to the standard spectrum and for it to be considered an adequate simulator there must be less than a 25% difference in all regions. Fig. 3.4 shows the spectrum of a solar simulator compared to the solar irradiance spectrum.

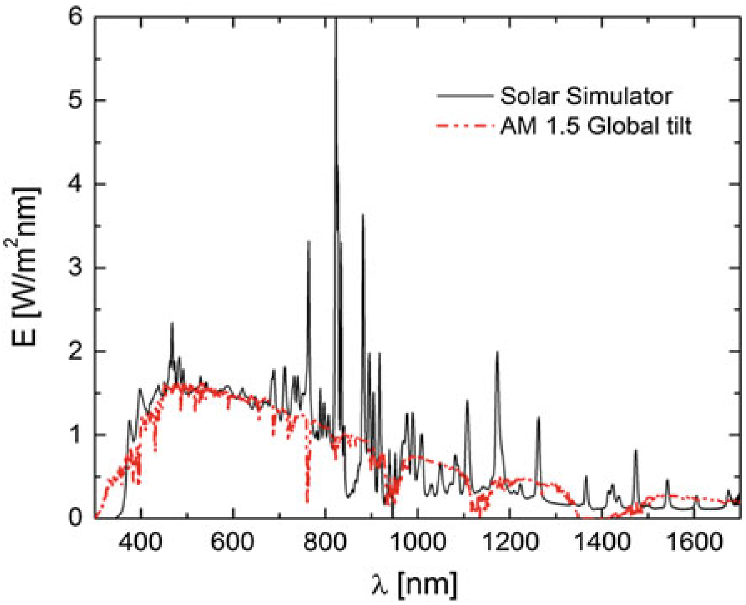

Figure 3.4: Solar simulator spectrum and standard solar AM 1.5 Global spectrum.

A Source Measure Unit (SMU) KEITHLEY 2425 is used to apply the voltage over the cell and measure the current simultaneously. For each cell a dark and an illuminated condition measure is made. Under dark conditions, the cell behave as a diode. Under illumination conditions, the IV curve moves to negatives current because of the photogenerated current is added. From the IV curve under illumination condition, the open circuit voltage, the short circuit current, the series resistance, the Fill Factor, the efficiency and the shunt resistance are estimated (see section 2.9).

3.4 Spectral Response

The spectral response consists in measuring the current produced in a cell by each light's wavelength. In principle, all photons with an energy higher than the bandgap should be absorbed but not all this absorption leads to current production. Because of that, this measures are important. It allows to see which components of light are actually generating current. Also, comparing the photocurrent for each wavelength with the incident photon flux allows to calculate the external quantum efficiency (EQE) which is the ratio between extracted carriers and the incident photons for each wavelength by unit area.

To do this measurements the cell is placed at the outcoming beam of a monochromator and the current produced by each wavelength is measured with the Source Measure Unit. For the EQE measurements a calibrated silicon cell NEWPORT 91150V is used to determine the incident photon flux at each wavelength.

3.5 IMPS and IMVS Measurements

Fig. 3.5 shows a diagram of the experimental setup for IMPS and IMVS measurements. A laser is used to stimulate the cell with a constant power (offset) and a modulated intensity component with a variable frequency. The amplitude of the modulated component is 10% of the offset amplitude. A frequency response analyser Moku:Go (FRA) is used to modulate the laser frequency and measure the current or voltage frequency response. To assure the open circuit for IMVS or the short circuit condition for IMPS during the measure, a potenciostat/galvanostat Stanford Research System (SRS) EC301 is connected to the cell.

The objective is that the offset intensity places the cell on the working conditions and the modulated component allows to analyse the charge dynamics in the cell through the frequency response.

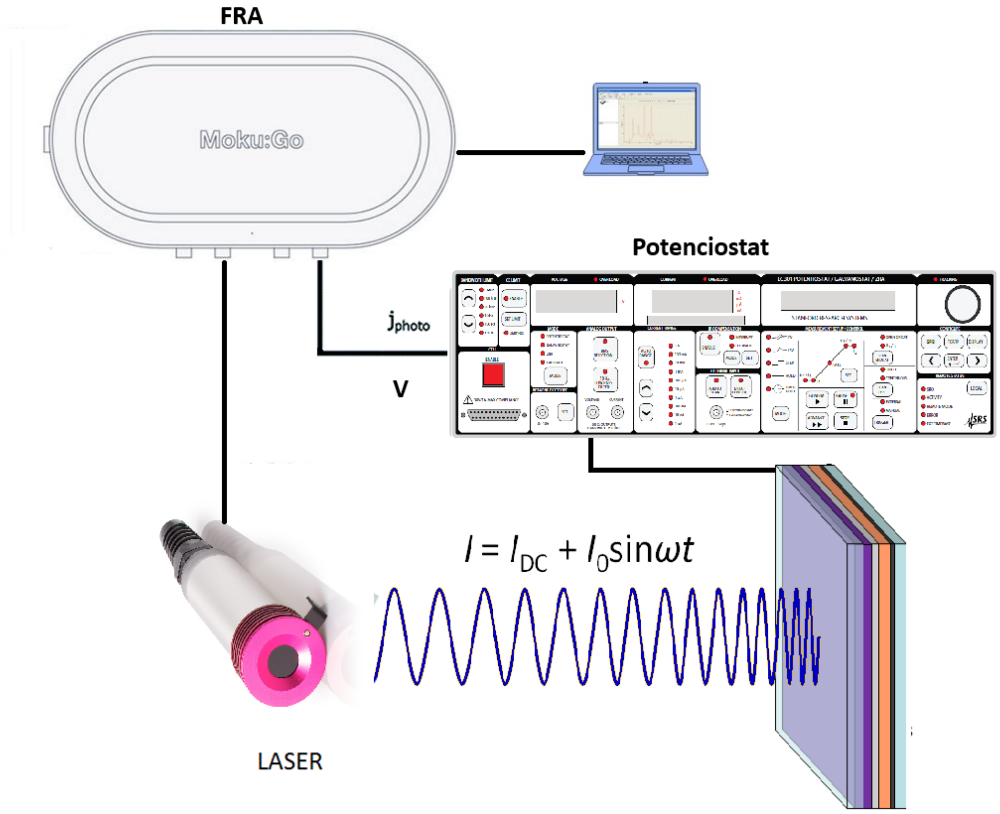

Figure 3.5: Experimental setup using a frequency response analyser to modulate a lasers amplitude and collect the frequency response of the cell from a potenciostat/galvanostat connected to the cell.

Chapter 4

Dependence with Temperature Measurements

4.1 Methylammonium Lead Halide Perovskite Optical Properties

The temperature evolution of the optical properties (absorbance and PL) of MAPI films were investigated. The MAPI film was placed inside the vacuum chamber of a closed cycle cryostat. The temperature was varied from room temperature to 11 K with a ramp set at 1K/min stopping to stabilise the temperature every 10 degrees.

The Elliott formula for absorption spectra presented in secction 2.2 was used to fit the measurements. Only the first excitonic absorption peak ($n = 1$) was consider. The Dirac delta distribution was implemented as a Gaussian function and the Heaviside step distribution was implemented as a sigmoidal function. The fitting were made using the least square method, first fitting only the amplitude, the peak position, and standard deviation of a Gaussian function in the peak proximity. This Gaussian function was subtracted from the measurement and then the amplitude, the center or midpoint i. e. the bandgap energy and the width of the Sigmoidal function was fitted. Finally, these parameters were used as seeds for another fit using the whole Elliott formula, with the previous mentioned parameters as seed parameters. The tolerance factor for the sum of the square difference between the fitting and the measurement was set to 10^{-6} in all cases.

The PL emission peaks were fitted with a Lorentzian, a pseudo-Voigt and

Gaussian functions using the least square method. The pseudo-Voigt converged to the Gaussian and Gaussian function showed a smaller relative squared residual than the Lorentzian, i. e. the squared 2-norm of the residual divided by the integration of the square of the fitted curve. In previous works it was also shown that fitting with a pseudo-Voigt the PL fitted peak converges to a Gaussian peak [87]. Physically this means there is a strong exciton-phonon coupling [44], see section 2.3.

Fig. **??** shows 3D plots of both the absorbance spectra and PL spectra for different temperatures. The low temperature absorbance spectra (fig. 4.1) show the characteristic peak of excitonic absorption plus the interband absorption, described by Elliott formula (2.68). The PL spectra (fig. 4.2) shows sharp emission peaks whose intensity increases as the temperature decreases. However, both spectra present discontinuities in their tendencies close to 125 K originated in a phase transition probably from orthorhombic (cold phase) to tetragonal (hot phase) according to [88] with a 100 meV absorption edge reduction (fig. 4.1) in the colder to hotter phase transition. Moreover, in the absorbance spectra (fig. 4.1 and fig. 4.3a), the absorption edge moves to lower energies when increasing the temperature in both phases. The excitonic absorption peak becomes more intense and sharper at lower temperatures. The PL (fig. 4.2) was only measurable under 200 K; a high energy peak is observed from 200 K that increases its intensity as the temperature decreases until the activation of a second wider low energy peak after the phase transition. As the temperature continues to drop, the second peak gains intensity and the first loses it.

Fitting the absorbance spectra with the Elliott formula was possible to estimate the energy position of the exciton absorption peak and the bandgap energy for both phases. The results are shown in fig. 4.3a. Its observable that the absorption edge moves to higher energies when increasing the temperature in both phases contrary to the observed behaviour in other covalent conventional semiconductors [89–91]. This behaviour can be attributed to the influence of the expansion of the crystal in the bandgap energy or the influence of the interaction with acoustic phonons [87, 92].

The exciton binding energy was estimated as the difference between the exciton absorption peak energy and the bandgap energy. This energy, shown in fig. 4.3b, diminishes from 32 meV at room temperature to 20 meV at 11 K. This decrement is more pronounced in the high temperature phase. The

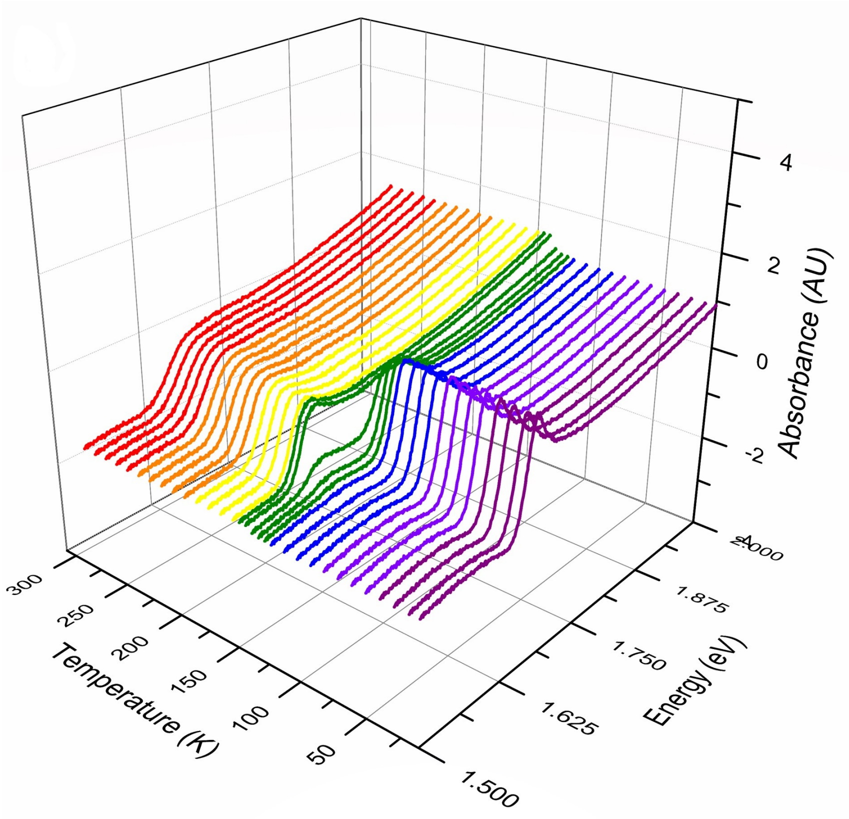

Figure 4.1: Absorbance spectra of MAPI film for different temperatures. The perspective of these figures was chosen to better observe the characteristics of each plot.

value of the exciton binding energy is almost continuous at the phase transition, increasing with the increase in temperature. This increasing behaviour is consistent with the discussed model of an hydrogen like system. The binding energy is related to the effective mass and the dielectric constant through the equation (2.2). As the temperature increase the bandgap energy increases (see fig. 4.3a), that is a widening of the bandgap. The widening in bandgap energy may imply flatter bands (conduction and valence band). Flatter bands will imply lower curvature of the energy bands and therefore higher effective masses, as effective masses are inversely proportional to the energy band curvatures [39, 92]. Therefore, as temperature increases μ increases. On the other hand, as the temperature increase there is an expansion of the material. Therefore, the density of dipoles is reduced. As the dielectric constant is proportional to the polarization (density of electric dipoles) [42], the dielectric constant ϵ would reduce as temperature increases. This effect tends to increase the exciton binding energy. This dependency was previously observed in $CsPbI_3$ and

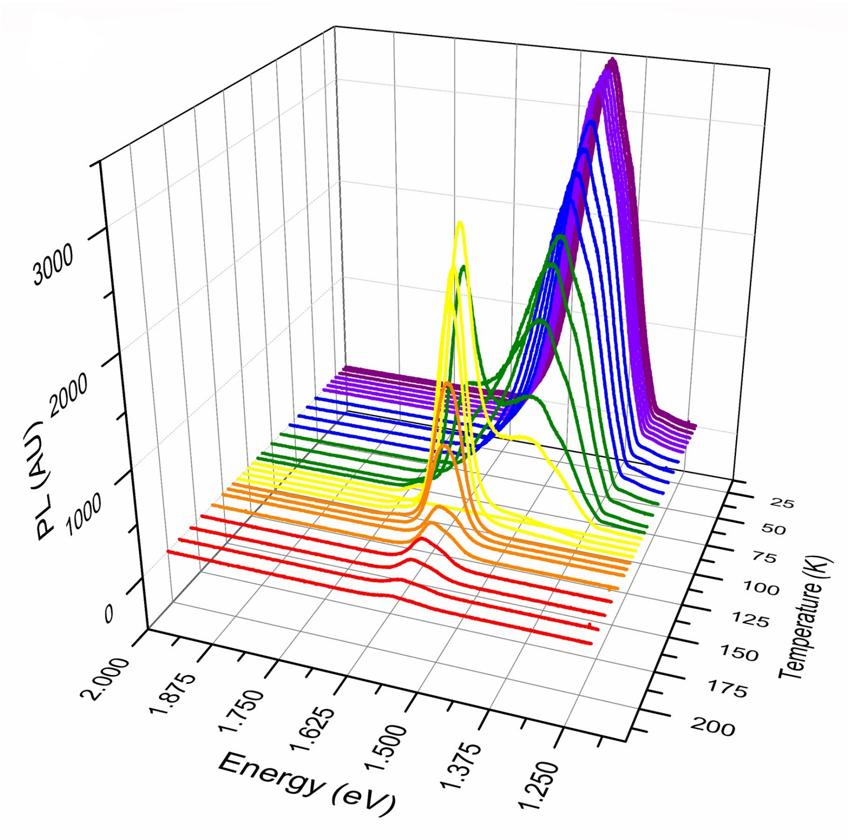

Figure 4.2: Photoluminescence spectra of MAPI film for different temperatures. The perspective of these figures was chosen to better observe the characteristics of each plot.

$CsPbBr_3$ [87, 92].

The PL spectra in fig. 4.2 were fitted with Gaussian functions and the results are shown in fig. 4.4a. This figure shows the energy position of the PL peaks that moves to lower energy when the temperature decreases, but not monotonically. Instead, an overshooting in the energy position of the high energy PL peak can be seen close to the phase transition region. This change in the PL behaviour start 25 K before the phase transition identified through the absorption spectra. This behaviour was previously observed by [93] and matches with a maximum of the amplitude of the PL peak intensity shown in fig. 4.4b. This amplitude reaches a maximum and starts to decrease below the phase transition while the lower energy peak starts to be measurable (and increasing its amplitude) as the temperature keeps dropping. The second peak rapidly overcomes the first one. The Stokes Shift (SS) calculated as the difference between the exciton absorption peak and the PL high energy

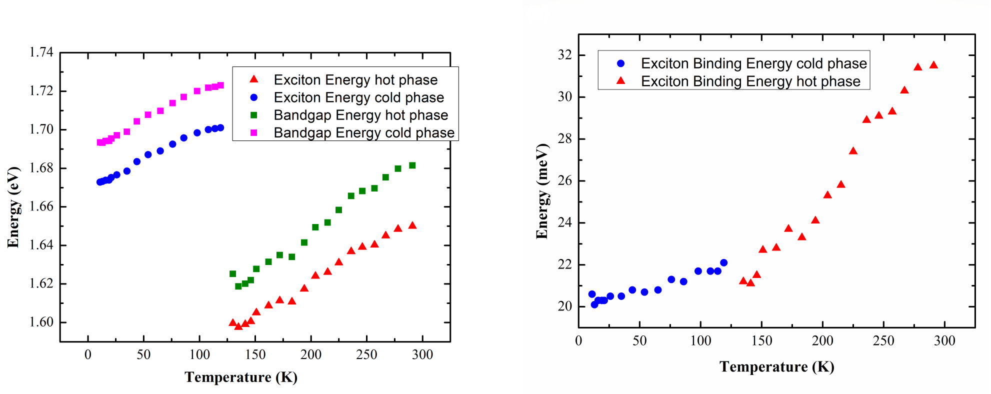

(a) Bandgap energy and exciton absorption peak energy as a function of temperature.

(b) Exciton binding energy estimated for both phases of MAPI film as a function of temperature.

Figure 4.3: Bandgap energy and exciton absorption peak energy (a) and exciton binding energy (b) spectra of MAPI film for different temperatures.

emission peak is shown in fig. 4.5a. It has a different behaviour for each crystal phase, while in the high temperature phase it tends to increase with the increase in temperature, at the low temperature phase the tendency is the opposite. Figure 4.5b shows a plot of the $SS \times K_BT \ vs \ (FWHM)^2$. For the hot phase a linear behaviour is observed. For the cold phase, this plot showed a completely different behaviour, and no linear trend was observed with neither of the peaks (this plot can be seen in Appendix B). But for the hot phase case plotted in fig. 4.5b, a linear regression by least square method shows a slope of 0.25 ± 0.02 with a correlation coefficient of 0.973 close enough to the theoretical value of 0.18 for a Gaussian profile (See section 2.5). This leads us to think that the origin of the hot phase PL is free exciton recombination.

The origin of PL in the cold phase is more difficult to determine. First, it should be noticed that the PL peak after the phase transition (From hot to cold) does not follow the jump tendency of the absorption spectra. This lead to an Stokes Shift of 160 meV for the cold phase which is to high to be a SS. In particular if its understood as a thermalization within the inhomogeneously broadened exciton band. It would be expected to see the PL peak to follow the exciton absorption peak tendency with a small energy difference due to a SS but this is not the case. The PL peak position in fig. 4.4a starts to increase close to the phase transition but it rapidly decreases below 110 K. There is a change in the tendency there. This behaviour in the PL was already reported for MAPI low temperature optical measurements. In fig. 4.6 it can be seen

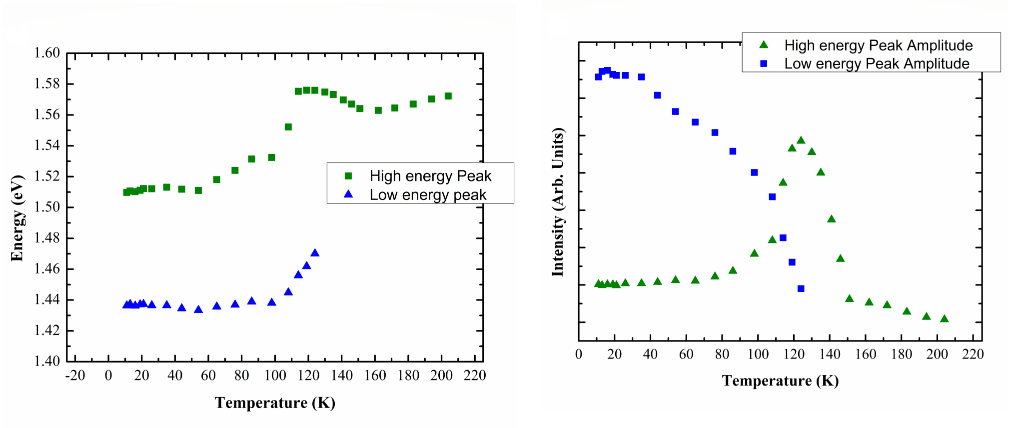

(a) Energy peak positions of the PL.

(b) Amplitude of the Gaussian fit of the PL peaks.

Figure 4.4: Energy peak positions (a) and PL (b) amplitude from the Gaussian fitting.

the temperature dependent PL of a MAPI film measured by Wright et alii [93]. Their measurement shows the same behaviour for the PL than ours. Also, in their measurements is possible to see another PL peak between 60 and 110 K above the main peak, with less than 750 nm of wavelength. This PL is energetically about 30 meV below the exciton absorption peak and that value is what is expected for a Stokes Shift. This PL above the main peak is not observable in our measurements because a 455 nm LED was used and the region were this PL is locate is covered by the LED emitting tail. In any case, this PL is weak because there is another PL emission mechanism of lower energy photons that quenches it and that is the main PL source in our measurements.

The previous discussion lead us to think that the free excitonic recombination in the orthorhombic (cold) phase is a quenched PL mechanism that is not observable in the measurements. Instead, the PL is emitted from a lower energy level that may be due to shallow states that trap the excitons. Observing the FWHM of the PL in fig. 4.7a can be seen that there is a strong change of behaviour after the phase transition. The FWHM duplicates its value after the phase transition and deceases with the deceasing temperature but at one point around 30 or 40 K starts to rise as predicted by the Localized-State PL model of section 2.6. If this model is compared with the peaks positions in fig. 4.4a it is observable that both peaks of the orthorhombic phase behave in accordance with the carrier redistribution model of eq. (2.110) without the

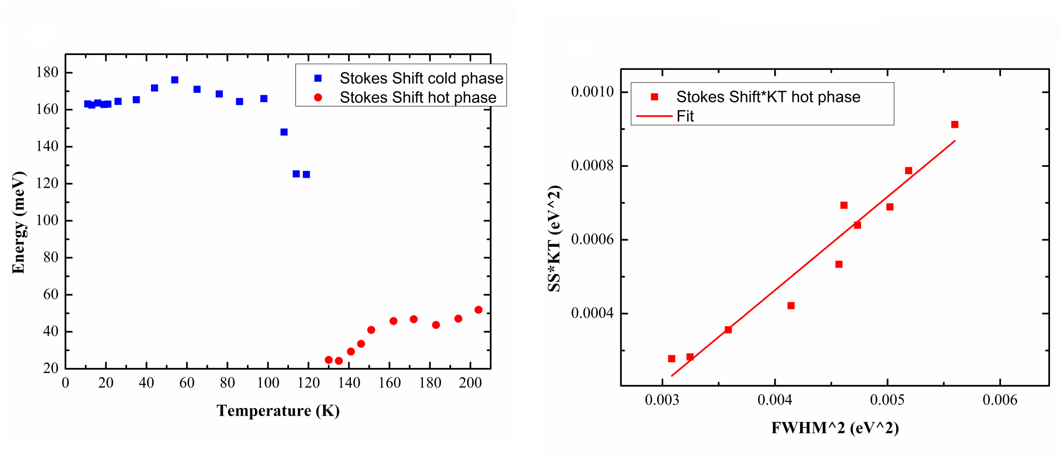

(a) Stokes Shift as the difference between exciton absorption peak and PL emission peak

(b) $SS \times K_B T$ vs $FWHM^2$ for the hot phase.

Figure 4.5: (a) Stokes Shift for both phases using the high energy PL peak for its calculation. (b) Gurioli model for the hot phase.

Varshni empirical formula for the band gap temperature dependency under 110 K. This empirical model is well behaved in ideal tetragonal semiconductors and some III-V and II-VI but perovskites band gap behave contrary to the traditional semiconductors [87, 92].

Finally, if we take a look to the integrated PL in fig. 4.7b its possible to see a quench behaviour while decreasing the temperature. The high energy peak rises as the temperature drop but as the low energy peak is activated, the high one drops fast. The low energy peak integrated intensity follows the localized state model of section 2.6 consistent with another set of shallow states below the ones responsible of the high energy PL peak of the orthorhombic phase.

In conclusion the PL observable in the MAPI perovskite shows strong excitonic optical properties with an exciton absorption peak visible even at room temperature. It was possible to measure its energy position and the band gap energy which shows an increase with the increasing temperature contrary to the traditional tetragonal semiconductors. This behaviour was previously reported for other perovskites [87, 92]. The phase transition was identified through the jump in the optical absorption edge showing a 100 meV decrease while going from the orthorhombic to the tetragonal phase.

The PL was studied and shows the same increasing tendency in the optical absorption edge with temperature. The origin of the tetragonal PL phase was associated with free exciton recombination due to its good agreement with Gurioli's model presented in section 2.5. The orthorhombic PL was associated

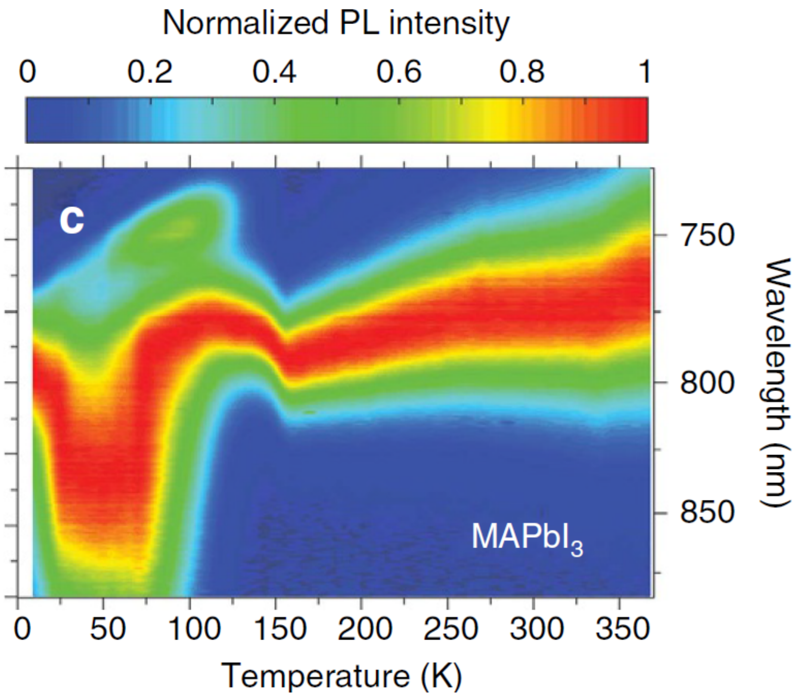

Figure 4.6: Temperature dependence of steady-state PL. Colour plots of normalized steady-state photoluminescence spectra of MAPI. Figure from [93]

with localized exciton recombination because, first, what would it be the corresponding Stokes Shift is too big to be a thermalization of inhomogeneous broadened excitonic states. Second, there is evidence provided by other researchers [93] of what could be the free excitonic recombination. And third, the behaviour of the PL it is explainable with the Localized states model of Li et alii [50]. This results are already published in [33].

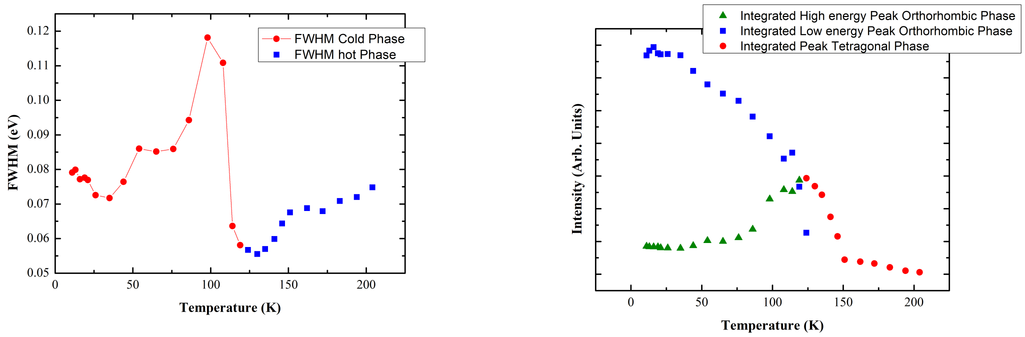

(a) Full Wight at Half Maximum of the main PL peak for both phases as function of the temperature.

(b) Integrated PL of each peak separately of MAPI film as a function of the temperature.

Figure 4.7: Full Wight at Half Maximum of the main PL peak for both phases and Integrated PL of each peak separately of MAPI film.

4.2 Comparison with recycled precursors synthesis

In this section will be presented our contribution to another already publish work on a novel synthesis technique for obtaining optoelectronic grade hybrid perovskites from lead-acid battery waste instead of commercial pure for analysis lead precursors [32].

Our contribution consisted of a comparison of the absorbance and photoluminescence of the MAPI perovskites synthesized from lead waste and from the commercial one. But first the purification process of the recycled lead will be briefly described.

4.2.1 Lead Recovery and Purification

4.2.1.1 Recovery

The separation of lead from plastic and the reduction of volume is achieved through a crushing process. The following step is melting it in a high-temperature oven. This melting stage results in the production of metallic lead and lead sludge in the form of cones. The subsequent step involves purification of the contaminated metallic lead in a refining process. Sulfur is introduced at 320–350 °C to remove the copper that emerges to the surface. After the temperature rises to 640–670 °C, calcium carbonate ($CaCO_3$) is added to remove Tin. In the following step, the antimony is removed by heating the mixture to 720–750 °C and by adding sodium nitrate ($NaNO_3$) and $CaCO_3$. Finally, the mixture is allowed to cool to 430 °C and a final cleaning is carried out by incorporating $NaNO_3$ and extracting the resulting material from the surface. Samples are extracted from the lead cast for a final control, which, once approved, proceeds to mold in ingots with a purity level of 99.9%. These refined ingots are subsequently employed in the lead iodide (PbI_2) synthesis process [32].

4.2.1.2 PbI_2 Synthesis

Lead nitrate ($Pb(NO_3)_2$) is synthesized by placing *100 g* lead slices in a round glass matrass and slowly adding *318.2 g* of concentrated nitric acid (HNO_3) over the lead. The mixture is heated gently until the lead dissolves completely, forming a transparent solution of $Pb(NO_3)_2$. In a different matrass, *165.6 g* of potassium iodide (KI) is dissolved in *500 ml* of distilled water to obtain a saturated solution of *KI*. The *KI* solution is slowly added to the $Pb(NO_3)_2$ solution while constantly stirring, resulting in a plum yellow color of PbI_2. The precipitate is filtered and washed with distilled water to remove any reactive in excess. PbI_2 is dried in a furnace at low temperature for several hours [32].

4.2.1.3 PbI_2 Purification

PbI_2 from the previous step is purified by recrystallization in aqueous solution to remove any impurities. For this the PbI_2 is dissolved at room temperature in slightly acidified water to prevent hydrolysis, and *KI* is added to compensate for probable iodide deficiency. Consequently, the process is summarized as follows: at atmospheric pressure, *2 g* of PbI_2 and *0.174 g* of *KI* are dissolved in *500 ml* of deionized water (DI) with *0.5 ml* of acetic acid (ACS reagent, $\geq$ 99%). The solution is covered with *Al* foil to avoid light exposure and is heated ensuring it does not boil for at least 60 min with continuous and vigorous stirring until the PbI_2 dissolves. The supernatant is quickly transferred to a preheated conical flask and allowed to cool overnight, precipitating PbI_2 crystals. The flakes of PbI_2 are vacuum filtered, washed with DI water, and dried in a vacuum oven at 60 °C for 24 h [32].

After this processes, the MAPI perovskite synthesis proceeds as described in section 3.1.

4.2.2 MAPI Films Optical Properties Characterization

The absorption coefficient spectra of MAPI films synthesized with recycled and commercial PbI_2 are depicted in fig. 4.8a and appears to be almost identical. The Elliott equation can be used to obtain the exciton binding energy and band gap through fitting. Both films exhibit identical exciton binding energies of 38 meV. Furthermore, both films have the same bandgap energy of 1.69 eV, suggesting that both exhibit identical optical absorption characteristics.

The PL spectra were divided by the integration time of the spectrometer for each measurement to make them comparable and can be seen in fig. 4.8b. The peak position for commercial precursors sample is 1.58 eV and for recycled precursors one is also 1.58 eV. The recycled precursors sample has 91% of the intensity of commercial precursors sample at peak position. The FWHM from the Gaussian fits is 0.182 eV for commercial precursors sample and 0.175 eV for recycled precursors sample. These findings suggest that both samples have nearly identical photoluminescence characteristics, including the same energy at which excitons recombine and the similar interaction between excitons and phonons. The presence of a single clearly defined peak indicates good crystallinity in both samples. More than one peak would indicate the presence of trap states due to defects that generate exciton localized recombination along with the free exciton recombination [33].

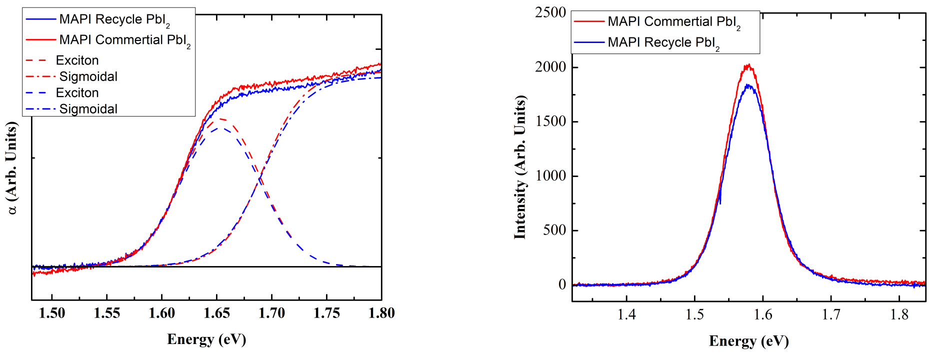

(a) Comparison of the absorbance of MAPI films synthesized from commercial PbI_2 and recycled one.

(b) Comparison of the photoluminescence of MAPI films synthesized from commercial PbI_2 and recycled one.

Figure 4.8: Comparison of the absorbance and the photoluminescence of MAPI films synthesized from commercial and recycled PbI_2.

4.3 Degradation Process

In this section it is presented the study of the initial degradation process of MAPI thin films through its optical properties from room temperature to 13 K. The sample absorbance and photoluminescence spectra were measured as a function of temperature using a cryostat on 3 different days, 6 days apart each other. Out of the cryostat, before and after each measurement, the samples were manipulated in an atmosphere with 40% relative humidity (RH) and stored at low vacuum in the dark. As the measurements were done with a strong ($9.5\ mW$) blue $455\ nm$ LED light and a tungsten halogen lamp, the possible ambient factors of degradation were identified as the exposure time in air and the blue light. From the results of Yang and collaborators it is known that MAPI degrades due to moisture but not with dry air [94] and that they also shown that in air with RH of 50% or less it takes many hours to degrade a MAPI film. It reasonable to consider that for the time that the sample was exposed to 40% RH air wasn't probably the main source of degradation. On the other hand, it has been shown that even in vacuum, blue light and higher energy photons can decompose methylammonium in MAPI films [95, 96] volatilizing the subproducts H_2 and CH_3NH_2 and creating cation vacancies.

4.3.1 XRD Diffraction and Optical Images

Fig. 4.9a shows X-Ray Diffraction (XRD) of the MAPI films right after synthesis. It can be seen a good crystallinity and the characteristic peaks of the tetragonal phase [94, 96]. After the measurements, the XRD shows the presence of all the original tetragonal phase MAPI peaks and a small peak at 12.6° corresponding to the (001) plane of PbI_2 as can be seen in fig. 4.9b [96]. This is a sub-product of both the degradation due to humidity and blue light in vacuum [96, 97]. This degradation involves the decomposition of methylammonium and the volatilization of its subproducts. This measurements were done in different XRD equipments which explain the different noise levels.

In fig. 4.10 it is possible to see the sample before and after the optical measurements on the cryostat. Besides some scratches due to manipulation, the sample has a uniform black color even after the measurements. The degradation of the sample is not perceptible to the human eye.

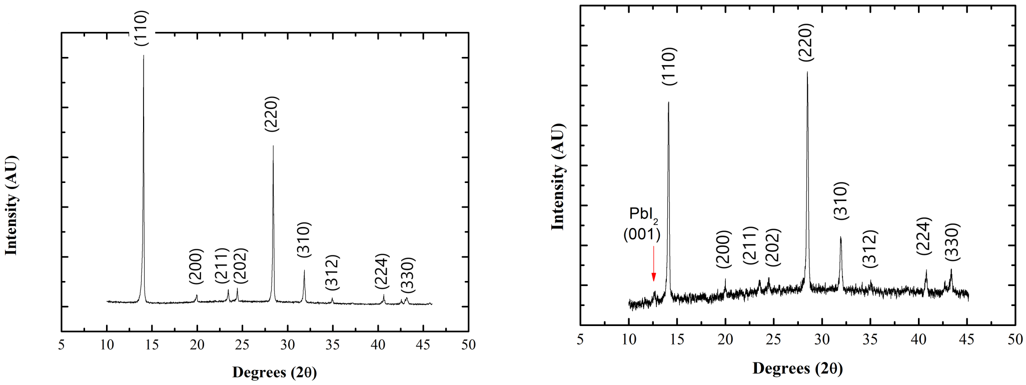

(a) Immediately after growth.

(b) After 3 days of optical measurements on a cryostat.

Figure 4.9: XRD of MAPI sample growth on glass.

(a) Immediately after growth.

(b) After 3 days of optical measurements on a cryostat.

Figure 4.10: Optical images of MAPI sample growth on glass.

4.3.2 Absorption

The absorbance spectra (see fig. 4.11) are adequate for identifying the phase transition temperature because of the tetragonal to orthorhombic [88] phase transition in MAPI implies a 100 meV blue shift in the bandgap energy [33], as the temperature is decreased. This blue shift can be seen in fig. 4.12 where the results of day one (fig. 4.12a), day two (fig. 4.12b) and day three (fig. 4.12c) are compared. The phase transition is easily identifiable, and the temperature of the phase transition clearly moves to higher temperatures for the successive measurement product of the degradation process. The first measurement located the phase transition at *110 K*, the second at *125 K* and the third one at *140 K*. This may imply that the tetragonal phase becomes more unstable (the orthorhombic more stable) as the degradation process begins. This may be due to the appearance of defect states by the degradation process, as it will be shown below, when studying the dependence of photoluminescence with temperature. Moreover, the absorption edge moves to higher energies when increasing the temperature in both phases contrary to the observed behaviour in other covalent conventional semiconductors [89–91]. This behaviour for the bandgap energy span increases for the orthorhombic phase (low temperature) with the advance of the degradation process but not for the tetragonal phase (high temperature). As the bandgap energy dependence with temperature in perovskites is due to lattice expansion (besides electron phonon coupling) [87, 92], this may imply that the orthorhombic phase can accommodate a large crystal expansion due to the presence of the defects.

The exciton binding energy is calculated as the difference between the bandgap energy and the exciton absorption peak energy position. It does not present changes for the successive measurements but it increases with temperature from 22 to 38 meV (see fig. 4.13). It is expected that, as the temperature is increased, the bands become flatter due to the bandgap energy increase (fig. 4.12), which would tend to increase the reduced relative exciton mass μ [39, 98]. Furthermore, the crystal would expand reducing the density of atomic dipoles, thus reducing the dielectric constant ϵ [42]. Both trends would increase the exciton binding energy according to eq. (2.1). This increment is most evident for the tetragonal phase. Although for the orthorhombic phase the tendency is smaller, there is no significant change in the exciton binding energy across the phase transition. However, it is very noticeable that there is almost no change in the exciton binding energy for the successive measurements in the different days. Nevertheless, the absorbance turns out to be less susceptible to degradation than the photoluminescence, as will be seen below.

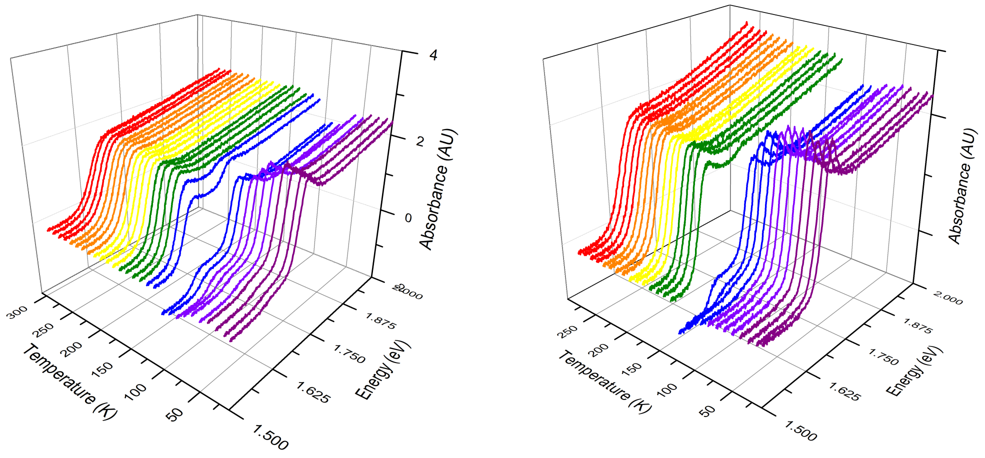

(a) First day of measurement.

(b) Second day of measurement.

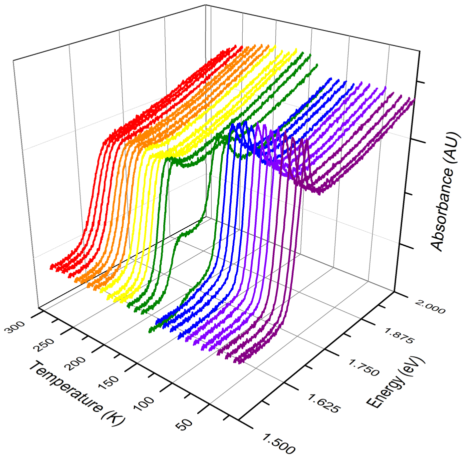

(c) Third day of measurement.

Figure 4.11: Absorbance spectra for each temperature.

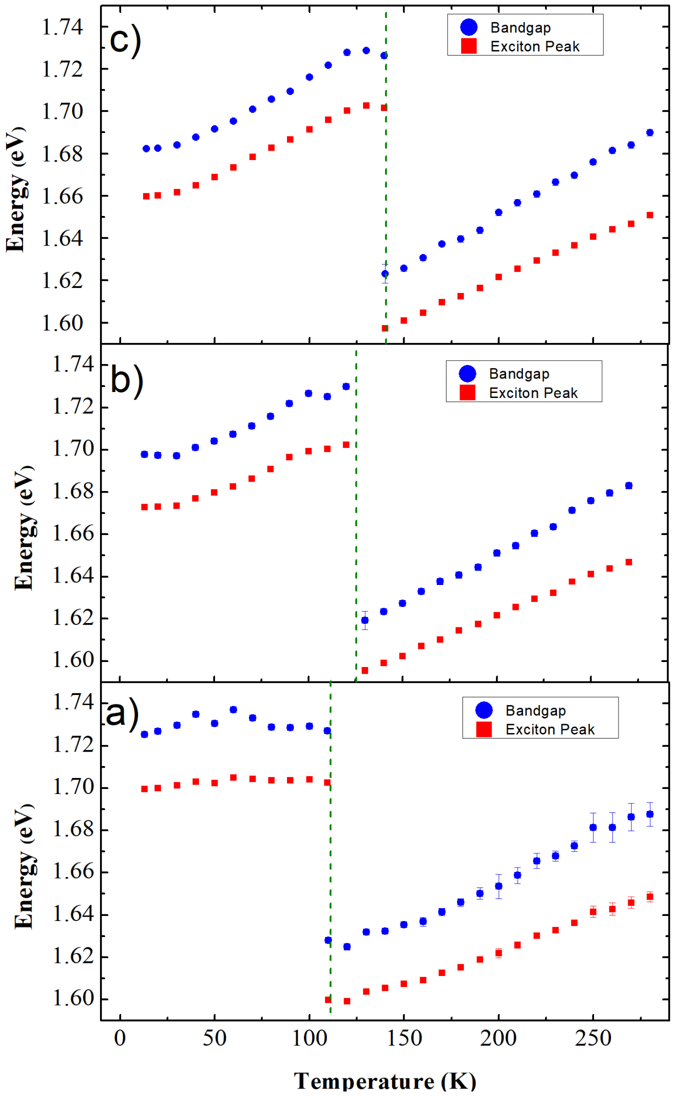

Figure 4.12: Bandgap and exciton peak energy as a function of temperature from fitting the absorbance spectra with Elliot formula. (a) First day of measurement. (b) Second day of measurement. (c) Third day of measurement.

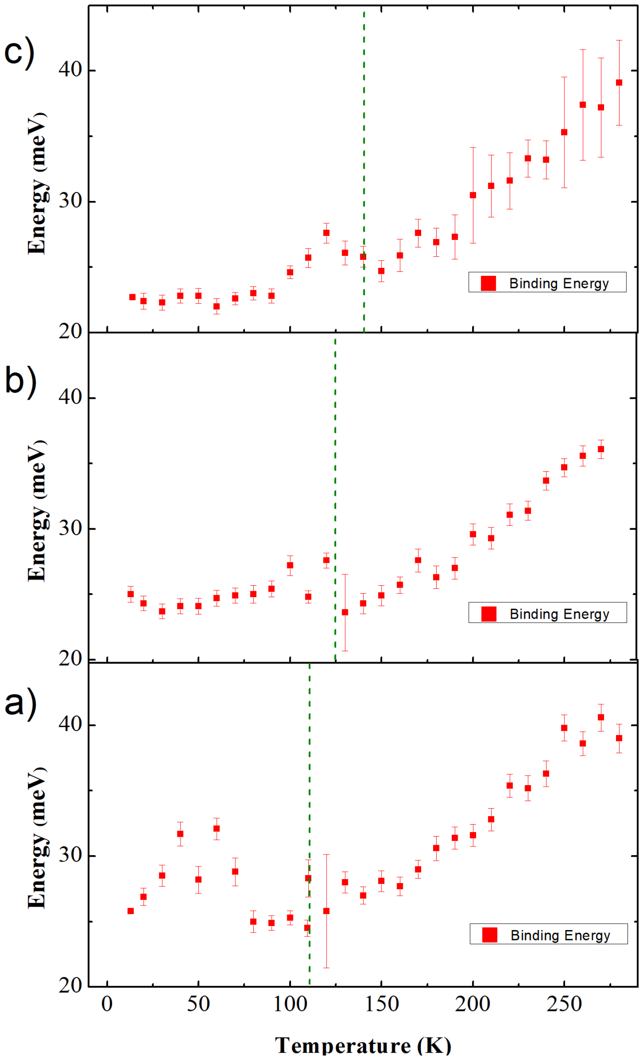

Figure 4.13: Exciton binding energy. (a) First day of measurement. (b) Second day of measurement. (c) Third day of measurement.

4.3.3 Photoluminescence

Fig. 4.14 shows the photoluminescence spectra, an increment in their intensity after changing from tetragonal to orthorhombic phase is observed. On the first day of measurement, it presents a narrow peak from room temperature to 13 K and a second wider peak at lower energy, which is only present below 80 K. This second peak quenches the intensity of the higher energy peak as observed in fig. 4.14a. On the second and third days of measurements, the narrow high-energy peak reduces its intensity, and the broader low-energy peak increases it. The second peak also becomes visible at higher temperatures as the degradation progresses. For the second day, in fig. 4.14b, this peak appears at 110 K and for the third day it appears at 120 K, increasing the quenching of the high energy peak (see fig 4.14c). By the third day, the high-energy peak is no longer visible for temperatures below 80 K. This effect and the quenching effect are clearer in fig. 4.15 where the integrated PL of each peak is plotted against temperature for all three measurements. Here, the increase in PL intensity is observed after the phase transition, as the temperature decreases, and it is also observed how the intensity of the higher-energy peak is quenched after the activation of the lower-energy peak.

When the peak positions are analyzed in fig. 4.16 it is observed that the low-energy peak (blue circles) has two different behaviours. An increasing energy position with temperature is observed for the first day and part of the measurements of the second day. This coincides with the measurements where the high energy peak has a considerable intensity. With the advancement of the degradation and the quenching of the high-energy peak, the second peak begins to be dominant, changing its behaviour and starting to reduce its energy position with the temperature. On the other hand, fig. 4.16 shows that the high-energy peak does not shift in energy as the bandgap energy does due to the phase transition seen in fig, 4.13. This trend was already reported by Wright et al. [93], and implies that for the orthorhombic phase the high-energy peak has not the same origin.

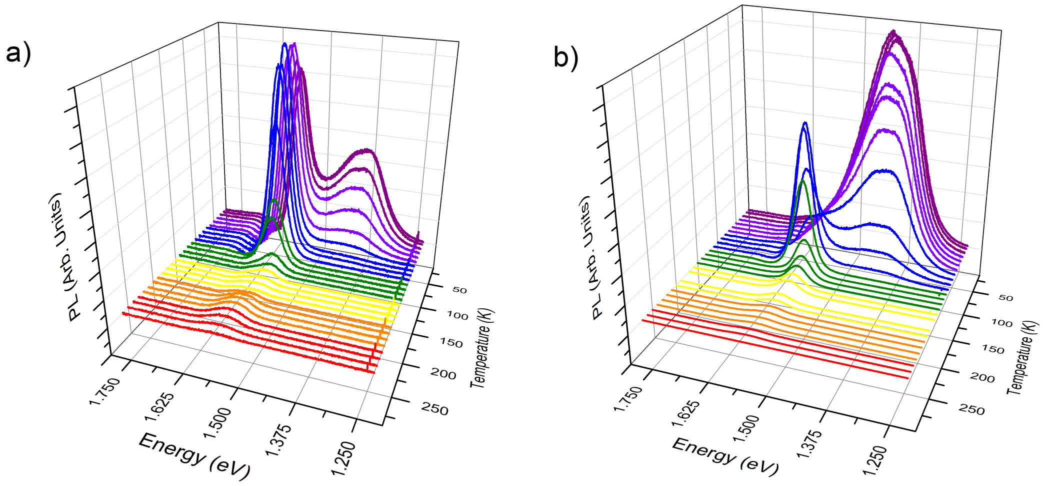

(a) First day of measurement.

(b) Second day of measurement.

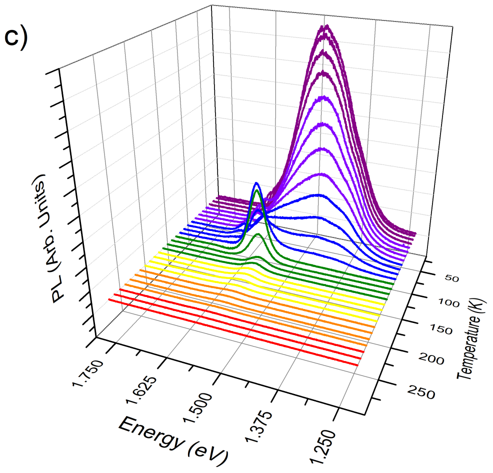

(c) Third day of measurement.

Figure 4.14: Photoluminescence spectra for each temperature.

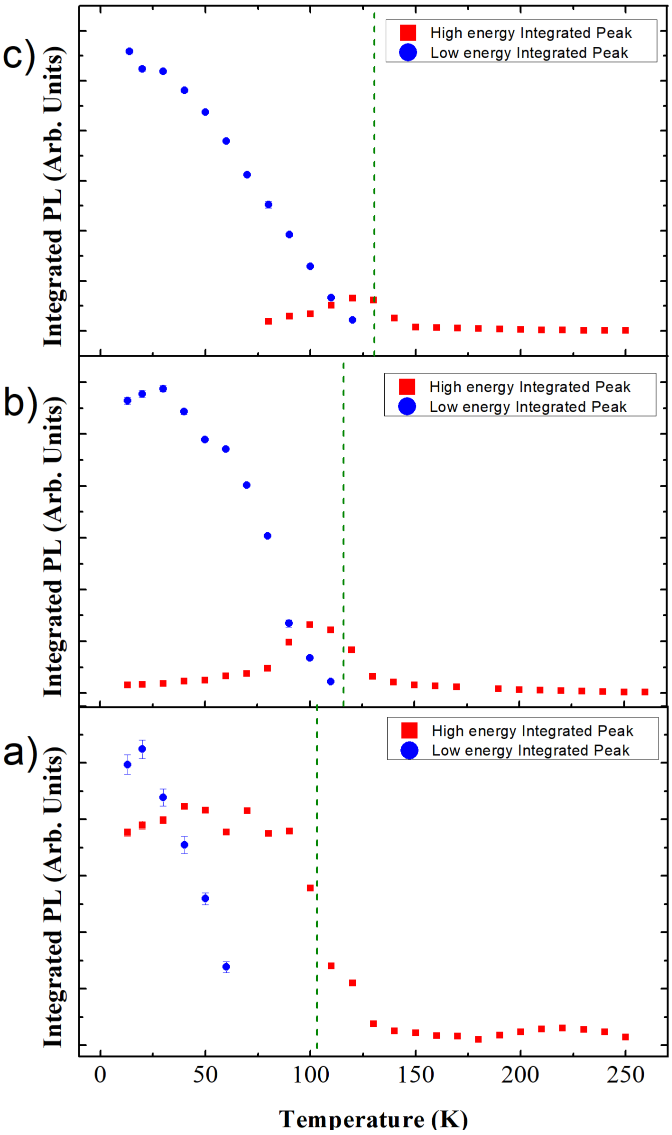

Figure 4.15: Integrated photoluminescence as a function of temperature for each peak. (a) First day of measurement. (b) Second day of measurement. (c) Third day of measurement. The vertical lines indicate the position of the phase transition.

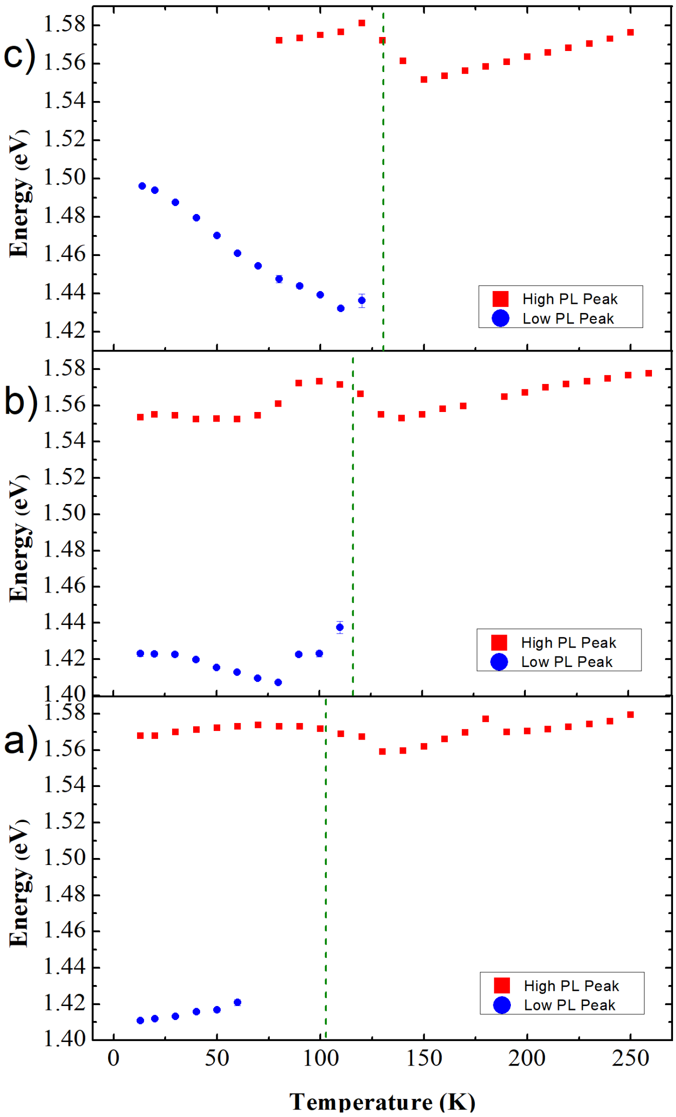

Figure 4.16: Photoluminescence peak energy position as a function of temperature. (a) First day of measurement. (b) Second day of measurement. (c) Third day of measurement. The vertical lines indicate the position of the phase transition.

4.3.4 Full Width at Half Maximum (FWHM) of Excitonic Absorption.

The dependence with the temperature of the full width at half maximum (Γ) of the excitonic absorption peak is presented in fig. 4.17. It increases with temperature and this behaviour was theoretically analyzed by Segall et al. [44] showing that the exciton-phonon coupling is responsible for this growth. This can be modeled with the Segall expression given by eq. (2.97). This expression has been widely used to analyze the exciton-phonon interaction in perovskites [87, 93, 99, 100].

In this case, it can be seen in fig. 4.17 that Γ reaches a constant value at low temperatures and grows exponentially with temperature, indicating a low contribution of the acoustic phonons. This has been observed previously for perovskites [87, 93] and other polar semiconductors [95, 101]. Moreover, before and after the phase transition, Γ follows the same behaviour and does not change its value, so all the values were fitted together. It must be noted that if the values for each phase were fitted separately, the results between phases are almost the same (See Table B.1 in the Appendix).

After fitting the results, the parameter γ_{def} gives values five orders of magnitude lower than γ_{LO} (See Table B.1), as expected, so it was neglected [87]. The rest of the results are summarized in table 4.1. From the fitting results, the contribution from the crystal disorder Γ_0 has been reduced in successive measurements. This could be due to a small change in crystallinity due to the successive phase transitions. Meanwhile, the energy associated with optical phonons decreases monotonously. Although the highest uncertainty associated with this measurement ($5\ meV$) is half the value of the highest energy shift ($10\ meV$), this decrement may indicate a weakening of the bonds associated with the vacancy creation due to the degradation process [95]. Finally, it must be noted that the PL FWHM for the tetragonal phase (when there is only one PL peak) has the same trend that the FWHM of the exciton absorption peak. For the orthorhombic phase the PL FWHM increases as the temperature decreases (see fig. B.2 in the Appendix), which is an indication of exciton localization according to Q. Li model [50], as it will be discussed below.

	Γ_0	γ_{LO}	E_{LO}
Day 1	$49 \pm 1\ meV$	$147 \pm 34\ eV$	$37 \pm 5\ eV$
Day 2	$47 \pm 1\ meV$	$130 \pm 26\ eV$	$36 \pm 4\ eV$
Day 3	$39 \pm 1\ meV$	$92 \pm 15\ eV$	$27 \pm 3\ eV$

Table 4.1: Results for the fitting of Γ for the three days of measurements with eq. (2.97)

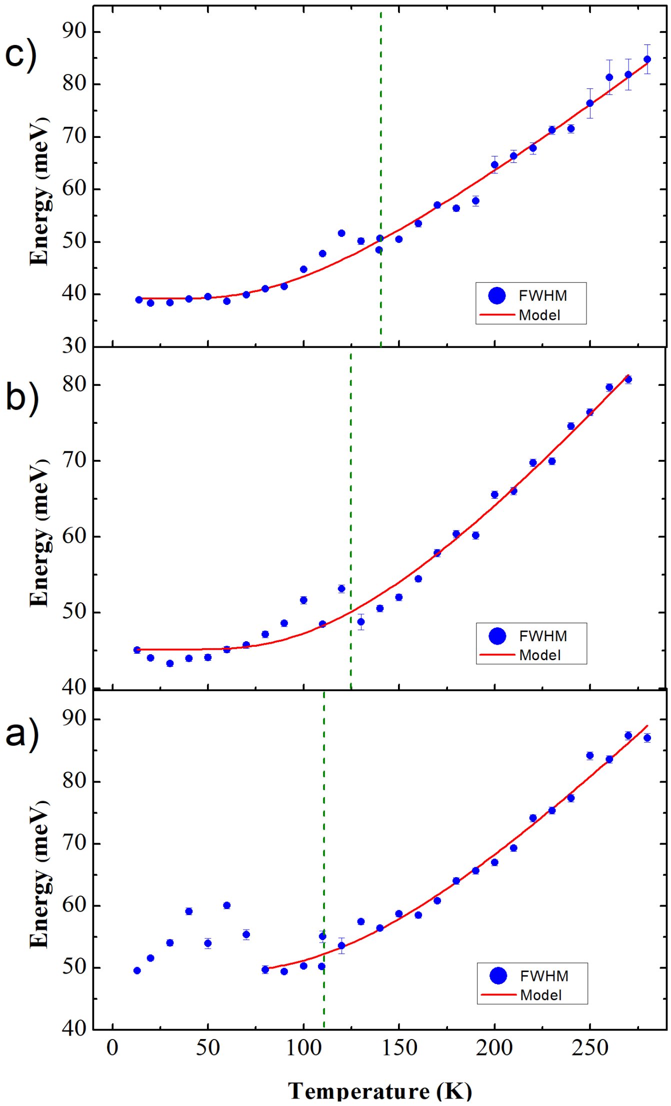

Figure 4.17: FWHM of the excitonic absorption peak as a function of the temperature. (a) First day of measurement. (b) Second day of measurement. (c) Third day of measurement. The vertical lines indicate the position of the phase transition.

4.3.5 Origin of the Tetragonal Phase Photoluminescence

To identify the PL origin, the Stokes shift, multiplied by the thermal energy, was plotted against the square of Γ in fig. 4.18. This plot shows a theoretical linear behaviour for a PL originating from recombination of thermalized free excitons as calculated by Gurioli, ideally with a slope of 0.18 [45]. In this case, the slope of the linear fittings was 0.22 for the first day, 0.28 for the second day, and 0.20 for the third day. This linear behaviour confirms the free excitonic recombination nature of the high-energy PL peak in the tetragonal phase. On the other hand, the peaks in the orthorhombic phase show a different behaviour without any linear trend (see fig. B.3 in the Appendix) indicating a different origin for this photoluminescence (vide infra).

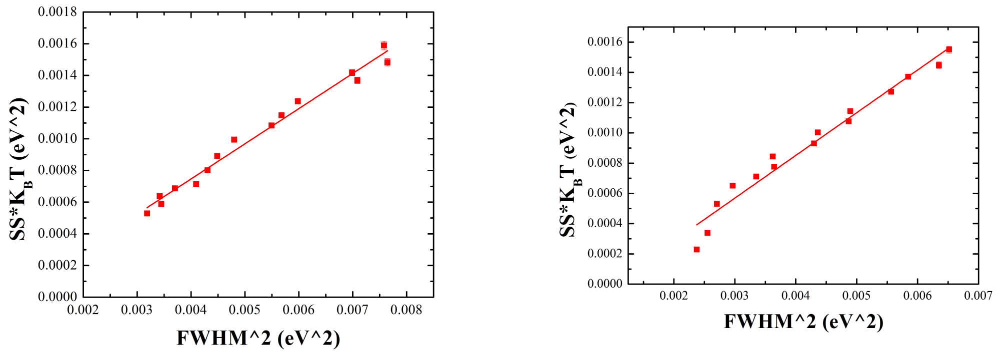

(a) First day of measurement.

(b) Second day of measurement.

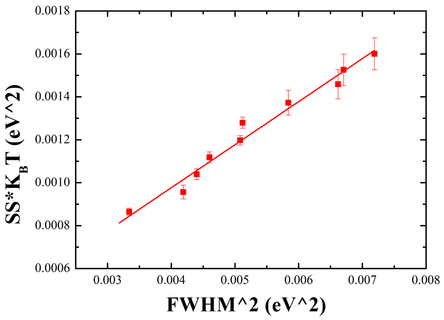

(c) Third day of measurement.

Figure 4.18: Stokes shift times thermal energy vs Γ^2 for the tetragonal phase.

4.3.6 Origin of the Orthorhombic Phase Photoluminescence

The cold phase PL peaks are attributed to localized exciton recombination because none of them show the expected behaviour of the Gurioli's model. Moreover, the difference between the excitonic absorption peak energy position and that of the PL reaches about *250 meV*, which is above what it may be expected for a Stokes Shift. This indicates the presence of states in the forbidden region for the orthorhombic phase, above the Fermi level, allowing them to capture the excitons. This also suggests that the phase transition moved the conduction band to higher energies. This recombination mechanism inhibits the free exciton recombination which should be close to the exciton absorption energy position. It must be stated that although perovskites are defect tolerant for deep states, shallow states are allowed [102]. Also, the observed behaviour of this PL peaks is consistent with the model proposed by Li et alli [50] presented in section 2.6.

The second peak observable at lower energy is only measurable at low temperatures when the Fermi level is low enough to leave these states empty. Furthermore, the change in the intensity from one peak to the other, shown in fig. 4.15, indicates that the PL emission mechanism of the low-energy peak is inhibiting the PL emission mechanism of the high-energy peak through the thermalization of the excitons to the lower localized states. This behaviour was previously observed in Cesium Lead Halide perovskites [103]. They also show the same trend for the peak position observed in figs. 4.16.b and 4.16.c. This behaviour is not observed in fig. 4.16.a probably because the degradation is in the early stages and the localization is not the dominant mechanism.

The changes with degradation in the PL spectra show an increase in the low-energy emission peak at the expense of the high-energy peak for the orthorhombic phase, and an increase in the deactivation temperature of the low-energy peak. Both behaviours indicate an increase in defect concentration that may be due to the creation of vacancies due to degradation.

4.3.7 Urbach energy

The Urbach energy is related to the disorder in the lattice material. This disorder has two contributions, one independent of temperature originating from the intrinsic crystal disorder and another temperature dependent originating from the excitation of the phonon modes [55, 56, 104]. The thermal energy dependency presented in section 2.7 increases monotonously with temperature as can be seen in fig. 4.19. This is a consequence of the increase in the carrier phonon interaction [56].

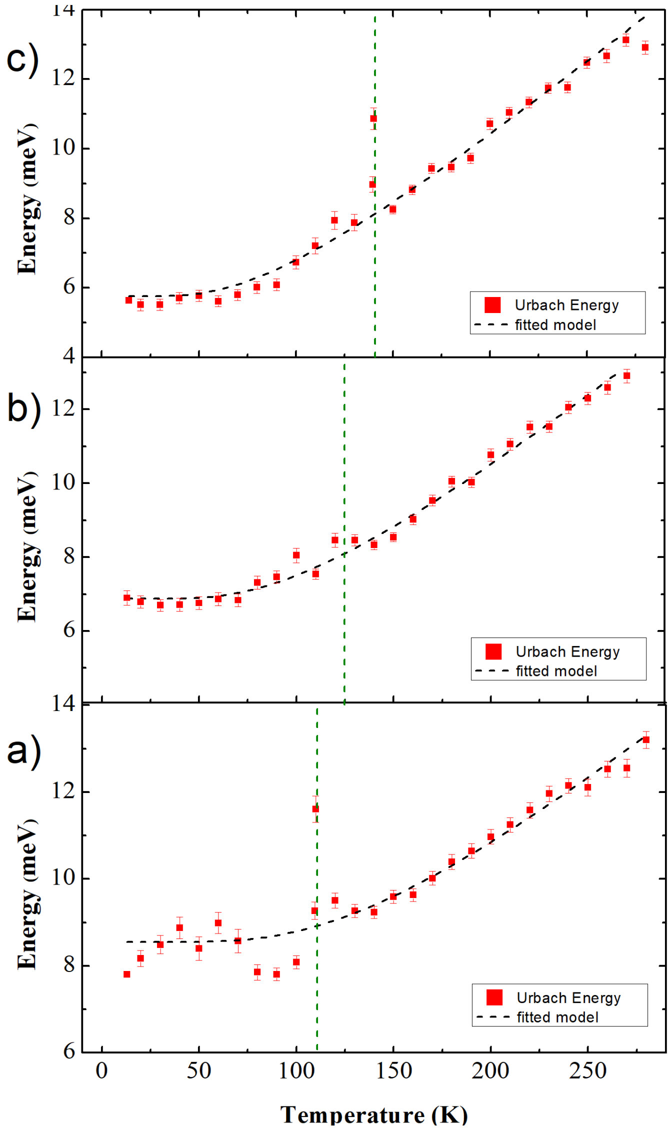

Figure 4.19: Urbach energy as a function of the temperature from the absorption measurements. (a) First day of measurement. (b) Second day of measurement. (c) Third day of measurement.

The parameters U_0 and E_{ph} extracted from the fits in fig 4.19 with the model of secction 2.7 show that U_0 has values of 8.6 ± 0.2 meV, 6.9 ± 0.1 meV and 5.8±0.2 meV for day 1, 2 and 3 respectively. This decrease could be related to a change in crystallinity due to the successive phase transitions experienced by the sample through the cooling and heating process as observed in table 4.1 for Segall model. Meanwhile, the E_{ph} energy is reduced from $36.8 \pm 1.7\ meV$ to $26.9 \pm 0.5\ meV$ and to $21.4 \pm 1.0\ meV$ for day 1, 2 and 3. These values are close to the values reported in Table 4.1, and show the same reduction with successive measurements. This reduction is in good agreement with the LO phonon energy observed from the Segall equation fitting of the FWHM of the exciton absorption, although in this case, the observed shift is much higher than the uncertainties of the measurements. The reduction in the energy of the LO phonon modes could be due to a weakening of the bonds associated with the increase in vacancies concentration resulting from the degradation process.

4.4 Conclusions

The absorbance of samples shows a strong excitonic behaviour even at room temperature that was fitted with the Elliott formula. The photoluminescence presented different behaviours for each crystal phase indicating different origins. Using the Gurioli and the Li models was possible to associate the high temperature phase (tetragonal) photoluminescence to free excitonic recombination and the low temperature phase (orthorhombic) photoluminescence to localized excitonic recombination.

The measurements of the absorbance and photoluminescence spectra for different temperatures of a sample of methylammonium lead iodide over different days and samples show changes due to degradation. This degradation originates mainly due to the irradiation with blue light in vacuum which decompose methylammonium. The absorbance spectra are less susceptible to the initial degradation process, remaining almost unchanged compared to photoluminescence. This may be because photoluminescence involves many more processes and is therefore more sensible to degradation. The phase transition moves to higher temperatures, indicating an increase in the stability of the orthorhombic phase. The photoluminescence changes from a sharp free exciton emission in the tetragonal phase to a lower energy localized exciton emission which does not follow the absorption edge movement of the phase transition. It also shows a lower and broader emission peak with increasing deactivation temperature, all this indicating an increase in the defect concentration associated with degradation. This is supported by the observed reduction in the optical phonon energy of both the exciton absorption peak width and mainly the Urbach energy. This can be attributed to the weakening of the bonds associated to the creation of vacancies from the decomposition of methylammonium.

Chapter 5

MAPI Cells Characterization

This chapter presents the results of the characterization of solar cells made with MAPI as the active layer. The description of the cells structure is in section 3.1.1. The cells electrical contacts were made using a graphite paste, four different measure points on each sample were made to control the uniformity of the cell. An image of a cell can be seen in fig. 5.1, over the perovskite there are the four graphite contacts for holes extraction and on a side, the perovskite was removed to contact the FTO with also graphite to extract the electrons. The cells were prepared under the same conditions and a similar behaviour between then is expected . Part of this study focuses on the usefulness of graphite as a contact material because it has already been shown that with Ag and Au contacts the degradation, accentuated by the ambient humidity generate a migration of I ions from the active layer through the selective layer to the contact metallic layer [105–107]. Graphite have a good charge mobility and it is easer to deposit contacts which were done by Doctor blade deposition. Which is a method for applying thin films by spreading a solution or paste onto a substrate using a blade.

During a research internship at INTEMA (Instituto de Investigaciones en Ciencia y Tecnología de Materiales, Mar del Plata, Argentina), two sets of cells were made, from this sets, six were selected to continue the analysis in Uruguay. Over these cells successive Current-Voltage (I-V) Characterization were made observing changes due to degradation. Also, spectral photoresponse measurements were carried out to determine their External Quantum Efficiency (EQE) which is the ratio between extracted electrons and incident Photons.

Finally, Intensity Modulated Photocurrent and Photovoltage Spectroscopy

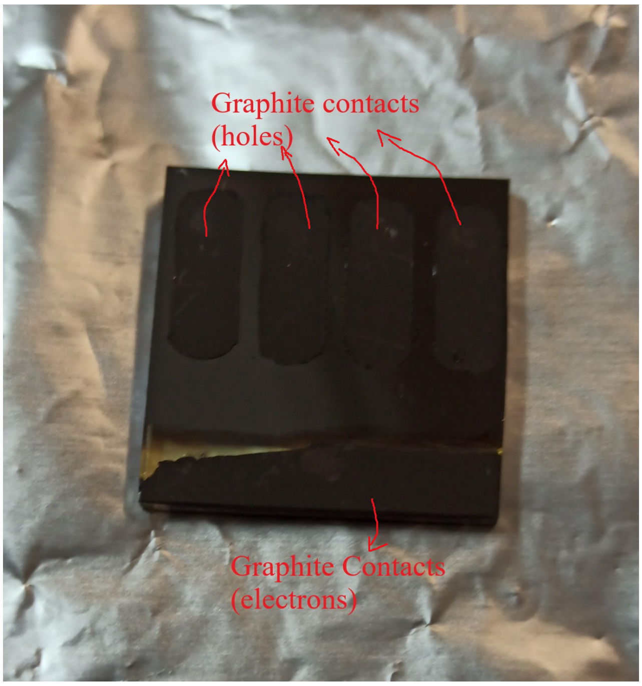

Figure 5.1: Photovoltaic solar cells of structure $Glass/FTO/c-TiO_2/mp-TiO_2/MAPI/C$, where the c- and mp- prefixes indicate compact and meso-porous titanium dioxide, respectively.

were carried out of the cells showing multiple cycles in the Nyquist diagrams. All these results are presented next.

5.1 Current vs Voltage Characterization

The cells were measured on the four point, each time, showing similar results on all of them. This can be seen in fig. 5.2 were the four I-V curves of cell number six after synthesis are plotted. This cell presented the highest efficiencies going from 2.79 % on the point 1 to 3.26 % on point 3. This difference in the efficiency come from the short circuit currents variations mostly while the open circuit voltage remind practically the same for the four points.

The series resistance (R_s) and the shunt plus the series resistance (R_s+R_{sh}) are extracted from the slope $\frac{dV}{dI}$ at the high voltage limit and at short circuit point respectively. For a good solar cell a small series resistance an a big shunt one is expected according to the model of fig. 2.10 [108]. And as can be seen in table 5.1, there is an order of magnitude of difference between the resistances. Still, the series resistance is to big and the photocurrent is low to make a highly efficient photovoltaic device. But it is a solar cell with 3.26 % of efficiency with many options to improve (like adding a hole transport layer). This shows the capacity that perovskites have to revolutionize the photovoltaic technologies with its simple synthesis processes and high light absorption capacities. Also shows that the graphite contacts are adequate for the purpose and no Schottky barrier is formed at their interfaces. Otherwise, it would be expected a s-shape in the current-voltage curves [109, 110].

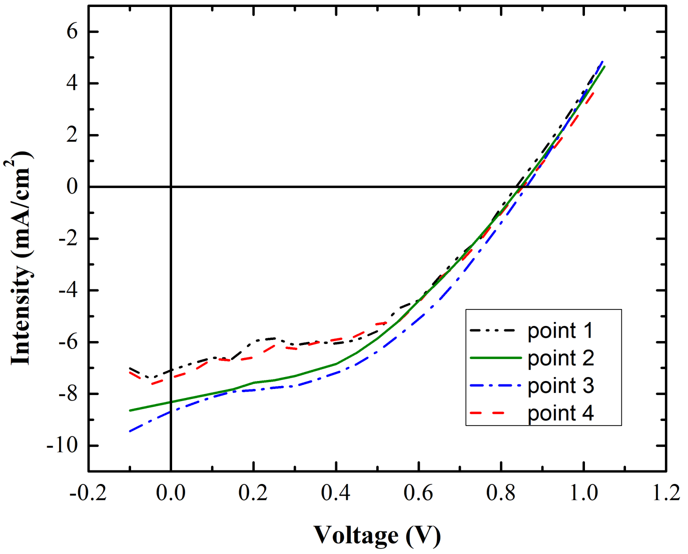

Figure 5.2: Current vs voltage for cell number six measured after synthesis.

Cell Point	$\eta(\%)$	I_{SC} (mA/cm^2)	V_{OC} (V)	FF	$R_s(\Omega)$	$R_s + R_{sh}(\Omega)$
1	2.79	7.081	0.84	0.47	317	3153
2	2.94	8.336	0.85	0.42	312	4145
3	3.26	8.725	0.85	0.44	284	1109
4	2.87	7.376	0.85	0.46	358	2735

Table 5.1: Parameters extracted from the Current vs voltage curves of cell six.

5.1.1 Degradation

The next stage was to study the stability of the cells. Current voltage curves under illumination were measured on different days for many cells on all of the four points. After the indoor illumination measurements the cells were stored at low vacuum in a desiccator. Still, changes due to the degradation of the cell become observable.

In fig. 5.3 there are plotted three current vs voltage curves on cell number eight and the corresponding extracted parameters are summarized in table 5.2. The first one, were made in INTEMA after making the graphite contacts. The other two were done in Uruguay. Even stored in our best possible conditions and extracting them only for measurements is possible to see that the degradation make important changes on it. From this plot it can be seen that the cell starts with the shape that is expected for a good solar cell. This cell presented an efficiency of 1.40% for the fist day of measurements but it decrease to almost a third of that for the last measurement. The successive measurements present higher open circuit voltages and short circuit currents. Although, they have a more ohmic behaviour with a poorer performance. All of this lead to a fill factor that drastically decrease from one measurement to another and also the efficiency. The successive measurements show an increase of the series resistance, but the shunt resistance presented the bigger changes indicating that the cell is increasing its resistance with the degradation to the point that the applied model of fig. 2.10 is no longer valid. The new behaviour of the cell in the fourth quadrant is consistent with the s-shape reported by Cheng et alii [111]. They made MAPI cells with different concentrations of PbI_2 within it by changing the deposition technique. The cells with PbI_2 had lower efficiencies and their I-V curves become more alike the degraded ones in fig. 5.3 while the PbI_2 concentration increases. This is an indication that the $MAPI$ in our cells is degrading to PbI_2.

Dates	$\eta(\%)$	I_{SC} (mA/cm^2)	V_{OC} (V)	FF	$R_s(\Omega)$	$R_s + R_{sh}(\Omega)$
27/9	1.40	5.02	0.75	0.37	107	28282
17/10	1.03	5.19	0.90	0.22	649	1579
1/11	0.56	5.45	0.90	0.11	439	422

Table 5.2: Parameters extracted from the Current vs voltage curves of cell eight.

Another important change is observed in the reverse breakdown voltage. Perovskite devices have a small reverse breakdown voltage compared to other semiconductor devices [63, 66]. This breakdown occurs via tunnelling rather

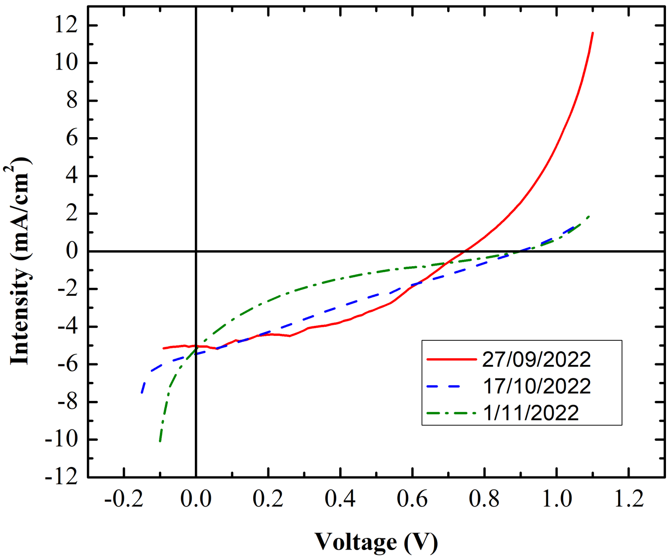

Figure 5.3: Current vs voltage for cell number eight measured three different days.

than avalanche multiplication. The applied biases are too low to cause impact ionization and tunnelling could be allowed by mobile ions accumulating at the contacts [66]. This tunnelling occurs due to the fact that the depletion regions are formed at the interfaces of the perovskite with the hole and electron transport layers as presented in section 2.8. This depletion regions are made of accumulation and depletion of iodine vacancies so the built-in potential is shielded in the bulk and concentrated at the contacts. There is a band bending effect in the interfaces (fig. 5.4.a) and when a reverse potential is applied, the band bending is more significant. When the reverse bias is large enough, holes can tunnel from the transport layer to the valence band of the perovskite absorber producing current (fig. 5.4.b).

It is possible to see in these measurements that the reverse breakdown voltage moves closer to zero and even almost reaching it for the third day of measurements. This could be explained by a depletion layer that become thinner due to an accumulation of ions at the ETL interface which facilitate the tunnelling effect. For this to happen the rearrangement of ions have to become irreversible perhaps due to a chemical reaction that create a new phase with a different ion mobility.

Addressing to that, it is known that the photo-catalytic effect of TiO_2 ETL introduce a problem as it can start a degradation process at the interface with

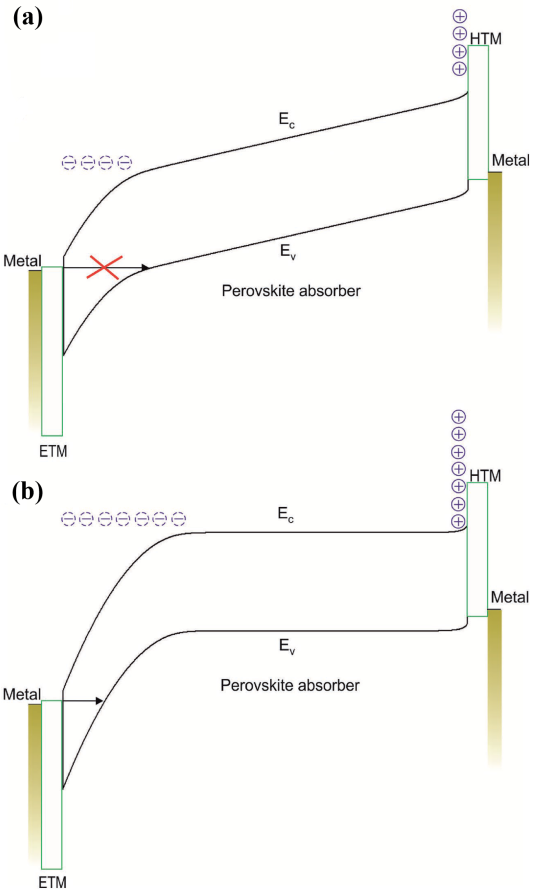

Figure 5.4: Band diagrams of the perovskite solar cell (a) in dark equilibrium at 0 V (b) applying a reverse bias (-1 V), and after ions have migrated to the contacts to equilibrate with the applied reverse bias. As ions accumulate at the contacts in reverse bias, the barrier to tunnelling becomes narrower and allows holes to tunnel from the ETM (also known as ETL) to the perovskite absorber. Figure from [66]

the perovskite [97, 112–114]. The TiO_2 have a band gap of 3.2 eV that allows it to absorb the UV part of the solar spectra. This absorption creates holes that migrate to the perovskite. Then photo-generated holes in $mp-TiO_2$ react with oxygen adsorbed at surface oxygen vacancies, which then become deep traps leading to charge recombination. As TiO_2 is commonly used as a electrode in dye-sensitized solar cells because it acts as a photo-catalysts extracting electrons from organic materials and from iodide anion (I^-). Therefore, the extraction of electrons from I^- by TiO_2 was assumed as the driving force of degradation [115].

Some authors have concluded that the process starts with the emergence of I_2 [112, 116]. They have shown that the electrons in the CB of TiO_2 could induce the oxygen adsorbed on the vacancies of TiO_2 into hydroxyl radicals and H_2O under UV light soaking, leading to a loss of $CH_3NH_3^+$, as shown in Equation (5.1) and (5.2). Meanwhile, both hydroxyl radicals and holes could oxidize I^- into I_2, as shown in Equation (5.4) and (5.3).

$$CH_3NH_3^+ + H_2O \rightarrow CH_3NH_2 + H_3O^+ \tag{5.1}$$

$$3e^- + O_2 + 3H^+ \rightarrow H_2O + OH\bullet \tag{5.2}$$

$$2h^+ + 2I^- \rightarrow I_2 \tag{5.3}$$

$$2I^- + 2OH\bullet \rightarrow I_2 + 2OH^- \tag{5.4}$$

As a result we end up with a photo-catalysis process as in (5.5) where the hydrogen ions will form water with the oxygen of the TiO_2

$$2CH_3NH_3PbI_3 \rightarrow 2PbI_2 + 2CH_3NH_2 + I_2 + 2H^+ \tag{5.5}$$

There are other proposed photo-catalysis degradation mechanisms that lead to the formation of HI but in all cases PbI_2 is formed [117, 118].

This photo-catalysis degradation creates PbI_2 at the ETL/MAPI interface which would explain the change in the shape of the I-V curve (with the fill factor and the efficiency loss) and, the rearrange of the bands energy levels could explain the creation of a thinner depletion region through which the carriers can tunnel easily.

In fig. 5.5 can be seen that this effect is repeated for all the cells when they degrade.

In summary the degradation probably started at the $TiO_2/MAPI$ interface by the formation of PbI_2 and later the volatilisation of methilamine and I_2[107]. This is a mayor issue because this catalysis problem is not resolved with encapsulation. But a UV filter is necessary to avoid it. Also, the $I_2(g)$ is highly corrosive and it is able to potentially destroy the encapsulation. The degradation process of the perovskite due to UV radiation is probably also present but the photo-catalysis degradation process have been reported as a faster mechanism [114, 118, 119].

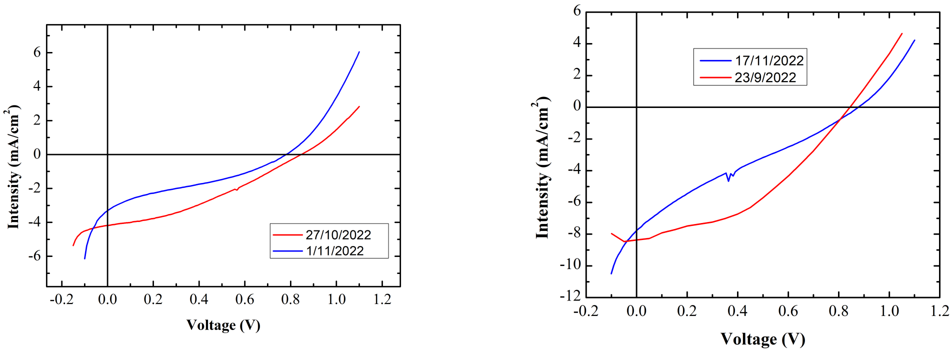

(a) Cell twelve

(b) Cell six

Figure 5.5: Cells number six and twelve measured on different days showing the changes due to the degradation.

5.2 External Quantum Efficiency

The cells spectral photo-response were measured with a mask that allow to measure later the photon flux through this area using a calibrated *Si* cell with the same mask. This measures allow us to calculate the external quantum efficiency (EQE) as the ratio between extracted carriers and the incident photons for each wavelength by unit area.

This was calculated for the cells number six, seven and eight and the results are presented in fig. 5.6. This measurement were done in Uruguay so probably the degradation was already started and probably because of that the cell with the initial highest efficiency is not the one with the highest EQE. Observing the EQE plots in fig. 5.6 it can be seen that above 800 *nm* the photons do not produce current. This is expected since this photons do not have enough energy to excite carriers in the MAPI perovskite. The observable structure between 700 and 800 *nm* is consistent with the excitonic absorption behaviour and have the same shape that the absorbance of fig. 4.8a. The three measurements present the same behaviour than the absorbance, it is growing toward the UV region. After that, a decrease of the EQE is observable which could be due to the absorbance in the TiO_2 layer which start in the UV region. But also could be associated with the drop of the response of the *Si* cell and beyond this point the measurement is no longer valid.

The EQE of the three cell is quite similar something experted for cell with the same synthesis and corroborates the uniformity of the samples.

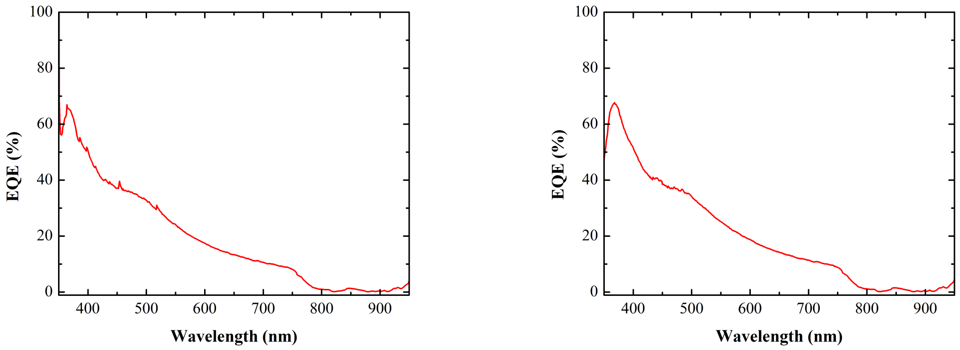

(a) Cell six. **(b)** Cell seven.

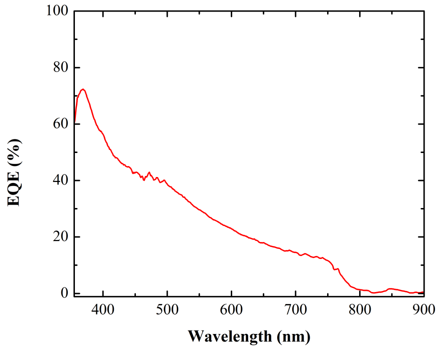

(c) Cell eight.

Figure 5.6: External quantum efficiency measured for cells six, seven and eight.

5.3 Intensity Modulated Photocurrent and Photovoltage Spectroscopy

Intensity modulated spectroscopy measurements were done on four cells. For each one, the frequency modulated short circuit current produced by a modulated 633 *nm* laser were measured applying four different DC powers. The open circuit modulated voltage were also measured for the four same situations. This frequency dependent measurements were carried out from 200 *Hz* to 200 *kHz* and the results are presented below.

IMPS measurement for each of the four cells are presented in fig. 5.7. They presented a really interesting behaviour with two lops which not only made it to the third quadrant in the Nyquist plot but also reached the second one. This behaviour was not seen before by us and was not found in the bibliography neither. Because of this, the possibility of being an experimental artifact was considered. A model for this was implemented and later discarded because it does not suit the different measurements. We will present it later in this section.

To model this behaviour one of the options was to took into consideration the ionic dynamic in the cell discussed in section 2.8 and how this affect the electronic currents. This lead us to the consideration of different models that will be presented in this section.

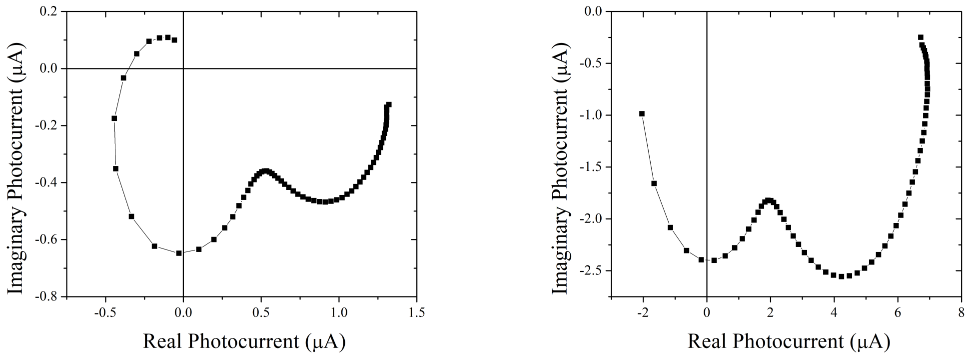

(a) IMPS of cell 1 mesured under 63.2 μW **(b)** IMPS of cell 6 mesured under 63.2 μW

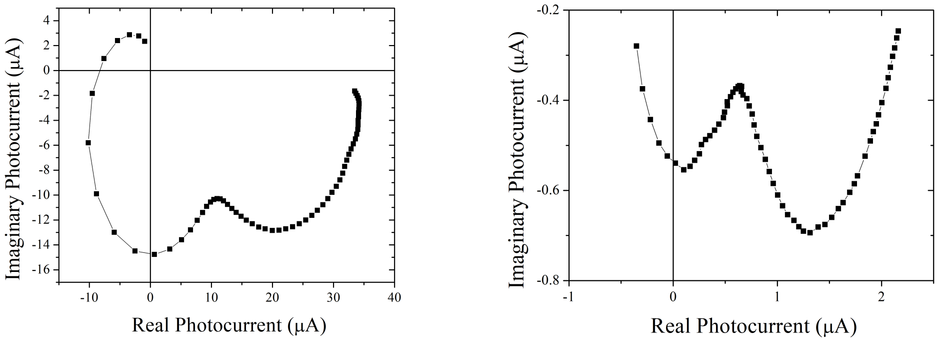

(c) IMPS of cell 7 mesured under 63.2 μW **(d)** IMPS of cell 8 mesured under 63.2 μW

Figure 5.7: Intensity modulated photocurrent spectroscopy measurements.

Some of the Intensity modulated photovoltage spectroscopy measurements for each cell are presented in fig. 5.8. In this measures is observed a cycle that in all cases is already started at 200 Hz indicating that the characteristic frequency of IMVS is smaller than the IMPS ones. There is also a high frequency structure present in all the measurements. This structure is observable in the inset of the plots of fig. 5.8. In this case, there is an structure that revolves around the origin also but at a lower amplitude. It was not possible to fit this structure but indicate the presence of other processes in addition to the main loop. We will present later adequate models for understand this measurements.

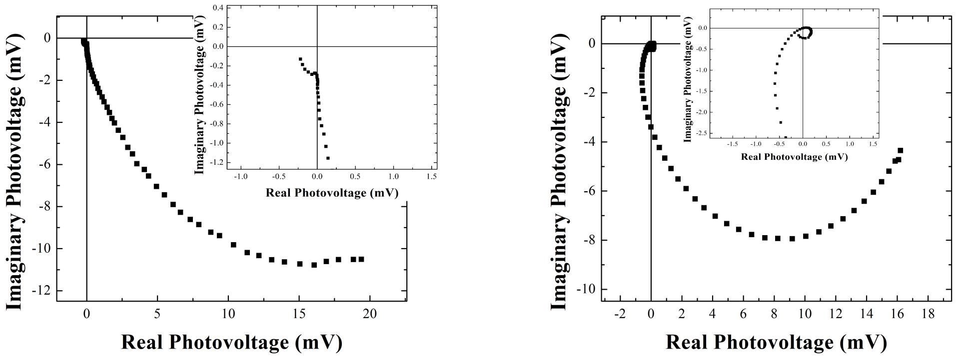

(a) IMVS of cell 1 mesured under 28.9 μW **(b)** IMVS of cell 6 mesured under 28.9 μW

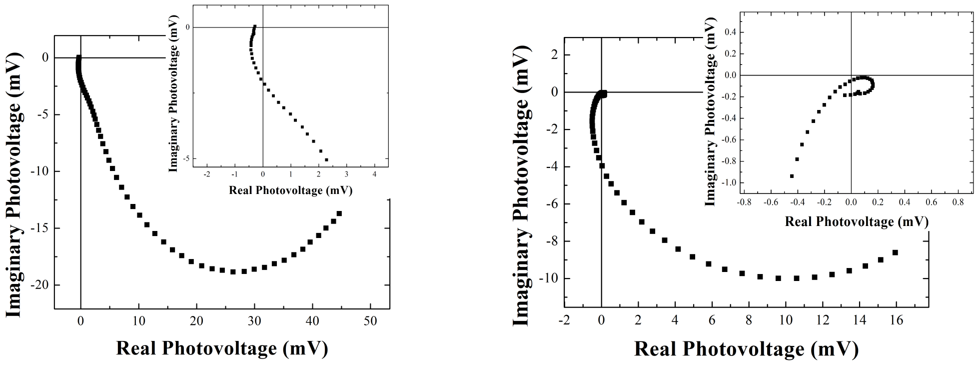

(c) IMVS of cell 7 mesured under 28.9 μW **(d)** IMVS of cell 8 mesured under 28.9 μW

Figure 5.8: Intensity modulated photovoltage spectroscopy measurements.

5.3.1 Measurements considering the reference electrode impedance and the potentiostat parasitics resistance

Every measuring equipment have intrinsic characteristics that have to be considered when are used to do a measurement. As an example, the input resistance of a voltmeter have to be at least three orders of magnitude higher than the output resistance of what is desired to measure otherwise you may have a considerable error in your measurement.

When performing Impedance Spectroscopy (IS) or other measurements that involve a potentiostat, the impedance of the equipment as well as the cell impedance have to be considered at least to discard artefacts in the measurement. High impedance cells are more sensitive to capacitive artefacts while the low impedance cells are more sensitive to inductive and resistive artefacts. Artefacts are even more important as the frequency of analysis tends to cross the megahertz boundary. Ignoring these artefacts can lead to misinterpretation of the results [120].

An instrument is made of real, hence imperfect components. At high frequencies, most of the artefacts comes from the input stray capacitances. A model of the instrument is shown in fig. 5.9 which includes the four stray capacitances between the counter and the reference electrodes, the reference electrode and the ground, the reference and the working electrodes, and the working electrode and the ground. A sinusoidal signal is generated and applied to the cell over a wide range of frequencies. The working electrode voltage versus the reference is measured by the voltmeter V_2. The current is calculated using the voltage V_1 measured across the precision resistor R_m. For an impedance measurement:

$$Z = \frac{V_2}{I} = \frac{V_2}{V_1} R_m \tag{5.6}$$

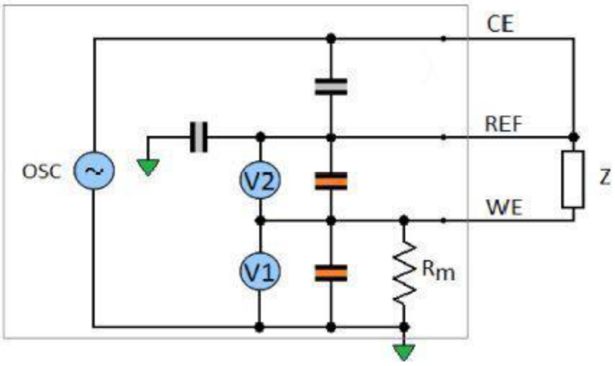

Figure 5.9: Equivalent model of the potentiostat with simplified artifacts. Figure from [120]

The influence of the stray capacitances of the reference to the working and of the working to the ground are canceled by the calibration of the instrument at the factory. To calibrate the instrument, standard devices are connected at the terminals of the standard cable and the instrument is adjusted (through computation/data storage) so that it measures within the specified accuracy.

An example of an impedance Z measurement can be seen in fig. 5.10

plotted in blue dots. The same experiment is now performed with a 10 $k\Omega$ resistor mimicking a poor reference electrode (modeled in fig.5.11) is plotted in red dots.

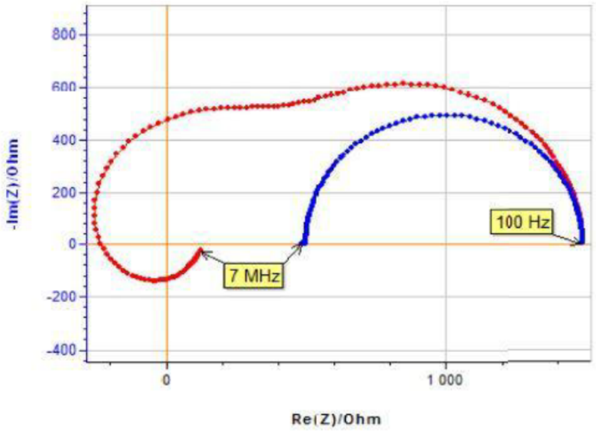

Figure 5.10: Measured impedance with poor reference electrode (red dots) and expected impedance diagram shown in Fig. 6 (blue dots). Figure from [120]

The measured impedance, represented in red in the Nyquist diagram is far from the previous one in blue. The equivalent measured impedance can be obtained from the Kirchhoff's laws:

$$Z_M = \frac{Z(1 + j\omega R_m C_2)(1 + j\omega R C_4) - j\omega R R_m C_3}{1 + j\omega R(C_1 + C_3 + C_4) + j\omega R_m(C_2 + j\omega R C_1 C_3 + j\omega R C_2(C_1 + C_3 + C_4))} \tag{5.7}$$

It can be noted that if R is zero, the measured impedance Z_M equals the effective impedance Z.

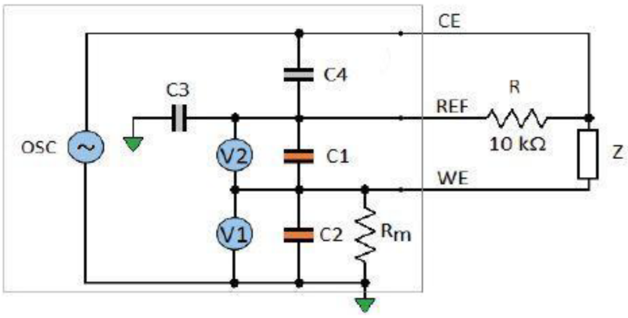

Figure 5.11: Model of the potentiostat with an additional resistor mimicking a poor reference electrode. Figure from [120]

This model for stray capacitances was considered to explain the otherwise strange measurements of fig. 5.7. This model of a bad reference electrode was implemented as an explanation of the measurements considering Z as our true measurement.

The problem with this model is that to have this same behaviour in a measure that only goes to 200 kHz, capacitances of 1 mF or more are needed. This was tested numerically with the model. Also, when trying to fit this model it did not converge well and led to different values for each measurement. All this combined with the measure of our reference electrode resistance of 3 Ω and the fact that no other measurement done with this electrode led to this behaviour before led us to the conclusion that the measurements were not affected by this kind of artefacts.

5.3.2 Ion Dynamic's Effects

In this section we will discus the ionic behaviours that may lead to an explanation of the measurements. In figure 5.7 is visible that there are two different processes with different dynamics being measured.

Perovskites apart from being semiconductors, they additionally show ionic conductivity. This is observable in their slow response times, reversible degradation, transient behaviour and hysteresis in the current-voltage characteristics of solar cells [62, 70]. In section 2.8 we have discussed that ions in perovskites migrate inside the material screening the electric field and creating depletion zones in the perovskite close to the ETL and HTL layers. The voltage drops is concentrated in these regions leaving the rest of the material free of macroscopic electric fields and governed by diffusion current.

It was also discussed that the reverse bias breakdown for small bias values is explained by carrier tunnelling which implies that the main voltage drop occur close to one of the contacts, allowing for a thin tunnelling barrier [66]. This was experimentally confirmed by Weber et alii [67] and provide evidence of that the ionic dynamics of perovskites are governed by one type of ion [62, 63]. To the date, most of studies suggest that ionic transport is mediated through halide vacancies (V_X^+) [68, 69].

The only analytical expression available in the literature to measure this ion concentrations is that proposed by Richardson et alii [70–73]. These authors developed a method called the "surface polarization" (SP) theory to semi-analytically solve the Poisson equation. In this approach, the ionic charge at the contacts is obtained by analytically calculating the first integral of the Poisson equation, with the condition that anions are immobile. This model predicts that the ionic vacancy charge is distributed asymmetrically (section 2.8.1):

$$Q_{ion}^{SP} = sign(V_s)\frac{\epsilon_0 \epsilon V_T}{L_D}\left(exp(\frac{V_s}{V_T}) - \frac{V_s}{V_T} - 1\right)^{1/2} \tag{5.8}$$

Where V_s is the voltage drop in the accumulation region, $V_T = 26mV$ at room temperature and L_D is the Debye length.

This model correctly predicts the asymmetry in the band diagram of fig. 2.6 and states that the vacancies depletion has an exponential profile with a dependence on the internal voltage across the interface. This indicates that the ion dynamics is more susceptible to applied voltages rather than incident light [62]. This ions dynamics and their dependence with voltage are responsible of the hysteresis observed in cyclic voltammetry under illumination [64, 65]. Meaning that is more important the applied voltage and the variation rate rather than the light intensity [62].

Under this situation, when a potential is applied or a current is generated a rearrangement of the ions is produced. This lead to charge or discharge process in this ion vacancy region. Associated with this interface charge $Q_s(V_s)$ of eq. (5.8) (renamed for simplicity) there will be a current $\dot{Q}_s(V_s)$. The potential in this region (V_s) is an internal surface polarization voltage associated to the vacancy-accumulation layer that results from the ionic displacement, and compensated by electrons in the contact layer side of the interface. This give place to a capacitance

$$C_s = \frac{dQ_s(V_s)}{dV_s} \tag{5.9}$$

The presence of ions at the interface implies that the build up and recovery of the equilibrium distribution is severely impeded by the rate of ion migration. Thus the internal voltage V_s cannot follow the external voltage instantaneously but reacts slowly to achieve the condition imposed by V. This characteristic behaviour can be described by a relaxation equation of the type

$$\frac{dV_s}{dt} = \frac{V - V_s}{\tau_s} \tag{5.10}$$

where V is the difference between the external and the built-in voltage. The relaxation kinetic constant τ_s is determined by the rapidity of ion displacement at the specified illumination, voltage and temperature [121, 122].

This model allows also to define a ionic conductivity g_{ion} from the capacitance of this ion charge region and the ion relaxation time [123].

$$g_{ion} = \frac{1}{\tau_s}\frac{dQ_s(V_s)}{dV_s} \tag{5.11}$$

This polarization current (j_s) associated to this charge is indeed necessary to explain the evolution of the transient responses, hysteresis effects and the impedance spectra, of perovskites. Since we have presented this current as the charge variation in a surface capacitance with a conductance associated with this ion charge motion. It is possible to imagine it as a parallel current to the others in the cell and represent it, under small perturbation conditions, as an interphase capacitance C_s in series with a resistance $\frac{1}{g_{ion}}$ that vanishes in dc conditions due to its ionic origin, playing a key role at medium time scales [121–124].

This ionic charge accumulation also affects the electronic current through it. On steady state conditions with an applied voltage for example, the electrons would flow through it as a current j_{stat} with an associated conductivity

$$g_{stat} = \frac{d\,j_{stat}}{dV} \tag{5.12}$$

But when the ions are on the moving, the electronic current through the interface gets affected by the ionic rearrangement. An ion-modulated electronic current is generated under a perturbation (j_d). Its response is slowly and delayed with a response time τ_d in contrast with the external voltage change. Thus the changes in this current can be represented as

$$\frac{d\,j_d}{dt} = \frac{j_{stat} - j_d}{\tau_d} \tag{5.13}$$

The dynamical behaviour of the current j_d, models the process that establishes an additional conductivity channel causing the memory effect by a slow recovery of relaxation time τ_d in response to the external stimulus V [121, 122]. In effect, metal halide perovskite devices commonly undergo a transformation in the dynamics of the slow current components, related to ionic-controlled recombination processes via surface polarization effects [123–125]. Since eq.

(5.13) states that this current have a delay response time, its possible to represent is as an inductor

$$L_d = \frac{\tau_d}{g_{stat}} \tag{5.14}$$

The kinetic properties at long time scales are modulated by slight variations of the characteristic time constants (τ_s and τ_d) that determine the dominant relaxation response (eq. (5.10) or (5.13)) at different voltage regions. In eq (5.13), j_{stat} the stationary value of the delayed current, is assumed as governed by an exponential dependence with voltage V [124].

Note that we have presented the ion dynamic divided in two effects, the charge and discharge of the ions in an interface which have a delayed response to the voltages changes then having a capacitive effect and a second conduction channel. A delayed electronic current slowly responding to changes in the current due to the ion movement, having then an inductive behaviour [121–125].

Keeping this line of work, with the aim of presenting an equivalent circuit to model the above ionic dynamic and include it in the model of a solar cell lets model a recombination current in the same way we presented the shunt resistance in fig. 2.10. Recombination depends of the concentration of carriers n and a certain rate k_{rec}:

$$j_{rec} = k_{rec} n q \tag{5.15}$$

The bulk electron density is $n(V) = n_0 \, exp\left(\frac{qV}{\eta k_B T}\right)$, where η is an ideality factor. Hence the recombination current in transient condition is

$$j_{rec} = j_{rec0} \, exp\left(\frac{qV}{\eta k_B T}\right) \tag{5.16}$$

This recombination current have a dependency with the voltage but obviously is affected also by an increase in the carrier concentration if the cell is illuminated. The associated conductivity is defined as

$$g_{rec} = \frac{dj_{rec}}{dV} \tag{5.17}$$

Finally, a geometric electronic capacitance C_g in parallel with the recombination resistance should be added to consider the electronic charge rearrangement. Putting together all this elements, we end up with the equivalent circuit of fig. 5.12 which is an impedance model superimposed on a cell diagram indi-

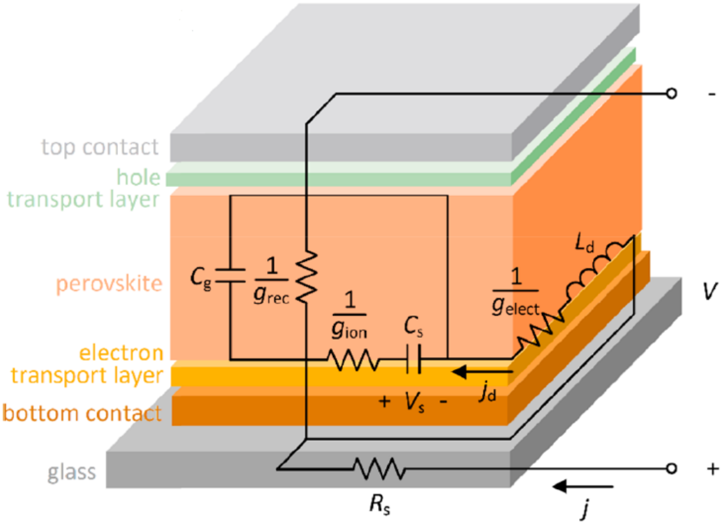

Figure 5.12: Equivalent circuit derived from the transient responses and the schematic of the layer structure composing the perovskite device. Figure from [124]

cating where processes occur. This shows that some of the involved processes are surface processes and are represented on the interface because of that. It has been recently used to explain the hysteresis and impedance spectroscopy measurements on perovskites solar cells [123, 124]. This models explain the inductive effects observed in impedance measurements and negative currents in transient photocurent measurements [123, 124]. We can see that the current has four contributions

$$j = C_g \frac{dV}{dt} + j_{rec} + j_d + \frac{dQ_s}{dt} \tag{5.18}$$

a displacement current that charges the geometrical capacitance C_g of the perovskite material; conduction channels in which the current may be extracted from the cell instantaneously via recombination processes J_{rec} or slowly with an ion-modulated current j_d; and an interfacial current in the sense of a corresponding charge Q_s.

To the date and as far as we know, this equivalent circuit has not been used for IMPS and IMVS measurement interpretation. With this goal in mind, we add to the model 5.12 a current source representing the photo-generation (j_{ph}) as is presented in fig. 5.13. Now for the IMPS response $\tilde{Q}(\omega)$ we need to calculate the short circuit current as a function of j_{ph}. The purpose of this is to calculate the function $\tilde{Q}(\omega)$, in the understanding that the response of a cell

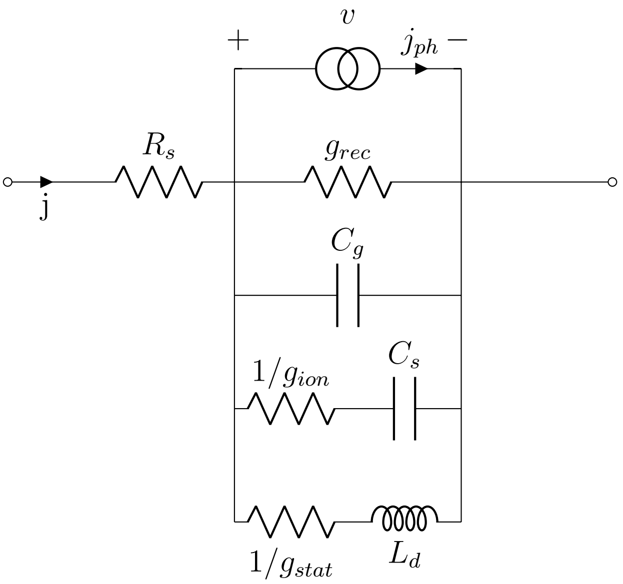

Figure 5.13: Electrical equivalent circuit representing the electronic and ionic dynamics in an operating perovskite solar cell.

to a modulated voltage or the generation of current by modulated illumination can be represented as follows [86]

$$\tilde{j} = \tilde{Y}\tilde{V} + \tilde{Q}\tilde{j}_{ph} \tag{5.19}$$

Here $\tilde{Y}$ is the admittance of the cell and the photocurrent $\tilde{j}_{ph}$ have a sinusoidal dependency with the photon flux and the absorbance of the cell. With this representation, the IMPS response function can be calculated under short circuit conditions (meaning $\tilde{V} = 0$) as

$$\tilde{Q} = \frac{\tilde{j}}{\tilde{j}_{ph}} \tag{5.20}$$

On the same way, the IMVS response $\tilde{W}$ can be calculated under open circuit conditions (meaning $\tilde{j} = 0$) as

$$\tilde{W} = \frac{\tilde{V}}{\tilde{j}_{ph}} = -\tilde{Q}\tilde{Y} \tag{5.21}$$

Now we have to calculate each of the currents of fig. 5.13 to substitute then in eq. (5.18) and add to it the photogenerated current. Using the Kirchhoff law we can see that under short circuit conditions, the voltage on each branch of the circuit (v) is opposite to the series resistance voltage jR_S. Using this is possible to write each current of eq. (5.18) as a function of the main current.

$$j_{rec} = vg_{rec} = -jR_s g_{rec} \tag{5.22a}$$

$$j_g = C_g \frac{dv}{dt} = C_g \; v \; i\omega = -jR_s C_g \; i\omega \tag{5.22b}$$

$$j_s = \frac{-jR_s}{\frac{1}{g_{ion}} + \frac{1}{i\omega C_s}} \tag{5.22c}$$

$$j_d = \frac{-jR_s}{\frac{1}{g_{stat}} + i\omega L_d} \tag{5.22d}$$

Where $i^2 = -1$ All this currents will be substituted in eq. (5.18) including the photogenerated j_{ph} current

$$j = C_g \frac{dv}{dt} + j_{rec} + j_d + \frac{dQ_s}{dt} + j_{ph} \tag{5.23}$$

After the substitution, the $\tilde{Q}$ function can be obtain

$$\tilde{Q} = \frac{\tilde{j}}{\tilde{j}_{ph}} = \left[1 + R_s g_{rec} + i\omega R_S C_g + \frac{R_s}{\frac{1}{g_{ion}} + \frac{1}{i\omega C_s}} + \frac{R_s}{\frac{1}{g_{stat}} + i\omega L_d} \right]^{-1} \tag{5.24}$$

The last two terms of this expression can be rearranged to be written using $\tau_s = C_s/g_{ion}$ and $\tau_d = L_d g_{stat}$.

$$\tilde{Q} = \frac{\tilde{j}}{\tilde{j}_{ph}} = \left[1 + R_s g_{rec} + i\omega R_S C_g + \frac{g_{ion} R_s}{1 + \frac{1}{i\omega \tau_s}} + \frac{g_{stat} R_s}{1 + i\omega \tau_d} \right]^{-1} \tag{5.25}$$

This way as the series resistance is common to almost all the terms, the conductances g_{ion} and g_{stat} can be interpreted as amplitudes of those currents. Therefore, the model has a total of two memory variables that interchange the governability of the response at long time scales in the current-voltage curves of perovskite solar cells due to the non linear ionic-electronic dynamic complexity of this material. However, the slow kinetic properties in perovskites, based on ionic-controlled surface recombination processes, are commonly regulated by a single relaxation time [70, 126, 127]

$$\tau_{Dyn} \sim \frac{C_s}{g_{ion}} \sim L_d g_{stat} \tag{5.26}$$

due to the characteristic memory-based coupling of these materials whose phenomenological consequence is that $\tau_s \sim \tau_d$ [128, 129]. In essence, this identification means that the slow current and surface polarization are both caused by a single variable, as reported experimentally [130].

The next step is to calculate the IMVS response function $\tilde{W}$.

In this case, we impose $\tilde{j} = 0$ and write every current as a function of the voltage which is $\tilde{V}$ in this case because there is no current through R_s

$$j_{rec} = \tilde{V} g_{rec} \tag{5.27a}$$

$$j_g = C_g \frac{dv}{dt} = C_g \, \tilde{V} \, i\omega \tag{5.27b}$$

$$j_s = \frac{\tilde{V}}{\frac{1}{g_{ion}} + \frac{1}{i\omega C_s}} \tag{5.27c}$$

$$j_d = \frac{\tilde{V}}{\frac{1}{g_{stat}} + i\omega L_d} \tag{5.27d}$$

Then the transfer function $\tilde{W}$ is

$$\tilde{W} = -\frac{\tilde{V}}{\tilde{j}_{ph}} = \left[g_{rec} + i\omega C_g + \frac{1}{\frac{1}{g_{ion}} + \frac{1}{i\omega C_s}} + \frac{1}{\frac{1}{g_{stat}} + i\omega L_d} \right]^{-1} \tag{5.28}$$

or using the time constants as in eq. (5.25)

$$\tilde{W} = -\frac{\tilde{V}}{\tilde{j}_{ph}} = \left[g_{rec} + i\omega C_g + \frac{g_{ion}}{1 + \frac{1}{i\omega \tau_{Dyn}}} + \frac{g_{stat}}{1 + i\omega \tau_{Dyn}} \right]^{-1} \tag{5.29}$$

Now this model has been presented, we will plot it for different values and discus it. For that, calculations were done in Matlab in the same spectral region as our measurements which is 100 Hz to 200 kHz. The parameters are in table 5.3 where can be seen that R_s, g_{rec} and C_g were fixed. This way we can see the changes that produce the different ionic related parameters.

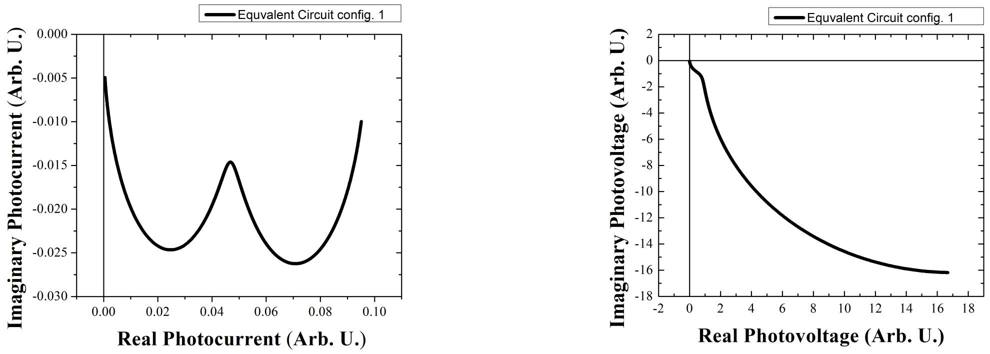

(a) IMPS config. 1 **(b)** IMVS config. 1

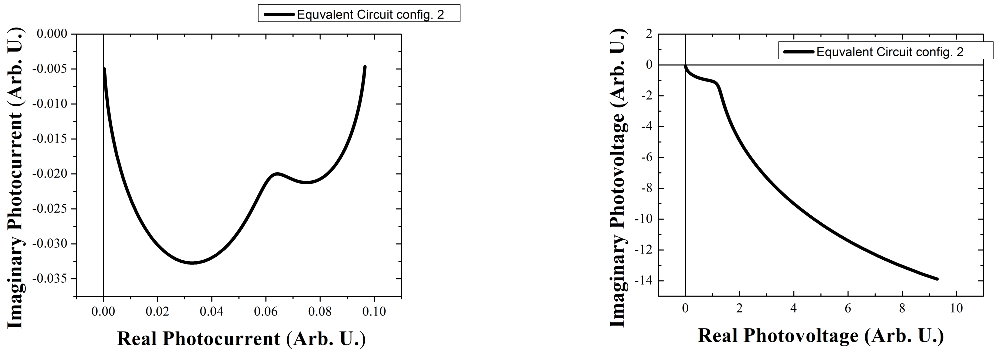

(c) IMPS config. 2 **(d)** IMVS config. 2

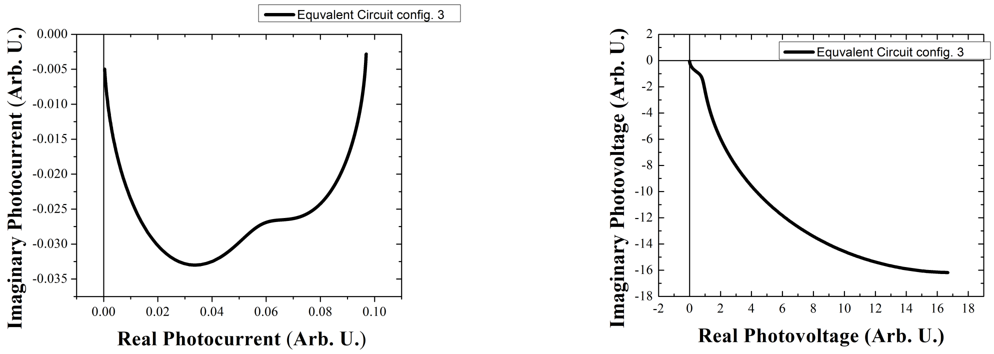

(e) IMPS config. 3 **(f)** IMVS config. 3

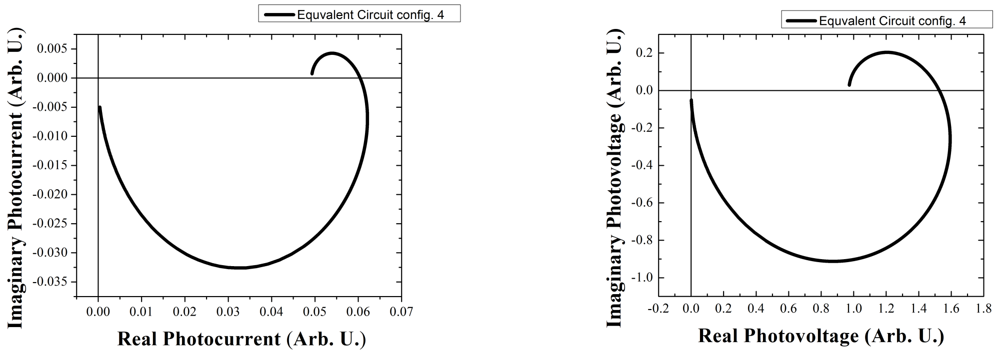

(g) IMPS config. 4 **(h)** IMVS config. 4

Figure 5.14: Simulations of IMPS and IMVS responses of the equivalent circuit of fig. 5.13 for the parameters of table 5.3

	Config. 1	Config. 2	Config. 3	Config. 4
R_s	10 Ω	10 Ω	10 Ω	10 Ω
g_{rec}	0.03 Ω^{-1}	0.03 Ω^{-1}	0.03 Ω^{-1}	0.03 Ω^{-1}
C_g	0.1 mF	0.1 mF	0.1 mF	0.1 mF
τ_{Dyn}	0.001 s	0.0008 s	0.0004 s	0.0008 s
g_{ion}	1 Ω^{-1}	0.5 Ω^{-1}	0.5 Ω^{-1}	0.5 Ω^{-1}
g_{stat}	0.0001 Ω^{-1}	0.0001 Ω^{-1}	0.0001 Ω^{-1}	1 Ω^{-1}

Table 5.3: Values of the parameters used for the simulations of figure 5.14.

As can be seen in the fig. 5.14 with this model is possible to obtain two loops both in IMPS and in IMVS responses. The configurations 1, 2 and 3 show similar behaviours to the MAPI cells measurements of fig. 5.7 and 5.8. The configurations 1,2 and 3 have small changes in the parameters τ_{Dyn} and g_{ion} and also a very small g_{stat} conductance. This could be the case of our MAPI cells measurements. The configuration 4, has a higher g_{stat} conductance and because of that show a low frequency inductive behaviour which is not present in our MAPI cells measurements but can be in other kind of perovskites cells.

The main difference between these simulations and the MAPI cells measurements is that this model does not simulate the high frequency shift to the third quadrant or the spiral of the IMPS. This behaviour is due to the delay introduced by the migration of carriers through the perovskite. As is explained in the rates model of section 2.10, in the cases when the material is a very good absorber the generation is done close to the light incident side of the material and the carriers have to migrate through it. This generate a delay which is traduced in a phase shift which this equivalent circuit model does not considerate. Because of its origin, this effect phase shift affects more the higher frequency points of the plot.

To help to visualize this, in fig. 5.15 it was added ad hoc a phase shift to the first configuration of parameters for the IMPS model. This was done by multiplying the equivalent circuit model by a pure imaginary exponential with different frequency dependent functions inside. The black curve its the original, the red one have a phase added that increase linearly with the frequency and the blue one have a sigmoidal increase of the phase. Even if this phase has no meaning to this equivalent circuit model, allows to visualize what happen if phase is increased non uniformly and how it resembles the IMPS measurements for the MAPI cells. The equivalent circuit model try to explain ions influence on the response which the rates model of section 2.10 does not include. But can not model the transport effects through the material which the rates model of section 2.10 does include it.

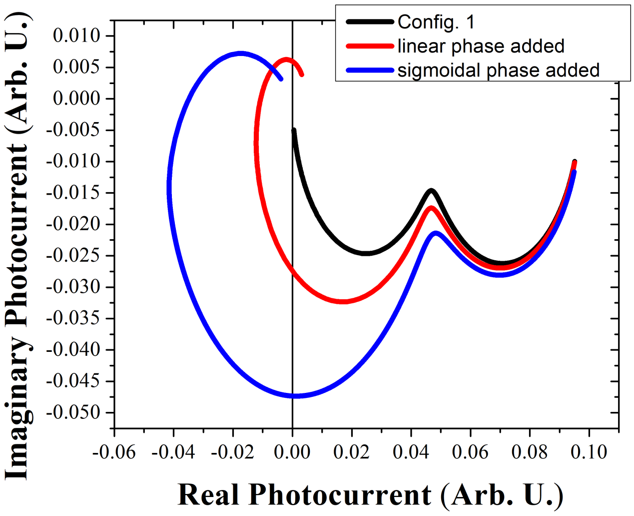

Figure 5.15: Simulated equivalent circuit model adding a phase shift to visualize the effect of carriers diffusing through the material.

Because of this phase shift, it is not possible to fit the IMPS measurements with this model but it partially explain the observed behaviour. We get to the conclusion that there are two conduction channels in the MAPI measurements as the equivalent circuit model states but also a phase shift due to the delay in the transport through the material.

On the other hand, the model of section 2.10 can model the delay explained here but does not consider the effect of ions in a perovskite as the equivalent circuit model. After noticing from the simulations that there is not inductive effect in the MAPI measurement, we propose to model the both loops effect in the same way than the electronic current is modelled in the section 2.10. To do this, we will use a second rate equation. One will be used to model the low frequency loop and the other one to model the high frequency loop.

In the case that the ions are responsible of the loop, the time constant of eq. (2.144) will represent a response time instead of a lifetime. Meanwhile, the exponential term would be a change in the ions charge Q_s of eq. (5.8) which also have an exponential profile.

The data fitting was made in a two step procedure. In the first step each of the loops of the IMPS MAPI measurements were fitted separately and then using this results as seeds a second fit with the whole measurement with two loops simultaneously were made.

5.3.3 IMPS Measurements of MAPI Cells

This IMPS measurements show two clear cycles associated to two different transport process with different rates. This was the initial motivation to implement a model that considerate the ions as the model of the equivalent circuit of figure 5.13. But this model does not consider the diffusion effect that was previously discussed. Because of that, a model that consider two rates equation was implemented to fit this measurements. To do this, first was fitted one of the cycles and the result was subtracted to the measurement. Then the second cycle was fitted from this and finally, using the results of this fits as initial parameters the whole measurement was fitted with two added equation as the eq. 2.149.

This fitting process were done using *450 nm* as the MAPI thickness which was obtained from a profilometry measurement and the absorption coefficient was estimated from this measurement and the transmittance measurements. This lead us to the results of fig. 5.16. It can be seen that the two process model is adequate to fit this measurements. The rest of the fits can be consulted in the appendix B.4.

The fitted curves in fig. 5.16 may be difficult to interpret because it lack the frequency dependence and is the result of the overlap of two complex functions. So, to better appreciate this fits we include in fig. 5.17 the imaginary part of each fitted cycle as a function of the frequency and the addition of both along with the measurement imaginary part. Here is easy to visualize the contribution of each cycle and its different frequency regimes.

The fitting of both cycles separately presented phase shifts associated with the transport of carriers through the material. Those shifts ended up added and being responsible of the whole shift observed in the measurements. Each of the cycles fitting gives a diffusion length and a characteristic time. This parameters have to be interpreted and to do that they are presented in fig. 5.18. In this figure there are the two time constants τ_{high} and τ_{low} for the four cells and the four laser powers and the two diffusion length for the four cells

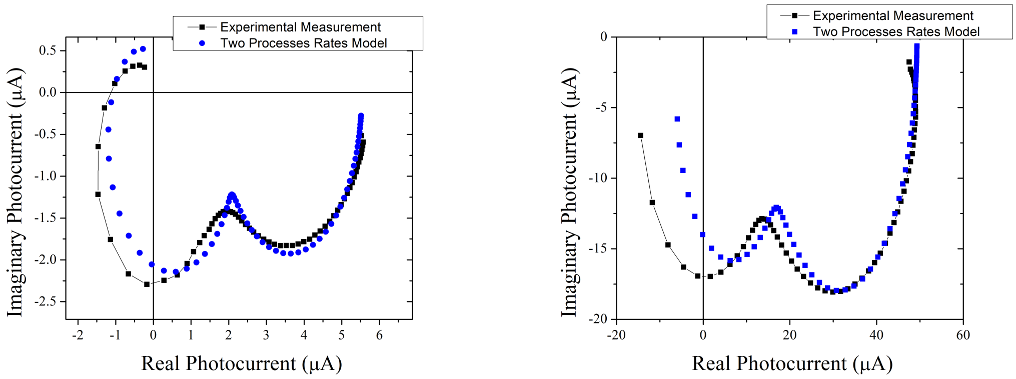

(a) Fitted IMPS of cell 1 mesured under 82.7 μW

(b) Fitted IMPS of cell 6 mesured under 63.2 μW

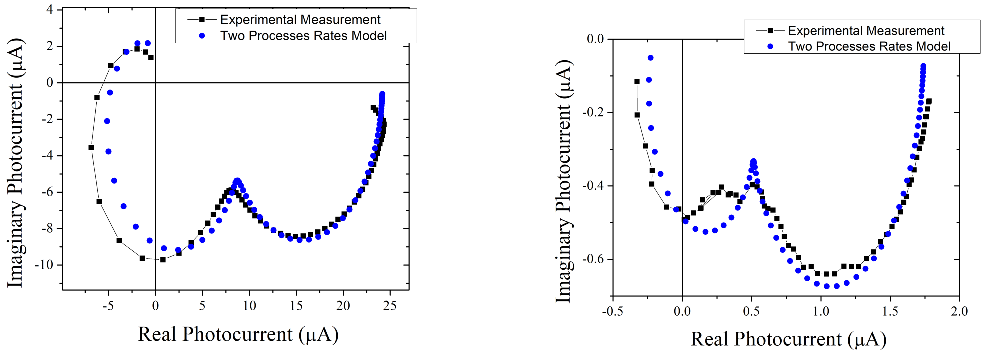

(c) Fitted IMPS of cell 7 mesured under 42.7 μW

(d) Fitted IMPS of cell 8 mesured under 63.2 μW

Figure 5.16: The IMPS measurements and its fits with the model of two diffusion equations.

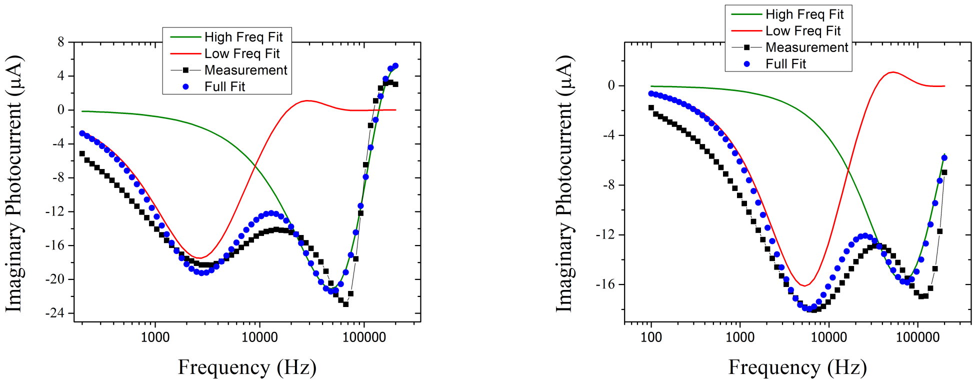

(a) Fitted IMPS of cell 1 mesured under 82.7 μW

(b) Fitted IMPS of cell 6 mesured under 63.2 μW

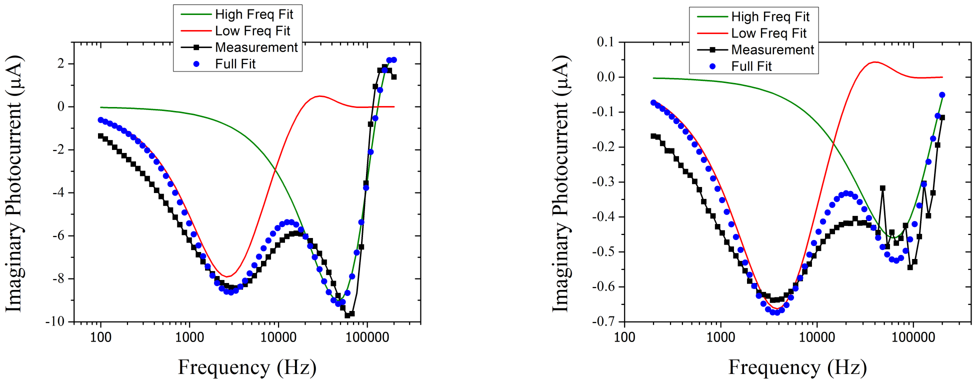

(c) Fitted IMPS of cell 7 mesured under 42.7 μW

(d) Fitted IMPS of cell 8 mesured under 63.2 μW

Figure 5.17: Imaginary part of the IMPS measurements and its fits with the model of two diffusion equations.

and the four laser powers.

Each of the cycles is associated with different processes which have three orders of magnitude of difference in the time constants and about one order of magnitude in the diffusion length. There are not big differences between the fit results among the cells which is expected as the cell were made equally. There is not a clear tendency with the power. The assignment of this processes is tricky. There is the possibility that we have measured two different electronic processes such as electrons and holes dynamics. On the other hand, we have discussed a model that uses an equivalent circuit to model the ionic dynamic in the cells and although is not applicable to this measurements it is not because it is incorrect but because it is incomplete. It lacks to model of the phase shift due to the delay of ions to move through the material. But the time scales presented by the time constant τ_{low} of fig. 5.18.a may be consistent with the ionic time scale [123–125]. This could mean that we are actually measuring the ion dynamics. Meanwhile, Fig 5.18.b shows a much shorter time constant τ_{high} that is consistent with the life time of electronic carriers in perovskites [85].

The figures 5.18.c and 5.18.d show the diffusion length for the carriers in each of the cycles. The length of fig. 5.18.d is reasonable for a hole or electron in materials in general but is little shorter than the expected for a perovskite [85]. On the other hand, the diffusion length of 5.18.c appear to be rather long for been ions, but ions in perovskites are almost free to move. There is also a possibility that because of the tricky of this fittings, some of the phase shift from one cycle is model by the other one generating uncertainty in these values.

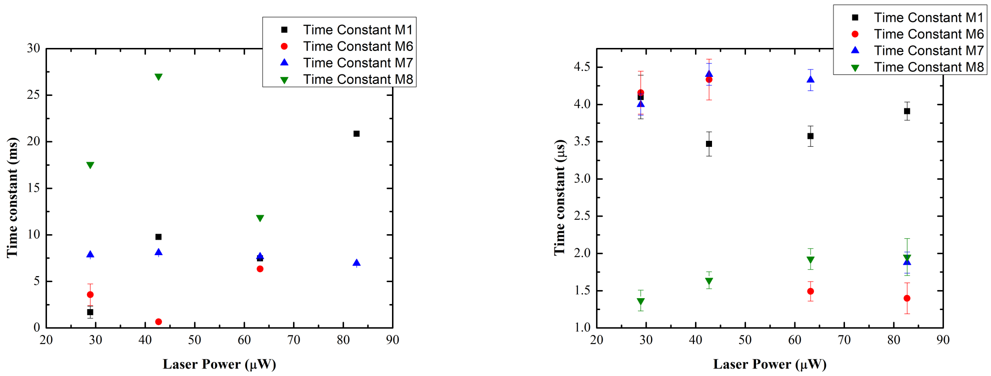

(a) Time Constant low frequency cycle **(b)** Time Constant high frequency cycle

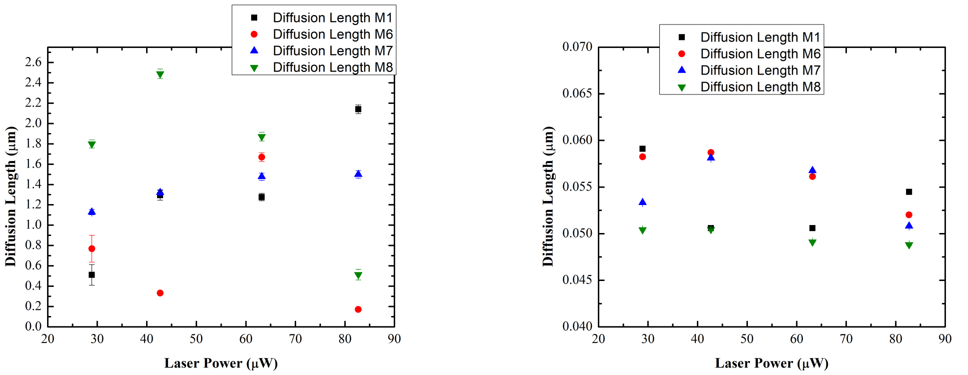

(c) Diffusion Length low frequency cycle **(d)** Diffusion Length high frequency cycle

Figure 5.18: Time constant and diffusion length fitted for the high frequency cycle ((b) and (d)) and for the low frequency cycle ((a) and (c)))

To help to elucidate this, the diffusion coefficients were calculated from the lifetimes and the diffusion length as:

$$D = \frac{L^2}{\tau} \tag{5.30}$$

The diffusion coefficients are presented in fig. 5.19. These parameters calculated for the high frequency cycle present a reduction tendency with power with the exception of the cell six. While for the low frequency cycle there is a clear growing tendency with power. The coefficients have for most of the cases less than one order of magnitude of difference. A greater difference would be expected if it were electrons and ions. This difference would indicate that carriers movement have a similar behaviour indicating the same type of carriers. If this is the case it indicates an electronic behaviour. The association would be electrons to the high frequency cycle and holes to the low one. This is because the carriers are generated close to the TiO_2 layer and the electrons are close to its selective layer but holes have to travel through the material. It would be expected then a faster transport for electrons than for holes. So we would be seeing the effect of the holes moving in our measurements as a slower process. Also, a slightly higher diffusion coefficient would be associated to a lighter effective mass. In this case the effective mass reported for electrons is lighter that the one for holes supporting our assignation of the processes [131–133]

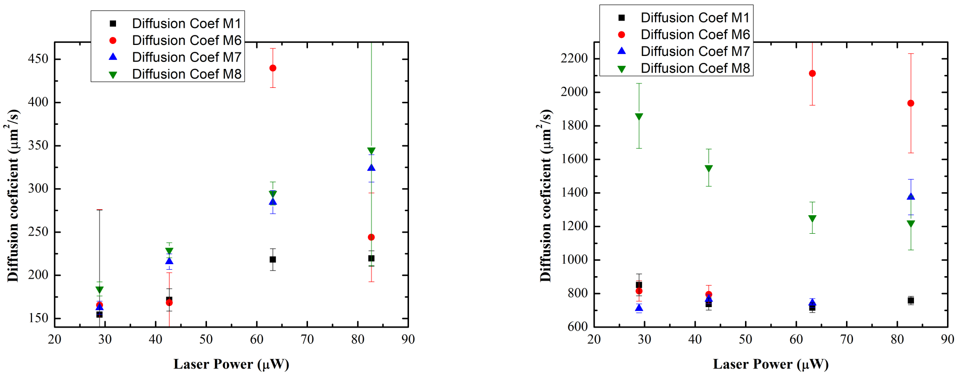

(a) Diffusion Coefficient low frequency cycle **(b)** Diffusion Coefficient high frequency cycle

Figure 5.19: Diffusion Coefficients calculated with eq. (5.30) for both cycles.

5.3.4 IMVS Measurements of MAPI Cells

The IMVS measurements of the MAPI cells were fitted using both models, the equivalent circuit of eq. (5.29) and the rates model of eq. (2.159). When using the rates model, only one cycle was considered because as can be seen in the measurements of fig. 5.8 there is a second process present in the measurement but is concentrated in the high frequency limit and have a small amplitude to be able to fit it. But it was possible to fit this second process using the equivalent circuit model.

In fig. 5.20 there are presented the results of using the rates model on the IMVS measurements. It can be seen that cells number 6 and 8 fit better although they do not have a particular difference with the other and actually they are from different batches. They main characteristic is that they go further into the third quadrant and have a twist in the high frequency limit (see inset) probably due to the second process observed more clearly in the other cells. Another particularity is that cells 1 and 7 which are from the same batch, have a wider real part compared to the imaginary one.

From these fits the parameters from fig. 5.21 were extracted. On then it can be seen that they are in the scale of the ms and μm meaning that this cycle correspond to the low frequency of the two from IMPS measurements and the structure from the high frequency limit correspond to the high frequency of IMPS measurements as someone would expect. This support the idea that there are both electronic processes since it is not expected that the cell response in IMVS is dominated by ion dynamics, especially reaching such high frequencies.

In this case we can see a more clear tendency in the fitted parameters which decrease with the light intensity. This behaviour is expected because if they are holes, a decrease in their time constant and diffusion length would come from an increase in the concentration due to the increase in the generation associated to the higher light intensity. In the same way, an increase in the carriers concentration would generate an increase in the potential causing a faster moving of ions but a reduction in its diffusion due to the increase in the moving ion concentration. The diffusion length of cell 7 is much bigger than the others but as can be seen in fig. 5.20 is the case where the fit deviates further from the measurement adding uncertainty. The rest of the fits can be consulted in the appendix B.4.

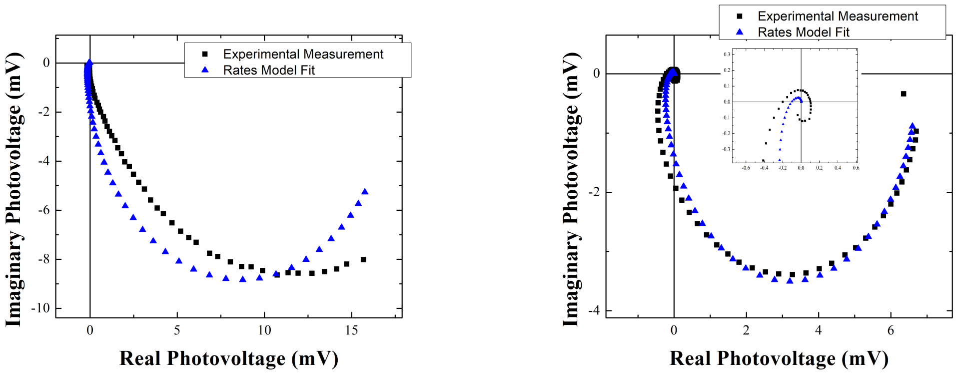

(a) Fitted IMPS of cell 1 mesured under 42.7 μW

(b) Fitted IMVS of cell 6 mesured under 63.2 μW

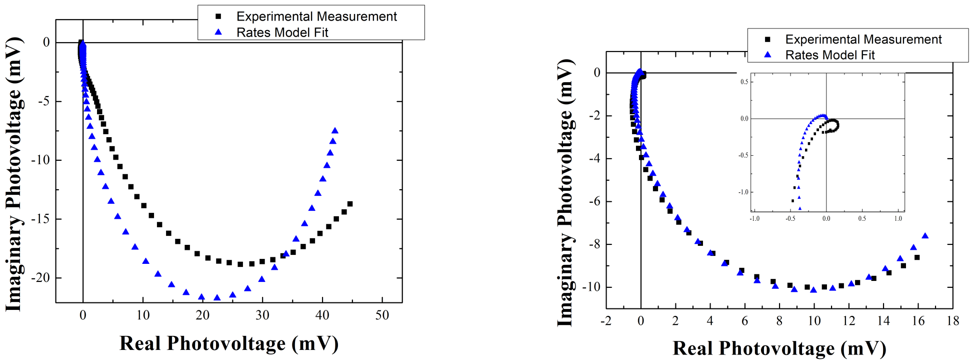

(c) Fitted IMVS of cell 7 mesured under 28.9 μW

(d) Fitted IMVS of cell 8 mesured under 28.9 μW

Figure 5.20: Different IMVS measurements and its fits with the diffusion equation model.

This time constant although related to the low frequency cycle of IMPS have a smaller value which is unusual. Because IMPS measurements have a superposition of recombination, transport and extraction process. Meanwhile, in IMVS measurements there is no extraction, only recombination. This would be ascribed to the uncertain in the IMPS fits exemplified in fig. 5.18.a were there is no clear tendency.

The tendency observed here may not been observed in the IMPS measurement perhaps because the difficulty of the fittings due to the presence of the partially overlapped two cycle structure. In that sense, the IMPS measurements offers more resolution allowing to distinguish processes that are not clear to see in IMVS measurements. Although this increases the fitting difficulty.

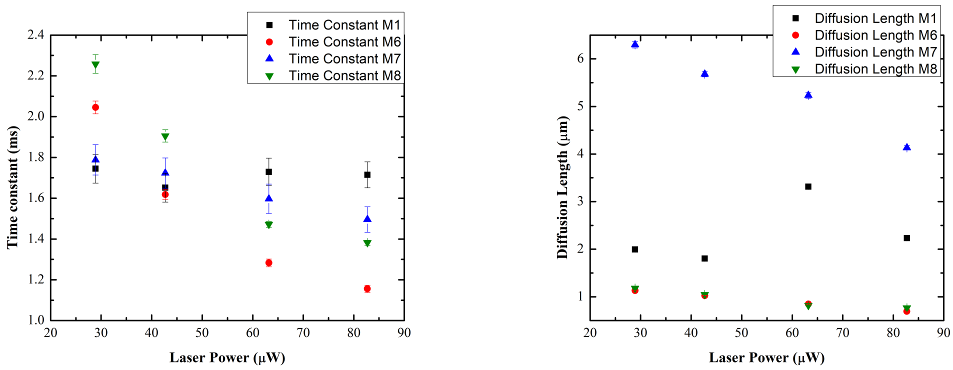

(a) Time Constant

(b) Diffusion Length

Figure 5.21: Time constant and diffusion length fitted from the IMVS measurements.

Once again we calculate the diffusion coefficient with eq. (5.30) and present it in fig. 5.22. Here the diffusion coefficients of the cell 7 fits were excluded because they end up much bigger than the others. This came from the estimated diffusion length of fig. 5.21b which result to be higher than the rest which traduces into a much higher diffusion coefficient but also is the cell where the fit deviates further from the measurement adding uncertainty. The rest of the parameters have similar values to those of the low frequency cycle of IMPS supporting the idea that is the same process.

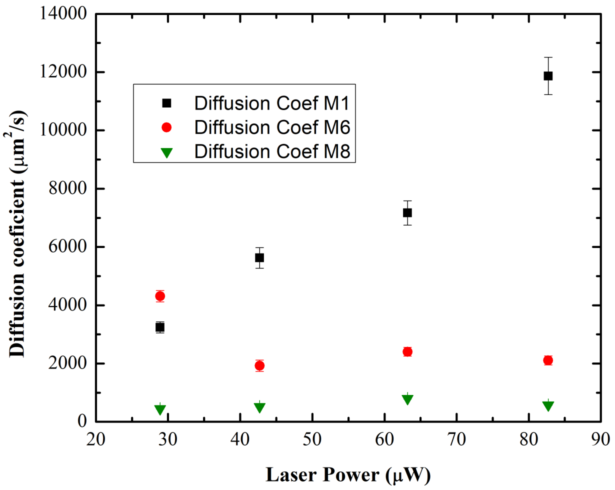

Figure 5.22: Diffusion Coefficients calculated with eq. (5.30) for IMVS fitted parameters.

Now, we move to the equivalent circuit model. To be able to fit with this model it was necessary to do a proper handling of the constraints because two partially overlapping cycles may model the curve but does not considerate the high frequency structure which means that we are reducing the difference between the measurement and the fit but the result is not representing the real situation. So, to improve this region fit we leave some of the low frequency points out of consideration. The result can be seen in fig. 5.23. The rest of the fits can be consulted in the appendix B.4. As can be seen, cells 6 and 8 are adequately fitted but the fits lack the shift to the third quadrant. Meanwhile, it was possible to reproduce the structures in the high frequency limit of the IMVS measurements of cells 1 and 7. Although lacking some phase shift as is observed in the insets of figures 5.23.a and 5.23.c.

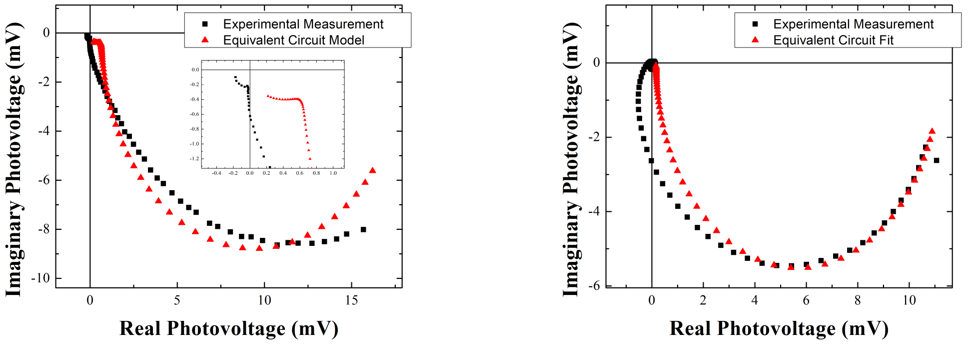

(a) Fitted IMPS of cell 1 mesured under 42.7 μW

(b) Fitted IMVS of cell 6 mesured under 63.2 μW

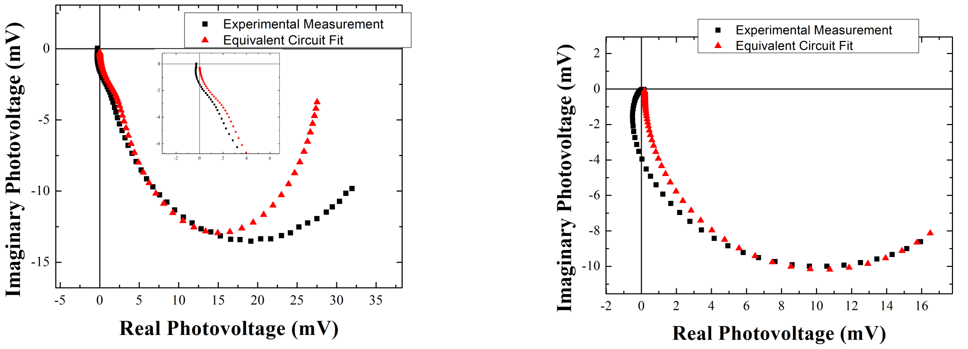

(c) Fitted IMVS of cell 7 mesured under 42.7 μW

(d) Fitted IMVS of cell 8 mesured under 28.9 μW

Figure 5.23: Different IMVS measurements and its fits with the equivalent circuit model of eq. (5.29).

The results from the fitting with the equivalent circuit model are presented in tables 5.4, 5.5, 5.6 and 5.7. The first to notice from this tables is that the parameter g_{stat} is remarkably small for all the cells. This is as expected for a measurement without any inductive behaviour.

The next that captures the attention is the previously called geometric capacitance. The results have values too high for the geometric capacitance of a small solar cell. The explanation for this is that its not actually the geometric capacitance what we have here but a parameter that only have meaning together with the g_{rec} conductance give place to a time constant. Must be remembered that this capacitance and the conductance are parallel elements of the circuit in fig. 5.13 so they quotient of C_g and g_{rec} originates the time constant τ_{rg} which is also included in the tables. Clearly this time constant is associated to the slow process observed in the measurements and is in reasonable agreement with the values in fig. 5.18.a.

Then we observe the time constant τ_{Dyn} which was introduced as an expected to be big time constant associated to a slow ionic processes. But in this fitting it converge to the small time constant. We have to keep in mind that we are fitting a measurement with two processes in different time scales and that this time constant came from an RC series branch of the circuit and must be interpreted as such. So, it's a small time constant and it is associated with the parameter g_{ion} which acts as an amplitude. This amplitude is bigger for the cells 6 and 8 in which it looks like the two cycles of the model are overlapped or only one is responsible of the shape. Meanwhile, for cells 1 and 7 g_{ion} is smaller and in this cases is where we can see another structure over the high frequency limit. In this cells besides, the time constants are closer between each other.

What we are seen then is that the RC series branch of the circuit is responsible for representing the high frequency process and the parallel RC is taking care of the low frequency process. The original meaning of each of the parameters has not been preserved and only the time constant of each RC branch have a meaning as such although they do not maintain their original meaning. While the time constant τ_{rg} is consistent with the previously presented IMVS fits and a higher time constant τ_{Dyn} seems to represent te time constant associated to the high frequency cycle of IMPS. That is to say, it lost its original meaning, which was to represent the ions dynamic.

This shows that the equivalent circuits can be useful to analyse the effective response of a devise but depends on a strong and careful interpretation of the results.

Cell 1	g_{stat} (Ω^{-1})	g_{ion} (Ω^{-1})	τ_{Dyn} (s)	$g_{rec}(\Omega^{-1})$	$C_g(mF)$	$\tau_{rg}(s)$
$28.9\ \mu W$	$4.9971e^{-14}$	1238	$3.59e^{-5}$	61.11	20.096	$3.288e^{-2}$
$42.7\ \mu W$	$3.8369e^{-14}$	1630	$3.35e^{-5}$	70.37	19.389	$2.755e^{-2}$
$63.2\ \mu W$	$1.1e^{-13}$	1884	$5.56e^{-5}$	109.15	15.973	$1.463e^{-2}$
$82.7\ \mu W$	$4.78e^{-13}$	3025	$4.23e^{-5}$	135.80	25.726	$1.894e^{-2}$

Table 5.4: Parameters obtained fitting the IMVS measurements of cell 1 with the equivalent circuit model.

Cell 6	g_{stat} (Ω^{-1})	g_{ion} (Ω^{-1})	τ_{Dyn} (s)	$g_{rec}(\Omega^{-1})$	$C_g(mF)$	$\tau_{rg}(s)$
$28.9\ \mu W$	$5.11e^{-14}$	4639	$2.56e^{-5}$	59.12	7.521	$1.272e^{-2}$
$42.7\ \mu W$	$3.75e^{-14}$	5266	$2.72e^{-5}$	89.24	8.327	$9.33e^{-1}$
$63.2\ \mu W$	$1.14e^{-13}$	3744	$5.07e^{-5}$	145.55	6.280	$4.31e^{-1}$
$82.7\ \mu W$	$1.52e^{-13}$	5511	$5.39e^{-5}$	244	8.270	$3.39e^{-1}$

Table 5.5: Parameters obtained fitting the IMVS measurements of cell 6 with the equivalent circuit model.

Cell 7	g_{stat} (Ω^{-1})	g_{ion} (Ω^{-1})	τ_{Dyn} (s)	$g_{rec}(\Omega^{-1})$	$C_g(mF)$	$\tau_{rg}(s)$
28.9 μW	$5.49e^{-14}$	55.04	$3.21e^{-4}$	25.06	19.8	$7.901e^{-2}$
42.7 μW	$4.65e^{-14}$	145.08	$1.97e^{-4}$	35.62	19.9	$5.587e^{-2}$
63.2 μW	$2.53e^{-13}$	236.57	$1.52e^{-4}$	45.57	19.9	$4.367e^{-2}$
82.7 μW	$2.41e^{-13}$	404.05	$1.42e^{-4}$	81.18	38.2	$4.706e^{-2}$

Table 5.6: Parameters obtained fitting the IMVS measurements of cell 7 with the equivalent circuit model.

Cell 8	g_{stat} (Ω^{-1})	g_{ion} (Ω^{-1})	τ_{Dyn} (s)	$g_{rec}(\Omega^{-1})$	$C_g(mF)$	$\tau_{rg}(s)$
28.9 μW	$3.25e^{-14}$	4715	$2.39e^{-5}$	48.68	7.5062	$1.542e^{-2}$
42.7 μW	$5.42e^{-14}$	3891	$3.82e^{-5}$	74.36	6.0994	$8.20e^{-1}$
63.2 μW	$3.62e^{-14}$	5943	$3.46e^{-5}$	123.26	8.9629	$7.27e^{-1}$
82.7 μW	$6.50e^{-14}$	5807	$5.86e^{-5}$	204.88	7.49	$3.66e^{-1}$

Table 5.7: Parameters obtained fitting the IMVS measurements of cell 8 with the equivalent circuit model.

5.4 Discussion

We have presented a series of characterizations of methylammonium lead halide perovskites solar cells. This is a prototype design in which the graphite contacts are being tested not only for the connection with the external circuit but also as a hole selective contact layer. The four cells whose results we present here were synthesized the same way to show repetitiveness.

The current-voltage curves shows that the structure is functional. The measured efficiency is acceptable for this kind of test devices and show that the fill factor have to be improved probably by reducing the high series resistance. Meanwhile, the open circuit voltage shows good and stable values, the photocurrent result are too small for a commercial device. This indicate a place to work. The current is something to improve and future tests with another hole selective layer should be carried to test their interaction with the graphite contacts.

We have to keep in mind that this particular perovskite may not end in commercial solar cells mostly because the rapid degradation of their organic components. But is a good perovskite to test new structures and complementary materials. Another reason to work with it is that its fast degradation allows to study in hours processes that in other perovskites takes more time. With this in mind, the degradation observed here shows that the S-shape is one of the first effects that appear in the cells as well as reduction of the already small reverse breakdown voltage. This two effect were linked to the decomposition of the perovskite and the formation of PbI_2 associated to the decomposition of the methylammonium through different processes which include a negative interaction with the TiO_2 as the electron selective layer. It is clear that this organic cation is not the best to ensure durability and probably another similar organic cation like the formamidinium, which is also used in this kind of perovskites solar cell would face similar problems. Inorganic cations are also considered and studied to this purpose and show better durability.

The external quantum efficiencies show a profile similar to the absorbance of the material indicating that there are not current limiting process and any particular energies and show a maximum efficiency for the generation between the blue and UV light. After these energies, we have a drop of the efficiency because of the light's energy reaches the TiO_2 band gap and also the equipment resolution limit may be reached.

The analysis of the intensity modulated photocurrent and photovoltage spectroscopy result quite challenging. These measurements have at least two clearly different frequency processes. The possibility of this being an instrumental artefact was considered and disproved. Two different models where presented and discussed. The first one presented in section 2.10 which consisted in a rates equation that considered the generation, recombination and diffusion of carriers through the cell. The second model, is an equivalent circuit model derived from previous impedance and hysteresis models presented in section 5.3.2 which consider the ions dynamics in the cell but it lack the phase shift due to the diffusion effect.

These two models where used to fit the IMVS measurements but only the rates model could be used for the IMPS measurements. For this last case, two added rates equations were used to model the two observed processes. From this two characteristic times and diffusion length were obtained in which one of the time constant is to big to be a recombination time.

Meanwhile the diffusion length associated with each cycle have an order of magnitude of difference and values which could be electronic carriers. To help to elucidate the diffusion coefficient were calculated and show similar values that could indicate the same type of carriers. If this is the case it indicates an electronic behaviour. The association would be electrons to the high frequency cycle and holes to the low one. This is because the carriers are generated close to the TiO_2 layer and the electrons are close to its selective layer but holes have to travel through the material. It would be expected then a faster transport for electrons than for holes. So we would be seeing the effect of the holes moving in our measurements as a slower process.

The IMVS measurements fitted with the rates model show values consistent with the lower frequency IMPS cycle. The diffusion coefficient here calculated is also consistent with the IMPS Diffusion coefficient. This plus the fact that it would not be expected that the cell response in IMVS is dominated by ion dynamics, especially reaching such high frequencies supports the idea that there are both electronic processes.

When the equivalent circuit model fit results are analysed, we see that some of the parameters does not behave as the physic effects they originally pretend to represent. But an equivalent circuit is a solid model with the adequate interpretation. It allows to model two parallel processes and to extract two time constants even in the cases like the IMVS measurements in which one of then is quite small and concentrated in the high frequency limit. This model lacks the phase shift associated to the diffusion of charge carriers and after the time constants are obtained they are subject to interpretation. It also does not provide any estimation about the transport parameters but results to be a very good starting point to fit modulated spectroscopy measurement and impedance measurements.

After analysing the results of the two mentioned models we can certainly conclude that we have two clearly distinguish processes with about three times orders of magnitude of difference. This processes are two electronic processes. But from the results from impedance measurements carried out by the master's candidate Nicolás Molina, we can confirm that only one cycle is observed in the impedance measurements under dark conditions while two cycles are observed when the impedance measurements are carried under illumination (see B.2). this indicate that one of this cycles is a light inducted effect. Specifically, the high frequency cycle indicating that the low frequency one is probably also an electronic effect and that the ionic effects are probably observable at lower frequencies.

5.5 Conclusions

These cells allow to conclude that the graphite contacts are a suitable option for contact perovskite solar cells. Although the cells have room for improvement, these showed comparable results with cells contacted with Au and Ag, and unlike these metals, graphite can act as a hole selective layer. Furthermore, applying graphite is much easier and cheaper than evaporating metals as contacts. Also, we have seen that repeatability can be achieved between samples in both their efficiency and their response.

The degradation of MAPI has been extensively studied in recent years and although it will probably not be used in commercial devices due to its rapid decline in efficiency, it allows us to understand the mechanisms that act in the degradation of organic components and different anions. These measurements allow us to see how these processes affect the performance and response of the devices. In particular, changes in the breakdown voltage and the change in the shape of the voltage-current curve to an S-shape could be attributed to degradation originating mainly at the TiO_2 interface. This is because it is known that the TiO_2 have photo-catalytic effect due to the absorption of UV photons. This photo-catalysis induces degradation that creates PbI_2 at the ETL/MAPI interface which would explain the change in the shape of the I-V curve (with the fill factor and the efficiency loss) and, the rearrange of the bands energy levels could explain the creation of a thinner depletion region through which the carriers can tunnel easily.

Spectral photo-response measurements proved to be quite challenging to interpret. This is probably why there are no studies of this type of measurement prior to 2017 in the analysed bibliography and in all cases, they are limited to analysing a portion of the frequency spectrum, either focusing on high-frequency electrons or low-frequency ions. This work attempted to study a wider frequency spectrum and for this purpose different models were implemented. This allowed us to conclude that IMPS measurements offer greater resolution regarding the different processes occurring in the material. Meanwhile, IMVS measurements indicate that they are dominated by one of these processes, the slower one.

Although the possibility of ionic effects being observed was considered, this was ruled out and it is concluded that the two processes observed are electronic processes. The association would be electrons to the high frequency cycle and holes to the low one. This is because the carriers are generated close to the TiO_2 layer and the electrons are close to its selective layer but holes have to travel through the material. It would be expected then a faster transport for electrons than for holes. So we would be seeing the effect of the holes moving in our measurements as a slower process. This was concluded because the modelled processes show similar diffusion coefficients and also, It is not expected that the response in IMVS is dominated by ions up to such high frequencies.

The equivalent circuit model failed at represent the physical effects originally assigned to each of its elements. It became clear that a resistor cannot represent recombination losses because it lacks a frequency dependence. The geometric capacitance lost its meaning and assumed the role of giving place to a time constant along with this resistance to model the observed behaviour. Meanwhile, the time constant τ_{dyn} whose original purpose was to represent ion dynamics, took on another role allowing the high frequency process to be represented.

Finally, these results do not mean that ion dynamics is not present or is not significant in these cells. But rather that they effect is probably observed at lower frequencies, and this should be taken into account in low frequency and time resolved measurements.

Chapter 6

$CsPbBr_3$ perovskite solar cells

Finally, we present the characterization of a solar cell with another type of perovskite as the active layer. It is a $CsPbBr_3$ perovskite which have Caesium, an inorganic cation replacing the Methylammonium and Bromine as the anion instead of Iodine [134]. This cell was synthesized at the University of Valparaíso. It is part of a batch with differences in the precursors concentration. We analyse the results of the one with the higher efficiency. This perovskite have a much longer stability and a band gap of $2.43\ eV$, with a exciton binding energy of about 40 meV [135–137]. This band gap energy is not the optimal value for a solar cell but it is still good to absorbing the light beyond the yellow color. We can see the cell in figure 6.1, the yellow layer is the perovskite and the black colour is the graphite.

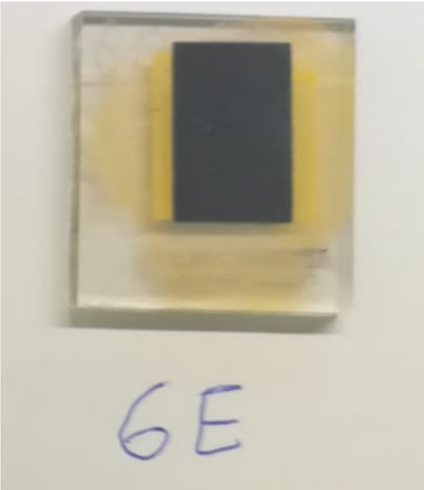

Figure 6.1: $CsPbBr_3$ perovskite solar cell.

The structure of this cell is composed of a glass substrate coated with floured doped tin oxide (FTO) with a TiO_2 compact layer grown by pyrolytic spay. Then a mesoporous TiO_2 layer was grown to increase the surface area and to act as electron transport layer. A mesoporous ZrO_2 and a mesoporous graphite layers were grown after, the ZrO_2 acts as a support material and the graphite as hole selective layer. The $CsPbBr_3$ perovskite was grew above this with a two step process as described in 3.1 using $CsBr$ and $PbBr_2$ as precursors. The idea of the structure is to enhance the surface area to improve the transport properties.

We will present the current-voltage characterization and intensity modulated photocurrent and photovoltage spectroscopy measurements next.

6.1 Current Vs Voltage Characterization

In this case the cell have only one spot to connect and measure so only one I-V curve were done for this cell. The cell I-V curve is shown in fig. 6.2 and like other perovskites have a high open circuit voltage. The short circuit current is a bit higher than those of the MAPI cells and have an efficiency of 3.29%. This cell also have a low fill factor of 0.424. We also estimate the shunt and series resistance from the slope $\frac{dV}{dI}$ at the high voltage limit and at short circuit point respectively. The values are $R_{series} = 188.7\ \Omega$ and $R_{shunt+series} = 1518\ \Omega$ with an order of magnitude of difference, they are not so bad but it would be desirable that the series resistance to be smaller and the shunt bigger.

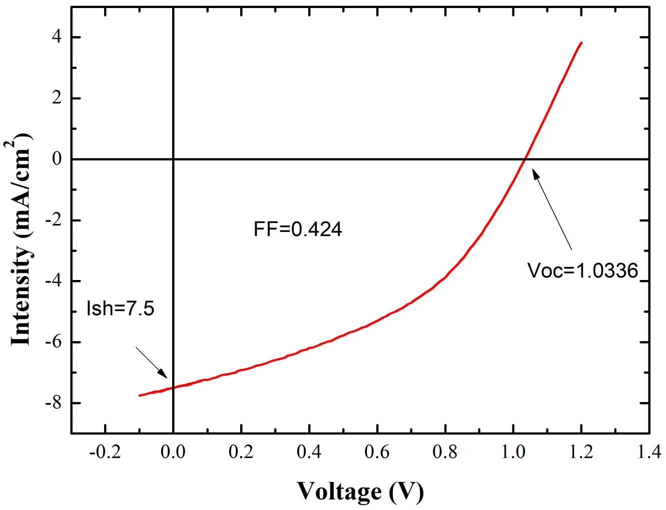

Figure 6.2: $CsPbBr_3$ perovskite solar cell´s current vs voltage curve.

6.2 Intensity Modulated Photocurrent and Photovoltage Spectroscopy

The intensity modulated photocurrent and photovoltage spectroscopy measurements were carried using a *455 nm* blue led. This was because the *633 nm* red laser have photons with an energy below the band gap and would not excite carriers in this perovskite. This measurements were done from 10 *Hz* to 200 *kHz* and using three different powers.

In this case, we observe in the IMPS measurements one cycle that spin around the origin in the high frequency limit (see fig. 6.3a). This curve is wider in the real axis than the imaginary one, which could be an indication of the overlapping of two different processes. The IMVS case showed in fig. 6.3b present a more round cycle which also enters the third quadrant at high frequency and have in the low frequency limit a cycle in the first quadrant resembling an inductor or a negative capacitor. As this is a cycle in the low frequency limit, we use the model presented in section 5.3.2 to fit it. We also use the rates model of section 2.10 to model the high frequency behaviour of the measurements. The implementation of these models is the same as in the previous chapter.

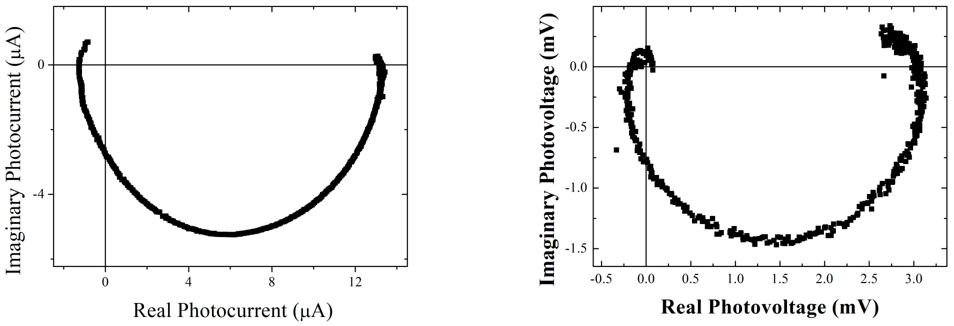

(a) Intensity modulated photocurrent spectroscopy **(b)** Intensity modulated photovoltage spectroscopy

Figure 6.3: $CsPbBr_3$ perovskite cell´s IMVS and IMPS measurements for 29.5 μW laser power.

6.2.1 Photovoltage Spectroscopy

Lets present first the results of the IMVS fits. We can see in fig. 6.4a that the equivalent circuit model provides a good fit with the IMVS measurements, being the high frequency limit the region were its depart more from the observed behaviour. This issue was already pointed out in the previous chapter. This model allow us to model the low frequency cycle and the results are presented in the table 6.1 . In this case, the conductance g_{stat} become relevant as it is associated with the low frequency, first quadrant cycle. The time constant associated to this cycle τ_{Dyn} is quite close to *1 s* and is way more clear that it is the ion response to the electronic rearrangement under slow power modulation.

Once again, the geometric capacitance present values to high to be actual capacitances. But instead we consider it together with the conductance g_{rec} as the representation of a dynamic process and the associated time constant τ_{rg} is presented also in the table 6.1. This characteristic time represent the main cycle and have values consistent with the carriers lifetime. Once again, it would be expected that this carriers to be holes because the absorption occur close to the ETL, the TiO_2 and ZrO_2 mesoporous layer.

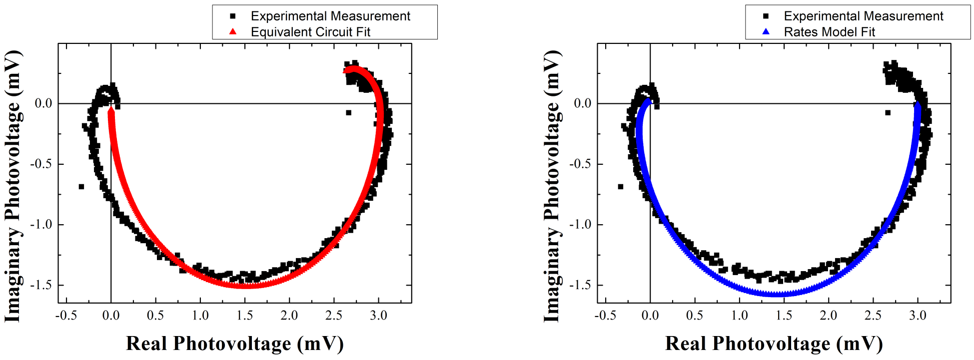

(a) Equivalent Circuit Model Constant **(b)** Rates Model

Figure 6.4: $CsPbBr_3$ perovskite cell´s 29.5 μW power IMVS fitted with the equivalent circuit model (a) and with the rates model (b).

$CsPbBr_3$	g_{stat} (Ω^{-1})	g_{ion} (Ω^{-1})	τ_{Dyn} (s)	$g_{rec}(\Omega^{-1})$	$C_g(F)$	$\tau_{rg}(s)$
9.8 μW	14.6	6.5	0.227	40.2	0.0293	7.29e^{-4}
17.4 μW	40.8	17.8	0.0678	116.2	0.0574	4.94e^{-4}
29.5 μW	123.1	43.8	0.0875	286.7	0.0976	3.40e^{-4}

Table 6.1: Parameters obtained from fitting the IMVS measurements of the $CsPbBr_3$ cell with the equivalent circuit model.

In 6.4b we have the fitting results using the rates model which allows us to also estimate the diffusion length. For this case, we estimate a short absorbance distance compared to the thickness of the absorbent material when we apply the rates model. This results are presented in table 6.2 and we can see that the recombination time obtained from the model are in good agreement with the values obtained with the equivalent circuit model. The diffusion coefficient was also calculated and included in this table showing values consistent with electronic carriers.

Both models present similar characteristic lifetimes that are reduced with the power. This could be explained because the higher optical power generates higher carriers concentration which leads to faster recombination. Finally, the diffusion length present values of about one μm which is high for most of semiconductors but is close to what is expected for a perovskite device [10, 11, 89].

The first quadrant, low frequency cycle would be assigned to the ions dynamic because its characteristic frequency is low enough to be consistent with it, it does not dominates the cell behaviour and also only the ions model of section 5.3.2 predicts this behaviour.

$CsPbBr_3$	$\tau_{rec}^{IMVS}(s)$	$L_{diff}^{IMVS}(\mu m)$	$Diff. Coef.(\mu m^2/s)$
9.8 μW	$5.8e^{-4}$	1.27	$2.78e^3$
17.4 μW	$3.8e^{-4}$	1.27	$4.24e^3$
29.5 μW	$2.8e^{-4}$	1.18	$4.97e^3$

Table 6.2: Parameters obtained fitting the IMVS of the $CsPbBr_3$ cell with the rates model.

6.2.2 Photocurrent Spectroscopy

Now we present the results of the fitting of the IMPS measurements.

In fig. 6.5.a the result of using the equivalent circuit model of fig. 5.13 is presented. The fitted curve have the shape of an RC response having a higher imaginary part in the middle and also departing from the measurement in the high frequency limit. In table 6.3 the parameters resulting from the fitting are presented. Using the conductance g_{rec} and the capacitance C_g we can get time constants τ_{rg} presented in this table which do not depart from the findings of the IMVS measurements. The conductances g_{stat} and g_{ion} are low enough not to affect the result. Although, one of the values of g_{ion} is comparable to g_{rec} it must be notice that the time constant τ_{Dyn} is at the lower frequency limit and in this particular case is beyond that value meaning that this conductances have no influence in the shape of the curve. In fig. 6.5.c is presented the imaginary part of the fitted curve showing that there is no observable contribution from the any second cycle in the fit. This also allow to clearly see that the RC model is sharper than the measurement although it have the same position for the peak indicating that the characteristic time should be correct.

In light of these results, in fig. 6.5.b we implement an equivalent circuit model with just one process and in this case using a constant phase element (CPE) instead of a capacitor. A CPE is an idealized electrical circuit element commonly used in electrochemical impedance spectroscopy and other areas of physics and engineering to model non-ideal capacitive behaviour [138]. It generalizes a capacitor by allowing a constant phase angle in its impedance response, regardless of frequency. This impedance element is implemented as:

$$Z_{CPE} = \frac{1}{P(j\omega)^n} \tag{6.1}$$

Here P is a frequency-independent constant (its units depend on n; not always a capacitance) and n is the phase exponent, with values between 0 and 1. When $n = 1$ it behaves like an ideal capacitor → $Z = 1/j\omega C$ meanwhile when $n = 0$ it behaves like an ideal resistor → $Z = 1/g$. This element flattens the imaginary part of the plot as the number n is reduced. It is normally used to model the effects of surface roughness of electrodes, inhomogeneous current distribution, porous materials, non-uniform diffusion paths and distribution of relaxation times among other effects [138].

In this case, probably a non-uniform diffusion process is responsible of this behaviour. Also, there is a possibility that there are actually two overlapping processes in the measurement. The parameters obtained from this fitting are summarised in table 6.4. Once again the obtained parameters only have meaning if they are correctly interpreted. The CPE constant and the resistance obtained here have no actual physical equivalent but together the obtained time constant represents the response time of the device. This time constant τ_{CPE} was calculated as

$$\tau_{CPE} = (RP)^{1/n} \tag{6.2}$$

and is included in the table. This results are very similar to the obtained from the previous model as expected. Finally, the n parameter of the CPE acts like an ideality factor and the lowest is 0.852 which do not depart too much from 1. In fig. 6.5.d the imaginary part of this fit is plotted. Here is observable that the change in the exponent make the fit wider and shorter.

The main harvest from this models is that the time constants are in very good agreement between each other and with the recombination times obtained from the IMVS measurements.

Next we use the the equation (2.149) to model the measurements and the first problem doing this was that this model create loops with higher imaginary parts that do not resemble the measurements. The variation of the recombination time and the diffusion length was not able to model the system. Because of this we change one of our work hypothesis which was that the absorption

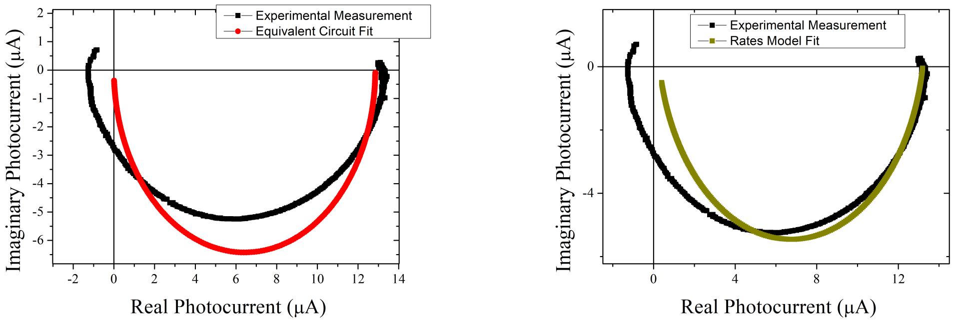

(a) Nyquist of the Eq. Circuit Model

(b) Nyquist of the CPE Model

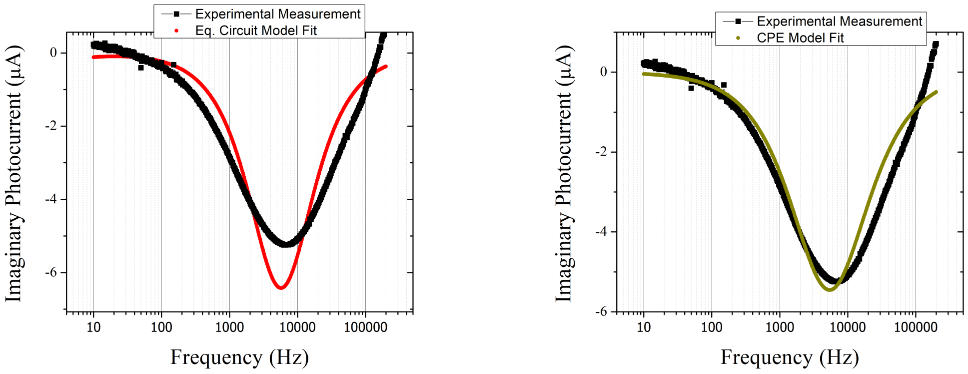

(c) Imaginary component of the Eq. Circuit Model

(d) Imaginary component of the CPE Model

Figure 6.5: $CsPbBr_3$ perovskite cell´s IMPS fitted with the equivalent circuit model (a) and with the CPE model (b). Its correspondent imaginary parts as function of the frequency (c) and (d) respectively.

$CsPbBr_3$	g_{stat} (Ω^{-1})	g_{ion} (Ω^{-1})	τ_{Dyn} (s)	$g_{rec}(\Omega^{-1})$	$C_g(F)$	$\tau_{rg}(s)$
9.8 μW	0.399	22.16	1.25	56.49	0.024	$4.25e^{-4}$
17.4 μW	0.0638	0.7249	0.177	14.12	0.00837	$5.93e^{-4}$
29.5 μW	0.165	1.73	0.452	17.50	0.00776	$4.44e^{-4}$

Table 6.3: Parameters obtained fitting the IMPS measurements of the $CsPbBr_3$ cell with the equivalent circuit model.

$CsPbBr_3$	R (Ω)	P $(F^{1/n})$	n $(adim)$	$\tau_{RP}(s)$
9.8 μW	0.00019	2.62	0.925	$2.69e^{-4}$
17.4 μW	0.00172	0.441	0.852	$2.18e^{-4}$
29.5 μW	0.00129	0.358	0.893	$1.83e^{-4}$

Table 6.4: Parameters obtained fitting the IMPS measurements of the $CsPbBr_3$ cell with the CPE equivalent circuit model.

length is much short than the thickness of the absorber. Until now we have been working using a fix value for α which is big enough to consider $\alpha \times d >> 1$. In this regime, the contribution of the terms in eq. (2.149) which depend on this product are fixed. Analysing the behaviour of this function when the absorbance is reduced it is observed that the imaginary part is reduced compared to the real part. This variation is represented in fig. 2.12. Because of this we start from a smaller initial value and we let it vary to also fit its value. We also decided to include a capacitive behaviour because this also contribute to twist around the origin and increase the extension to the third quadrant in the high frequency limit. To do this, we include the multiplicative term of eq. (2.154) in the IMPS model. We start with the reasonable values of 10 Ω and 1 μF. Although there are not impedance measurements of this cell, this values are reasonable for a cell of this characteristic and comparable to those of the previous chapter. But decided to also let the capacitance vary anyway because there is no measurement of it for this particular cell.

In fig. 6.6 we use the equation (2.149) with the equation (2.154) included to model the measurements and in this case we have to estimate four variable parameters in addition to an amplitude. Here we present the fitting results after fitting with slightly different initial α values. As can be seen in tables 6.5 and 6.6 the absorbance have converge to a much smaller value than the $2e^9$ $1/m$

originally used in the IMVS fittings. On the other hand the capacitance did not change considerably from the initial value of 1 μF. This is because lower values would move the RC time constant to a higher frequency beyond the measured region making it not noticeable and higher values would be unrealistic but also would move the contribution of this term to lower frequencies overlapping it with the already high imaginary part of the middle. We present in fig. 6.6 the result of two different fits that try to model the measured behaviour. To do this, the model of eq. (2.149) was implemented with 5 variables; The time constant, the diffusion length, the absorbance and the capacitance besides an amplitude. This model was used to fit the measurements and two of the best were selected and included here. The main difference between them is that one have smaller absorbance and higher capacitance while the other have higher absorbance and smaller capacitance. This is because in this region of values, both contribute to increase and twist the high frequency limit.

It should also be noted that although the recombination time is consistent with the IMVS and the previous IMPS fits, the diffusion length converge to smaller values. Nether the diffusion length or the absorbance obtained here are consistent with the IMVS fits.

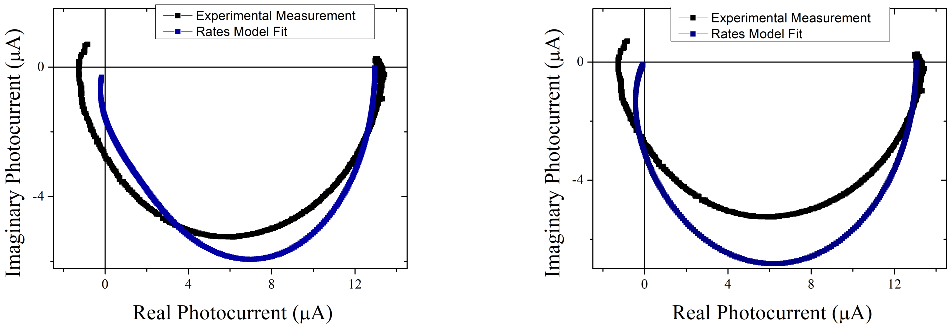

(a) Rates model with capacitive effect **(b)** Rates model with capacitive effect

Figure 6.6: $CsPbBr_3$ perovskite cell´s IMPS fitted with the rates model including the capacitive factor.

$CsPbBr_3$	$\tau_{rec}^{IMPS}(s)$	$L_{diff}^{IMPS}(\mu m)$	$\alpha(1/m)$	C (μF)
9.8 μW	$6.05{-}4$	0.31	$1.60e^6$	2.01
17.4 μW	$6.06e^{-4}$	0.54	$1.21e^6$	2.01
29.5 μW	$5.23e^{-4}$	0.51	$8.35e^5$	1.52

Table 6.5: Parameters obtained by fitting the IMPS of the $CsPbBr_3$ cell with the rates model including the capacitive factor. Parameters corresponding to the fig. 6.6a

$CsPbBr_3$	$\tau_{rec}^{IMPS}(s)$	$L_{diff}^{IMPS}(\mu m)$	$\alpha(1/m)$	C (μF)
9.8 μW	$6.02e^{-4}$	0.376	$9.28e^5$	4.85
17.4 μW	$6.04e^{-4}$	0.714	$5.74e^5$	4.38
29.5 μW	$5.97e^{-4}$	0.602	$6.09e^5$	4.70

Table 6.6: Parameters obtained by fitting the IMPS of the $CsPbBr_3$ cell with the rates model including the capacitive factor. Parameters corresponding to the fig. 6.6b

After observing this discrepancy in the model of IMVS and IMPS we plotted in fig. 6.7 the result without the capacitive contribution. Clearly the main contribution to the high frequency region is the RC term and the rest of the model departs from the measurement. Going back to fig. 2.12 we can see that we depart from our original working region. If we calculate αd (using $d = 700\ nm$) we obtain *0.62* and *0.43* and for L_h/d we obtain *0.73* and *0.86* for each of the plotted results respectively. The model have departed to match from the reasonable conditions of high absorbance and high diffusion length for a perovskite. With this considerations plus the fact that the CPE model (fig. 6.6b) show a non ideal behaviour we came to the conclusion that these fit are not modelling correctly the measurements and also that in the same way that the MAPI cell present two electronic processes, here there also may be two processes but more overlapped.

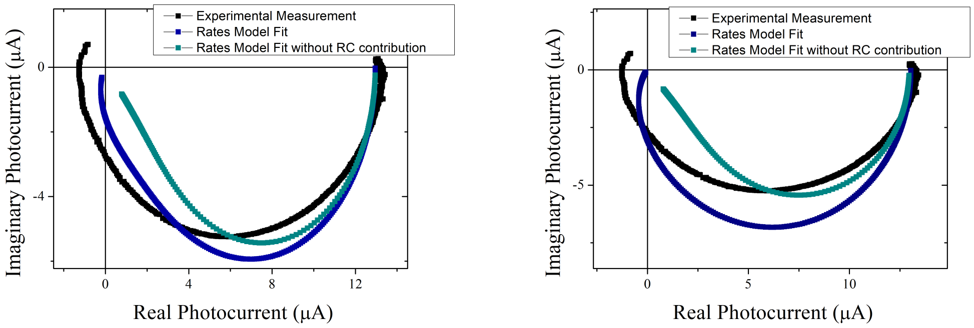

(a) Rates model with higher absorbance and lower capacitive effect

(b) Rates model with lower absorbance and higher capacitive effect

Figure 6.7: $CsPbBr_3$ perovskite cell´s IMPS fitted with the rates model excluding the capacitive factor.

Finally we apply a model of two processes composed of a rates model without the capacitive term to fit the high region part and an equivalent circuit model with a resistance and a CPE to model the low frequency region. The aim is to discern if two different processes are present. The reason why this model was used and not two rates model as in the previous chapter is because if there are indeed two processes they would be much more overlapped and a two rates model would have more uncertainly in the parameters. This way there are only a extra time constant that help to discern if there are or not two processes.

To implement this we divide the measurement and first fit each of the models separately in their application regions. Then we use this results as the initial values to fit with a function with the two models simultaneously.

Now we plot in fig. 6.8 the fitting result for a measurement showing that it fit better with this two processes model (the rest of the fits can be consulted in the appendix B.5.). We also include each of the used models separately and the imaginary part as function of the frequency to better appreciation. It is possible to see that the rates model have the expected shape. In table 6.7 we present the parameter obtained from this fits. We can see that the lifetime and the diffusion length are now in much better agreement with the IMVS fits. There is also a time constant which would be associated to another transport process and an ideality factor which now is closer to the ideal *1* value. The characteristic times obtained from both overlapped models show close values. This may indicate that there are not two different processes but only one with a non-uniform diffusion process which is responsible of this behaviour.

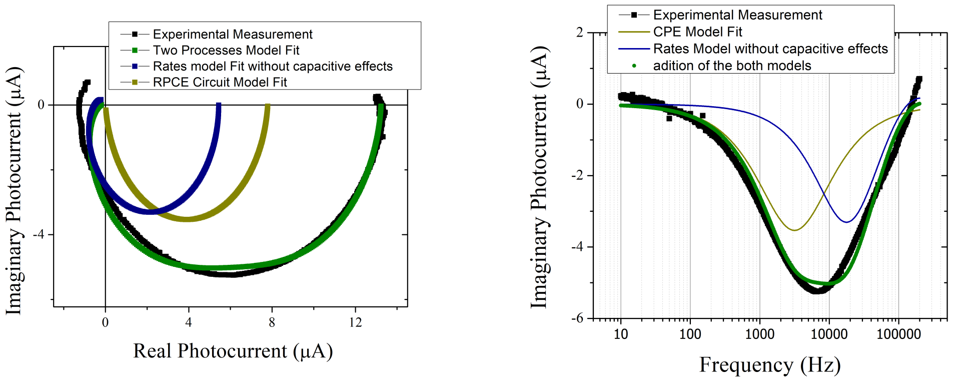

(a) Nyquist dayagram of the 29.5 μW power measurement

(b) Imaginary part of the 29.5 μW power measurement

Figure 6.8: $CsPbBr_3$ perovskite cell´s IMPS Nyquist and imaginary part fitted with the double processes model. It includes each of the models separately.

$CsPbBr_3$	$\tau_{rec}^{IMPS}(s)$	$L_{diff}^{IMPS}(\mu m)$	$Diff.\ Coef.(\mu m^2/s)$	$\tau_{CPE}(s)$	n (CPE) (Adim)
9.8 μW	5.15e^{-4}	1.30	235	4.2e^{-4}	0.85
17.4 μW	5.31e^{-4}	1.31	845	4.01e^{-4}	0.92
29.5 μW	5.09e^{-4}	1.32	607	3.16e^{-4}	0.93

Table 6.7: Parameters obtained fitting the IMPS of the $CsPbBr_3$ cell with the double processes model. It include the results from the rates model and the time constant and the ideality factor from the CPE model.

6.2.3 Discussion

We have presented the characterization of a $CsPbBr_3$ perovskite solar cell. From its current-voltage curve we estimate a 3.29 % efficiency with a *1 V* open circuit voltage and a short circuit current of 7.5 mA/cm^2. The fill factor have a low value of 0.424 which is closely related with the high series resistance and low shunt one. This could be related to the interface resistances and the lack of a hole transport layer.

When the performance of this perovskite cells is analysed it must be considered that for the band gap of this material the theoretical maximum efficiency according to the Shockley–Queisser limit [139] is 20 %, a limit that surely could never be reached due to be an upper limit, as a Carnot efficiency limit.

From the intensity modulated photovoltage spectroscopy measurements it was possible to observe in the low frequency limit an ion related inductive like behaviour, which was introduced in the previous chapter but was not observed. This behaviour is related to the ion movement in the cell as a response to variation in the electronic current in the cell. As expected this characteristic time is close to *1 s*.

The result from the equivalent circuit fit shows one clear cycle. This is an indication that at least the open circuit voltage is dominated by one main process. This model lacks to model the third quadrant behaviour in the high frequency limit as expected. To take this problem into account we used the rates model of eq. (2.159) which is, to the date, the best or more complete model to explain the electronic dynamic in a solar cell. Excepting the low frequency limit behaviour which is ion related and is not considered by this model, it provides very good fitting with the measurements and take in to account the high frequency limit behaviour. It leads to a time response of some hundred μs with a decrease with power and a long diffusion length of approximately one μm stable with power. This high values are consistent with what is expected for a perovskite and explain its moderate high efficiency.

The intensity modulated photocurrent spectroscopy also show the high frequency twist and the beginning of what looks like a inductive behaviour in the low frequency limit but this last effect was not possible to fit. This measurements were substantially harder to model. Its wider real part span in comparison to the imaginary one make it differ to the expected shape from the models.

The implementation of two different equivalent circuit models show that although the measurement behave like one cycle/process the RC equivalent circuit does not fit it properly. The implementation of a model with a constant phase element in parallel with a resistance show that the measurement is effectively flatter than a single process cycle. This is an indication of a probable superposition of processes, or a non ideal diffusion or a distributed set of lifetimes. Anyway both fits shown that the time constant associated to the main process is of the same order of magnitude of the IMVS fits.

Next, the rates model of eq. (2.149) was implemented to fit the measurements. This model also presented a wider imaginary part span than the measurements. The inclusion of a RC effect and the variation of the absorbance (which was assumed considerably high until this point for being a perovskite) was also considered to try to improve the quality of the fits. This end up leading to the results in fig. 6.7. Where although similar values to those expected for the lifetime were obtained, the diffusion length and the absorbance converged to values much smaller and not consistent with the IMVS results. This also lead us to a different regime of work in which both the diffusion length and the absorption length are shorter than the estimated thickness of the absorber material. This result is in strong discrepancy with the IMVS results which are better fitted and consistent with the knowledge of perovskites. This problem come from the RC term which partially compensate the difference between the model and the measurement. The inclusion of this term is based in the expected value of the capacitance of $1 \mu F$. If the real capacitance is smaller, something possible for this kind of cells, its effect would not be observable. The lack of a dark impedance measurement leads us to estimate this value but the results indicate that the capacitance is not responsible of this observable response.

Finally, we implement a model which combine the model of eq. 2.149 and a constant phase element model. This allow us to better fit the measurement with the superposition of two cycles associated to similar time constants. The high frequency region was model with the eq. 2.149 and this time it leads to values consistent with those expected and with the IMVS fits. The low frequency region, fitted with the constant phase element circuit model allow us to present a model with the same shape than the measurement but this whole model needs an interpretation.

The wider real part of this measurement may be the result of the superposition of two processes with similar rates or the result of a distributed set of transport paths with differences in its diffusion coefficients. It is difficult to distinguish this two scenarios. If two electronic processes are superposed as seems to be the case with the cells of MAPI it could be an indication of a common double transport effect in perovskites.

The widening observed could also be a non discrete but continuous distribution of diffusions paths. This would affect and increase more the low frequency region, while the distribution of lifetimes would not affect significantly the low frequency region, and also, in a situation of overlapping recombination times, the fastest would dominate and determine the observed effects. A model of this variations can be consulted in the appendix figs. B.7a and B.7b.

The possibility of that the widening is due to the ions dynamic is discarded because it would be associated to a lower frequency of tens of Hz as high not to a characteristic frequency of more than 1000 Hz. Although, ions have a contribution that is observed in the low frequency limit they would not be responsible of this widening in this frequency region.

6.3 Conclusions

Although $CsPbBr_3$ have a non ideal band gap it prove to be useful as a solar absorber material. It would also be useful as a complementary material for a tandem cell. Its non organic composition make it more stable making it more suitable for commercial applications. Also, the graphite contacts prove to be a good option to replace evaporated metal contacts. This is because its deposition is simpler and cheaper while it shows good results as a contact and even as a hole transport layer.

The intensity modulated spectroscopy measurements allowed to measure a response time of the order of μs and a diffusion length of μm. The photocurrent measurements result quite difficult to model. From the final applied model we obtain two close time constants which indicate that we are measuring a non ideal transport process rather than two separated ones.

The photovoltage measurements present a more clear cycle dominated by a more ideal process. This indicate that the dominant recombination process is responsible of the main behaviour here while the IMPS measurements is influenced by the transport and extraction process leading to an extended response time. This support the idea that IMPS measurements offers more resolution while IMVS measurements are dominated by one process. If this is the case, similar extraction and recombination times would explain the low efficiency. The structure of the cell is such that absorption occurs close to the electron transport layer, meaning that holes have to travel through the absorber. Because of this, the observed dynamic is associated to the holes.

Finally, the IMVS measurements allow us to measure a ion related process in the low frequency limit. Something we had not been able to achieve before and was the original goal of the equivalent circuit model. This process prove to be slow and unobservable if the measurement do not go down to at least 10 Hz. This shows that ion dynamics can be important in low frequency regimes.

Chapter 7

Conclusions

7.1 Low Temperature MAPI Measurements

The temperature evolution of the optical properties (absorbance and photoluminescence) of methylammonium lead iodine (MAPI) perovskite with temperature were investigated.

The absorbance of samples show a strong excitonic behaviour even at room temperature that was modelled with the Elliott formula. The photoluminescence presented different behaviours for each crystal phase indicating different origins. Using the Gurioli and the Li models was possible to associate the high temperature phase (tetragonal) photoluminescence to free excitonic recombination and the low temperature phase (orthorhombic) photoluminescence to localized excitonic recombination.

The measurements of the absorbance and photoluminescence spectra for different temperatures of a sample of methylammonium lead iodide over different days and samples show changes due to degradation. This degradation originates mainly due to the irradiation with blue light in vacuum which decomposes the methylammonium. The absorbance spectra are less susceptible to the initial degradation process, remaining almost unchanged compared to photoluminescence. This may be because photoluminescence involves many more processes and is therefore more sensible to degradation. The phase transition moves to higher temperatures, indicating an increase in the stability of the orthorhombic phase. The photoluminescence changes from a sharp free exciton emission in the tetragonal phase to a lower energy localized exciton emission which does not follow the absorption edge movement of the phase transition. It also shows a lower and broader emission peak with increasing deactivation temperature, all this indicating an increase in the defect concentration associated with degradation. This is supported by the observed reduction in the optical phonon energy of both the exciton absorption peak width and mainly the Urbach energy. This can be attributed to the weakening of the bonds associated to the creation of vacancies from the decomposition of methylammonium.

The MAPI photoluminescence has proved to be highly susceptible to degradation in a perovskite with many degradation mechanisms, some of of which are not easily solvable. Most of this fast degradation is related to the organic components of this perovskite. This organic component is also responsible for the phase transition at low temperatures.

MAPI optical properties are similar to those of other perovskites, such as its strong excitonic absorption and its photoluminescence, also of excitonic origin. These characteristics common to most of perovskites and have not been observed in other materials at room temperature at least. Because of these, its rapid degradation allowed us to obtain information that could be extrapolated to other similar perovskites with slower degradation times. In this way, it is expected that other inorganic perovskites will change little their excitonic absorption with the appearance of defects but these defects will rapidly affect the photoluminescence. Sufficient defects could also cause localized exciton photoluminescence to appear and quench the free exciton one. Defects would also be responsible, as in here, of generating instability in certain perovskites phases. Something of particular importance in perovskites of more complex compositions.

Although the lead dependency is still present, we have contributed to the validation of a new lead recycling process from recycled car batteries obtaining the same purity as commercial lead precursors. The work presented here have lead to three peer reviewed publications, two as first author.

7.2 Perovskite Cells Characterization

In chapters five and six the characterization of solar cells made from two different perovskites were presented. Both type of cells, were made with the structure *n-i-p* and with graphite as the hole transport layer and as contact material. The obtained results, allow to conclude that graphite contacts are a suitable option for contact perovskite solar cells. Although the cells have room for improvement, these showed comparable results with cells contacted with Au and Ag, and unlike these metals, graphite can act as a hole selective layer. Furthermore, applying graphite is much easier and cheaper than evaporating metals contacts. Also, we have seen that repeatability can be achieved between samples in both their efficiency and their optoelectronic response.

Both perovskites give place to cells with comparable efficiencies of $\sim 3\%$. It is notable that the $CsPbBr_3$ perovskites have a suboptimal gap but much greater durability. This makes the latter a good material for tandem cells.

The intensity modulated spectroscopy response of the MAPI cells showed two cycles for their photocurrent response. Therefore, the association would be electrons to the high frequency cycle and holes to the low one. This is because the carriers are generated close to the TiO_2 layer and the electrons are close to its selective layer but holes have to travel through the material. Is expected a faster transport for electrons than for holes. So we would be seeing the effect of the holes moving in our measurements as a slower process. Meanwhile, IMVS measurements indicate that they are dominated by one of these processes, the slower one. This allowed us to conclude that IMPS measurements offer greater resolution regarding the different processes occurring in the material.

A dynamic model was proposed to consider the contribution of ions to the cell response. This model consisted of an equivalent circuit in which the different elements represent the different ionic/electronic processes within the material. By using this model in the MAPI cell measurements, the different elements lost their original meaning. This occurred because the measurements did not have an ionic influence as they were not measured below 200 Hz. But they also have two cycles, which gives them greater complexity than the part of the circuit that models electronic dynamics.

We conclude from this that while the model places great emphasis on modelling ion dynamics, it is not adequate for modelling the electronic component of the measurements. This component is modelled by a parallel RC which may be sufficient for the impedance of a simpler cell. But it is not enough for this type of cells in which more than one electronic process is visible. As future work, we could try to combine the ion model proposed here with the electron carrier balance model also presented in this thesis.

Modulated spectroscopy measurements for $CsPbBr_3$ showed a non-ideal cycle for the photocurrent, which can be attributed to a distribution of transport processes. Meanwhile, the photovoltage measurements present a more clear cycle dominated by a more ideal process. Once again, IMPS measurements have a higher resolution to the processes occurring in the cell, which is probably why they are so difficult to fit and interpret.

Finally, the IMVS measurements allow us to measure a ion related process in the low frequency limit. Something we had not been able to achieve before and was the original goal of the equivalent circuit model. This process prove to be slow and unobservable if the measurement do not go down to at least 10 Hz. This shows that ion dynamics can be important in low frequency regimes.

All cells showed that the IMVS measures are easier to model because they are dominated by one process, while the influence of several processes can be seen in the IMPS measurements.

7.3 General Conclusions

MAPI perovskite has shown to have many degradation mechanisms and some of then are still not easily solvable problems that make it unsuitable for commercial applications. On the other hand, $CsPbBr_3$ have better stability and have proven to be also a good absorber making it suitable for a tandem cell for example.

Besides this, perovskites have proven to have remarkable properties and its study has grown enormously from zero in less than eighteen years. In this time, perovskites devices have reach efficiencies comparable to the traditional Si solar cells. But they still lack the necessary stability for its technology spread over the world. The study of they properties even those with the lowest stability contribute to understanding then as a whole. The knowledge of the fast degradation ones, as MAPI, allows to extrapolate the degradation mechanisms and its consequences.

Here we have studied the excitonic origin of optical properties of MAPI but this is something transversal to perovskites. The quench of the photoluminescence observed because of the defects creation allow us to know more about excitons and also, it probably can be extrapolated to other perovskites.

We have contributed to the validation of a newly recycling process of Pb for MAPI optical grade synthesis and have tested several times and with different perovskites the viability of graphite as a contact material and also as a hole selective layer. Furthermore, applying graphite is much easier and cheaper than evaluating metals.

The spectral photo-response measurements proved to be quite challenging to interpret. This is probably why there are no studies of this type of measurement prior to 2017 in the analysed bibliography and in all cases, they are limited to analysing a portion of the frequency spectrum, either focusing on high-frequency electrons or low-frequency ions. This work attempted to study a wider frequency spectrum and for this purpose different models were implemented. This allowed us to conclude that IMPS measurements offer greater resolution regarding the different processes occurring in the material. Meanwhile, IMVS measurements indicate that they are dominated by one of these processes, the slower one. Also, we have seen that ions can have influence in the low frequency regime not only in impedance spectroscopy measurements but also in the intensity modulated ones.

Furthermore, we have been able to see two electronic processes in MAPI cell which were related to the electrons and holes dynamic. This is something unobservable in impedance spectroscopy because only one kind of carrier is injected in this measures. This demonstrates the value of intensity modulated spectroscopies. Clearly, although they proved to be difficult to interpret, they are a valuable source of information. And a tool to be applied in any perovskite device characterization, a task in which this work has certainly contributed.

Finally, this thesis lead to three peer reviewed publications, two as first author [32–34].

7.4 Perspectives

The study of perovskites still has a long way to go, and we hope to continue contributing to it. In this regard, the study of optical properties at low temperatures has shown that it can yield a great deal of knowledge, and this technique can be applied to other perovskites and materials in general that exhibit photoluminescence.

On the other hand, and continuing the international collaborations that led to this thesis, we hope to continue characterizing solar cells with perovskites. In the future, we will also investigate those synthesized with recycled *Pb*, looking for differences and similarities with those made with commercial *Pb*.

The modulated intensity measurements proved to be a window into the charges dynamics in perovskite cells and much remains to be done. New sets of cells would allow us to corroborate whether the two cycles observed in the measurements made on the MAPI cells are also observed in other cells with variations in the synthesis. In addition, measurements should be made reaching *mHz* to obtain more information on ionic dynamics. Although recognized for years, ion dynamics in perovskites has had few studies, and even fewer have been conducted using this intensity-modulated spectroscopic technique. A model that considers the ion balance within the cells can be developed in a similar way to that already used here for the electronic balance.

There is still many possible contributions to understand the lead halide perovskites dynamics and its degradation mechanisms in which we can contribute.

Bibliography

[1] Ying Jiang, Xiao Wang, and Anlian Pan. Properties of Excitons and Photogenerated Charge Carriers in Metal Halide Perovskites. *Advanced Materials*, 31(47):1806671, nov 2019.

[2] Henry J. Snaith. Present status and future prospects of perovskite photovoltaics. *Nature Materials*, 17(5):372–376, may 2018.

[3] Fabian Ruf. *Excitonic Effects and Bandgap Instabilities in Perovskite Solar Cells*. KIT Scientific Publishing, 2020.

[4] Akihiro Kojima, Kenjiro Teshima, Yasuo Shirai, and Tsutomu Miyasaka. Organometal Halide Perovskites as Visible-Light Sensitizers for Photovoltaic Cells. *Journal of the American Chemical Society*, 131(17):6050–6051, may 2009.

[5] Chuang Yang, Wenjing Hu, Jiale Liu, Chuanzhou Han, Qiaojiao Gao, Anyi Mei, Yinhua Zhou, Fengwan Guo, and Hongwei Han. Achievements, challenges, and future prospects for industrialization of perovskite solar cells. *Light: Science & Applications*, 13(1):227, 2024.

[6] Martin A Green. Photovoltaic technology and visions for the future. *Progress in Energy*, 1(1):013001, jul 2019.

[7] Martin A. Green and Anita Ho-Baillie. Perovskite Solar Cells: The Birth of a New Era in Photovoltaics. *ACS Energy Letters*, 2(4):822–830, apr 2017.

[8] Pabitra K. Nayak, Suhas Mahesh, Henry J. Snaith, and David Cahen. Photovoltaic solar cell technologies: analysing the state of the art. *Nature Reviews Materials*, 4(4):269–285, mar 2019.

[9] Stefaan De Wolf, Jakub Holovsky, Soo-Jin Moon, Philipp Löper, Bjoern Niesen, Martin Ledinsky, Franz-Josef Haug, Jun-Ho Yum, and Christophe Ballif. Organometallic halide perovskites: Sharp optical absorption edge and its relation to photovoltaic performance. *The Journal of Physical Chemistry Letters*, 5(6):1035–1039, 2014.

[10] Guichuan Xing, Nripan Mathews, Shuangyong Sun, Swee Sien Lim, Yeng Ming Lam, Michael Grätzel, Subodh Mhaisalkar, and Tze Chien Sum. Long-range balanced electron- and hole-transport lengths in organic-inorganic $CH_3NH_3PbI_3$. *Science*, 342(6156):344–347, 2013.

[11] Samuel D. Stranks, Giles E. Eperon, Giulia Grancini, Christopher Menelaou, Marcelo J. P. Alcocer, Tomas Leijtens, Laura M. Herz, Annamaria Petrozza, and Henry J. Snaith. Electron-hole diffusion lengths exceeding 1 micrometer in an organometal trihalide perovskite absorber. *Science*, 342(6156):341–344, 2013.

[12] Makhsud I. Saidaminov, Md Azimul Haque, Jawaher Almutlaq, Smritakshi Sarmah, Xiao-He Miao, Raihana Begum, Ayan A. Zhumekenov, Ibrahim Dursun, Namchul Cho, Banavoth Murali, Omar F. Mohammed, Tom Wu, and Osman M. Bakr. Inorganic lead halide perovskite single crystals: Phase-selective low-temperature growth, carrier transport properties, and self-powered photodetection. *Advanced Optical Materials*, 5(2):1600704, 2017.

[13] Joseph S. Manser, Jeffrey A. Christians, and Prashant V. Kamat. Intriguing optoelectronic properties of metal halide perovskites. *Chemical Reviews*, 116(21):12956–13008, 2016. Published: 2016/11/09.

[14] Chun-Ying Huang, Chen Zou, Chenyi Mao, Kathryn L. Corp, Yung-Chi Yao, Ya-Ju Lee, Cody W. Schlenker, Alex K. Y. Jen, and Lih Y. Lin. $CsPbBr_3$ Perovskite Quantum Dot Vertical Cavity Lasers with Low Threshold and High Stability. *ACS Photonics*, 4(9):2281–2289, sep 2017.

[15] Y. Xu, Q. Chen, C. Zhang, R. Wang, H. Wu, X. Zhang, G. Xing, W. W. Yu, X. Wang, Y. Zhang, and M. Xiao. Two-photon-pumped perovskite semiconductor nanocrystal lasers. *Journal of the American Chemical Society*, 138(11):3761–3768, 2016.

[16] H. Zhu, Y. Fu, F. Meng, X. Wu, Z. Gong, Q. Ding, M. V. Gustafsson, M. T. Trinh, S. Jin, and X. Y. Zhu. Lead halide perovskite nanowire lasers with low lasing thresholds and high quality factors. *Nature Materials*, 14(6):636–642, 2015.

[17] A. S. Polushkin, E. Y. Tiguntseva, A. P. Pushkarev, and S. V. Makarov. Single-particle perovskite lasers: From material properties to cavity design. *Nanophotonics*, 9(3):599–614, 2020.

[18] Xiaoli Zhang, Weigao Wang, Bing Xu, Sheng Liu, Haitao Dai, Dun Bian, Shuming Chen, Kai Wang, and Xiao Wei Sun. Thin film perovskite light-emitting diode based on $CsPbBr_3$ powders and interfacial engineering. *Nano Energy*, 37:40–45, jul 2017.

[19] X. Di, Z. Hu, J. Jiang, M. He, L. Zhou, W. Xiang, and X. Liang. Use of long-term stable $CsPbBr_3$ perovskite quantum dots in phospho-silicate glass for highly efficient white leds. *Chemical Communications*, 53(76):11068–11071, 2017.

[20] Tongtong Xuan, Shaoqiang Guo, Wenhao Bai, Tianliang Zhou, Le Wang, and Rong-Jun Xie. Ultrastable and highly efficient green-emitting perovskite quantum dot composites for Mini-LED displays or backlights. *Nano Energy*, 95:107003, may 2022.

[21] Z. Yao, C. Bi, A. Liu, M. Zhang, and J. Tian. High brightness and stability pure-blue perovskite light-emitting diodes based on a novel structural quantum-dot film. *Nano Energy*, 95:106974, 2022.

[22] J. Yu, X. Chen, Y. Wang, H. Zhou, M. Xue, Y. Xu, Z. Li, C. Ye, J. Zhang, P. A. van Aken, P. D. Lund, and H. Wang. A High-Performance Self-Powered Broadband Photodetector Based on a $CH_3NH_3PbI_3$ Perovskite/ZnO Nanorod Array Heterostructure. *Journal of Materials Chemistry C*, 4(32):7302–7308, 2016.

[23] L. F. Gao, W. J. Luo, Y. F. Yao, and Z. G. Zou. An all-inorganic lead halide perovskite-based photocathode for stable water reduction. *Chemical Communications*, 54(83):11459–11462, 2018.

[24] S. Nam, C. T. K. Mai, and I. Oh. Ultrastable photoelectrodes for solar water splitting based on organic metal halide perovskite fabricated by

lift-off process. *ACS Applied Materials & Interfaces*, 10(17):14659–14665, 2018.

[25] D. Cardenas-Morcoso, A. F. Gualdrón-Reyes, A. B. F. Vitoreti, M. García-Tecedor, S. J. Yoon, M. S. de la Fuente, I. Mora-Seró, and S. Gimenez. Photocatalytic and photoelectrochemical degradation of organic compounds with all-inorganic metal halide perovskite quantum dots. *The Journal of Physical Chemistry Letters*, 10(3):630–636, 2019.

[26] P. Roy, N. K. Sinha, S. Tiwari, and A. Khare. A review on perovskite solar cells: Evolution of architecture, fabrication techniques, commercialization issues and status. *Solar Energy*, 198:665–690, 2020.

[27] I. Spanopoulos, W. Ke, and M. G. Kanatzidis. In quest of environmentally stable perovskite solar cells: A perspective. *Helvetica Chimica Acta*, 104:e2000173, 2021.

[28] N. K. Noel, S. D. Stranks, A. Abate, C. Wehrenfennig, S. Guarnera, A.-A. Haghighirad, A. Sadhanala, G. E. Eperon, S. K. Pathak, and M. B. Johnston. Lead-free organic–inorganic tin halide perovskites for photovoltaic applications. *Energy & Environmental Science*, 7(9):3061–3068, 2014.

[29] A. Babayigit, A. Ethirajan, M. Muller, and B. Conings. Toxicity of organometal halide perovskite solar cells. *Nature Materials*, 15(3):247–251, 2016.

[30] X. Li, F. Zhang, H. He, J. J. Berry, K. Zhu, and T. Xu. On-device lead sequestration for perovskite solar cells. *Nature*, 578:555–560, 2020.

[31] W. Ke and M. G. Kanatzidis. Prospects for low-toxicity lead-free perovskite solar cells. *Nature Communications*, 10:965, 2019.

[32] Mariana Berruet, Matías A. Córdoba, Enzo L. Spera, Ricardo E. Marotti, Javier C. Pereyra, Analía V. Monti, and Kurt R. Taretto. Sustainable up-cycling of lead-acid battery waste for hybrid perovskite solar cells. *MRS Energy & Sustainability*, 11(2):606–615, 2024.

[33] Enzo L. Spera, Carlos J. Pereyra, Daniel L. Gau, Mariana Berruet, and Ricardo E. Marotti. Excitonic optical properties of $CH_3NH_3PbI_3$ per-

ovskite and its dependence with temperature. *MRS Advances*, 9(2):39–44, jul 2023.

[34] Enzo L. Spera, Carlos J. Pereyra, Daniel L. Gau, Mariana Berruet, and Ricardo E. Marotti. Temperature dependent optical properties of methylammonium lead iodine perovskite: Influence of the initial degradation process. *Journal of Alloys and Compounds*, 1027:180553, 2025.

[35] Enzo L Spera, Carlos J Pereyra, Yesica Di Iorio, Mariana Berruet, Marcela Vazquez, and Ricardo E Marotti. Charge dynamics in $CuInS_2$ photovoltaic devices with In_2S_3 as buffer layer. *Materials Chemistry and Physics*, 282:125871, apr 2022.

[36] Leunam Fernandez-Izquierdo, Enzo Luigi Spera, Boris Durán, Ricardo Enrique Marotti, Enrique Ariel Dalchiele, Rodrigo del Rio, and Samuel A. Hevia. CVD Growth of Hematite Thin Films for Photoelectrochemical Water Splitting: Effect of Precursor-Substrate Distance on Their Final Properties. *Molecules*, 28(4):1954, feb 2023.

[37] Monique Combescot and Shiue-Yuan Shiau. *Excitons and Cooper Pairs*. Oxford University Press, dec 2015.

[38] Mark Fox. *Optical Properties of Solids*. Oxford, 2010.

[39] M Cardona and P Y Yu. *Fundamentals of Semiconductors*. Springer, 2010.

[40] R J Elliott. Intensity of Optical Absorption by Excitons. *Phys. Rev.*, 108(6):1384–1389, 1957.

[41] E. M. Lifshitz L. D. Landau. *Quantum mechanics: non-relativistic theory Volume 3*. Course on Theoretical Physics, Vol 3. Pergamon Pr, 3 edition, 1981.

[42] O Stenzel. *The Physics of Thin Film Optical Spectra*. Springer, 2016.

[43] Y. Toyozawa. Interband effect of lattice vibrations in the exciton absorption spectra. *Journal of Physics and Chemistry of Solids*, 25(1):59–71, 1964.

[44] S. Rudin, T. L. Reinecke, and B. Segall. Temperature-dependent exciton linewidths in semiconductors. *Physical Review B*, 42(17):11218–11231, dec 1990.

[45] Massimo Gurioli, Anna Vinattieri, Juan Martinez-Pastor, and Marcello Colocci. Exciton thermalization in quantum-well structures. *Physical Review B*, 50(16):11817–11826, oct 1994.

[46] J. Humlíček, E. Schmidt, L. Bočánek, R. Švehla, and K. Ploog. Exciton line shapes of GaAs/AlAs multiple quantum wells. *Phys. Rev. B*, 48:5241–5248, Aug 1993.

[47] XA Cao, SF LeBoeuf, LB Rowland, CH Yan, and H Liu. Temperature-dependent emission intensity and energy shift in InGaN/GaN multiple-quantum-well light-emitting diodes. *Applied Physics Letters*, 82(21):3614–3616, 2003.

[48] S. Sanguinetti, M. Henini, M. Grassi Alessi, M. Capizzi, P. Frigeri, and S. Franchi. Carrier thermal escape and retrapping in self-assembled quantum dots. *Phys. Rev. B*, 60:8276–8283, Sep 1999.

[49] Z.Y. Xu, Z.D. Lu, Z.L. Yuan, X.P. Yang, B.Z. Zheng, J.Z. Xu, W.K. Ge, Y. Wang, J. Wang, and L.L. Chang. Thermal activation and thermal transfer of localized excitons in InAs self-organized quantum dots. *Superlattices and Microstructures*, 23(2):381–387, 1998.

[50] Q. Li, S. J. Xu, M. H. Xie, and S. Y. Tong. A model for steady-state luminescence of localized-state ensemble. *Europhysics Letters*, 71(6):994, aug 2005.

[51] Q Li, SJ Xu, WC Cheng, MH Xie, SY Tong, CM Che, and H Yang. Thermal redistribution of localized excitons and its effect on the luminescence band in ingan ternary alloys. *Applied Physics Letters*, 79(12):1810–1812, 2001.

[52] Yatendra Pal Varshni. Temperature dependence of the energy gap in semiconductors. *physica*, 34(1):149–154, 1967.

[53] PG Eliseev. The red σ^2/K_BT spectral shift in partially disordered semiconductors. *Journal of applied physics*, 93(9):5404–5415, 2003.

[54] Hitoshi Sumi and Yutaka Toyozawa. Urbach-martienseen rule and exciton trapped momentarily by lattice vibrations. *Journal of the Physical Society of Japan*, 31(2):342–358, 1971.

[55] Shivam Singh, Cheng Li, Fabian Panzer, K. L. Narasimhan, Anna Graeser, Tanaji P. Gujar, Anna Köhler, Mukundan Thelakkat, Sven Huettner, and Dinesh Kabra. Effect of Thermal and Structural Disorder on the Electronic Structure of Hybrid Perovskite Semiconductor $CH_3NH_3PbI_3$. *The Journal of Physical Chemistry Letters*, 7(15):3014–3021, aug 2016.

[56] Stefan Zeiske, Oskar J. Sandberg, Nasim Zarrabi, Christian M. Wolff, Meysam Raoufi, Francisco Peña-Camargo, Emilio Gutierrez-Partida, Paul Meredith, Martin Stolterfoht, and Ardalan Armin. Static Disorder in Lead Halide Perovskites. *The Journal of Physical Chemistry Letters*, 13(31):7280–7285, aug 2022.

[57] Franz Urbach. The long-wavelength edge of photographic sensitivity and of the electronic absorption of solids. *Phys. Rev.*, 92:1324–1324, Dec 1953.

[58] Werner Martienssen. Über die excitonenbanden der alkalihalogenidkristalle. *Journal of Physics and Chemistry of Solids*, 2(4):257–267, 1957.

[59] B. Segall. Optical absorption edge in cdte: Theoretical. *Phys. Rev.*, 150:734–747, Oct 1966.

[60] M. N. Kabler. Low-temperature recombination luminescence in alkali halide crystals. *Phys. Rev.*, 136:A1296–A1302, Nov 1964.

[61] Kikuo Cho and Yutaka Toyozawa. Exciton-phonon interaction and optical spectra –self-trapping, zero-phonon line and phonon sidebands–. *Journal of the Physical Society of Japan*, 30(6):1555–1574, 1971.

[62] Wolfgang Tress. Metal halide perovskites as mixed electronic–ionic conductors: Challenges and opportunities—from hysteresis to memristivity. *The Journal of Physical Chemistry Letters*, 8(13):3106–3114, 2017. PMID: 28641009.

[63] Luca Bertoluzzi, Caleb C. Boyd, Nicholas Rolston, Jixian Xu, Rohit Prasanna, Brian C. O'Regan, and Michael D. McGehee. Mobile ion concentration measurement and open-access band diagram simulation platform for halide perovskite solar cells. *Joule*, 4:109–127, 1 2020.

[64] Rebecca A. Belisle, William H. Nguyen, Andrea R. Bowring, Philip Calado, Xiaoe Li, Stuart J. C. Irvine, Michael D. McGehee, Piers R. F. Barnes, and Brian C. O'Regan. Interpretation of inverted photocurrent transients in organic lead halide perovskite solar cells: proof of the field screening by mobile ions and determination of the space charge layer widths. *Energy Environ. Sci.*, 10:192–204, 2017.

[65] Luca Bertoluzzi, Rebecca A. Belisle, Kevin A. Bush, Rongrong Cheacharoen, Michael D. McGehee, and Brian C. O'Regan. In Situ Measurement of Electric-Field Screening in Hysteresis-Free $PTAA/FA_{0.83}Cs_{0.17}Pb(I_{0.83}Br_{0.17})_3/C_{60}$ Perovskite Solar Cells Gives an Ion Mobility of $\sim$ 310–$7cm2/(Vs)$, 2 Orders of Magnitude Faster than Reported for Metal-Oxide-Contacted Perovskite Cells with Hysteresis. *Journal of the American Chemical Society*, 140(40):12775–12784, 2018. PMID: 30189142.

[66] Andrea R. Bowring, Luca Bertoluzzi, Brian C. O'Regan, and Michael D. McGehee. Reverse bias behavior of halide perovskite solar cells. *Advanced Energy Materials*, 8(8):1702365, 2018.

[67] Stefan A. L. Weber, Ilka M. Hermes, Silver-Hamill Turren-Cruz, Christopher Gort, Victor W. Bergmann, Laurent Gilson, Anders Hagfeldt, Michael Graetzel, Wolfgang Tress, and Rüdiger Berger. How the formation of interfacial charge causes hysteresis in perovskite solar cells. *Energy Environ. Sci.*, 11:2404–2413, 2018.

[68] Tae-Youl Yang, Giuliano Gregori, Norman Pellet, Michael Grätzel, and Joachim Maier. The significance of ion conduction in a hybrid organic–inorganic lead-iodide-based perovskite photosensitizer. *Angewandte Chemie International Edition*, 54(27):7905–7910, 2015.

[69] Gee Yeong Kim, Alessandro Senocrate, Tae-Youl Yang, Giuliano Gregori, Michael Grätzel, and Joachim Maier. Large tunable photoeffect on

ion conduction in halide perovskites and implications for photodecomposition. *Nature Materials*, 17(5):445–449, 2018.

[70] Giles Richardson, Simon E. J. O'Kane, Ralf G. Niemann, Timo A. Peltola, Jamie M. Foster, Petra J. Cameron, and Alison B. Walker. Can slow-moving ions explain hysteresis in the current–voltage curves of perovskite solar cells? *Energy Environ. Sci.*, 9:1476–1485, 2016.

[71] Simon E. J. O'Kane, Giles Richardson, Adam Pockett, Ralf G. Niemann, James M. Cave, Nobuya Sakai, Giles E. Eperon, Henry J. Snaith, Jamie M. Foster, Petra J. Cameron, and Alison B. Walker. Measurement and modelling of dark current decay transients in perovskite solar cells. *J. Mater. Chem. C*, 5:452–462, 2017.

[72] N. E. Courtier, J. M. Foster, S. E. J. O'kane, A. B. Walker, and G. Richarson. Systematic derivation of a surface polarisation model for planar perovskite solar cells. *European Journal of Applied Mathematics*, 30(3):427–457, 2019.

[73] Nicola E. Courtier, James M. Cave, Jamie M. Foster, Alison B. Walker, and Giles Richardson. How transport layer properties affect perovskite solar cell performance: insights from a coupled charge transport/ion migration model. *Energy Environ. Sci.*, 12:396–409, 2019.

[74] Susanne T. Birkhold, Jake T. Precht, Rajiv Giridharagopal, Giles E. Eperon, Lukas Schmidt-Mende, and David S. Ginger. Direct observation and quantitative analysis of mobile frenkel defects in metal halide perovskites using scanning kelvin probe microscopy. *The Journal of Physical Chemistry C*, 122(24):12633–12639, 2018.

[75] M. Parans Paranthaman, Winnie Wong-Ng, and Raghu N. Bhattacharya. *Semiconductor Materials for Solar Photovoltaic Cells.* Springer, 2016.

[76] Chunfu Zhang, Jincheng Zhang, Yue Hao, Zhenhua Lin, and Chunxiang Zhu. A simple and efficient solar cell parameter extraction method from a single current-voltage curve. *Journal of Applied Physics*, 110(6):064504, sep 2011.

[77] R. Tamrakar and A. Gupta. A review: extraction of solar cell modelling parameters. *International journal of innovative research in electrical, electronics, instrumentation and control engineering*, 3:55–60, 2015.

[78] C. Sah, R. Noyce, and W. Shockley. Carrier generation and recombination in p-n junctions and p-n junction characteristics. *IEEE*, 45:1228–1243, 1957.

[79] J. Shah, Y. L. Li, T. Gessmann, and E. F. Schubert. Experimental analysis and theoretical model for anomalously high ideality factors ($n \gg 2$) in $AlGaN/GaN$ p-n junction diodes. *Journal of Applied Physics*, 94:2627–2630, 2003.

[80] David Kiermasch, Andreas Baumann, Mathias Fischer, Vladimir Dyakonov, and Kristofer Tvingstedt. Revisiting lifetimes from transient electrical characterization of thin film solar cells; a capacitive concern evaluated for silicon, organic and perovskite devices. *Energy & Environmental Science*, 11(3):629–640, 2018.

[81] G Schlichthörl, N G Park, and A. J. Frank. Evaluation of the Charge-Collection Efficiency of Dye-Sensitized Nanocrystalline TiO_2 Solar Cells. *The Journal of Physical Chemistry B*, 103(5):782–791, feb 1999.

[82] Juan Bisquert. Theory of the impedance of electron diffusion and recombination in a thin layer. *The Journal of Physical Chemistry B*, 106(2):325–333, 2002.

[83] L Dloczik, O Ileperuma, I Lauermann, L M Peter, E A Ponomarev, G Redmond, N J Shaw, and I Uhlendorf. Dynamic Response of Dye-Sensitized Nanocrystalline Solar Cells: Characterization by Intensity-Modulated Photocurrent Spectroscopy. *The Journal of Physical Chemistry B*, 101(49):10281–10289, dec 1997.

[84] Sandheep Ravishankar, Antonio Riquelme, Shaibal K. Sarkar, Marisé Garcia-Batlle, Germà Garcia-Belmonte, and Juan Bisquert. Intensity-modulated photocurrent spectroscopy and its application to perovskite solar cells. *The Journal of Physical Chemistry C*, 123(41):24995–25014, 2019.

[85] Agustín Bou, Haralds Abolins, Arjun Ashoka, Héctor Cruanyes, Antonio Guerrero, Felix Deschler, and Juan Bisquert. Extracting in situ charge carrier diffusion parameters in perovskite solar cells with light modulated techniques. *ACS Energy Letters*, 6(6):2248–2255, 2021. PMID: 34778561.

[86] Juan Bisquert and Mathijs Janssen. From Frequency Domain to Time Transient Methods for Halide Perovskite Solar Cells: The Connections of IMPS, IMVS, TPC, and TPV. *The Journal of Physical Chemistry Letters*, 12(33):7964–7971, aug 2021.

[87] Daniel L Gau, Isabel Galain, Ivana Aguiar, and Ricardo E Marotti. Origin of photoluminescence and experimental determination of exciton binding energy, exciton-phonon interaction, and urbach energy in $\gamma - CsPbI_3$ nanoparticles. *Journal of Luminescence*, 257:119765, 2023.

[88] Jarvist M. Frost and Aron Walsh. What is moving in hybrid halide perovskite solar cells? *Accounts of Chemical Research*, 49(3):528–535, 2016. PMID: 26859250.

[89] Valerio D'Innocenzo, Giulia Grancini, Marcelo J. P. Alcocer, Ajay Ram Srimath Kandada, Samuel D. Stranks, Michael M. Lee, Guglielmo Lanzani, Henry J. Snaith, and Annamaria Petrozza. Excitons versus free charges in organo-lead tri-halide perovskites. *Nature Communications*, 5(1):3586, apr 2014.

[90] Fabian Ruf, Meltem F. Aygüler, Nadja Giesbrecht, Bettina Rendenbach, Alice Magin, Pablo Docampo, Heinz Kalt, and Michael Hetterich. Temperature-dependent studies of exciton binding energy and phase-transition suppression in $(Cs, FA, MA)Pb(I, Br)_3$ perovskites. *APL Materials*, 7(3):031113, mar 2019.

[91] Adrián Francisco-López, Bethan Charles, Oliver J. Weber, M. Isabel Alonso, Miquel Garriga, Mariano Campoy-Quiles, Mark T. Weller, and Alejandro R. Goñi. Equal Footing of Thermal Expansion and Electron–Phonon Interaction in the Temperature Dependence of Lead Halide Perovskite Band Gaps. *The Journal of Physical Chemistry Letters*, 10(11):2971–2977, jun 2019.

[92] Daniel L. Gau, Daniel Ramírez, Gonzalo Riveros, Patricia Díaz, Javier Verdugo, Gerard Núñez, Susy Lizama, Pamela Lazo, Enrique A.

Dalchiele, and Ricardo E. Marotti. Excitonic origin of the optical properties of $CsPbBr_3$. *Optical Materials*, 157:116316, 2024.

[93] Adam D Wright, Carla Verdi, Rebecca L Milot, Giles E Eperon, Miguel A Pérez-Osorio, Henry J Snaith, Feliciano Giustino, Michael B Johnston, and Laura M Herz. Electron–phonon coupling in hybrid lead halide perovskites. *Nature Communications*, 7(1):11755, 2016.

[94] Jinli Yang, Braden D. Siempelkamp, Dianyi Liu, and Timothy L. Kelly. Investigation of $CH_3NH_3PbI_3$ Degradation Rates and Mechanisms in Controlled Humidity Environments Using in Situ Techniques. *ACS Nano*, 9(2):1955–1963, feb 2015.

[95] Norbert H. Nickel, Felix Lang, Victor V. Brus, Oleksandra Shargaieva, and Jörg Rappich. Unraveling the Light-Induced Degradation Mechanisms of $CH_3NH_3PbI_3$ Perovskite Films. *Advanced Electronic Materials*, 3(12), dec 2017.

[96] Qiu-Ming Hong, Rui-Peng Xu, Teng-Yu Jin, Jian-Xin Tang, and Yan-Qing Li. Unraveling the light-induced degradation mechanism of $CH_3NH_3PbI_3$ perovskite films. *Organic Electronics*, 67:19–25, apr 2019.

[97] Jing Wei, Qiuwen Wang, Jiangding Huo, Feng Gao, Zhenyu Gan, Qing Zhao, and Hongbo Li. Mechanisms and Suppression of Photoinduced Degradation in Perovskite Solar Cells. *Advanced Energy Materials*, 11(3), jan 2021.

[98] Karlheinz Seeger. *Semiconductor Physics: An Introduction*, volume 40 of *Springer Series in Solid-State Sciences*. Springer, Berlin, Heidelberg, 7th edition, 1997.

[99] Rinku Saran, Amelie Heuer-Jungemann, Antonios G. Kanaras, and Richard J. Curry. Giant Bandgap Renormalization and Exciton–Phonon Scattering in Perovskite Nanocrystals. *Advanced Optical Materials*, 5(17), sep 2017.

[100] Daniel L. Gau, Daniel Ramírez, Fernando Iikawa, Gonzalo Riveros, Patricia Díaz, Javier Verdugo, Gerard Núñez, Susy Lizama, Pamela Lazo, Enrique A. Dalchiele, Lidia Contreras, Jesús Idigoras, Juan Anta, and

Ricardo E. Marotti. Photophysical and Photoelectrochemical Properties of $CsPbBr_3$ Films Grown by Electrochemically Assisted Deposition. *ChemPhysChem*, 23(19), oct 2022.

[101] X B Zhang, T Taliercio, S Kolliakos, and P Lefebvre. Influence of electron-phonon interaction on the optical properties of III nitride semiconductors. *Journal of Physics: Condensed Matter*, 13(32):7053–7074, aug 2001.

[102] Maksym V. Kovalenko, Loredana Protesescu, and Maryna I. Bodnarchuk. Properties and potential optoelectronic applications of lead halide perovskite nanocrystals. *Science*, 358(6364):745–750, nov 2017.

[103] Xiangzhou Lao, Zhi Yang, Zhicheng Su, Zilan Wang, Honggang Ye, Minqiang Wang, Xi Yao, and Shijie Xu. Luminescence and thermal behaviors of free and trapped excitons in cesium lead halide perovskite nanosheets. *Nanoscale*, 10(21):9949–9956, 2018.

[104] G. D. Cody, T. Tiedje, B. Abeles, B. Brooks, and Y. Goldstein. Disorder and the Optical-Absorption Edge of Hydrogenated Amorphous Silicon. *Physical Review Letters*, 47(20):1480–1483, nov 1981.

[105] S. Cacovich, L. Ciná, F. Matteocci, G. Divitini, P. A. Midgley, A. Di Carlo, and C. Ducati. Gold and iodine diffusion in large area perovskite solar cells under illumination. *Nanoscale*, 9:4700–4706, 2017.

[106] Kyle M Fransishyn, Soumya Kundu, and Timothy Kelly. Elucidating the failure mechanisms of perovskite solar cells in humid environments using in situ grazing-incidence wide-angle x-ray scattering. *ACS Energy Letters*, 3(9):2127–2133, aug 2018.

[107] Soumya Kundu and Timothy L. Kelly. In situ studies of the degradation mechanisms of perovskite solar cells. *EcoMat*, 2(2), jun 2020.

[108] Jay M. Shah, Y.-L. Li, Th. Gessmann, and E F Schubert. Experimental analysis and theoretical model for anomalously high ideality factors (n¿¿2.0) in AlGaN/GaN p-n junction diodes. *Journal of Applied Physics*, 94(4):2627–2630, aug 2003.

[109] Jérémie Werner, Guy Dubuis, Arnaud Walter, Philipp Löper, Soo-Jin Moon, Sylvain Nicolay, Monica Morales-Masis, Stefaan De Wolf, Bjoern Niesen, and Christophe Ballif. Sputtered rear electrode with broadband transparency for perovskite solar cells. *Solar Energy Materials and Solar Cells*, 141:407–413, 2015.

[110] Rebecca Saive. S-Shaped Current–Voltage Characteristics in Solar Cells: A Review. *IEEE Journal of Photovoltaics*, 9(6):1477–1484, nov 2019.

[111] Yuanhang Cheng, Ho-Wa Li, Jinfeng Zhang, Qing-Dan Yang, Taili Liu, Zhiqiang Guan, Jian Qing, Chun-Sing Lee, and Sai-Wing Tsang. Spectroscopic study on the impact of methylammonium iodide loading time on the electronic properties in perovskite thin films. *J. Mater. Chem. A*, 4:561–567, 2016.

[112] X L.CHEN, Y M ZHANG, J F WAN, J L DU, Z L ZHAO, and G.WANG. Synthesis of chalcopyrite $CuInSe_2$(CIS) nanosheets using vitamin C as an adjuvant and photoelectric properties of cis thin films. *Chalcogenide Letters*, 17(12):593–603, 2020.

[113] Sean P. Dunfield, Lyle Bliss, Fei Zhang, Joseph M. Luther, Kai Zhu, Maikel F. A. M. van Hest, Matthew O. Reese, and Joseph J. Berry. From Defects to Degradation: A Mechanistic Understanding of Degradation in Perovskite Solar Cell Devices and Modules. *Advanced Energy Materials*, 10(26), jul 2020.

[114] Ranran Liu, Li Wang, Yingping Fan, Zhipeng Li, and Shuping Pang. Uv degradation of the interface between perovskites and the electron transport layer. *RSC Adv.*, 10:11551–11556, 2020.

[115] Tomas Leijtens, Giles E. Eperon, Sandeep Pathak, Antonio Abate, Michael M. Lee, and Henry J. Snaith. Overcoming ultraviolet light instability of sensitized TiO_2 with meso-superstructured organometal trihalide perovskite solar cells. *Nature Communications*, 4(1):2885, 2013.

[116] Seigo Ito, Soichiro Tanaka, Kyohei Manabe, and Hitoshi Nishino. Effects of Surface Blocking Layer of Sb_2S_3 on Nanocrystalline TiO_2 for $CH_3NH_3PbI_3$ Perovskite Solar Cells. *The Journal of Physical Chemistry C*, 118(30):16995–17000, 2014.

[117] Wenzhe Li, Jiangwei Li, Guangda Niu, and Liduo Wang. Effect of cesium chloride modification on the film morphology and uv-induced stability of planar perovskite solar cells. *J. Mater. Chem. A*, 4:11688–11695, 2016.

[118] Jun Ji, Xin Liu, Haoran Jiang, Mingjun Duan, Benyu Liu, Hao Huang, Dong Wei, Yingfeng Li, and Meicheng Li. Two-stage ultraviolet degradation of perovskite solar cells induced by the oxygen vacancy-Ti^{4+} states. *iScience*, 23(4):101013, 2020.

[119] Tian Chen, Jiangsheng Xie, and Pingqi Gao. Ultraviolet photocatalytic degradation of perovskite solar cells: Progress, challenges, and strategies. *Advanced Energy and Sustainability Research*, 3(6):2100218, 2022.

[120] BioLogic Science Instruments. Equivalent model of an electrochemical cell including the reference electrode impedance and the potentiostat parasitics. `https://www.google.com/url?sa=t&source=web&rct=j&opi=89978449&url=https://www.biologic.net/wp-content/uploads/2019/08/battery-eis-artifacts-precautions_electrochemistry-an44.pdf&ved=2ahUKEwjUk9aK2cuNAxXNrJUCHasvDjIQFnoECBUQAQ&usg=AOvVaw0PAc_MI4kzGn7O8jty5Kmd`, 2013. Application Note No. 44, Nombre del equipo o serie.

[121] Sandheep Ravishankar, Osbel Almora, Carlos Echeverría-Arrondo, Elnaz Ghahremanirad, Clara Aranda, Antonio Guerrero, Francisco Fabregat-Santiago, Arie Zaban, Germà Garcia-Belmonte, and Juan Bisquert. Surface polarization model for the dynamic hysteresis of perovskite solar cells. *The Journal of Physical Chemistry Letters*, 8(5):915–921, 2017.

[122] Elnaz Ghahremanirad, Agustín Bou, Saeed Olyaee, and Juan Bisquert. Inductive loop in the impedance response of perovskite solar cells explained by surface polarization model. *The Journal of Physical Chemistry Letters*, 8(7):1402–1406, 2017.

[123] Enrique H. Balaguera and Juan Bisquert. Mapping of internal ionic/electronic transient dynamics in current–voltage operation of perovskite solar cells. *Small*, 21(2):2409534, 2025.

[124] Enrique H. Balaguera and Juan Bisquert. Accelerating the assessment of hysteresis in perovskite solar cells. *ACS Energy Letters*, 9(2):478–486, 2024.

[125] Juan Bisquert and Antonio Guerrero. Chemical inductor. *Journal of the American Chemical Society*, 144(13):5996–6009, 2022. Published: 2022-04-06.

[126] Rafael S. Sanchez, Victoria Gonzalez-Pedro, Jin-Wook Lee, Nam-Gyu Park, Yong Soo Kang, Ivan Mora-Sero, and Juan Bisquert. Slow dynamic processes in lead halide perovskite solar cells. characteristic times and hysteresis. *The Journal of Physical Chemistry Letters*, 5(13):2357–2363, 2014. Published on July 3, 2014.

[127] Hongxia Wang, Antonio Guerrero, Agustín Bou, Abdullah M. Al-Mayouf, and Juan Bisquert. Kinetic and material properties of interfaces governing slow response and long timescale phenomena in perovskite solar cells. *Energy Environ. Sci.*, 12:2054–2079, 2019.

[128] Firouzeh Ebadi, Nima Taghavinia, Raheleh Mohammadpour, Anders Hagfeldt, and Wolfgang Tress. Origin of apparent light-enhanced and negative capacitance in perovskite solar cells. *Nature Communications*, 10(1):1574, 2019.

[129] Juan Bisquert. Electrical charge coupling dominates the hysteresis effect of halide perovskite devices. *The Journal of Physical Chemistry Letters*, 14(4):1014–1021, 2023.

[130] Cedric Gonzales, Antonio Guerrero, and Juan Bisquert. Transition from capacitive to inductive hysteresis: A neuron-style model to correlate i–v curves to impedances of metal halide perovskites. *The Journal of Physical Chemistry C*, 126(32):13560–13578, 2022. Published on August 18, 2022.

[131] Paolo Umari, Edoardo Mosconi, and Filippo De Angelis. Relativistic GW calculations on $CH_3NH_3PbI_3$ and $CH_3NH_3SnI_3$ Perovskites for Solar Cell Applications. *Scientific Reports*, 4(1):4467, 2014.

[132] Krzysztof Galkowski, Anatolie Mitioglu, Atsuhiko Miyata, Paulina Plochocka, Oliver Portugall, Giles E. Eperon, Jacob Tse-Wei Wang, Thomas

Stergiopoulos, Samuel D. Stranks, Henry J. Snaith, and Robin J. Nicholas. Determination of the exciton binding energy and effective masses for methylammonium and formamidinium lead tri-halide perovskite semiconductors. *Energy Environ. Sci.*, 9:962–970, 2016.

[133] I. Sankara, S. Ouédraogo, D. Oubda, B. Traoré, M. Kébré, A. Zongo, and F. Zougmoré. Influence of defect density, band gap discontinuity and electron mobility on the performance of perovskite solar cells. *Advances in Materials Physics and Chemistry*, 13:151–160, 2023.

[134] Saad Ullah, Jiaming Wang, Peixin Yang, Linlin Liu, Shi-E. Yang, Tianyu Xia, Haizhong Guo, and Yongsheng Chen. All-inorganic CsPbBr 3 perovskite: a promising choice for photovoltaics. *Materials Advances*, 2(2):646–683, 2021.

[135] Daniel Ramírez, Gonzalo Riveros, Patricia Díaz, Javier Verdugo, Gerard Núñez, Susy Lizama, Pamela Lazo, Enrique A. Dalchiele, Daniel L. Gau, Ricardo E. Marotti, Juan A. Anta, Lidia Contreras-Bernal, Antonio Riquelme, and Jesús Idigoras. Electrochemically assisted growth of $cspbbr_3$-based solar cells without selective contacts. *ChemElectroChem*, 7(19):3961–3968, 2020.

[136] Loredana Protesescu, Sergii Yakunin, Maryna I. Bodnarchuk, Franziska Krieg, Riccarda Caputo, Christopher H. Hendon, Ruo Xi Yang, Aron Walsh, and Maksym V. Kovalenko. Nanocrystals of Cesium Lead Halide Perovskites ($CsPbX_3$, X = Cl, Br, and I): Novel Optoelectronic Materials Showing Bright Emission with Wide Color Gamut. *Nano Letters*, 15(6):3692–3696, 2015.

[137] D. Fröhlich, K. Heidrich, H. Künzel, G. Trendel, and J. Treusch. Cesium-trihalogen-plumbates a new class of ionic semiconductors. *Journal of Luminescence*, 18-19:385–388, 1979.

[138] Mark E. Orazem and Bernard Tribollet. *Electrochemical Impedance Spectroscopy.* John Wiley & Sons, Inc., Hoboken, NJ, USA, 2008.

[139] William Shockley and Hans J Queisser. Detailed Balance Limit of Efficiency of p-n Junction Solar Cells. *Journal of Applied Physics*, 32(3):510–519, mar 1961.

[140] Bernard Sapoval and Claudine Hermann. *Physics of Semiconductors.* Springer-Verlag, New York, 1993.

APPENDIX

Appendix A

Dynamics of a Bloch Electron

The Bloch functions are the solutions to the Schrödinger equation for the electrons taking into account the crystal potential. These functions have the shape:

$$\psi_{n,k}(\vec{r}) = e^{i\vec{k}\cdot\vec{r}} u_{n,k}(\vec{r}) \tag{A.1}$$

with $u_{n,k}(\vec{r})$ having the periodicity of the potential [140]. Lets notice that the wave vector $\vec{k}$ introduced by the Bloch function is a quantum number with three components which is not related in a simple way to the momentum operator $\vec{p} = -i\hbar\nabla$, unlike in the case of plane waves. That would be the case, for example with a constant potential for the crystal. In that case the solution to the Schrödinger equation would be a plane wave function like:

$$\psi_k(\vec{r}) = Ce^{i\vec{k}\cdot\vec{r}} \tag{A.2}$$

with C a normalization constant. In that case, the mean momentum would be:

$$\vec{p}\psi_k(\vec{r}) = -i\hbar\nabla\left(Ce^{i\vec{k}\cdot\vec{r}}\right) = \hbar\vec{k}\psi_k(\vec{r}) \tag{A.3}$$

But for Bloch functions:

$$\begin{aligned}
\langle \vec{p}_{n,k} \rangle &= \left\langle n, \vec{k} \middle| \vec{p} \middle| n, \vec{k} \right\rangle \\
&= \int \psi^*_{n,k}(\vec{r}) \left(-i\hbar\nabla \right) \psi_{n,k}(\vec{r}) dr^3 \\
&= \int u^*_{n,k}(\vec{r}) \left(\hbar\vec{k} - i\hbar\nabla \right) u_{n,k}(\vec{r}) dr^3 \\
&= \hbar\vec{k} - i\hbar \int n^*_{n,k}(\vec{r}) \nabla n_{n,k}(\vec{r}) dr^3 \\
&\neq \hbar\vec{k}
\end{aligned} \tag{A.4}$$

In a crystal there is no simple relation between the mean value of the momentum in a Bloch state and the wave vector $\vec{k}$ which defines the state. However the vector $\hbar\vec{k}$ plays a very important role. We call this vector the crystal momentum.

A.1 Group Velocity

Lets see that the mean value of the momentum is related in a simple manner to the behavior of the dispersion relations of the energy bands $E_n(\vec{k})$. Using a first-order Taylor series we write the energy at the point $\vec{k} + \vec{q}$ as:

$$E_n(\vec{k} + \vec{q}) = E_n(\vec{k}) + \vec{q} \cdot \nabla_k E_n(\vec{k}) + ... \tag{A.5}$$

this second term can be calculated by perturbation theory. Now, the hamiltonian that the bloch functions are eigestates is

$$H_k = \frac{1}{2m} \left(\hbar\vec{k} - i\hbar\nabla \right)^2 + V(\vec{r}) \tag{A.6}$$

Similarly, at the point $\vec{k} + \vec{q}$ it will be

$$H_{k+q} = H_k + \vec{q} \cdot \frac{\hbar^2}{2m} \left(\vec{k} - i\nabla \right) + \frac{\hbar^2 q^2}{2m} \tag{A.7}$$

We see that for small $|q|$ the second term is small and the third is negligible. We can thus obtain $E_n(\vec{k} + \vec{q})$ from $E_n(\vec{k})$ by using first-order perturbation theory, which gives

$$E_n(\vec{k}+\vec{q}) = E_n(\vec{k}) + \int n^*_{n,k}(\vec{r})\frac{\hbar^2}{2m}\vec{q}\cdot\left(\vec{k}-i\nabla\right)n_{n,k}(\vec{r})dr^3 + ... \tag{A.8}$$

or equally

$$E_n(\vec{k}+\vec{q}) = E_n(\vec{k}) + \int \psi^*_{n,k}(\vec{r})\vec{q}\cdot\left(-\frac{\hbar^2}{2m}i\nabla\right)\psi_{n,k}(\vec{r})dr^3 + ... \tag{A.9}$$

Comparing with eq. (A.5) is possible to see that:

$$\nabla_k E_n(\vec{k}) = \frac{\hbar}{m}\left\langle p\right\rangle_{n,k} \tag{A.10}$$

Meanwhile, Ehrenfest's theorem gives the group velocity as

$$\vec{v} = \frac{d\left\langle \vec{r}_{n,k}\right\rangle}{dt} = \frac{1}{m}\left\langle p\right\rangle_{n,k} \tag{A.11}$$

Combining this

$$\vec{v} = \frac{1}{\hbar}\nabla_k E_n(\vec{k}) \tag{A.12}$$

In fact the motion of an electron regarded as a particle should be described by a wave packet. For an electron in a crystal this is a packet of Bloch waves centered on $\vec{k} = \vec{k}_0$, which is constructed by introducing other neighboring states $\vec{k}$ belonging to the same band n.

Note that, as the Bloch states are eigenstates of H the velocity of an electron in a Bloch state is constant: an electron in such a state suffers no collisions in the crystalline potential included in H. This is a fundamental fact: a periodic potential does not scatter Bloch electrons; it determines their constant velocity through eq. (A.12).

In a perfectly periodic crystal electrons suffering no collisions would thus have infinite conductivity. The deviations from periodicity determine the finite value of the conductivity. The defects that are most effective in producing scattering are the presence of impurities and the fact that at a finite temperature the crystal undergoes thermal vibrations which deform the perfect crystalline lattice. This excitations are call phonons and play an important role in limiting the mobility of electrons and holes in semiconductors.

A.2 Acceleration Theorem in the Reciprocal Space

Under the effect of an external electric field $\vec{E}$ the energy of an electron is modified. Lets assume that $\vec{E}$ varies little over the scale of the cell, and only slowly with time at the scale of the transition frequencies between permitted energy bands. The work dW done on an electron of speed $\vec{v}$ and charge $-e$ over the time interval dt changes its energy $E_n(\vec{k})$ by modifying the value of $\vec{k}$ and thus the crystal momentum. Hence we have the relation

$$dW = -e\vec{E} \cdot \vec{v}dt = \frac{dE_n(\vec{k})}{dt}dt \tag{A.13}$$

and with eq. (A.12) we get

$$-e\vec{E} \cdot \frac{1}{\hbar}\nabla_k E_n(\vec{k}) = \nabla_k E_n(\vec{k}) \cdot \frac{d\vec{k}}{dt} \tag{A.14}$$

then

$$\hbar\frac{d\vec{k}}{dt} = -e\vec{E} = \vec{F} \tag{A.15}$$

Here $\vec{F}$ is the applied force. This is the acceleration theorem in the reciprocal space. The essential result is that the response to an external force varying slowly in space and time is equal to the derivative of the crystal momentum and not the derivative of the electron momentum. In the presence of an electric field and a magnetic field B it is possible to generalize to

$$\hbar\frac{d\vec{k}}{dt} = -e(\vec{E} + \vec{v} \wedge \vec{B}) = \vec{F} \tag{A.16}$$

This equation describe the behavior of a packet of Bloch waves, localized to about Δr in real space, and to about $\Delta k \sim \frac{1}{\hbar \Delta r}$ in the reciprocal space. If the force $\vec{F}$ varies in time at the scale of the transition frequencies between bands the evolution of the system can no longer be described by the motion of the point $\vec{k}$ within a given band, but by transitions between bands. This is true for example for the effect of light on a semiconductor because optical frequencies are of the order of 10^{14} *Hz*.

A.3 Acceleration Theorem in Real Space and the Effective Mass

Differentiating the velocity $\vec{v}$ given by eq. (A.12) with respect to time, and using the acceleration theorem, we obtain

$$\frac{d\vec{v}}{dt} = (\nabla_k \vec{v}) \cdot \frac{d\vec{k}}{dt} = \frac{1}{\hbar^2} \nabla_k [\nabla_k E_n(\vec{k})] \cdot \vec{F} \tag{A.17}$$

or

$$\frac{dv_\alpha}{dt} = \sum_\beta \left(\frac{1}{m^*}\right)_{\alpha,\beta} F_\alpha \tag{A.18}$$

with

$$\left(\frac{1}{m^*}\right)_{\alpha,\beta} = \frac{1}{\hbar^2} \frac{\partial^2 E_n(\vec{k})}{\partial k_\alpha \partial k_\beta} \tag{A.19}$$

which defines the effective mass tensor $\overset{\leftrightarrow}{m}^*$ at a point $\vec{k}$ of a given band n. Expressions (A.18) and (A.19) constitute the acceleration theorem in real space, which is subject to the same restrictions of slow variations in space and time on the force $\vec{F}$ as eq. (A.16) from which it results. From its definition we see that the effective mass tensor is symmetric. The notion of effective mass is of most interest in the vicinity of an extremum of the band, where, to lowest order,

$$E_n(\vec{k}) - E_n(\vec{k}_0) \simeq \sum_{\alpha,\beta} \frac{\hbar^2}{m^*_{\alpha,\beta}} \Delta k_\alpha \Delta k_\beta \tag{A.20}$$

been $\vec{k}_0$ the wave vector at the extremum and $\vec{k} = \vec{k}_0 + \Delta\vec{k}$. At the zone center of a cubic crystal, if the energy is not degenerate, the constant energy surfaces are spheres. The effective mass is thus isotropic and has a value m^*. It is positive near a band minimum and negative near a band maximum. A negative effective mass implies from eq. (A.18), that the velocity resulting from the action of F_β is in the opposite direction from that acquired by an electron in vacuum acted on by F_β. This apparently paradoxical behavior can be compared with Hall effect experiments which in certain materials imply the existence of positive charge carriers. This is the origin of the concept of a *hole*. It shows that in a solid the response of an electron to an applied force is strongly influenced by the reaction to the crystal potential. Even when the effective mass has the same sign as m, the mass of a free electron, we can have values of m^*/m very different from unity. While in metals $m^*/m \sim 1$, this is not always true of semiconductors: the effective mass of the conduction band is $+0.067m$ in $GaAs$, and $+0.014m$ in $InSb$.

We note that the momentum formula for the simplest case can be written

$$m^* \frac{d\vec{v}}{dt} = \vec{F} \tag{A.21}$$

so that it is not the derivative of the ordinary momentum $md\vec{v}/dt$ which is equal to the external force. In this special case, the velocity (A.12) and crystal momentum are related by

$$\vec{v} = \frac{\hbar\vec{k}}{m^*} \tag{A.22}$$

Appendix B

Extra Plots and tables

B.1 Low Temperature Measurements

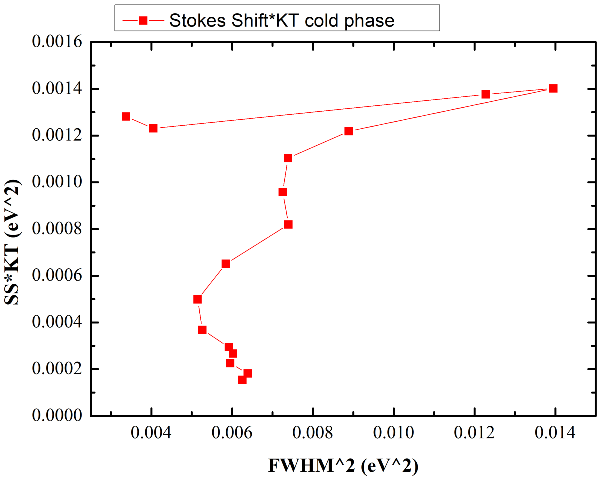

Figure B.1: $SS \times K_B T \ vs \ FWHM^2$ for the cold phase high energy peak in MAPI.

	Γ_0	ϕ_{AC}	ϕ_{LO}	E_{LO}
Day 2 Orthorhombic phase	$43.93\ meV$	$1.1 \times 10^{-29}\ eV$	$40.9\ meV$	$18.17\ meV$
Day 2 Tetragonal phase	$35.68\ meV$	$9.5037 \times 10^{-10}\ eV$	$60.3\ meV$	$19.57\ meV$
Day 3 Orthorhombic phase	$38.63\ meV$	$7.74331 \times 10^{-4}\ eV$	$141.2\ meV$	$27.42\ meV$
Day 3 Tetragonal phase	$33.35\ meV$	$3.98898 \times 10^{-2}\ eV$	$68.6\ meV$	$20.53\ meV$

Table B.1: Results of fitting of Γ for the second and third days of measurements with eq. (2.97) for each phase separately.

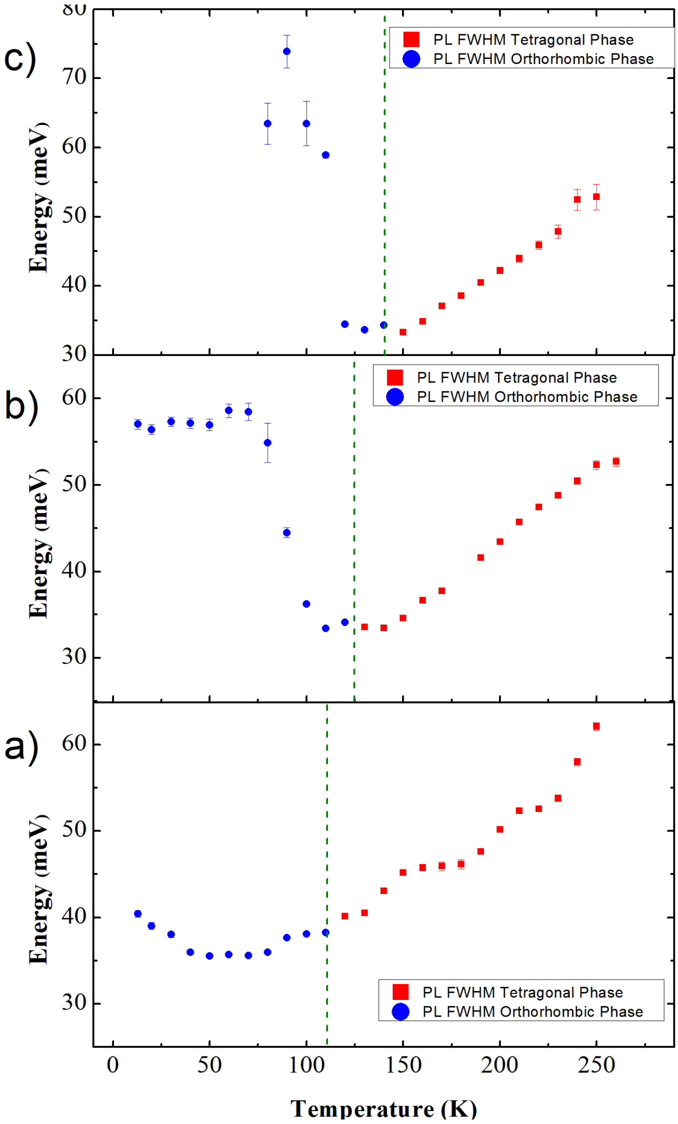

Figure B.2: FWHM of the excitonic photoluminescence peak as a function of the temperature. (a) First day of measurement. (b) Second day of measurement. (c) Third day of measurement. The vertical lines indicate the position of the phase transition.

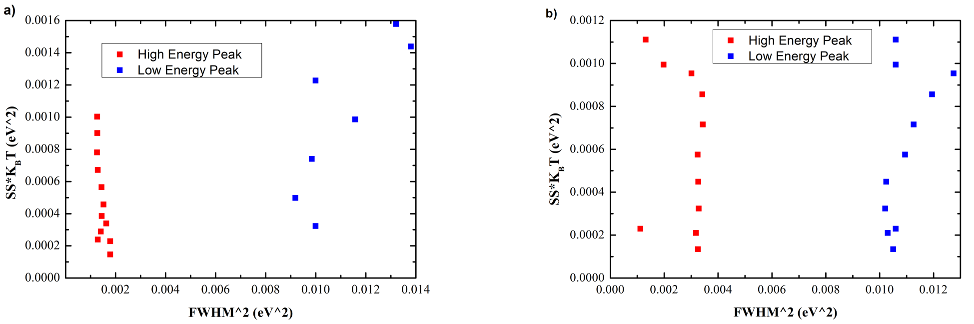

(a) First day of measurement. **(b)** Second day of measurement.

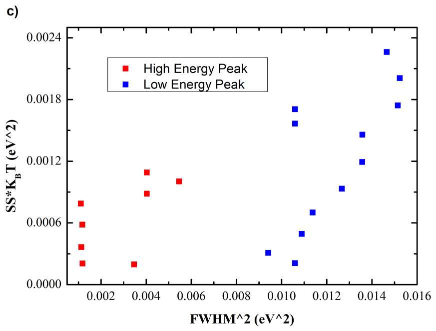

(c) Third day of measurement.

Figure B.3: Stokes shift times thermal energy vs Γ^2 for the orthorhombic phase including both peaks.

B.2 Impedance Measurements

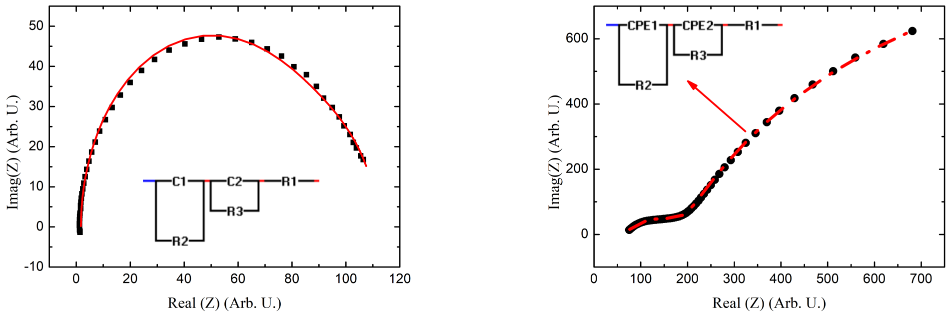

(a) Cell 1 under dark conditions **(b)** Cell 1 under light conditions

Figure B.4: Impedance measurements on cell 1 illuminated and under darck conditions. Courtesy od Master's candidate Nicolás Molina.

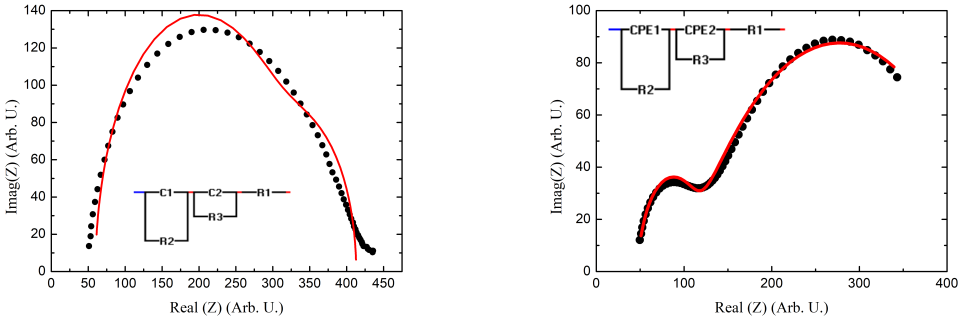

(a) Cell 4 under dark conditions **(b)** Cell 4 under light conditions

Figure B.5: Impedance measurements on cell 4 illuminated and under darck conditions. Courtesy od Master's candidate Nicolás Molina.

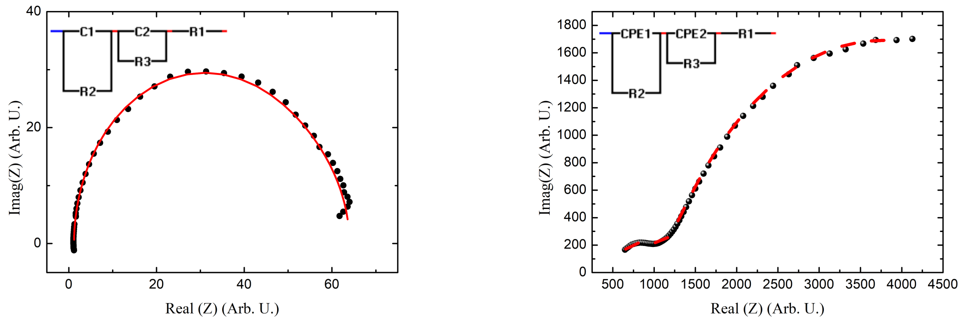

(a) Cell 7 under dark conditions

(b) Cell 7 under light conditions

Figure B.6: Impedance measurements on cell 7 illuminated and under darck conditions. Courtesy od Master's candidate Nicolás Molina.

B.3 Rates Model Example

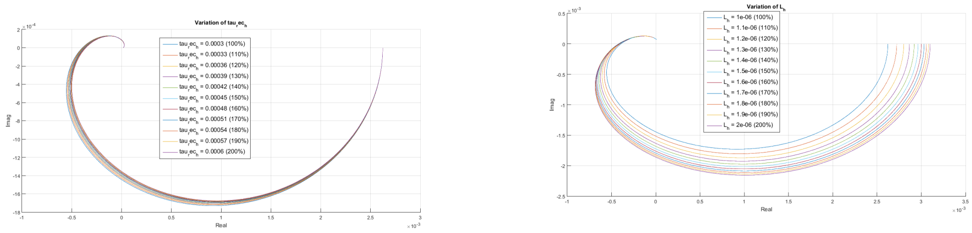

(a) Model of eq. 2.149 varying the lifetime

(b) Model of eq. 2.149 varying the diffusion length

Figure B.7: Implementation of the model of eq. 2.149 with $\alpha = 2e9$, thickness $7e^{-7}$ and varying the lifetime and the diffusion length.

B.4 Extra Plots of Chapter 5

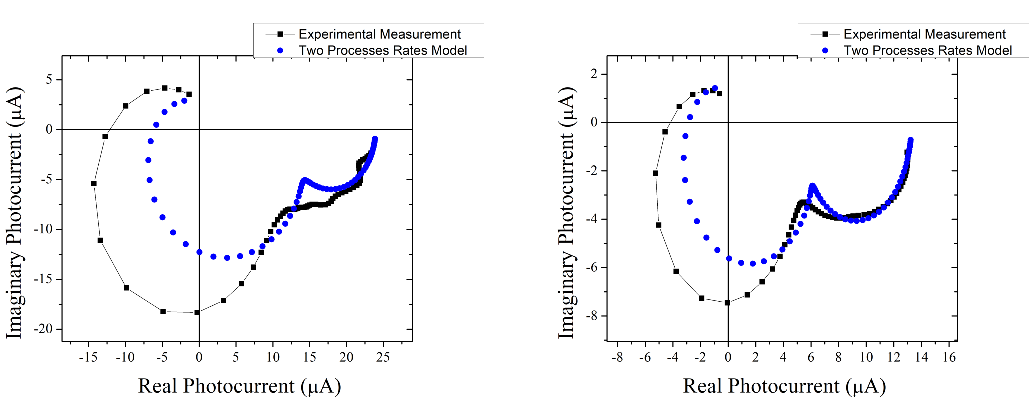

(a) Power 28.9 μW

(b) Power 42.7 μW

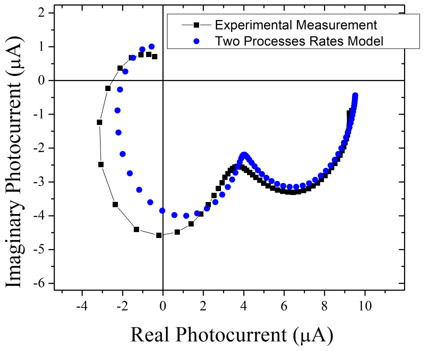

(c) Power 63.2 μW

Figure B.8: Intensity modulated photocurrent (black) and rates model fit (blue) for cell 1.

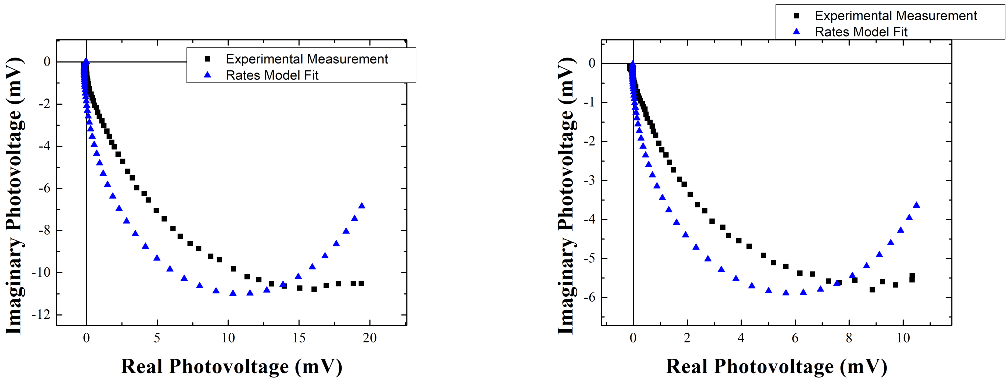

(a) Power 28.9 μW

(b) Power 63.2 μW

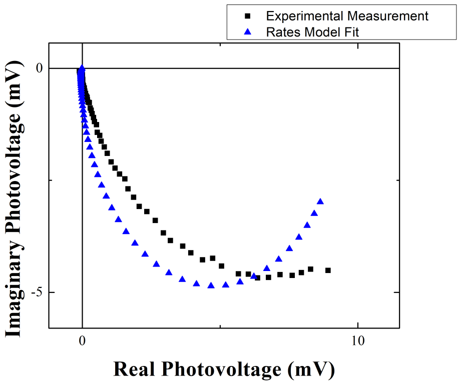

(c) Power 82.7 μW

Figure B.9: Intensity modulated photovoltage (black) and rates model fit (blue) for cell 1.

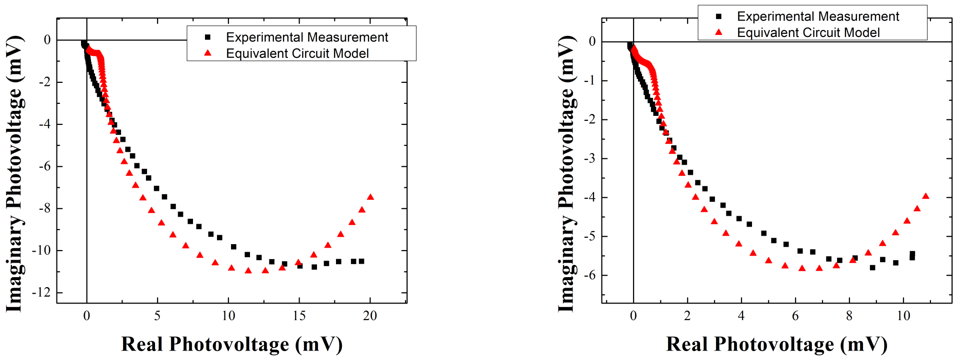

(a) Power 28.9 μW

(b) Power 63.2 μW

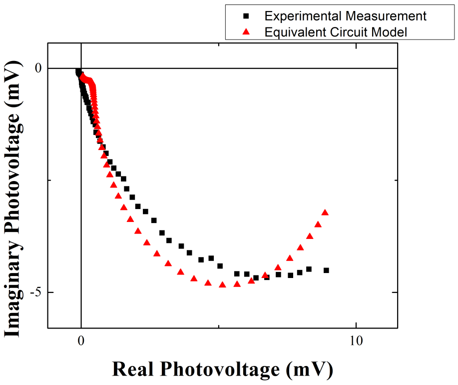

(c) Power 82.7 μW

Figure B.10: Intensity modulated photovoltage (black) and equivalent circuit model fit (red) for cell 1.

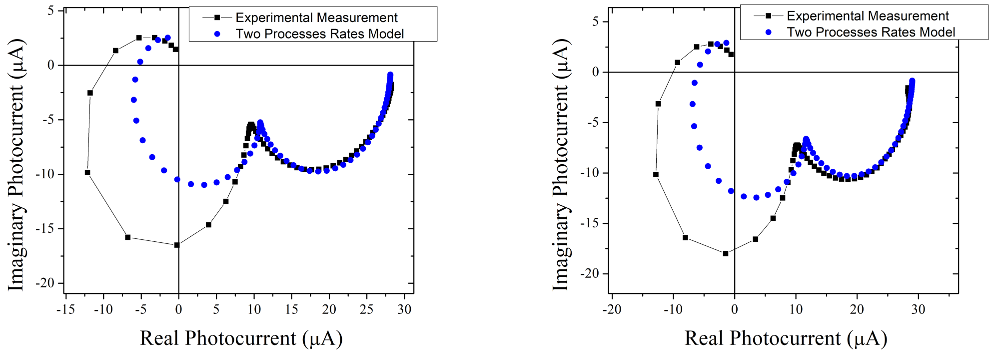

(a) Power 28.9 μW **(b)** Power 42.7 μW

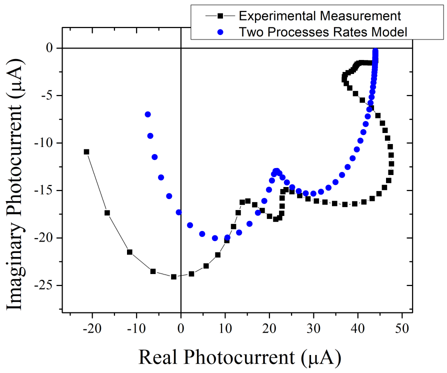

(c) Power 82.7 μW

Figure B.11: Intensity modulated photocurrent (black) and rates model fit (blue) for cell 6.

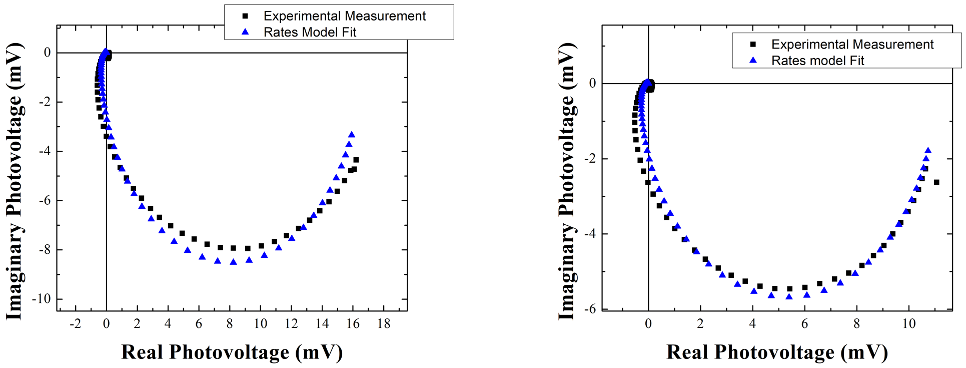

(a) Power 28.9 μW **(b)** Power 42.7 μW

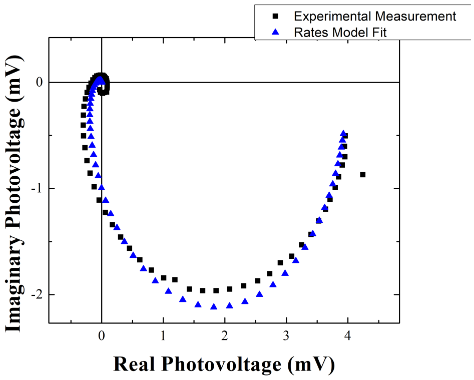

(c) Power 82.7 μW

Figure B.12: Intensity modulated photovoltage (black) and rates model fit (blue) for cell 6.

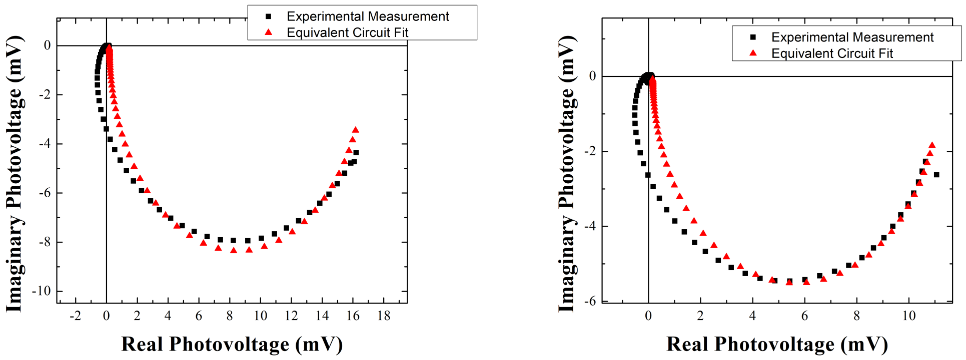

(a) Power 28.9 μW

(b) Power 42.7 μW

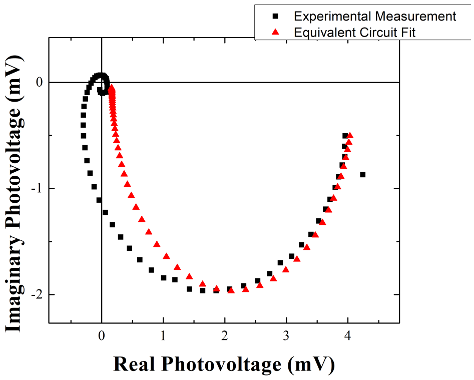

(c) Power 82.7 μW

Figure B.13: Intensity modulated photovoltage (black) and equivalent circuit model (red) fit for cell 6.

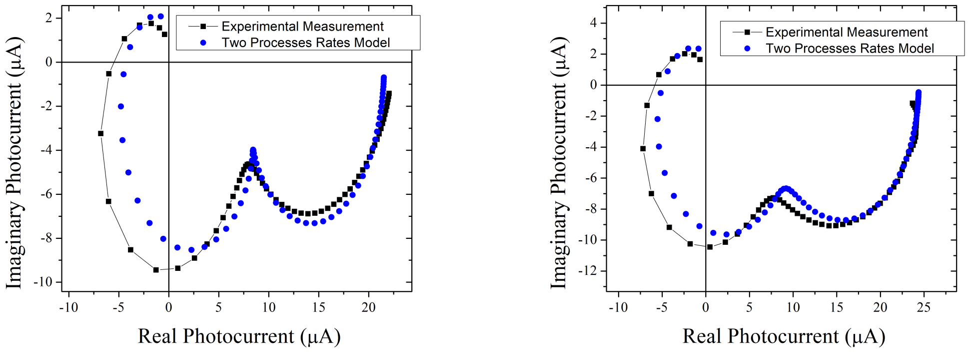

(a) Power 28.9 μW

(b) Power 63.7 μW

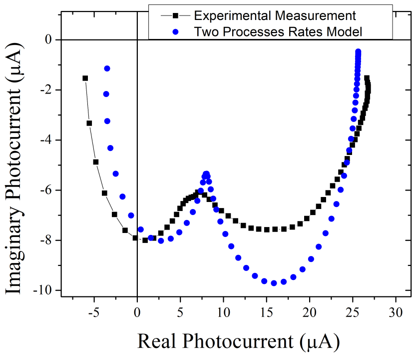

(c) Power 82.7 μW

Figure B.14: Intensity modulated photocurrent (black) and rates model fit (blue) for cell 7.

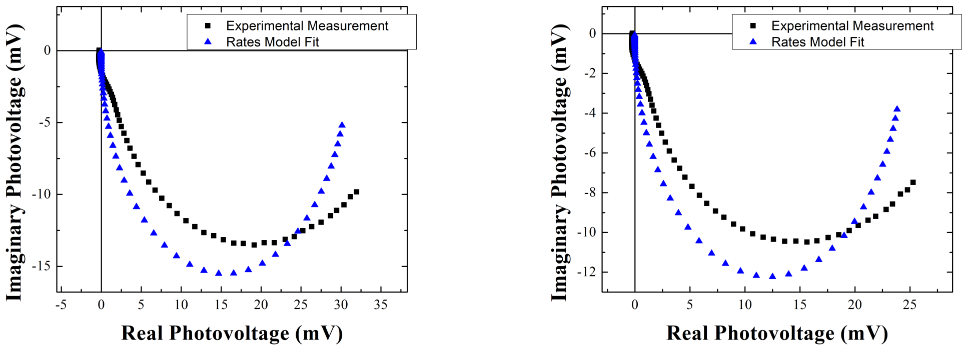

(a) Power 42.7 μW

(b) Power 63.7 μW

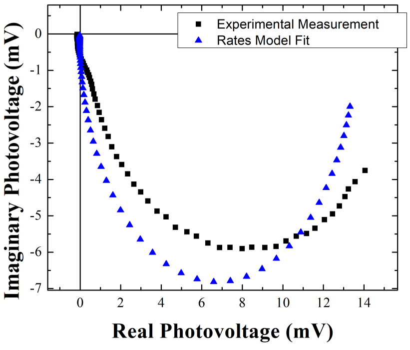

(c) Power 82.7 μW

Figure B.15: Intensity modulated photovoltage (black) and rates model fit (blue) for cell 7.

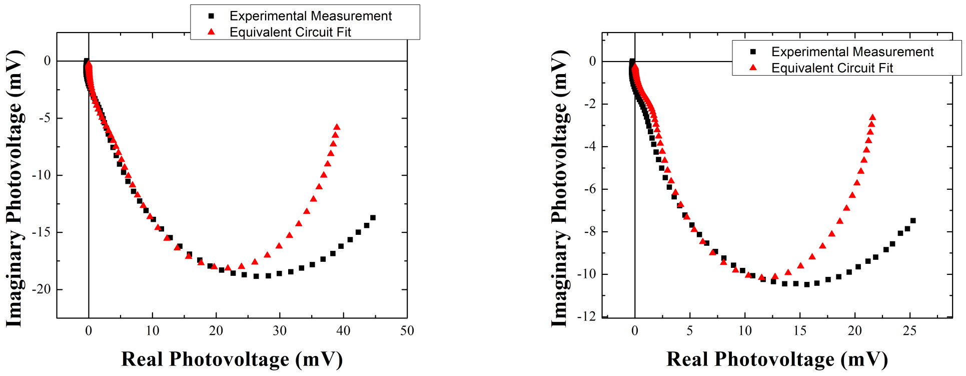

(a) Power 28.9 μW

(b) Power 63.7 μW

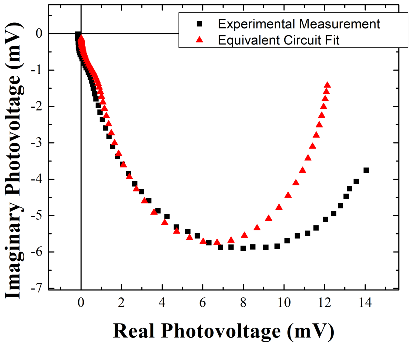

(c) Power 82.7 μW

Figure B.16: Intensity modulated photovoltage (black) and equivalent circuit model fit (red) for cell 7.

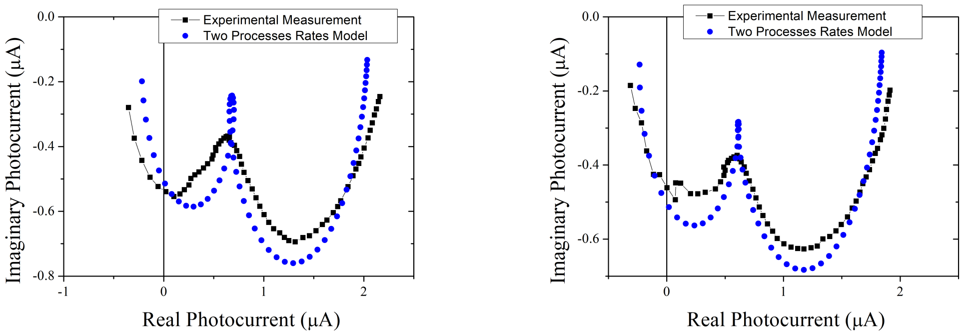

(a) Power 28.9 μW

(b) Power 42.7 μW

Figure B.17: Intensity modulated photocurrent (black) and rates model fit (blue) for cell 8.

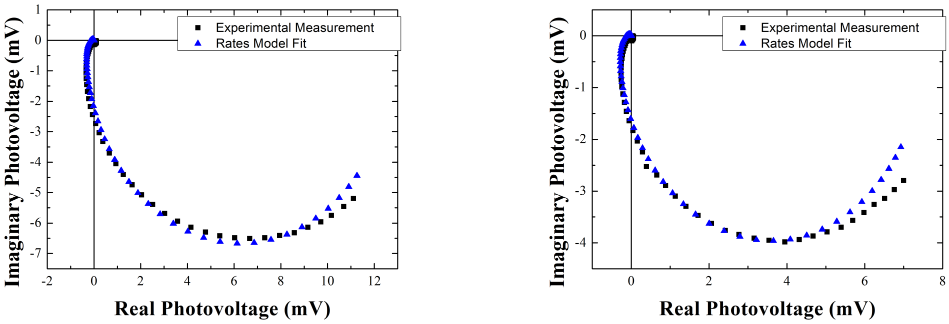

(a) Power 42.7 μW

(b) Power 63.7 μW

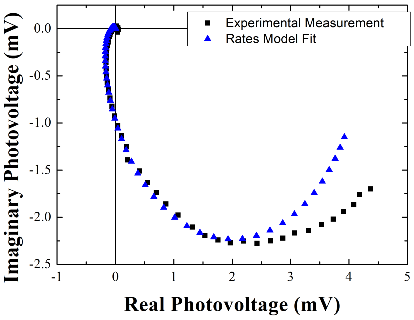

(c) Power 82.7 μW

Figure B.18: Intensity modulated photovoltage (black) and rates model fit (blue) for cell 8.

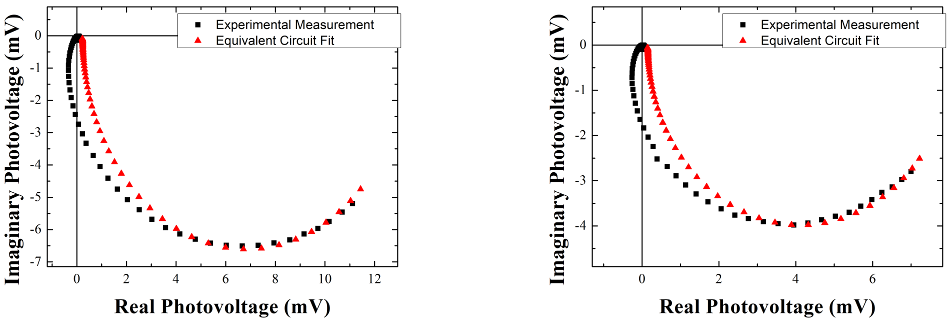

(a) Power 42.7 μW **(b)** Power 63.7 μW

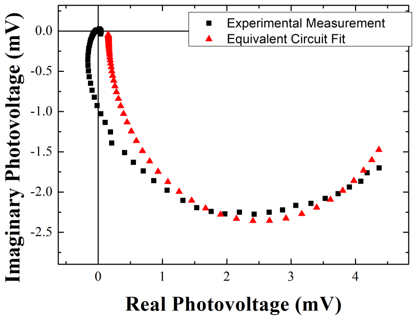

(c) Power 82.7 μW

Figure B.19: Intensity modulated photovoltage (black) and equivalent circuit model fit (red) for cell 8.

B.5 Extra Plots of Chapter 6

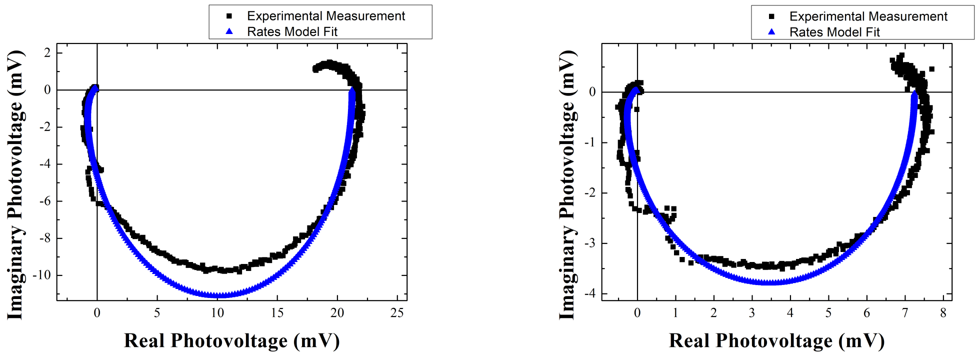

(a) Power 9.8 μW **(b)** Power 17.4 μW

Figure B.20: Intensity modulated photovoltage (black) and rates model fit (blue) for cell 6E.

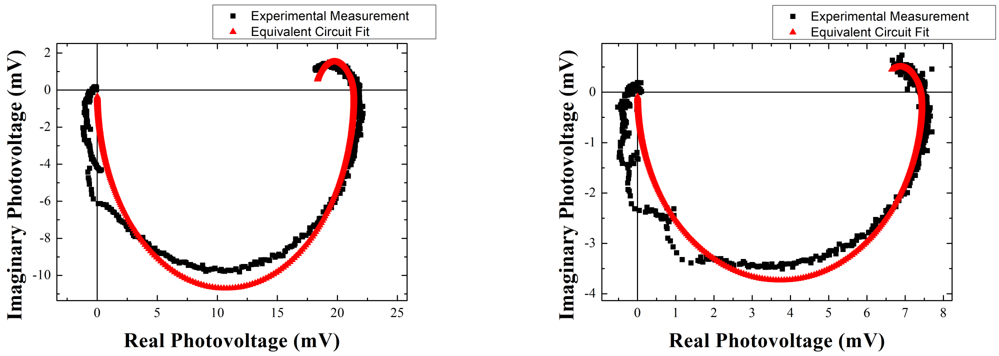

(a) Power 9.8 μW **(b)** Power 17.4 μW

Figure B.21: Intensity modulated photovoltage (black) and equivalent circuit model fit (red) for cell 6E.

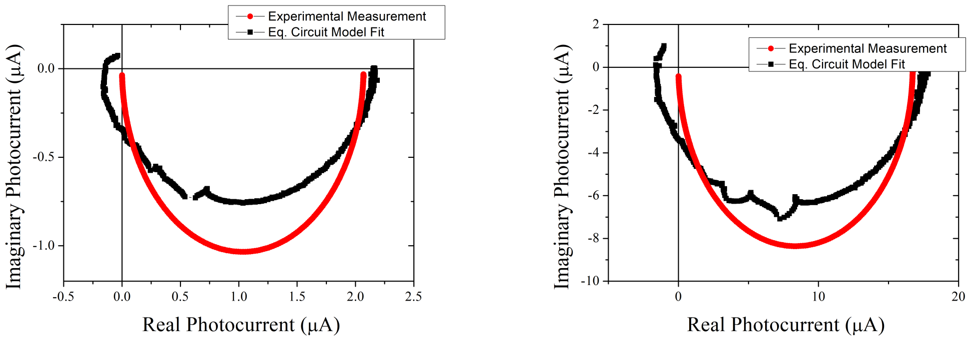

(a) Power 9.8 μW

(b) Power 17.4 μW

Figure B.22: Intensity modulated photocurrent (black) and equivalent circuit model fit (red) for cell 6E.

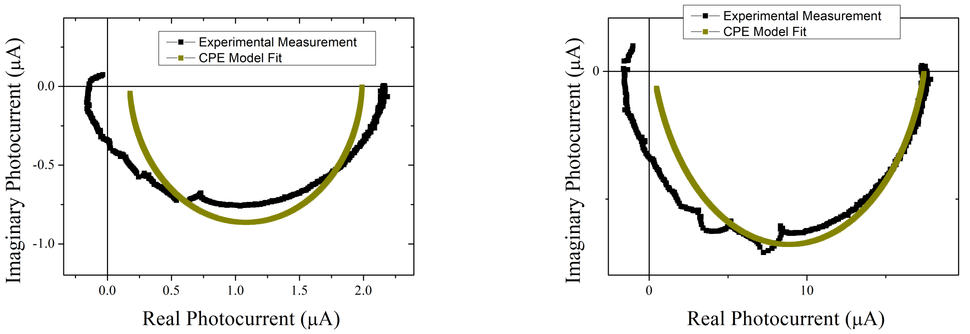

(a) Power 9.8 μW

(b) Power 17.4 μW

Figure B.23: Intensity modulated photocurrent (black) and constant phase element model fit (yellow) for cell 6E.

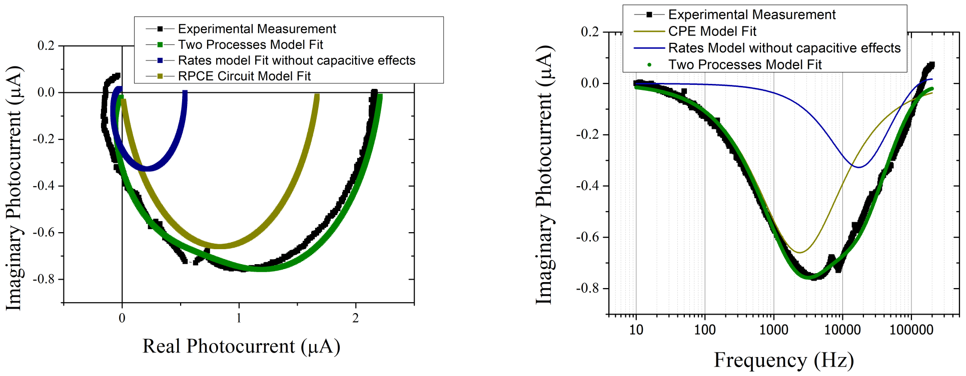

(a) Power 9.8 μW Nyquist

(b) Power 9.8 μW Imaginary component

Figure B.24: Intensity modulated photocurrent Nyquist plot and the imaginary component with the final model for cell 6E.

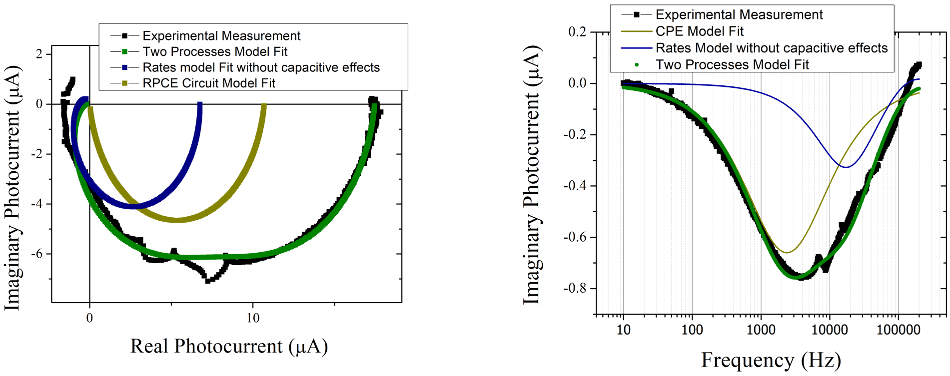

(a) Power 17.4 μW Nyquist

(b) Power 17.4 μW Imaginary componet

Figure B.25: Intensity modulated photocurrent Nyquist plot and the imaginary component with the final model for cell 6E.